Modeling Atmospheric Mercury Deposition to the Great Lakes: Projected Consequences of Alternative Future Emissions Scenarios

Final Report
for work conducted with FY2012 funding from the
Great Lakes Restoration Initiative

Oct 9, 2014

Mark Cohen, Roland Draxler, Richard Artz
NOAA Air Resources Laboratory
College Park, MD, USA

This page intentionally left blank

1 Contents

Acknowledgments

We would like to thank the following individuals, organizations, and programs for their important contributions to this analysis:

- Rick Jiang, Chief Information Officer at the Air Resources Laboratory, for maintenance, troubleshooting, and development of the Linux-based computational server used to carry out the modeling in this study;
- Hang Lei , NOAA, for providing emissions scenarios based on the Lei *et al*. (2013, 2014) analyses, that were adapted for use in this project;
- Eric Miller, Ecosystems Research Group, Norwich, Vermont, for providing 2005 ambient mercury monitoring data from the Underhill, Vermont site;
- Tom Holsen, Young-Ji Han[1], and colleagues at Clarkson University, for providing 2005 ambient mercury monitoring data from the Potsdam and Stockton, New York sites;
- Seth Lyman[2], Mae Gustin, and colleagues at the Desert Research Institute (DRI) in Reno, Nevada, for providing 2005 ambient mercury monitoring data for the Paradise, Gibbs Ranch, and Reno sites in Nevada;
- Seth Lyman, Dan Jaffe and colleagues at the University of Washington-Bothell, for providing 2005 ambient mercury monitoring data for the Mt. Bachelor, Oregon site;
- Environment Canada, for 2005 CAMNet ambient mercury monitoring data downloaded from the Canadian National Atmospheric Chemistry (NAtChem) Toxics Database;
- The following CAMNet Principal Investigators and their teams, responsible for contribution of Total Gaseous Mercury data for 2005 used in this analysis to the NAtChem Toxics Database:
    - Laurier Poissant and Martin Pilote (St. Anicet)
    - Frank Froude (Burnt Island, Egbert, and Point Petre)
    - Rob Tordon (Kejimkujik)
    - Alexandra Steffen and Cathy Banic (Alert)
    - Brian Wiens (Bratt’s Lake)
- National Atmospheric Deposition Program (NADP), Illinois State Water Survey, Champaign, IL, for 2005 mercury wet deposition data at sites in the NADP’s Mercury Deposition Network.

---

[1] Current affiliation: Kangwon National University, Kangwon Do, South Korea
[2] Current affiliation: Utah State University, Vernal, Utah

Executive Summary

This study examined the impact of alternative future emissions scenarios on the amount and source attribution of atmospheric mercury deposition to the Great Lakes. It represents an extension of the baseline analysis carried out with FY2010 Great Lakes Restoration Initiative (GLRI) funding (Cohen *et al.*, 2011) and sensitivity analysis carried out with FY2011 GLRI funding (Cohen *et al.*, 2013). The modeling analysis was carried out with the NOAA HYSPLIT-Hg model.

A baseline emissions inventory for the year 2000 and three future-scenario inventories for the year 2050 were adapted from the work of Lei *et al*. (2013, 2014) for this analysis. The inventories include anthropogenic emissions, emissions from biomass burning, emissions from land and ocean surfaces, prompt reemissions of recently deposited mercury, and emissions from volcanos. The three future scenarios encompass a range of potential technological and regulatory possibilities. The *2050 B1* scenario envisions a future with an emphasis on the introduction of clean and resource-efficient technologies. The *2050 B1* emissions are very similar to the baseline emissions, as pollution prevention and control balance out population growth and development. The *2050 A1B* and *2050 A1FI* scenarios envision a future with higher economic growth and more limited transition to clean technologies, assuming a relatively balanced energy supply (*2050 A1B*) or a fossil-fuel-intensive energy supply (*2050 A1FI*). These two scenarios both project substantially higher anthropogenic emissions of mercury than the baseline or *2050 B1* scenario. A graphical summary of the emissions inventories used in the analysis is shown in Figure 1.

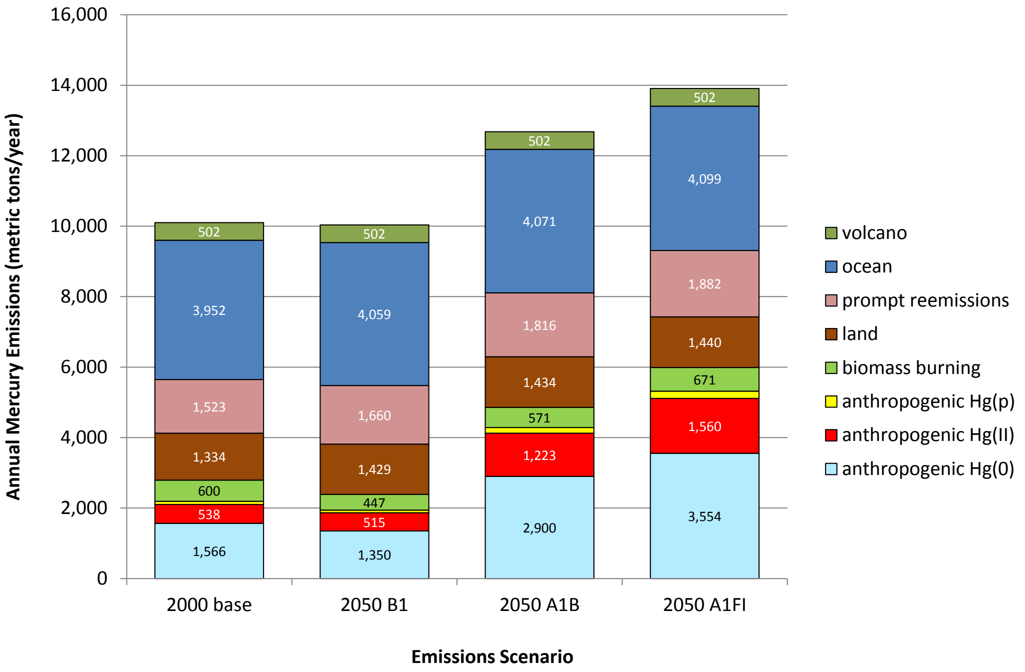

Figure 1. Emissions inventories used in this analysis

The fate and transport of the emitted mercury from each inventory was modeled using the HYSPLIT-Hg model. In carrying out this modeling, all of the emissions in a given inventory or inventory subset were modeled simultaneously. This methodology differs from that used in earlier phases of this work, which employed unit-emission standard source locations and interpolation. While the source-attribution results that can be obtained with the new approach are less detailed, useful results can still be developed using only a small fraction of the computational resources required in the previous methodology.

The modeling results were evaluated by comparison against ambient measurements of atmospheric mercury concentrations and wet deposition, representing a significant extension over the wet-deposition only evaluation carried out in earlier phases of this work. This evaluation resulted in several important findings:

- The model spin-up time used in the earlier work (3 months), while generally sufficient for deposition estimates, was not long enough to produce realistic elemental mercury (Hg(0)) concentrations. Extensive testing led to the conclusion that 24 months of model spin-up was necessary. Thus, the model had to be run for the years 2003 and 2004 before realistic results could be obtained for 2005.
- The rates of reactions oxidizing Hg(0) used in earlier phases of this work appear to have been too fast, leading to unrealistically low Hg(0) concentrations. Reducing these rates by a factor of 2-3 resulted in concentrations encouragingly consistent with measurements. The reduction of these rates is plausible given the large uncertainty – and potential overestimation -- in their experimental determination.
- The assumed generation of particulate mercury (Hg(p)) from the oxidation of Hg(0) by ozone, hydroxyl radical and hydrogen peroxide appears to result in unrealistically high Hg(p) concentrations. The product of these reactions was changed to ionic mercury (Hg(II)). This change was considered plausible given the substantial uncertainty in the product profile of these reactions, and the fact that this assumption is also now made in other models.

The model was evaluated by comparing its predictions with measurements. Ambient concentration measurement data for 2005 are relatively limited. However, comparisons of modeled vs. measured Hg(0) concentrations could be made at 13 sites, and comparisons of Hg(II) and/or Hg(p) could be made at 7 sites. Wet deposition data are more widely available and modeled vs. measured comparisons could be carried out at 86 sites, including 32 in the Great Lakes region. There are inherent difficulties in matching estimates from a relatively coarse-grid model -- a 2.5^{o} x 2.5^{o} grid was used in this analysis -- with measurements made at specific “point” locations. Moreover, there are large, acknowledged uncertainties in the atmospheric chemistry and physics of mercury. Nevertheless, the modeling was found to produce mercury concentrations and wet deposition reasonably consistent with measurements. This agreement lends credibility to the results.

Using the new model configurations indicated above, the amounts and source-attribution of atmospheric mercury deposition to the Great Lakes and their watersheds was estimated for each scenario and for selected subsets of each scenario. A complete analysis was carried out for two separate configurations: one that assumed the Hg(0) oxidation reactions were reduced to 33% of their initial rate ("oxid33") and one that assumed reduction to 50% of their original rate ("oxid50"). In each configuration the Hg(p) fraction in the products of the O_3, OH, and H_2O_2 oxidation reactions were assumed to be zero ("pf0"). Detailed results for all of the Great Lakes are presented in the body of the report, but a few illustrative examples will be provided here in the Executive Summary. The deposition flux amounts arising from different inventory components in each scenario and for each model configuration are shown for Lake Erie (Figure 2) and Lake Superior (Figure 3).

Based on these figures and other results presented in this work, several key findings can be summarized. First, for any given scenario, there is little difference between the results using the different "oxid33" and "oxid50" configurations. This suggests that the results are not highly sensitive to this uncertainty in the atmospheric chemistry of mercury. Next, the deposition arising from the *2050 B1* inventory is very similar to that in the *2000 baseline* inventory, an expected result given the similarity in emissions. The deposition arising from the two higher-emissions future scenarios (*2050 A1B* and *2050 A1FI*) is significantly increased. In fact, in comparing the increases in emission from Figure 1 (~20-40%) with the relative increases in deposition shown in Figure 2 and Figure 3 (a factor of almost 2-3), it can be seen that the model-estimated deposition is disproportionately higher than the overall increase in emissions. The reason for this disproportionality is likely the increase in anthropogenic Hg(II) emissions in the Great Lakes region, which have a greater local and regional depositional impact than other forms of emitted mercury, i.e., Hg(0) and Hg(p). The higher-emission future scenarios contain a higher proportion of Hg(II) emissions in the Great Lakes region and elsewhere, compared to the *2000 baseline* and *2050 B1* emissions.

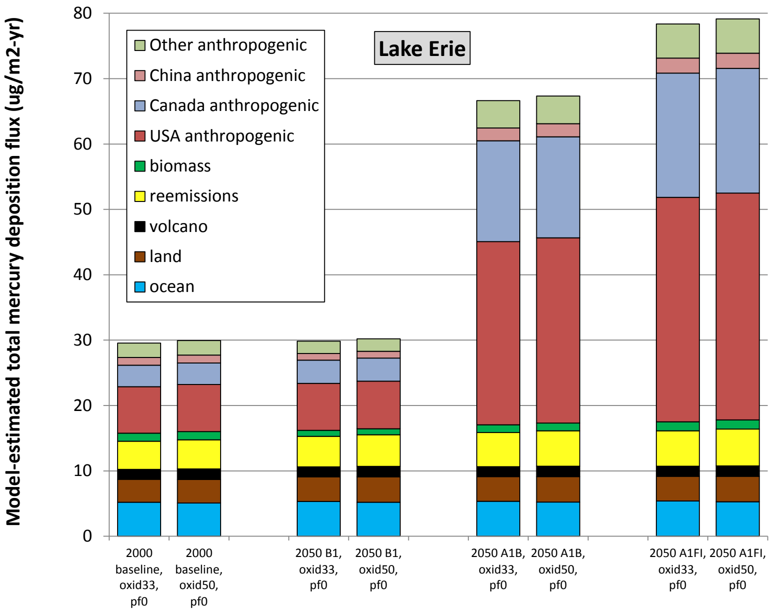

Figure 2. Overall source-attribution synthesis for deposition flux amounts for Lake Erie

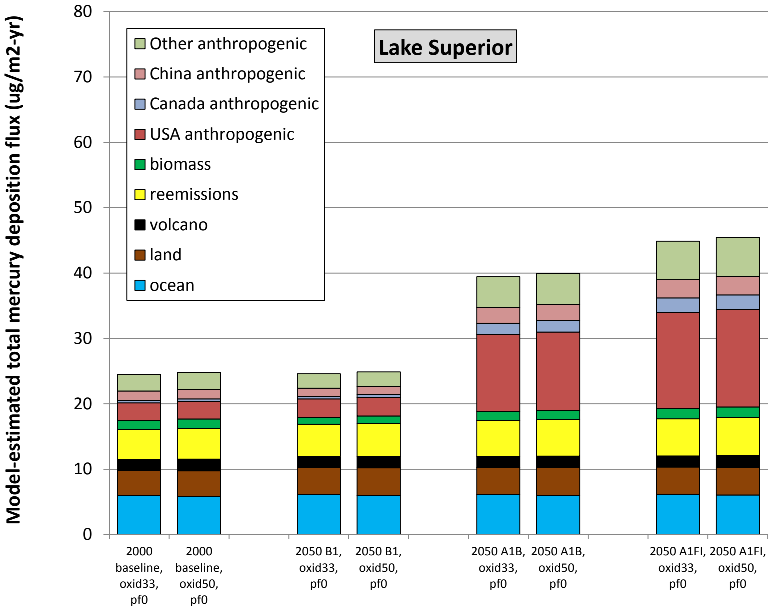

Figure 3. Overall source-attribution synthesis for deposition flux amounts for Lake Superior

For Lake Erie (and also Lake Ontario and Lake Michigan), these model-based estimates show that that direct anthropogenic emissions from the USA contribute the largest amount of atmospheric mercury deposition, on the order of ~20% of the total for the *2000 baseline* and *2050 B1* inventories, and on the order of ~40% for the *2050 A1B* and *2050 A1FI* scenarios. For Lake Superior (and Lake Huron), the contribution from direct anthropogenic emissions in the USA are smaller, on the order of 10-15% in the *2000 baseline* and *2050 B1* inventories, and on the order of ~30% in the *2050 A1B* and *2050 A1FI* inventories.

Cohen, M., R. Draxler, R. Artz (2011). *Modeling Atmospheric Mercury Deposition to the Great Lakes. Final Report for work conducted with FY2010 funding from the Great Lakes Restoration Initiative.* NOAA Air Resources Laboratory, Silver Spring, MD. 160 pages.

Cohen, M., R. Draxler, R. Artz (2013). *Modeling Atmospheric Mercury Deposition to the Great Lakes: Examination of the Influence of Variations in Model Inputs, Parameters, and Algorithms on Model Results. Final Report for work conducted with FY2011 funding from the Great Lakes Restoration Initiative.* NOAA Air Resources Laboratory, Silver Spring, MD. 157 pages.

Lei, H., Liang, X.-Z., Wuebbles, D.J., Tao, Z. (2013). Model analyses of atmospheric mercury: present air quality and effects of transpacific transport on the United States. *Atmos Chem Phys* **13**: 10807-10825.

Lei, H., Wuebbles, D.J., Liang, X.-Z., Tao, Z., Olsen, S., Artz, R., Ren, X., and Cohen, M. (2014). Projections of atmospheric mercury levels and their effect on air quality in the United States. *Atmos Chem Phys* **14**: 783-795.

1. Introduction

Mercury contamination in the Great Lakes Basin remains an important public and wildlife health concern as well as an economic issue (Bhavsar *et al*., 2010; Cohen *et al*., 2007; Evers *et al*., 2011ab; Gandhi *et al*., 2014). This report describes work done during the 3rd phase of an ongoing project, supported by FY2012 funding through the Great Lakes Restoration Initiative (GLRI).

The first phase of the project, carried out with FY2010 GLRI funding, was summarized in Cohen *et al*. (2011). In that initial work, a 2005 baseline analysis of atmospheric deposition to the Great Lakes was carried out, including source-attribution for the model-estimated deposition. The modeling results were found to be consistent with measurements of mercury wet deposition in the Great Lakes region. The 2nd phase of the project, carried out with FY2011 GLRI funding, was summarized in Cohen *et al*. (2013. In that FY2011 work, a detailed sensitivity analysis was carried out to examine the influences of important uncertainties in model inputs and methodologies.

The overarching goal of this FY2012 "3rd phase" work is to estimate the consequences of potential future emissions scenarios on atmospheric mercury deposition to the Great Lakes and their watersheds (Figure 4).

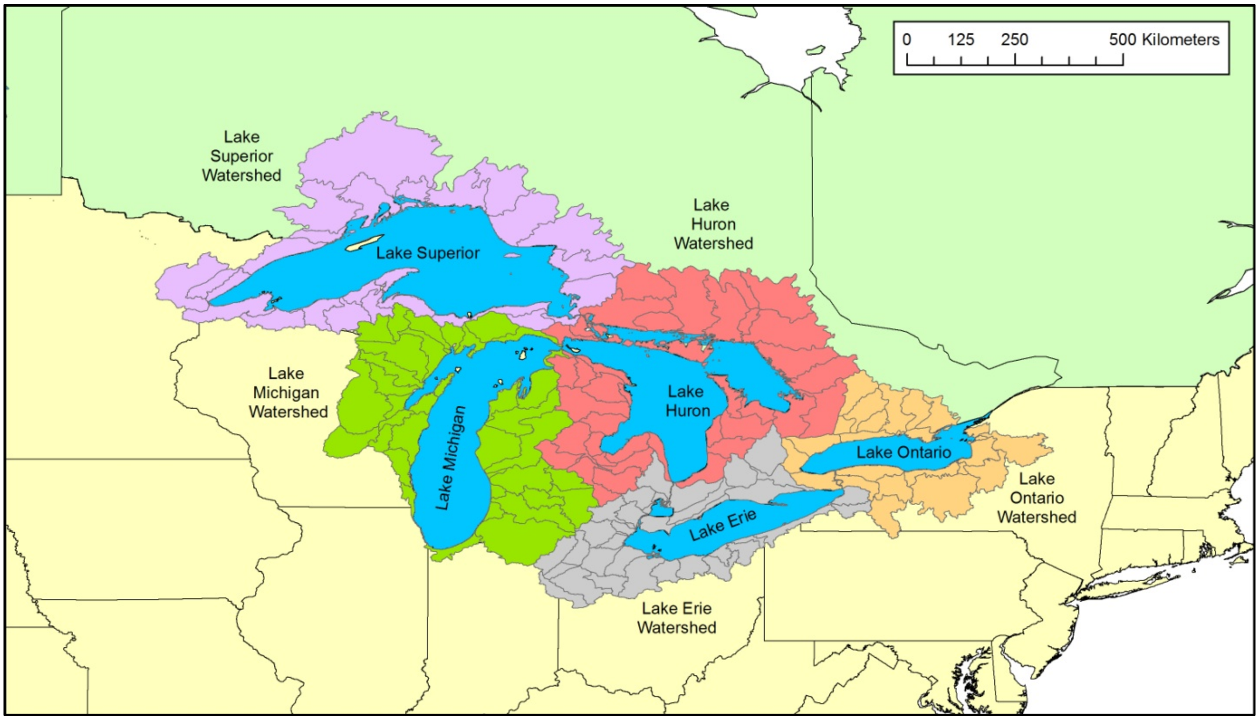

Figure 4. Great Lakes and their watersheds

In this report we will refer to three "kinds" of atmospheric mercury: (i) elemental mercury, Hg(0), also called Gaseous Elemental Mercury or GEM; (ii) soluble oxidized mercury (Hg(II)), also referred to as reactive gaseous mercury (RGM); and (iii) particulate mercury, or Hg(p). Except where noted, e.g., in the model evaluation section, results presented in this report are for total mercury (the sum of the three different forms), for simplicity and brevity's sake, even though the entire modeling analysis has been done with explicit treatment of the different mercury forms.

2. Emissions Scenarios

The baseline and future mercury emissions scenarios used in this work are based on the recent analysis of Lei *et al*. (2014). As described in that analysis, the "baseline" scenario is for the year 2000. This differs from the 2005 baseline used in earlier phases of this study. The year-2000 baseline emissions inventory was adopted for this work because it was the starting point for the Lei *et al*. (2014) future emissions scenarios, and so, was considered the most appropriate baseline inventory to compare those future scenarios with.

Three different "future" emissions scenarios have been analyzed, each for the year 2050: A1B, A1FI, and B1. As described by the Intergovernmental Panel on Climate Change (IPCC, 2000), the scenarios are based on the "storylines" as shown in Table 1 below.

Table 1. Main Characteristics of Future Emissions Scenarios (as described in IPCC, 2000)

Scenario	Main Scenario Storyline	Subgroup Storyline
2050 A1B	"The A1 storyline and scenario family describes a future world of very rapid economic growth, global population that peaks in mid-century and declines thereafter, and the rapid introduction of new and more efficient technologies. Major underlying themes are convergence among regions, capacity building, and increased cultural and social interactions, with a substantial reduction in regional differences in per capita income. The A1 scenario family develops into three groups that describe alternative directions of technological change in the energy system. The three A1 groups are distinguished by their technological emphasis: fossil intensive (A1FI), non-fossil energy sources (A1T), or a balance across all sources (A1B)."	*Technological emphasis*: a balance across all sources, "…defined as not relying too heavily on one particular energy source, on the assumption that similar improvement rates apply to all energy supply and end use technologies."
2050 A1FI		*Technological emphasis*: fossil fuel intensive
2050 B1	"The B1 storyline and scenario family describes a convergent world with the same global population that peaks in midcentury and declines thereafter, as in the A1 storyline, but with rapid changes in economic structures toward a service and information economy, with reductions in material intensity, and the introduction of clean and resource-efficient technologies. The emphasis is on global solutions to economic, social, and environmental sustainability, including improved equity, but without additional climate initiatives."	

As described in Lei *et al*. (2013, 2014), mercury emissions were estimated for the 2000 baseline and for each of the future scenarios, following the procedure presented by Streets *et al*. (2009). The emissions are summarized in Table 2 and Figure 5[3]. It is noted that the subtotal of direct anthropogenic and biomass emissions shown in Table 2 are consistent with the totals estimated by Streets *et al*. (2009)[4].

Table 2. Annual mercury emissions (metric tons/year) in the 2000 (baseline) and future emissions scenarios

Emissions Category	Description of Category	Scenario			
		2000	**2050 B1**	**2050 A1B**	**2050 A1FI**
anthropogenic Hg(0)	Emissions from industrial, commercial, residential, and mobile sources, separated into three different mercury forms	1,566	1,350	2,900	3,554
anthropogenic Hg(II)		538	515	1,223	1,560
anthropogenic Hg(p)		87	75	165	203
biomass burning	Emissions of Hg(0) from intentional and unintentional burning of biofuels, forests, crops, grassland, and other biomass	600	447	571	671
Subtotal anthropogenic industrial + biomass		**2,791**	**2,387**	**4,859**	**5,988**
land	Emissions of Hg(0) from the land surface to the air, e.g., from mercury present in soil and vegetation (not including the prompt re-emissions noted below)	1,334	1,429	1,434	1,440
reemission	A portion (~20%) of Hg(II) deposited to land is assumed to be promptly re-emitted as Hg(0)	1,523	1,660	1,816	1,882
Subtotal land + reemission		**2,857**	**3,088**	**3,250**	**3,322**
ocean	Emissions of Hg(0) from the ocean surface to the air from the near-surface mercury pool	3,952	4,059	4,071	4,099
volcanos	Emissions of Hg(0) from volcanoes	502	502	502	502
total		**10,102**	**10,036**	**12,681**	**13,910**

The land, reemissions, ocean, and biomass burning emissions categories were specified on a monthly basis, and the modeling was done using these temporally varying, monthly emissions estimates. The monthly emission periods used were actually 1/12 of year (30.42 days) and did not exactly correspond to the calendar months. However, for simplicity, the periods are designated according to months in the example graphs shown for biomass burning and total mercury emissions, for the 2000 baseline inventory, in Figure 6 and Figure 7, respectively. In the tables, graphs, and maps shown in this report,

---

[3] In Figure 5, numerical values for anthropogenic Hg(p) emissions are not shown explicitly, due to space limitations and readability. For reference, the values are 87, 75, 165, and 203 Mg/yr, respectively for the 2000, 2050 B1, 2050 A1B, and A1FI scenarios.

[4] In Table 3 of Streets *et al*. (2009), the total anthropogenic emissions shown for the year 2000 were 2190 Mg/yr, but this did not include ~600 Mg/yr from biomass burning. So, the Streets *et al* (2009) year-2000 subtotal for anthropogenic + biomass burning emissions amounts to 2790 Mg/yr, essentially the same as that used here (2791 Mg/yr). In Table 4 of Streets *et al*. (2009), the anthropogenic/biomass subtotals are given directly for the 2050 A1B and 2050 B1 scenarios as 4856 Mg/yr and 2386 Mg/yr, respectively, which are again essentially the same subtotals that are used in here. Streets *et al*. (2009) did not present estimates for the 2050 A1FI scenario.

the annual totals are generally shown, unless otherwise indicated. In contrast, the anthropogenic and volcano emissions were assumed to be constant throughout the year. While these categories might be expected to show some intra-annual variation, data regarding temporal variations in these sources is not generally available and is not generally included in emissions inventories.

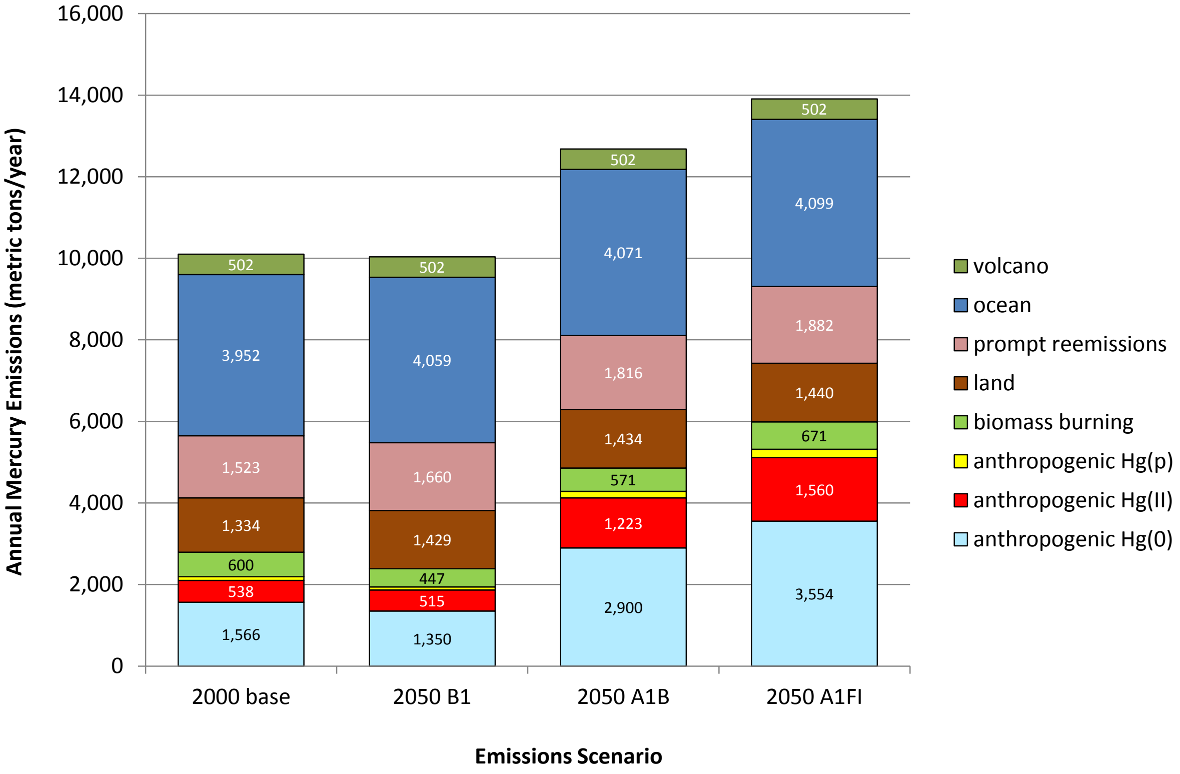

Figure 5. Graphical summary of emissions inventories used in this analysis

In the Lei *et al*. (2013, 2014) studies, the CAM-Chem/Hg model was used, with a horizontal grid resolution of 2.5° x 1.9°. The grid used in this HYSPLIT-Hg analysis, however, has a horizontal resolution of 2.5° x 2.5°. In order to use the Lei *et al*. emissions inventories, the emissions data had to be translated from the original grid to the HYSPLIT-Hg grid. An interpolation procedure was developed to re-grid the data, taking care to ensure that the total emissions in any dataset remained the same across the different grids. As an example, the total emissions in the 2000 baseline inventory on the CAM-Chem/Hg of 2.5° x 1.9° grid is shown in Figure 9, and the same inventory transformed to the HYSPLIT-Hg of 2.5° x 2.5° grid is shown in Figure 10. It can be seen in comparing the two figures that the transformation appears to have faithfully reproduced the distribution of emissions, allowing for small, inherent, expected differences due to spatial averaging and interpolation.

Examples of the geographical distribution of annual emissions in the different inventory categories (anthropogenic, biomass burning, land, etc.) for the 2000 baseline emissions inventory are shown side by side in Figure 11. These figures are relatively small, and a complete larger set of comparable figures for the 2000 baseline inventory and other scenarios are provided in the Appendix. Total annual mercury emissions maps for the future scenarios, showing the geographical distribution of emissions, are presented in Figure 12 (2050 B1), Figure 13 (A1B), and Figure 14 (A1FI).

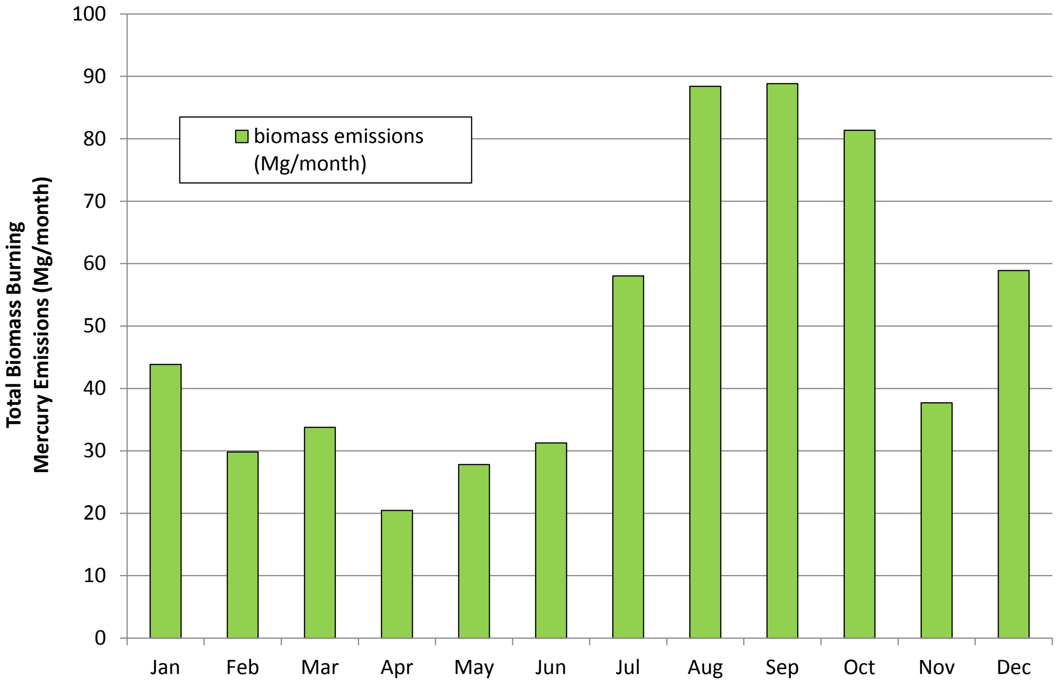

Figure 6. Monthly total biomass burning mercury emissions in the 2000 baseline inventory

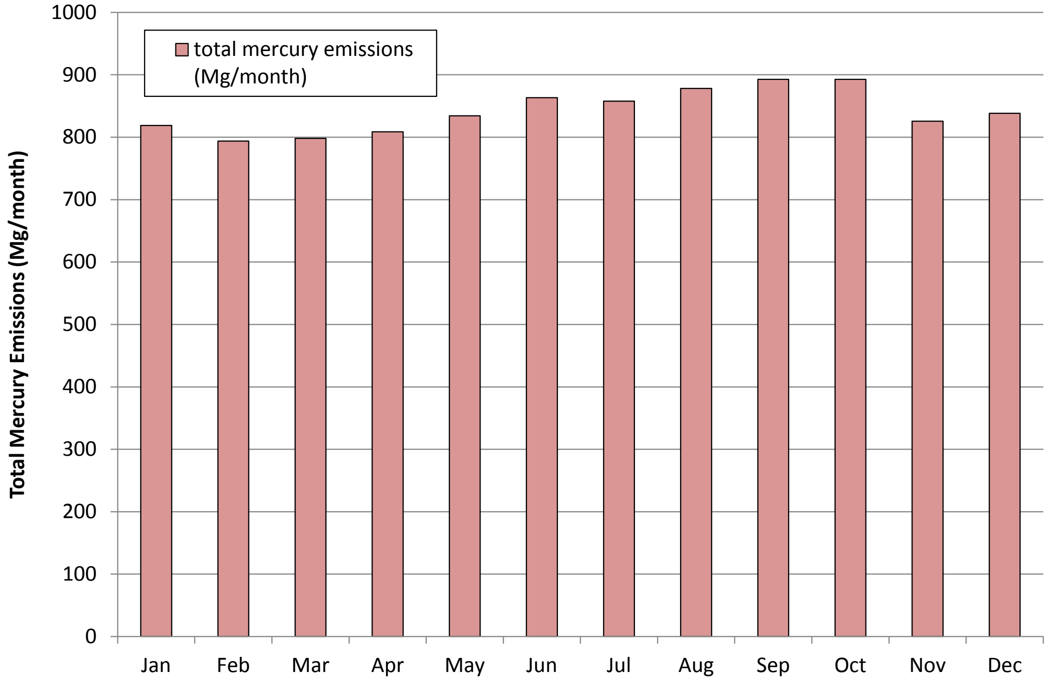

Figure 7. Monthly total mercury emissions in the 2000 baseline inventory

As noted above, the baseline year 2000 inventory used in Lei *et al*. (2013, 2014), with a total mercury emissions of ~10,000 Mg/yr differs from the 2005 inventories used in earlier phases of this work (Cohen *et al*., 2011, 2013), with emissions of ~6,000 and ~8000 Mg/yr, depending on the assumptions used regarding re-emissions. The inventories are compared in Figure 8 and Table 3. The GLRI FY10 and FY11 inventories for 2005 are designated by their land and water (ocean) re-emissions subtotals:

- *2005: L750 W1250* refers to an inventory with land re-emissions of 750 Mg/yr and water re-emissions of 1250 Mg/yr.

- *2005: L750 W1250* refers to an inventory with land re-emissions of 750 Mg/yr and water re-emissions of 1250 Mg/yr.

The emissions are categorized differently and so it is difficult to compare subtotals. For example, in the Cohen *et al*. (2011, 2013) inventories, emissions from land surfaces are divided into "natural" emissions and re-emissions of previously deposited anthropogenic mercury. However, in the Lei *et al*. (2013, 2014) inventory, emissions from land are divided into "prompt re-emissions" and "long-term emissions/re-emissions", with no distinction made between natural and anthropogenic. The largest differences between the inventories are the inclusion of biomass burning and substantially larger emissions from the ocean in Lei *et al*. (2013, 2014) inventory.

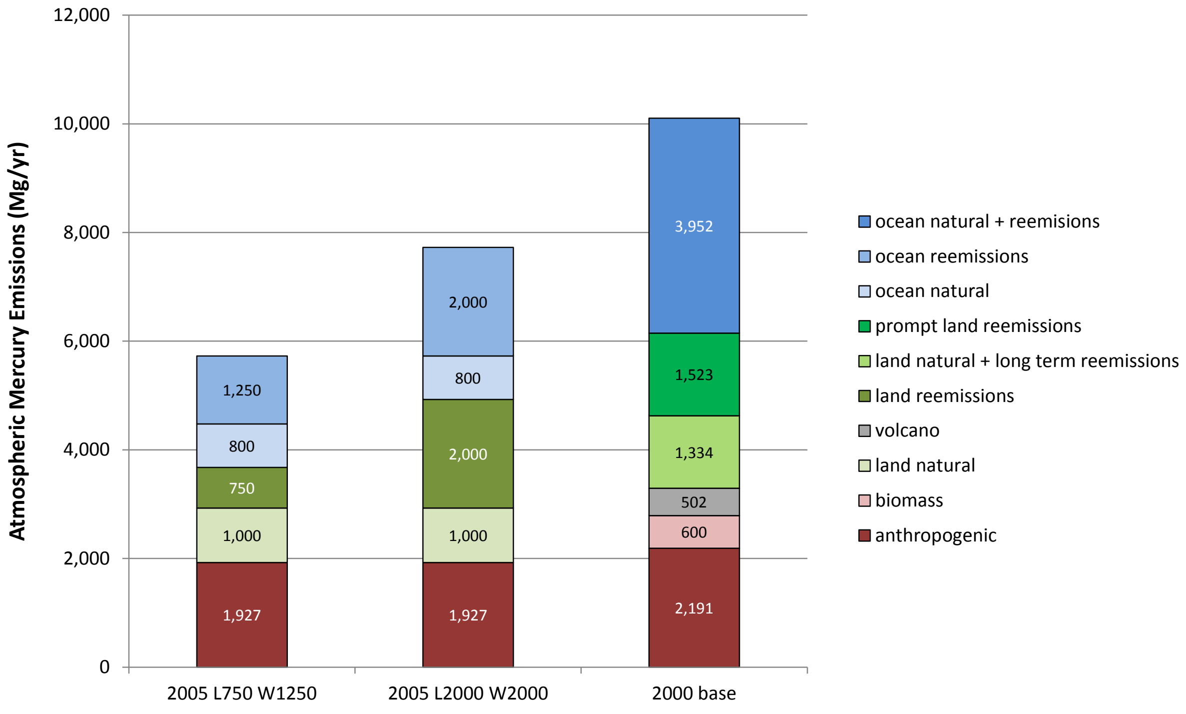

Figure 8. Comparison of Emissions Inventories used in Previous Work with Current Estimates

Table 3. Comparison of Emissions Inventories used in Previous Work with Current Estimates

		Mercury Emissions to the Air (Mg/yr)		
		A: Cohen *et al*., 2011, 2013		B: Lei *et al*., 2013, 2014
Emissions Category	**Notes**	**2005: L750 W1250**	**2005: L2000 W2000**	**2000-base**
Anthropogenic	“A” includes some biomass burning	1,927	1,927	2,191
Biomass	Includes intentional and unintentional biomass burning			600
Subtotal Anthropogenic		**1,927**	**1,927**	**2,791**
Land Natural	Includes some continuously gassing volcanic	1,000	1,000	
Volcano	Continuously gassing volcanic			502
Land Re-Emissions	From previously deposited anthropogenic	750	2,000	
Land Natural + Long-Term Re-Emissions				1,334
Prompt Land Re-Emissions				1,523
Subtotal Land: Natural (incl. volcano) + Re-Emissions		**1,650**	**2,900**	**3,359**
Ocean Natural		800	800	
Ocean Re-Emissions	From previously deposited anthropogenic	1,250	2,000	
Ocean Natural + Re-Emissions				3,952
Subtotal Ocean: Natural + Re-Emissions		**2,150**	**2,900**	**3,952**
Subtotal Land + Ocean (Natural + Re-Emissions)		**3,800**	**5,800**	**7,311**
Total		**5,727**	**7,727**	**10,102**

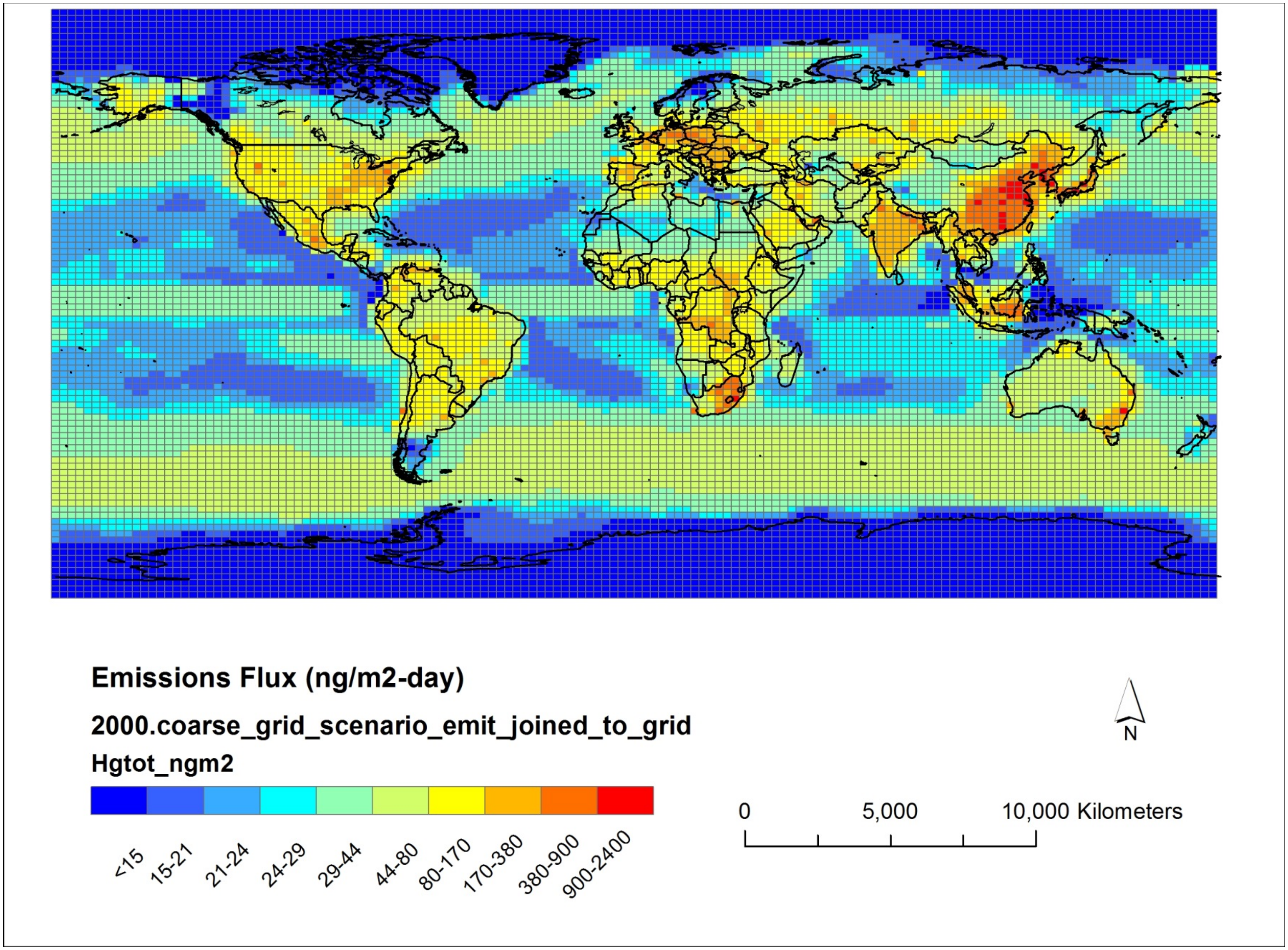

Figure 9. Geographical distribution of mercury emissions, 2000, 2.5x1.9 degree CAM-Chem/Hg model grid

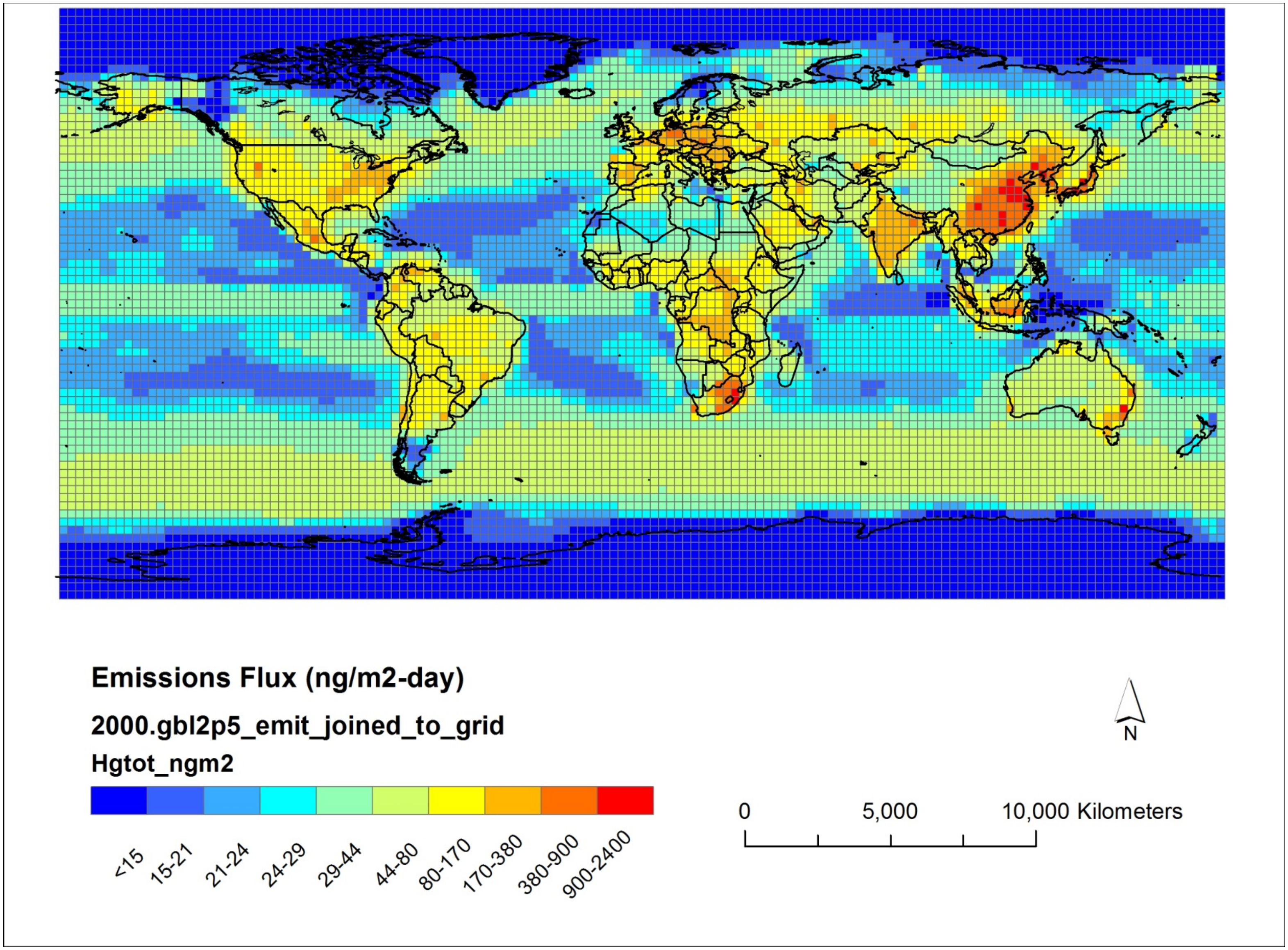

Figure 10. Geographical distribution of mercury emissions, 2000, 2.5x2.5 degree HYSPLIT-Hg model grid

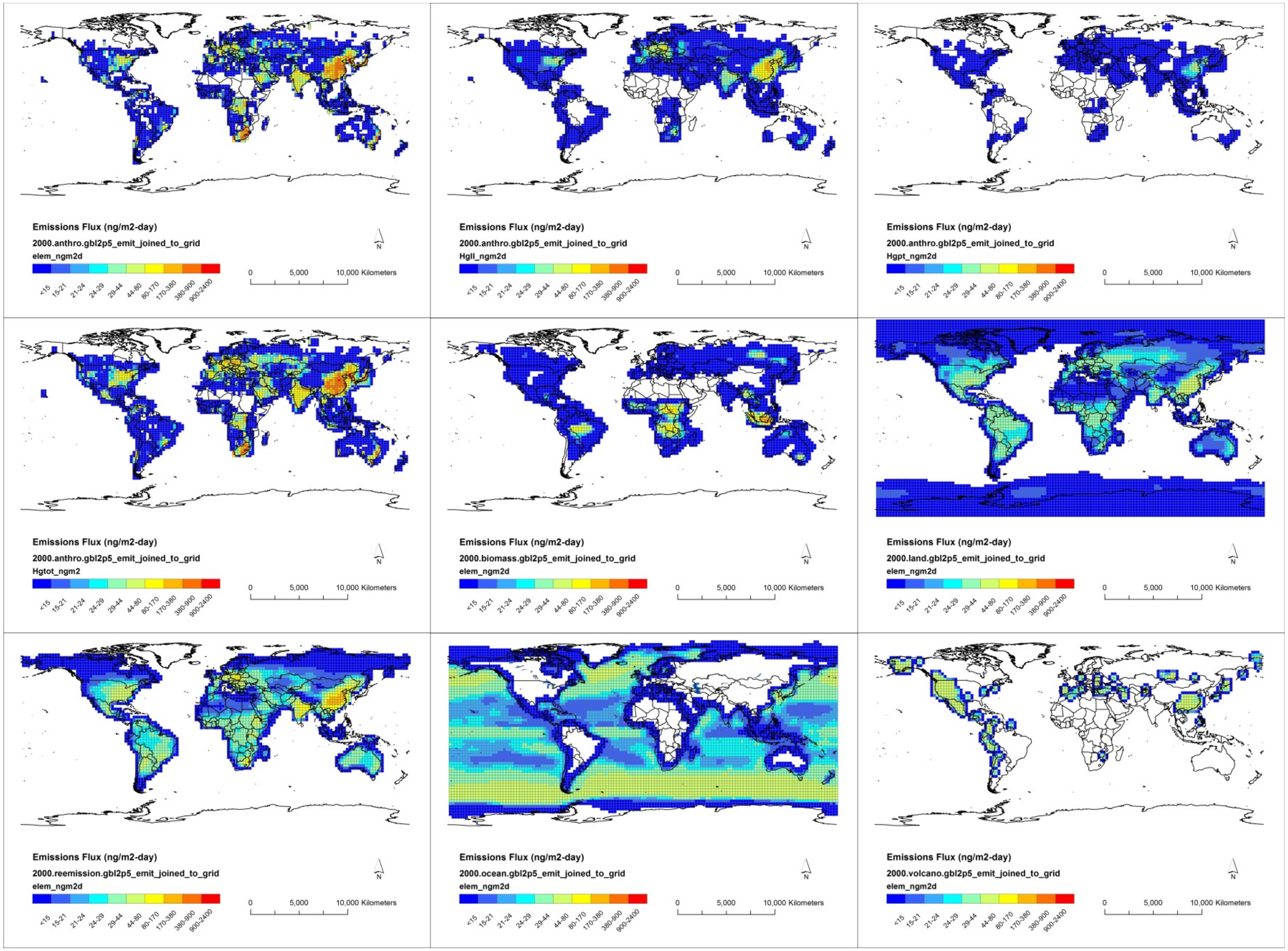

Figure 11. Mercury emissions in different categories (2000 baseline inventory)

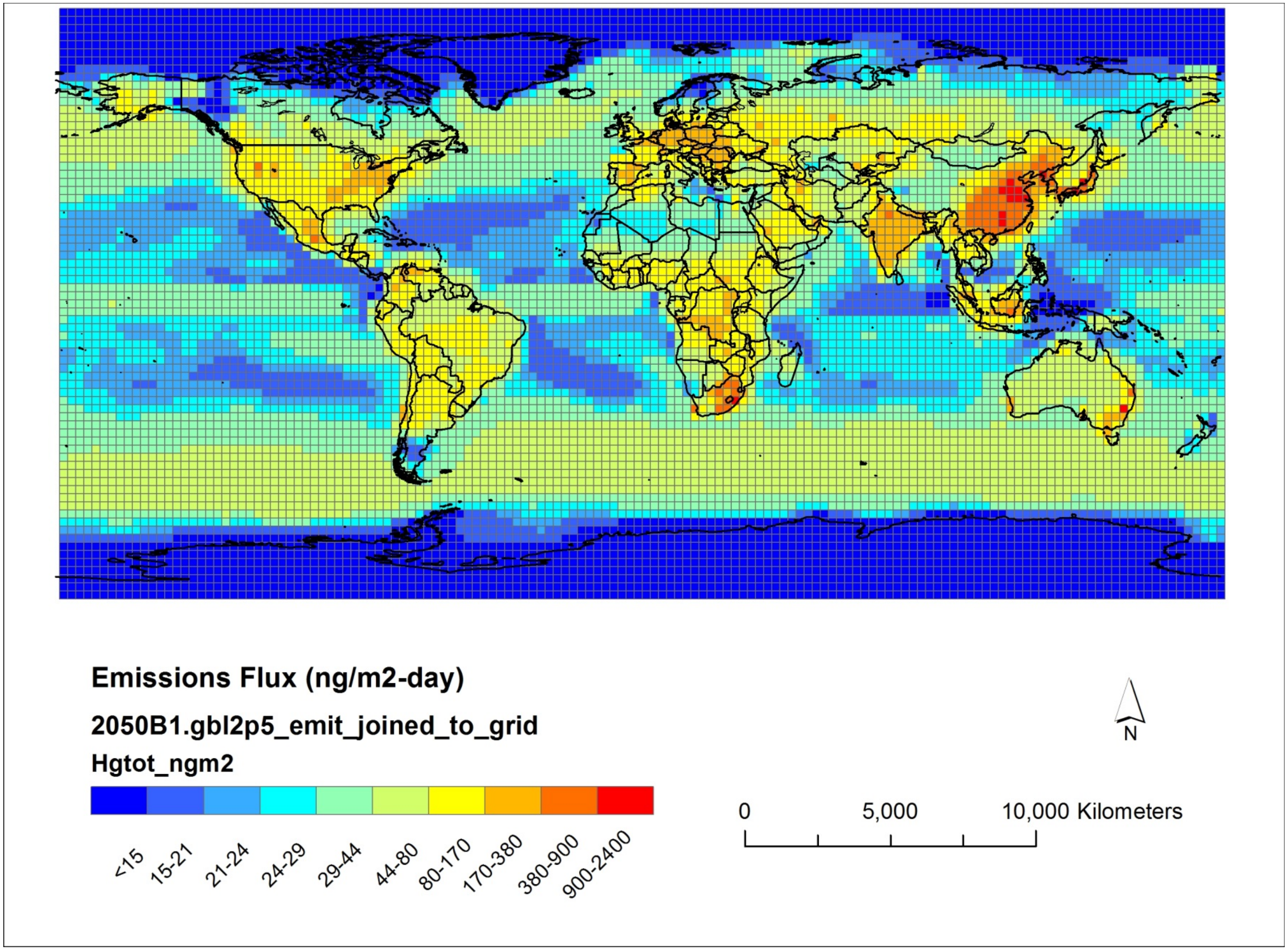

Figure 12. Geographical distribution of mercury emissions, 2050 B1, 2.5x2.5 degree HYSPLIT-Hg model grid

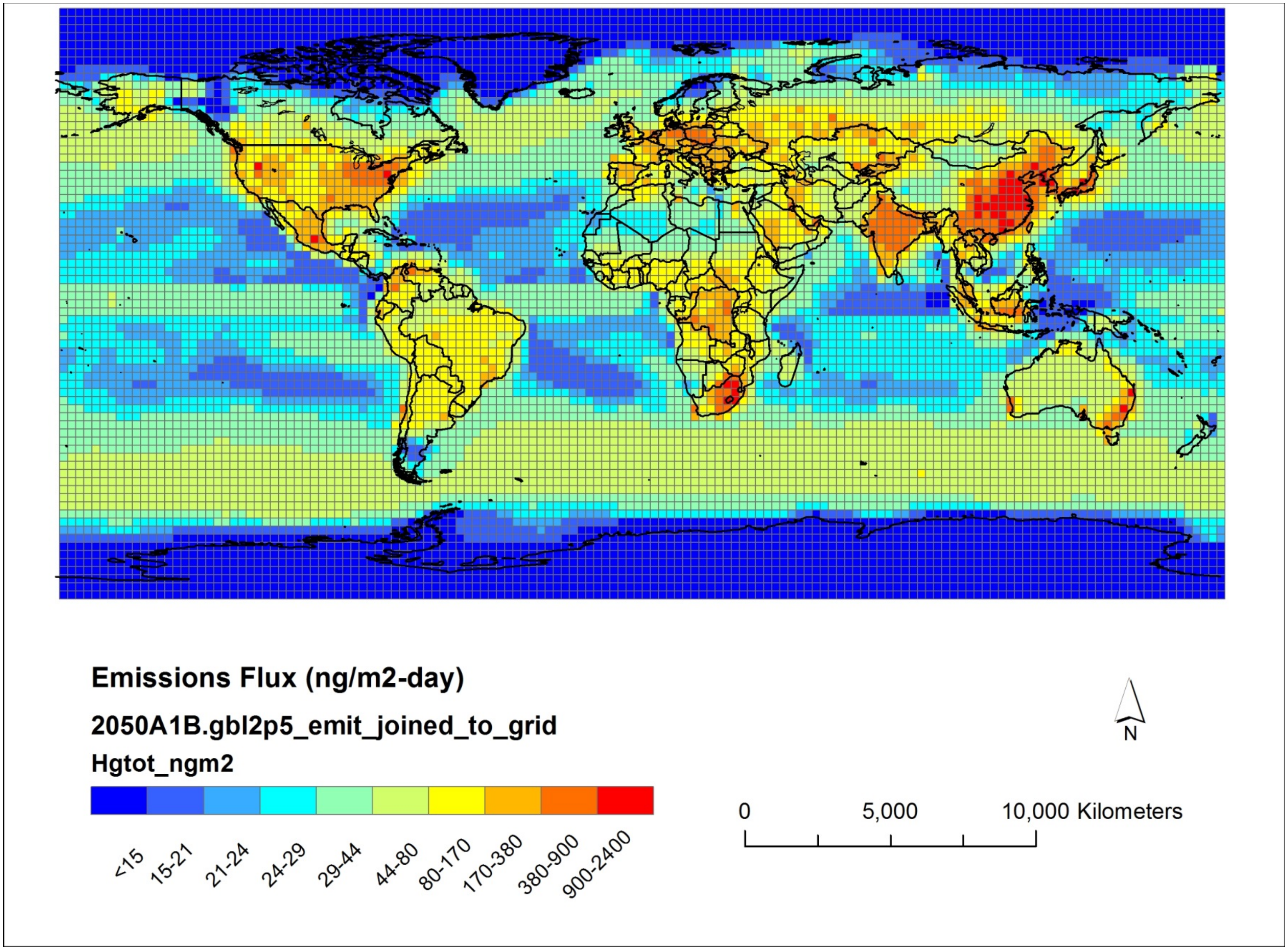

Figure 13. Geographical distribution of mercury emissions, 2050 A1B, 2.5x2.5 degree HYSPLIT-Hg model grid

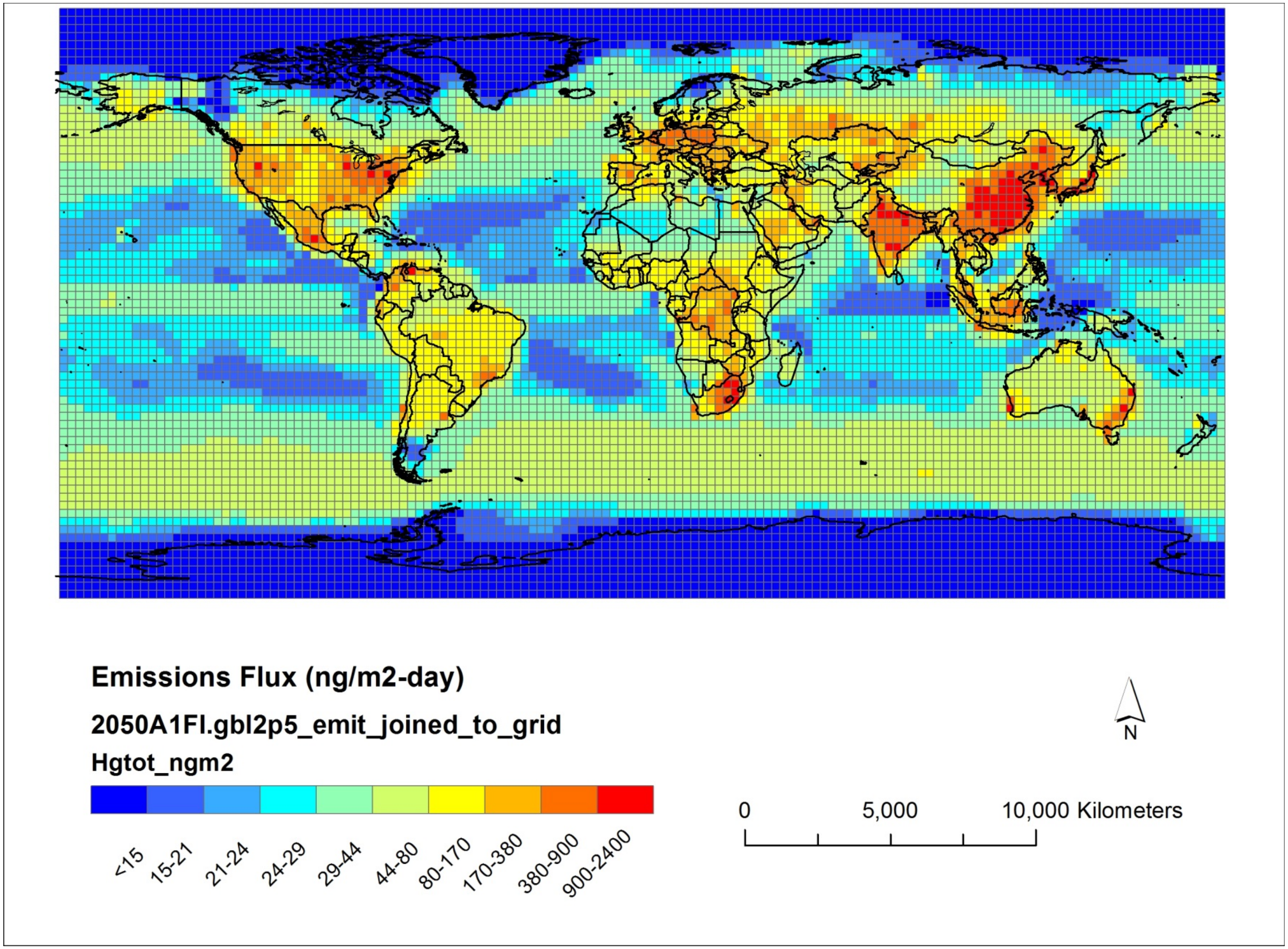

Figure 14. Geographical distribution of mercury emissions, 2050 A1FI, 2.5x2.5 degree HYSPLIT-Hg model grid

In order to develop approximate estimates of country-specific source-attribution for atmospheric mercury deposition to the Great Lakes, an attempt was made to allocate portions of the inventories used in this analysis to specific countries. Given the relatively coarse 2.5° x 2.5° grid, this process introduced inherent uncertainties in the assignment of emissions to a given country, particularly at the borders between countries, when a grid cell overlapped more than one country. In order to partially reduce the uncertainty in this situation, the 2005 inventory used in earlier GLRI modeling work (Cohen *et al*., 2011, 2013) -- with *much* higher spatial resolution – was employed to estimate the sub-grid-cell breakdown of emissions for grid cells on country borders. In this process, it was assumed that the split within a grid cell for the 2005 direct anthropogenic inventory would be the same split in the 2000 baseline and future scenario inventories used in this work. Six countries were selected to develop country-specific emissions estimates: USA, Canada, Mexico, China, India, and Russia. These six countries were chosen because they generally had the highest contributions to Great Lakes mercury deposition in the results of the earlier work in the earlier GLRI modeling work. The country-specific emissions estimates are shown for the 2000 baseline inventory in Figure 15, and for the three 2050 future scenario inventories in Figure 16, Figure 17, and Figure 18. As a point of comparison, the independent estimates for the year 2005 used in the earlier GLRI modeling analysis for the USA, Canada, and Mexico, along with the total anthropogenic emissions in that inventory, are shown in Figure 19. It can be seen that the emissions from the USA and Canada decreased somewhat from the 2000 baseline to the 2005 inventory, an expected finding given that the emissions are indeed believed to have decreased over that period for these two countries.

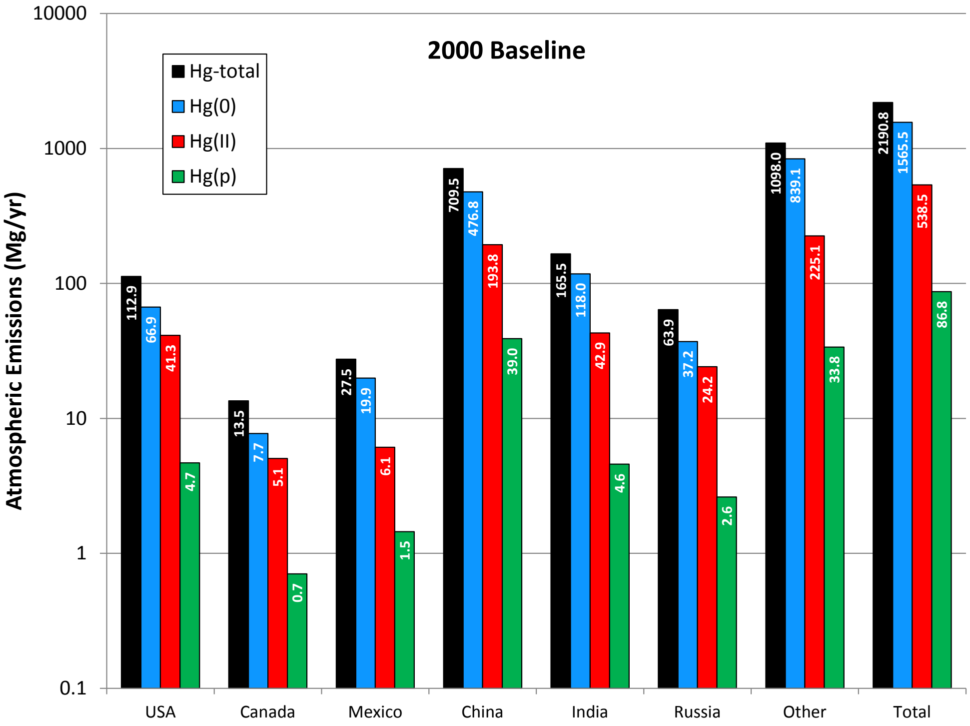

Figure 15. Country-specific and total direct anthropogenic emissions in the 2000 baseline inventory

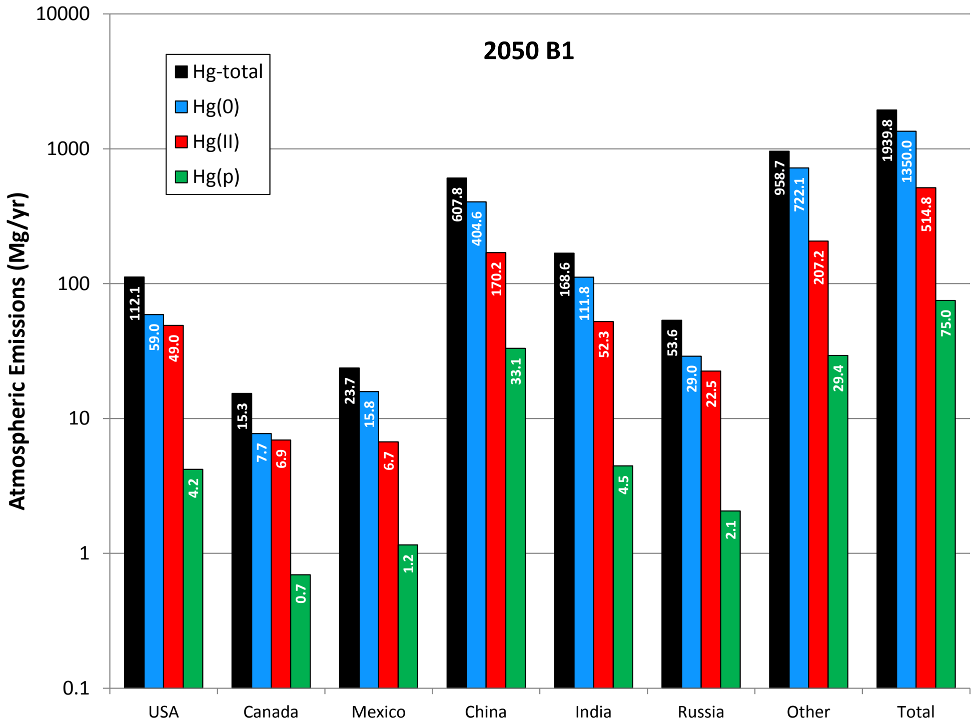

Figure 16. Country-specific and total direct anthropogenic emissions in the 2050 B1 scenario

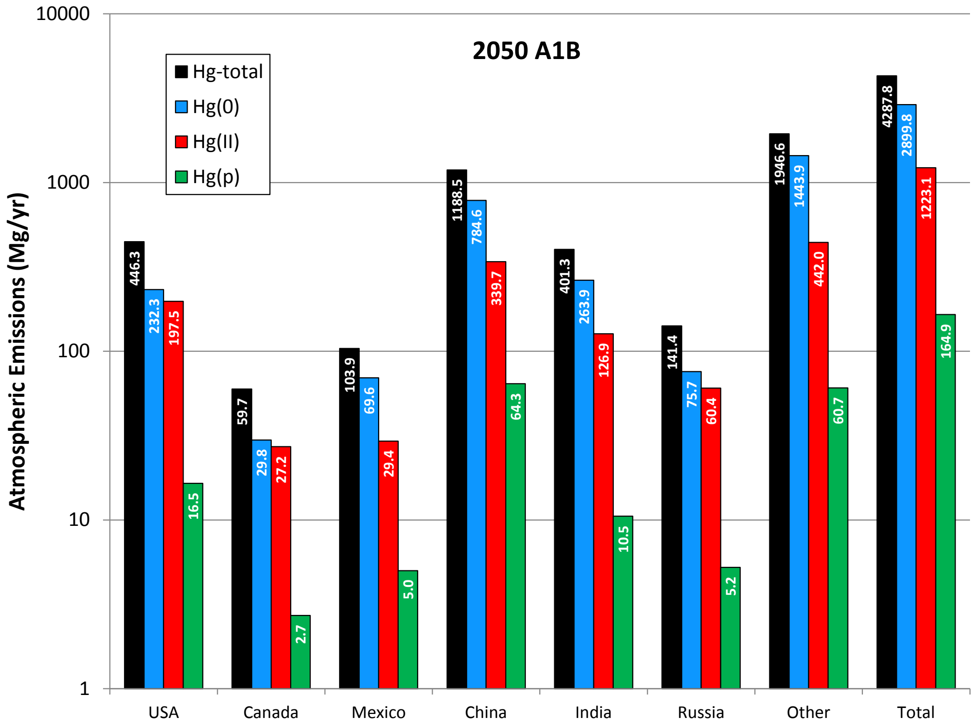

Figure 17. Country-specific and total direct anthropogenic emissions in the 2050 A1B scenario

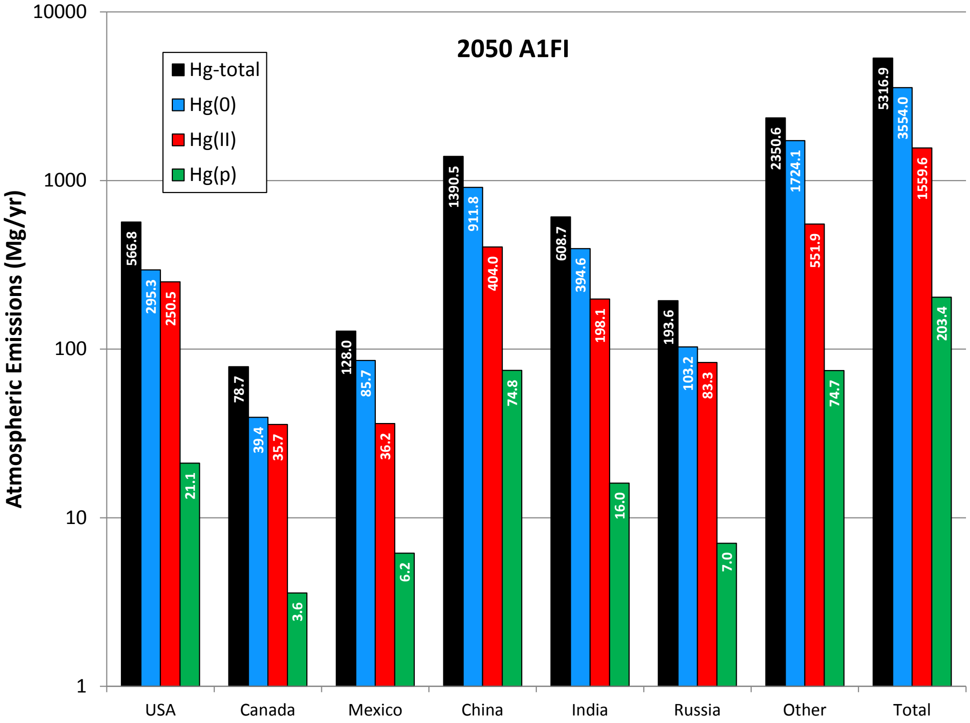

Figure 18. Country-specific and total direct anthropogenic emissions in the 2050 A1FI scenario

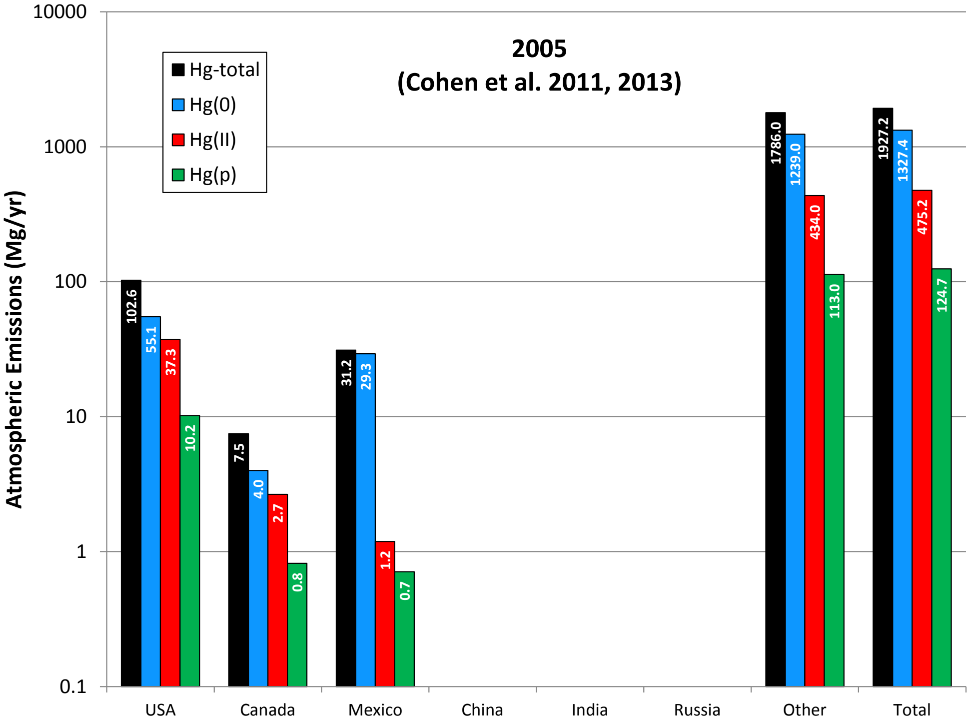

Figure 19. Country-specific and total direct anthropogenic emissions (2005 inventory from earlier GLRI work)

3. Simulation Methodology

3.1. Combined-emissions simulations vs. earlier analysis using standard sources and interpolation

In the FY10 and FY11 GLRI mercury modeling work (Cohen *et al*., 2011, 2013), the overall methodology used to carry out the analysis involved unit source simulations from “standard source locations”. These unit source simulations were then combined with the actual emissions inventory using a spatial and chemical interpolation methodology to estimate the impact of each source in the emissions inventory on each receptor of interest. This technique produces uniquely detailed source-receptor estimates. However, it requires a great deal of computational resources. Resource constraints dictated that a less computationally intensive approach be adopted for the present analysis.

In the analysis presented here, an entire simulation for a given inventory was carried out in a combined fashion, i.e., with the entire globe’s emissions simulated in one model run. The simulations used essentially the same Global Eulerian Model (GEM) methodology used in the earlier studies, except that in this case, a large combination of sources were simulated in any given run, rather than one particular unit source location. In these GEM simulations, a 2.5^{o} x 2.5^{o} grid was utilized, corresponding to the meteorological data grid used (see the following section). Pollutants emitted as puffs were immediately transferred to the global Eulerian grid and their fate and transport were simulated on that grid for the remainder of the run.

The emissions inventories for each scenario were broken down to their component parts, and individual simulations were run for each inventory subsection, i.e., anthropogenic, biomass, land, re-emissions, ocean, and volcano. Further, an overall combined simulation with all emissions was conducted for each scenario, as a QA/QC check (the overall simulation should be the same as the sum of the individual component simulations for each scenario). An example of this comparison is shown in Figure 20, for concentrations at ~30 model evaluation sites and deposition at ~100 receptors in North America. It can be seen in this figure that the combined and summed results are indeed identical, as expected. Finally, the anthropogenic emissions inventory subsection was subdivided into country-specific categories: USA, Mexico, Canada, China, India, Russia, and the rest of the world. The specific countries chosen were estimated to have the highest contributors to the Great Lakes in the FY10 and FY11 GLRI modeling work. Using these country-specific inventories, country-specific simulations for each country were carried out for each scenario. As a QA/QC check, the sum of the country-specific simulations was compared to the combined anthropogenic emissions simulation. An example of this anthropogenic-emissions-only comparison is shown in Figure 21 for the analogous concentration and deposition results. Again, it is seen that the combined and summed results are identical as expected.

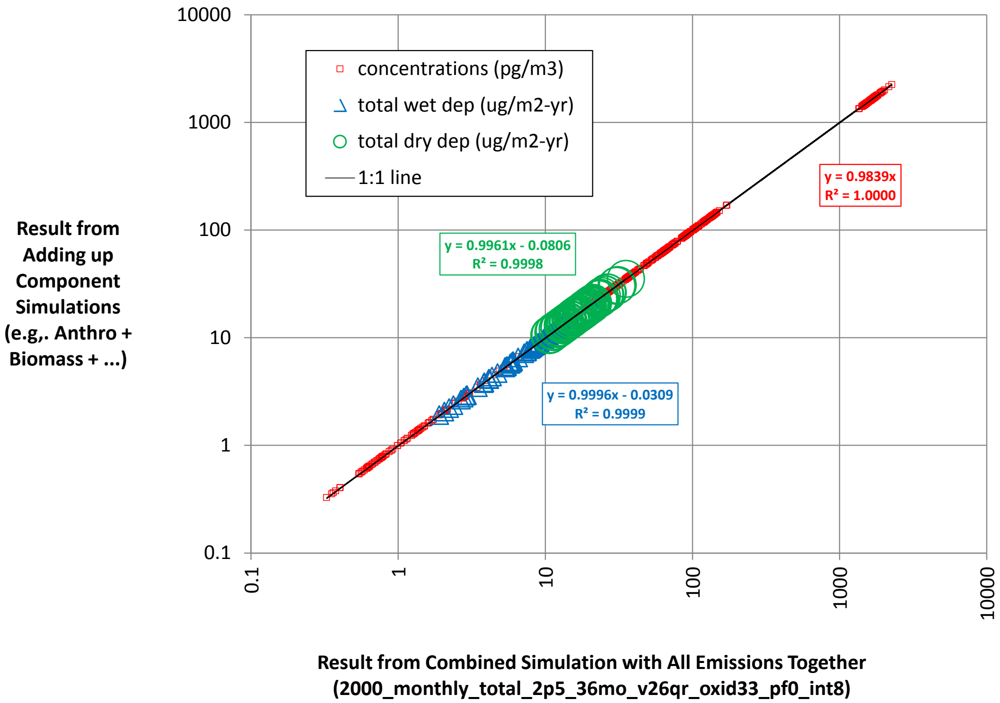

Figure 20. Comparison of combined simulation with sum of simulations using inventory components

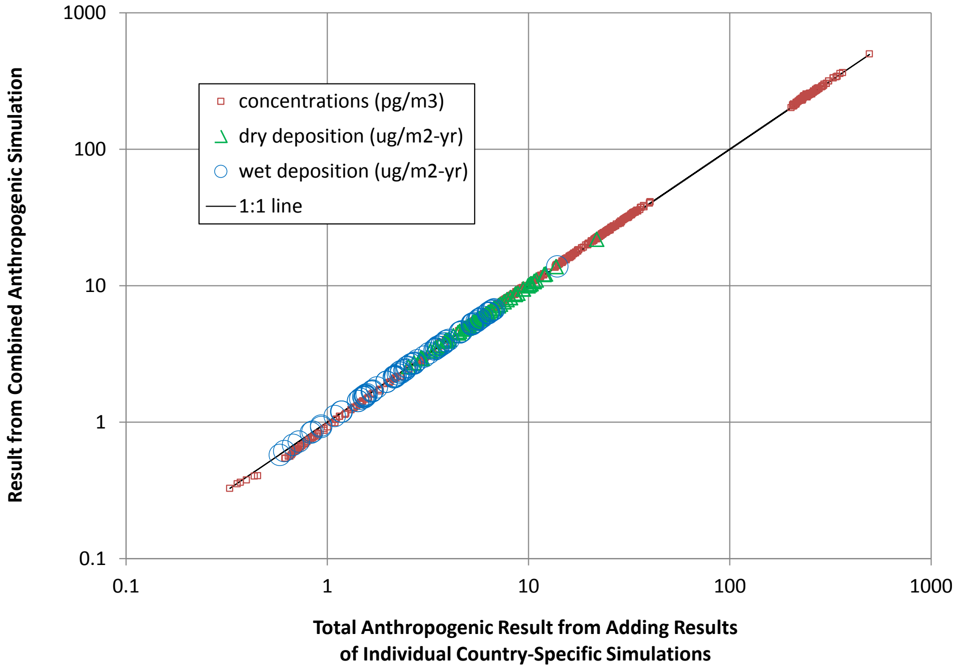

Figure 21. Comparison of combined anthropogenic emissions simulation with sum of country=specific anthropogenic emissions simulations

3.2. Meteorological Data

The meteorological data used in the simulations were developed from the NCEP/NCAR Global Reanalysis (NCAR/NWS, 1994…; NOAA ARL, 2003…). These data are specified on a 2.5o x 2.5o grid, with a surface layer and 17 vertical levels above the surface, up to a height of ~30 km (10 hPa). The data are specified on the 3-D grid every 6 hours. As can be seen in Figure 22 and Figure 23, the NCEP/NCAR Global Reanalysis data shows a systematic over-prediction of precipitation at Mercury Deposition Network sites in the Great Lakes region.

As can also be seen in Figure 23, for other MDN sites, the correlation between measured and modeled precipitation is not very satisfactory (it is less than zero) but the average is very consistent (e.g., the slope of the best fit line has a slope of ~1.0). Given the relatively coarse grid of the global data (2.5 degrees, or roughly 250 km), it would not be expected that the modeled and measured precipitation would be overly consistent. Therefore, the degree of consistency found, while not perfect, is somewhat unexpected. It is noted that there is some uncertainty in the "measured" precipitation at the MDN sites. The precipitation at the sites is reported in two ways: (a) based on a precipitation gauge at the site and (b) based on the amount of precipitation collected in the sample. Ideally, the two measures of precipitation would be identical, but they are sometimes different.

These two measures of precipitation are shown in Figure 22, and it is seen that in some cases, the sample-precipitation value is closer to the modeled value than the rain-gauge measured precipitation. A comparison of rain-gauge vs. sample-measured precipitation at all MDN sites with 2005 data is shown in Figure 24. It is seen that there are non-trivial differences between the two at many of the sites, suggesting that the precipitation measurements are somewhat uncertain.

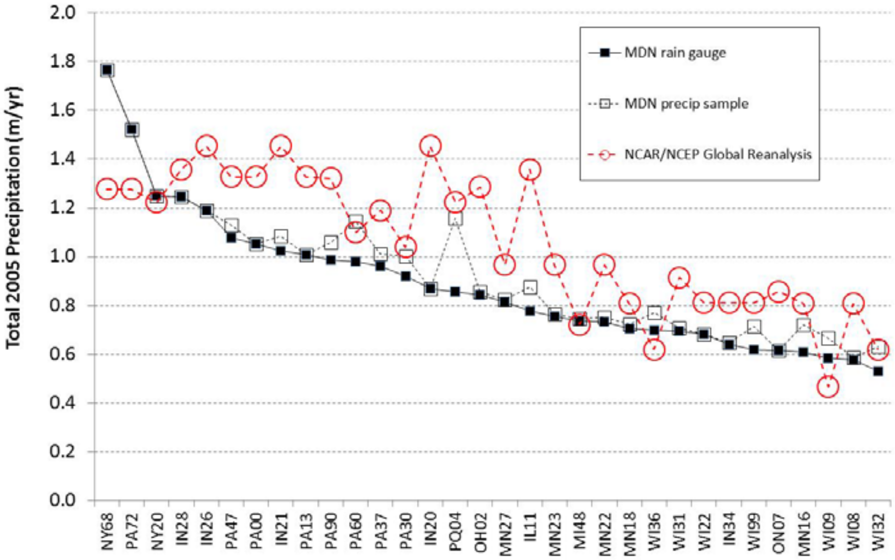

Figure 22. Comparison of measured and modeled precipitation at MDN sites in the Great Lakes region

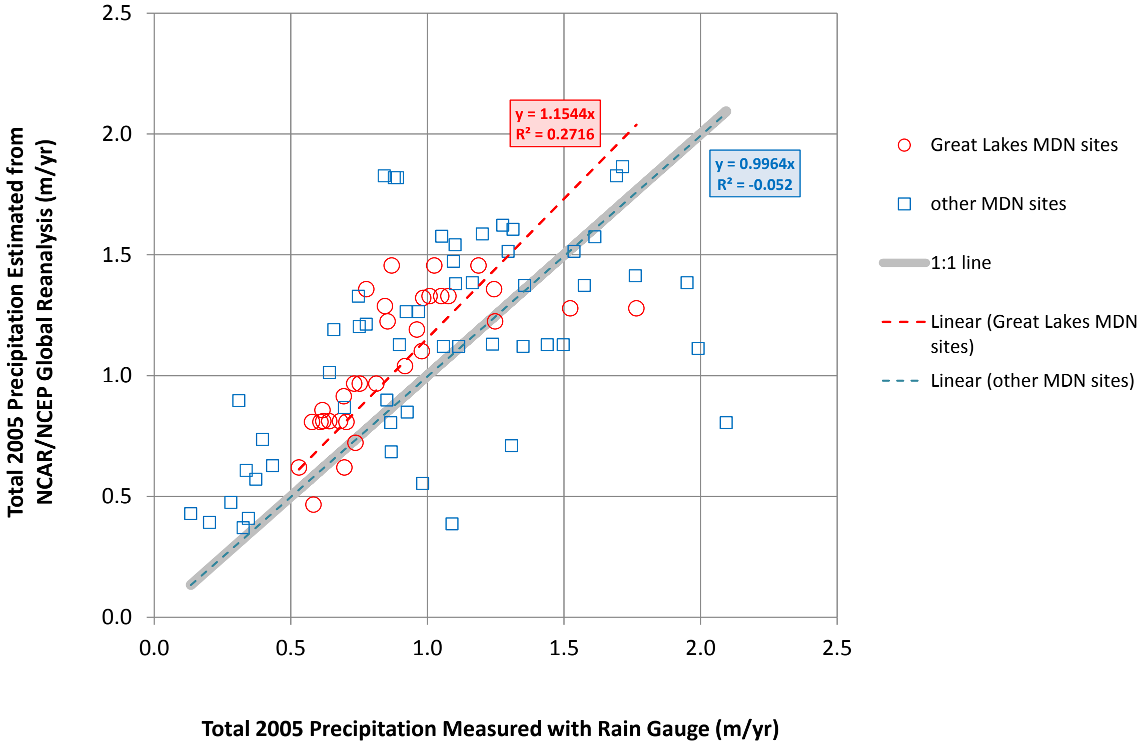

Figure 23. Comparison of measured and modeled precipitation at MDN sites with data for 2005

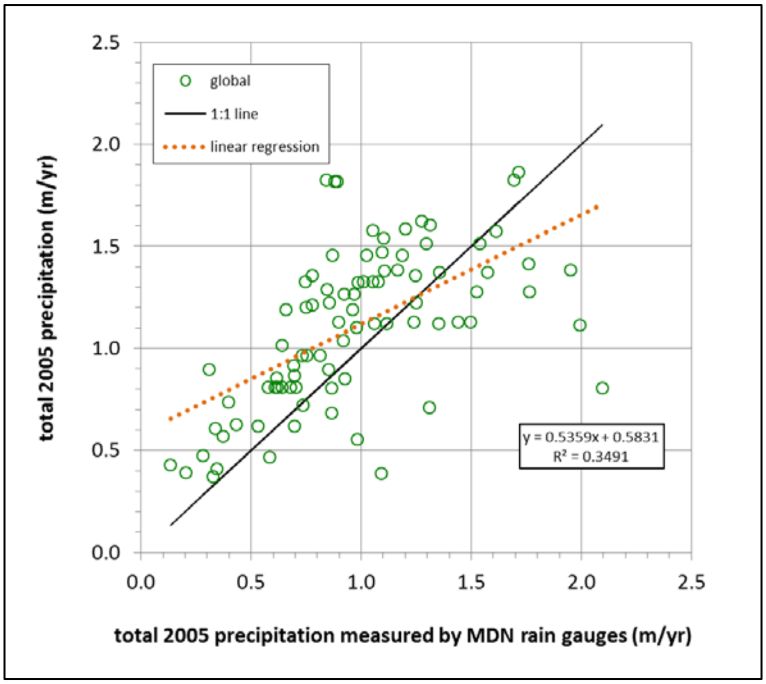

Figure 24. Comparison of precipitation measured by rain gauges at MDN sites with that in the NCEP-NCAR Global Reanalysis meteorological dataset

3.3. Model Spin-up

In the earlier GLRI model analyses (Cohen *et al*., 2011, 2013), a model spin-up period of 3 months was used. In other words, the simulation was carried out for Oct-Nov-Dec 2004, before the 2005 period for which the results were tabulated. The decision to use the 3-month spin-up period was made based on consideration of the tradeoffs between computation resource requirements and accuracy. It was recognized that a longer spin-up would yield more accurate results, but the uncertainty introduced by the use of the 3-month spin appeared minimal.

In this FY12 GLRI model analysis, the "combined" runs being conducted afforded a dramatic savings in computational resources required, and so, longer spin-up periods could be considered. The spin-up period was varied from 3-months to 24 months, and it was found that with increasing spin-up periods, the concentrations and deposition estimates tended to increase at any given location. Examples of these results are shown in Figure 26 for atmospheric concentrations and Figure 27 for atmospheric deposition fluxes estimated by the model at selected receptors. The receptors used for the concentration comparison in Figure 26 are listed in Table 4 and Figure 25, and the receptors used for the deposition comparison were the 86 MDN sites with data in 2005 along with locations at the center of each of the Great Lakes, the Gulf of Maine, and the Chesapeake Bay, for a total of 93 sites.

For some of the selected concentration receptors shown in Table 4, measurement data was able to be obtained for some or all of 2005.

It can be seen in Figure 26 and Figure 27 that there is a systematic increase in estimated concentrations and deposition using a 24-month spin-up over a 3-month spin-up, typically on the order of 30-40%. It can also be seen from Figure 26 that the effect is greater for the higher-altitude results (3000-4000m) than the low-altitude results (0-100m). This makes sense given that the sources are all near the earth's surface and it takes longer for the mercury to be mixed up towards higher altitudes.

The total length of the 24-month spin-up simulations (24+12=36 months) is more than twice the total length of the 3-month spin-up simulations (3+12=15 months). Using a 24-month spin-up with the discretized standard source location approach used in the earlier work would have been impractical, as it would have required more than 3 months *added* computational time – in addition to the 2.5 months required for the 3-month spin up -- given the available computational resources.

However, the longer spin-up periods were possible with the combined "all-in-one" simulation approach utilized in the present study. For example, a single simulation took approximately 8 CPU-days. But, for any given model configuration, only 14 simulations were required for each of the four scenarios (total, anthropogenic, biomass, re-emissions, land, ocean, volcano, USA, Canada, Mexico, China, India, Russia, Other), for a total of 56 required simulations. With the 16-processor work-station available for this work, these 56 simulations could be carried out in approximately 1 month. Of course, a number of other simulations were carried out during development and testing, and to investigate sensitivities to various parameters and model inputs. The 1 month period noted above simply refers to the calendar time required for the "final" set of "production" simulations used in this analysis.

Table 4. Key receptors for atmospheric concentration evaluations

Site name	Latitude	Longitude	Elevation (m)
St. Anicet	45.117	-74.283	49
Harcum	37.531	-76.493	10
Alert	82.500	-62.330	210
Kejimkujik	44.433	-65.203	127
Point Petre	43.840	-77.152	75
Egbert	44.230	-79.780	251
Burnt Island	45.808	-82.951	75
Bratt’s Lake	50.201	-104.711	577
Mt. Bachelor	43.980	-121.690	2,763
Reno DRI	39.570	-119.800	1,340
Paradise	41.500	-117.500	1,388
Gibbs Ranch	41.550	-115.210	1,849
Piney Reservoir	39.706	-79.012	770
Underhill	44.528	-72.868	400
Potsdam	44.750	-75.000	100
Stockton	42.270	-79.380	500
Grand Bay	30.412	-88.404	10
Beltsville	39.028	-76.817	50
Mauna Loa	19.536	-155.576	3,400
OLF	30.550	-87.375	50
Lake Superior	47.750	-88.000	0

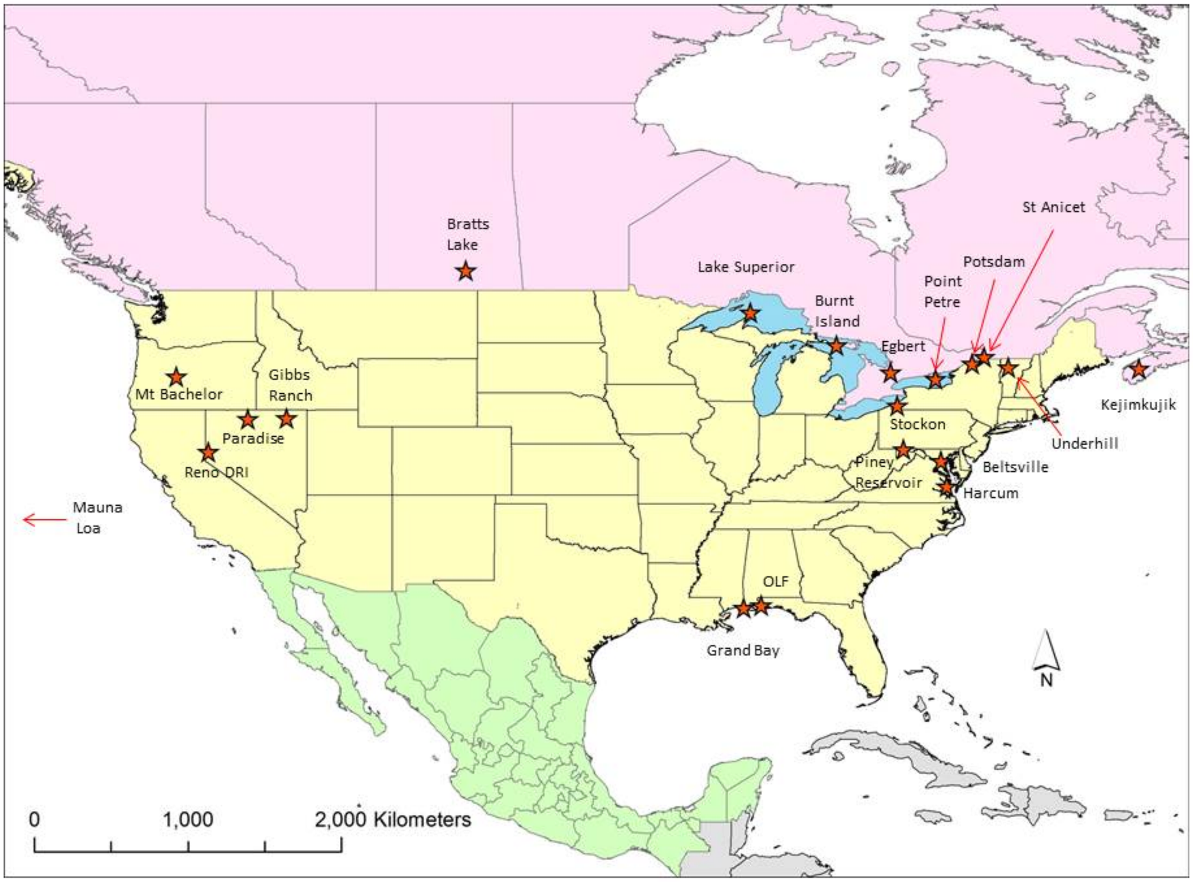

Figure 25. Key receptors for atmospheric concentration evaluations

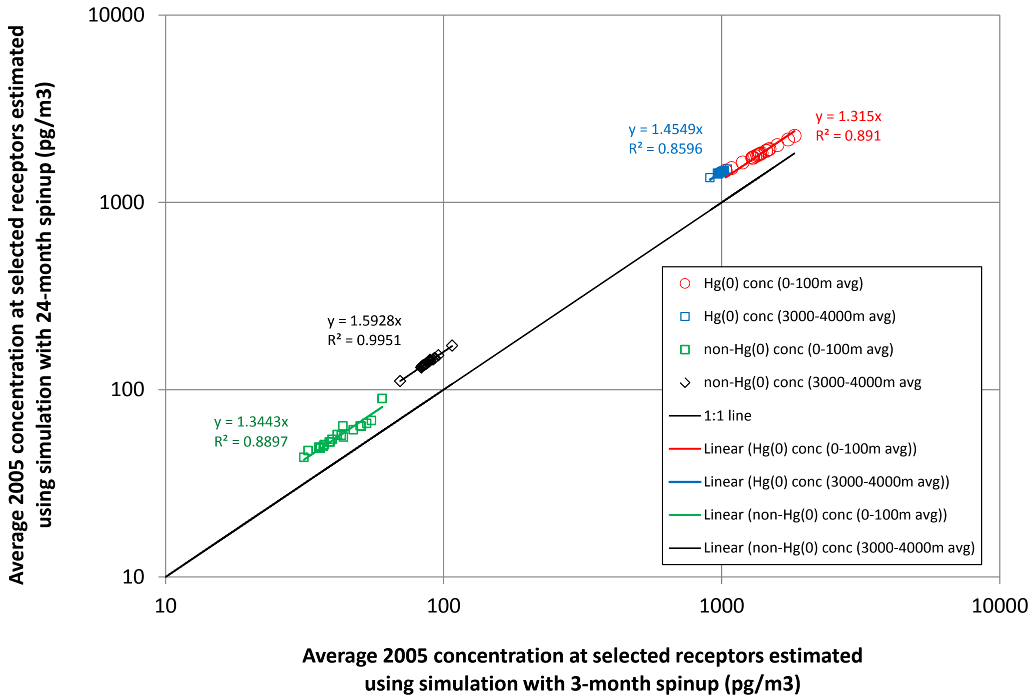

Figure 26. Influence of simulation spin-up period on model-estimated atmospheric mercury concentrations

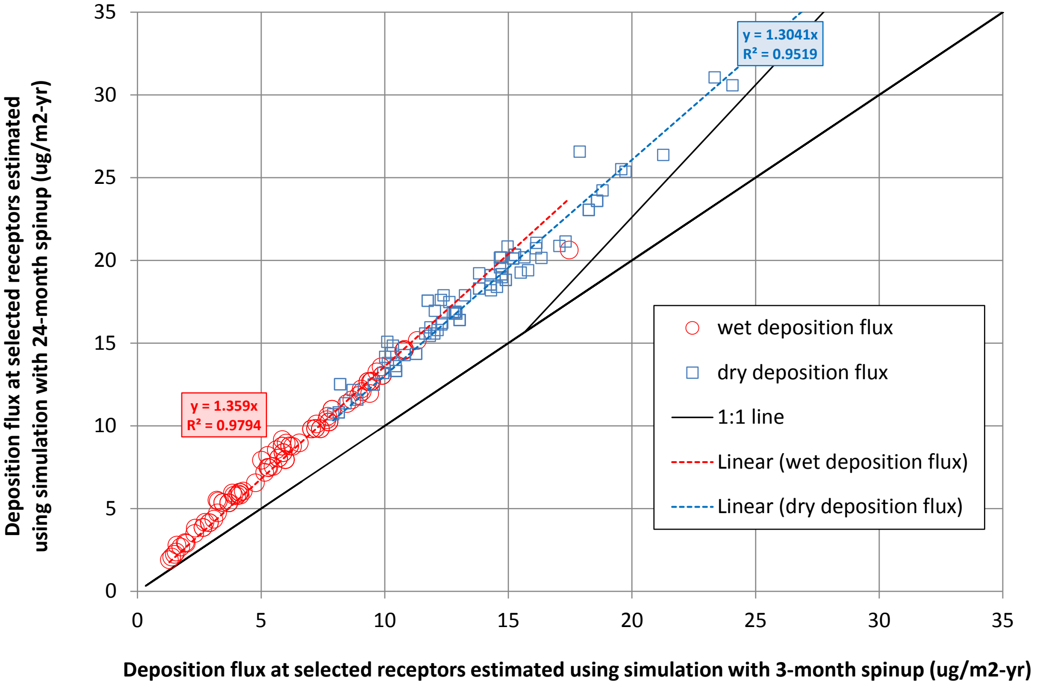

Figure 27. Influence of simulation spin-up period on model-estimated atmospheric mercury deposition fluxes

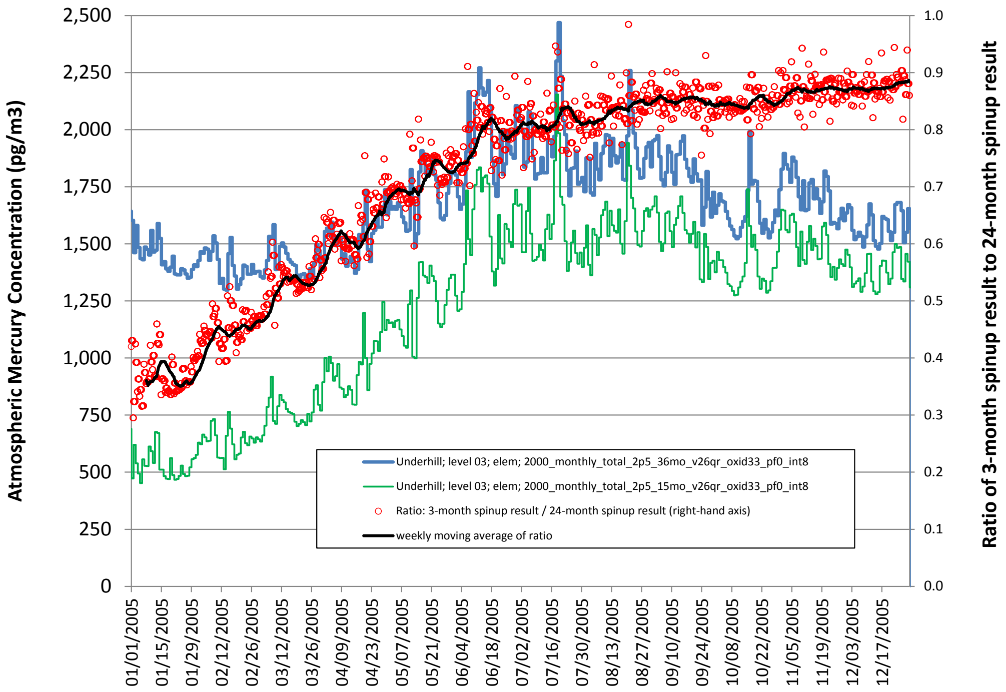

Figure 28. Time series of modeled Hg(0) concentrations at Underhill showing influence of model spin-up period

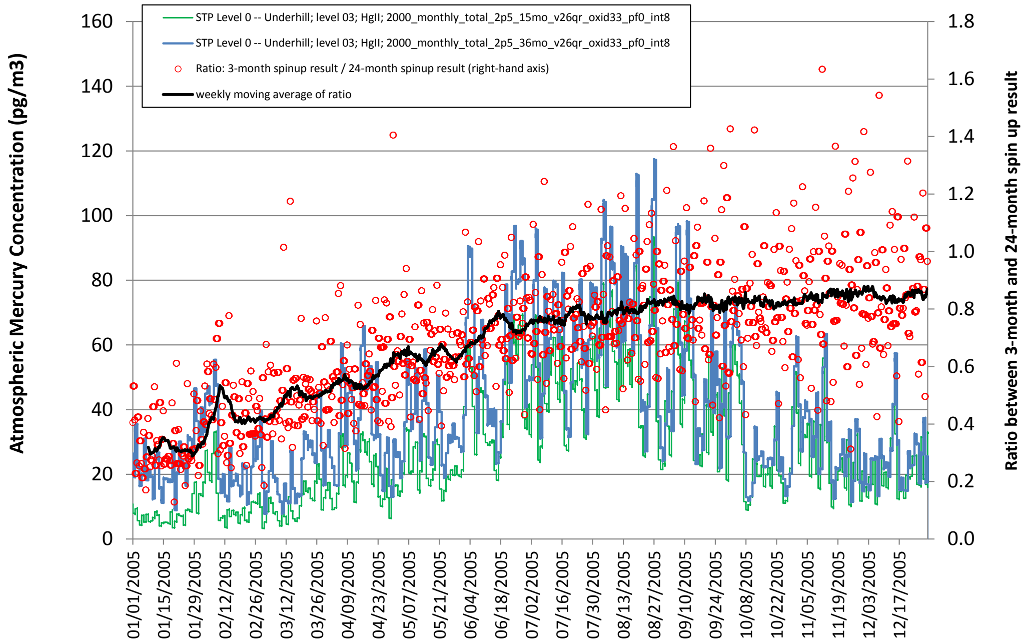

Figure 29.Time series of modeled Hg(II) concentrations at Underhill showing influence of model spin-up period

3.4. Chemical Mechanism

In the HYSPLIT-Hg model, atmospheric mercury can be transformed by chemical and physical processes from one form to another. In the model, there are four forms of mercury tracked: Hg(0), Hg(II), Hg(p), and Hg(II) adsorbed to soot, which is abbreviated “Hg2s”. The chemical transformations used in earlier analyses for the gas and liquid phase, as well as the process of Hg(II)-aqueous sorption to aqueous soot, are shown in Figure 30 and Table 5 .

In the earlier analyses, the primary method of model evaluation, or “ground-truthing”, was by comparison of modeled mercury wet deposition to measured mercury wet deposition at MDN sites in the Great Lakes region. The modeled and measured wet deposition values were encouragingly consistent in those analyses.

In the current analysis, atmospheric concentration results, for Hg(0), Hg(II), and Hg(p), were added to the model evaluation procedures. After extensive testing and analysis, it was determined that the chemical mechanism used in the earlier analysis appeared to be depleting the Hg(0) concentrations too quickly, via reactions to form Hg(II) and Hg(p). The primary evidence for this conclusion was that the model-predicted concentrations of Hg(0) showed systematic under-predictions compared to typical levels found at measurement sites.

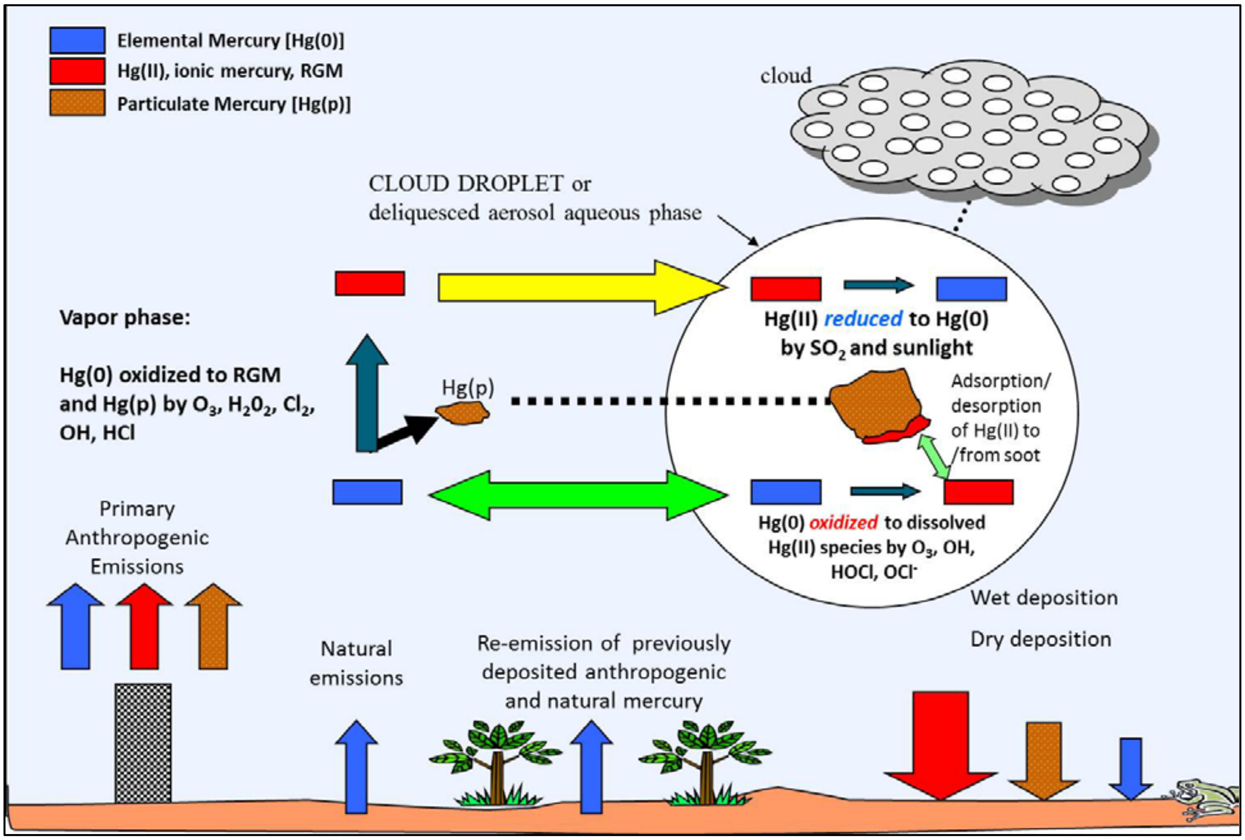

Figure 30. Schematic of mercury transformations in the HYSPLIT-Hg model

Table 5. Chemical Transformations in the HYSPLIT-Hg Model

Reaction	Rate	Units	Reference
GAS PHASE REACTIONS			
1. $Hg^0 + O_3 \rightarrow Hg(p)$	3.0E-20	cm^3/molec-sec	Hall (1995)
2. $Hg^0 + HCl \rightarrow HgCl_2$	1.0E-19	cm^3/molec-sec	Hall and Bloom (1993)
3. $Hg^0 + H_2O_2 \rightarrow Hg(p)$	8.5E-19	cm^3/molec-sec	Tokos *et al*. (1998) (upper limit based on experiments)
4. $Hg^0 + Cl_2 \rightarrow HgCl_2$	4.0E-18	cm^3/molec-sec	Calhoun and Prestbo (2001)
5. $Hg^0 + OH \rightarrow Hg(p)$	8.7E-14	cm^3/molec-sec	Sommar *et al*. (2001)
AQUEOUS PHASE REACTIONS			
6. $Hg^0 + O_3 \rightarrow Hg^{+2}$	4.7E+7	$(molar\text{-}sec)^{-1}$	Munthe (1992)
7. $Hg^0 + OH \rightarrow Hg^{+2}$	2.0E+9	$(molar\text{-}sec)^{-1}$	Lin and Pehkonen(1997)
8. $HgSO_3 \rightarrow Hg^0$	$T{*}e^{((31.971*T)-12595.0)/T}$ sec^{-1} [T = temperature (K)]		Van Loon *et al*. (2002)
9. $Hg(II) + HO_2 \rightarrow Hg^0$	~ 0	$(molar\text{-}sec)^{-1}$	Gardfeldt & Jonnson (2003)
10. $Hg^0 + HOCl \rightarrow Hg^{+2}$	2.1E+6	$(molar\text{-}sec)^{-1}$	Lin and Pehkonen(1998)
11. $Hg^0 + OCl^{-1} \rightarrow Hg^{+2}$	2.0E+6	$(molar\text{-}sec)^{-1}$	Lin and Pehkonen(1998)
12. $Hg(II) \leftrightarrow Hg(II)_{(soot)}$	9.0E+2	liters/gram; t = 1/hour	eqlbrm: Seigneur *et al*. (1998) rate: Bullock & Brehme (2002).
13. $Hg^{+2} + hv \rightarrow Hg^0$	6.0E-7	$(sec)^{-1}$ (maximum)	Xiao *et al*. (1994); Bullock and Brehme (2002)

An example of this evidence can be seen in Figure 31, in which a number of different simulation results for Hg(0) are compared with measurement data, if it could be obtained for a given site, for the sites listed in Table 4. In all of the modeling results shown in Figure 31, the baseline “2000” inventory of Lei *et al*. (2013, 2014) was used, with a 24-month model spin-up period. The primary model variations shown involve changes in the rate of the Hg(0) oxidation reactions used in the chemical mechanism. Specifically, the rates of reactions 1-5, 10, and 11 in Table 5 were reduced from their nominal rate (“oxid100”, referring to 100% of the oxidation reaction rates) to 50% and 33% of their nominal rates (“oxid33” and “oxid50”, respectively).

The primary conclusion that can be drawn from Figure 31 is that the model predictions using the fastest oxidation rates (“oxid100”) show a systematic under-prediction of Hg(0) concentrations, relative to measurements. In contrast, the slower oxidation rates – “oxid50” and “oxid33” -- representing rates 50% and 33% as fast as the “100%” rates shown in Table 5, respectively, appear to be far more consistent with the ambient measurements, for all of the sites. Accordingly, the “oxid50” and “oxid33” mechanisms were used in the modeling analysis of the Great Lakes impacts of baseline and future emissions scenarios, and the “oxid100” mechanism was not utilized. Additional details regarding the evaluation and choice of chemical mechanism parameters are provided in the section below regarding Model Evaluation. In particular, it was found that the assumption of 100% Hg(p) (“pf100”) resulting from the hydroxyl radical (OH) , ozone (O_3), and hydrogen peroxide (H_2O_2) oxidation reactions (reactions 1, 3, and 5 in Table 5) led to mode-estimated Hg(p) concentrations that appeared to be unrealistically high. Accordingly, an assumption of 0% Hg(p) (“pf0”) from these reactions was utilized in the analysis. It is noted that other models now use this same assumption (e.g., Grant *et al*., 2014).

There are additional considerations involved in this model evaluation exercise that will be discussed in more detail in the Model Evaluation section below.

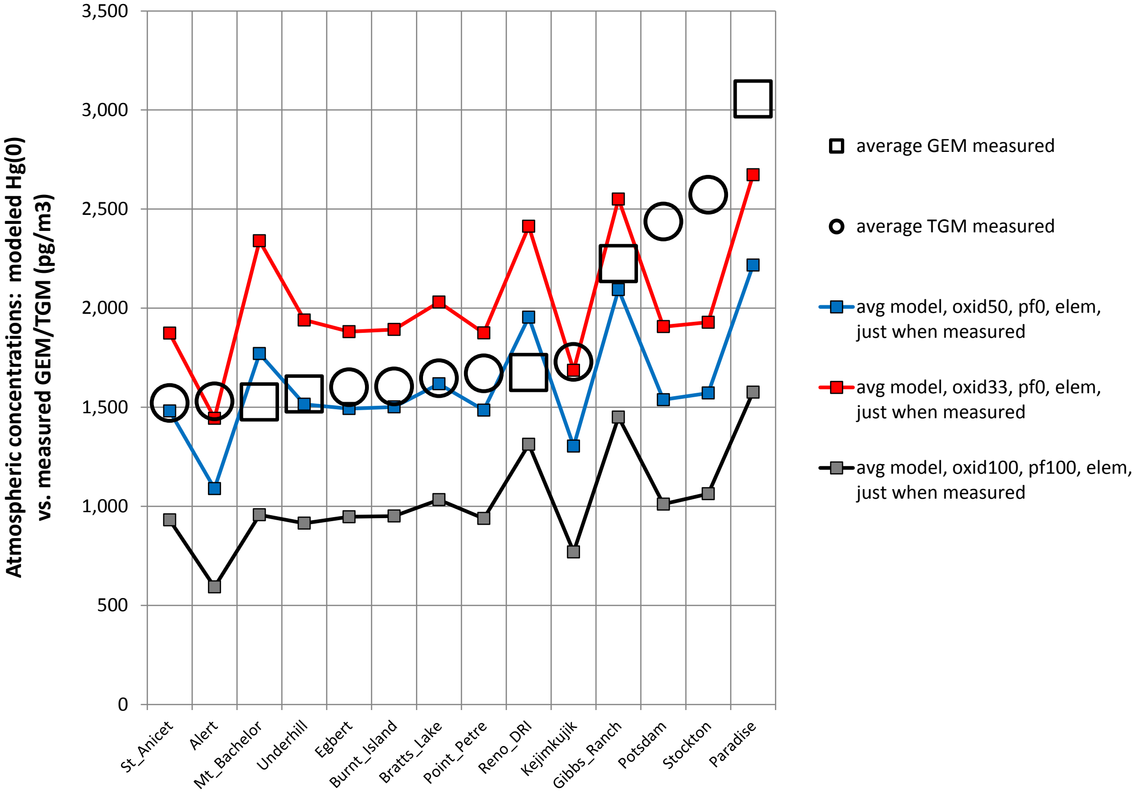

Figure 31. Comparison of modeled Hg(0) vs. measured GEM and TGM

4. Simulations Carried Out for this Analysis

A number of different simulation configurations – using different emissions inventories and/or different computational methodologies – were carried out. The results of these simulations will be presented in subsequent sections. In this section, the universe of runs will be described, and the "naming conventions" for the various configurations will be explained. To begin, Table 6 shows the names of 23 different simulations in which a total "global" mercury emissions inventory was used. Additional simulations using different subsets of the inventories were also carried out and these will be described below. The "total inventory" simulations in the table below are numbered (from 1-23), for ease in explanation.

Table 6. Simulations using a "total inventory" (as opposed to inventory subsets)

Run Number	Run Name
1	L750_W1250_2p5_15mo_v26qr_oxid100_pf100
2	L750_W1250_2p5_15mo_v26qr_oxid33_pf0
3	L750_W1250_2p5_36mo_v26qr_oxid100_pf100
4	L750_W1250_2p5_36mo_v26qr_oxid33_pf0
5	LW2000_2p5_15mo_v26qr_oxid100_pf100
6	LW2000_2p5_15mo_v26qr_oxid33_pf0
7	LW2000_2p5_36mo_v26qr_oxid100_pf100
8	LW2000_2p5_36mo_v26qr_oxid33_pf0
9	2000_monthly_total_2p5_15mo_v26qr_oxid100_pf100_int8
10	2000_monthly_total_2p5_36mo_v26qr_oxid100_pf100_int8
11	2000_monthly_total_2p5_15mo_v26qr_oxid33_pf0_int8
12	2000_monthly_total_2p5_36mo_v26qr_oxid33_pf0_int8
13	2000_monthly_total_2p5_36mo_v26qr_oxid33_pf25_int8
14	2000_monthly_total_2p5_36mo_v26qr_oxid33_pf50_int8
15	2000_monthly_total_2p5_36mo_v26qr_oxid50_pf0_int8
16	2000_monthly_total_2p5_36mo_v26qr_oxid50_pf0_int8_v2
17	2000_monthly_total_2p5_36mo_v26qr_oxid50_pf50_int8
18	2050_B1_monthly_total_2p5_36mo_v26qr_oxid33_pf0_int8
19	2050_B1_monthly_total_2p5_36mo_v26qr_oxid50_pf0_int8
20	2050_A1B_monthly_total_2p5_36mo_v26qr_oxid33_pf0_int8
21	2050_A1B_monthly_total_2p5_36mo_v26qr_oxid50_pf0_int8
22	2050_A1FI_monthly_total_2p5_36mo_v26qr_oxid33_pf0_int8
23	2050_A1FI_monthly_total_2p5_36mo_v26qr_oxid50_pf0_int8

The first part of the name of each run, e.g., those listed in Table 6, describes the emissions inventory that was used for the simulation. The inventories utilized are summarized in Table 7 and described in much more detail in Section 2 above (beginning on page 12).

Table 7. Inventory descriptions in run-label text

Label text	Run Numbers	Description	Total emissions (Mg/yr)	Source
L750_W1250	1-4	Reemissions of 750 Mg/yr from land and 1250 Mg/yr from the ocean	5,727	Cohen *et al.* (2011, 2013)
LW2000	5-8	Reemissions of 2000 Mg/yr from land and 2000 Mg/yr from the ocean	7,727	
2000_monthly*	9-17	2000 baseline emissions	10,102	Based on Lei *et al.* (2013, 2014); includes monthly variations
2050_B1_monthly*	18-19	2050 B1 future emissions scenario	10,036	
2050_A1B_monthly*	20-21	2050 A1B future emissions scenario	12,681	
2050_A1FI_monthly*	22-23	2050 A1FI future emissions scenario	13,910	

** Note that in the case of some inventory subsets – anthropogenic and volcanic emissions -- monthly variations were not available, and so, the "monthly" descriptor is left off of the inventory descriptor for runs using these inventory subsets. However, for most runs using these inventories or their subsets, monthly variations in emissions were utilized; hence the "monthly" descriptor is included. This was true for the biomass, land, ocean, and reemissions subsets of the inventories. When the "total" inventory was used, made up of some monthly varying components and some components without monthly variations, the "monthly" descriptor was also used, even though not all portions of the inventory had such variations.*

<u>The second part</u> of the run-label text is an optional descriptor describing the inventory subset used for the run. For the L750_W1250 and LW2000 inventories, only "total inventory" runs will be presented, and the "total" label is omitted. However, subsets are sometimes used for the 2000 baseline and three future 2050 inventories. For these inventories, the "total inventory" runs are denoted with the term "total" in the run-label text, e.g., **2000_monthly_total_2p5_36mo_v26qr_oxid33_pf0_int8**

Other inventory subset runs with just anthropogenic, biomass, land, ocean, volcanic, and reemissions were also carried out, e.g., **2000_monthly_biomass_2p5_36mo_v26qr_oxid33_pf0_int8**. The complete set of such inventory subset runs presented here is shown in Table 8 and Table 9.

In addition, an analogous set of country-specific anthropogenic emissions subsets simulations was also carried out, e.g., **2000_anthro_USA_2p5_36mo_v26qr_oxid33_pf0.** The complete set of such country-specific anthropogenic emissions simulations presented here is shown in Table 10 and Table 11. As noted above, monthly variations were not available for some inventory subsets, and so, the "monthly" descriptor is left off of the inventory descriptor. An example of this is seen for the "2000_anthro_USA…" run immediately above.

Table 8. Inventory Component Runs using the "oxid50, pf0" model configuration

Run Number	Run Name	Group
24	2000_monthly_anthro_2p5_36mo_v26qr_oxid50_pf0_int8 (*)	2000 baseline, inventory
25	2000_monthly_biomass_2p5_36mo_v26qr_oxid50_pf0_int8	
26	2000_monthly_land_2p5_36mo_v26qr_oxid50_pf0_int8	
27	2000_monthly_ocean_2p5_36mo_v26qr_oxid50_pf0_int8	
28	2000_monthly_reemission_2p5_36mo_v26qr_oxid50_pf0_int8	
29	2000_monthly_volcano_2p5_36mo_v26qr_oxid50_pf0_int8 (*)	
30	2050_B1_monthly_anthro_2p5_36mo_v26qr_oxid50_pf0_int8 (*)	2050 B1 future emissions scenario
31	2050_B1_monthly_biomass_2p5_36mo_v26qr_oxid50_pf0_int8	
32	2050_B1_monthly_land_2p5_36mo_v26qr_oxid50_pf0_int8	
33	2050_B1_monthly_ocean_2p5_36mo_v26qr_oxid50_pf0_int8	
34	2050_B1_monthly_reemission_2p5_36mo_v26qr_oxid50_pf0_int8	
35	2050_A1B_monthly_anthro_2p5_36mo_v26qr_oxid50_pf0_int8 (*)	2050 A1B future emissions scenario
36	2050_A1B_monthly_biomass_2p5_36mo_v26qr_oxid50_pf0_int8	
37	2050_A1B_monthly_land_2p5_36mo_v26qr_oxid50_pf0_int8	
38	2050_A1B_monthly_ocean_2p5_36mo_v26qr_oxid50_pf0_int8	
39	2050_A1B_monthly_reemission_2p5_36mo_v26qr_oxid50_pf0_int8	
40	2050_A1B_monthly_volcano_2p5_36mo_v26qr_oxid50_pf0_int8 (*)	
41	2050_A1FI_monthly_anthro_2p5_36mo_v26qr_oxid50_pf0_int8 (*)	2050 A1FI future emissions scenario
42	2050_A1FI_monthly_biomass_2p5_36mo_v26qr_oxid50_pf0_int8	
43	2050_A1FI_monthly_land_2p5_36mo_v26qr_oxid50_pf0_int8	
44	2050_A1FI_monthly_ocean_2p5_36mo_v26qr_oxid50_pf0_int8	
45	2050_A1FI_monthly_reemission_2p5_36mo_v26qr_oxid50_pf0_int8	
46	2050_A1FI_monthly_volcano_2p5_36mo_v26qr_oxid50_pf0_int8 (*)	

(*) The “monthly” descriptor is included in the run-label text for these anthropogenic and volcano emissions runs, but in fact, the emissions were constant throughout the year in these runs. Monthly varying emissions data were not available for these inventory subsets. It should also be noted that the “volcano” emissions subsets are identical for the different inventories, and so, separate “volcano” runs were not carried out for all configurations. When they were carried out, their equivalence was used as a QA/QC check on the computations.

Table 9. Inventory Component Runs using the "oxid33, pf0" model configuration

Run Number	Run Name	Group
75	2000_monthly_anthro_2p5_36mo_v26qr_oxid33_pf0_int8	2000 baseline, inventory
76	2000_monthly_biomass_2p5_36mo_v26qr_oxid33_pf0_int8	
77	2000_monthly_land_2p5_36mo_v26qr_oxid33_pf0	
78	2000_monthly_land_2p5_36mo_v26qr_oxid33_pf0_int8	
79	2000_monthly_ocean_2p5_36mo_v26qr_oxid33_pf0	
80	2000_monthly_reemission_2p5_36mo_v26qr_oxid33_pf0_int8	
81	2000_monthly_volcano_2p5_36mo_v26qr_oxid33_pf0_int8	
82	2050_B1_monthly_anthro_2p5_36mo_v26qr_oxid33_pf0_int8	2050 B1 future emissions scenario
83	2050_B1_monthly_biomass_2p5_36mo_v26qr_oxid33_pf0_int8	
84	2050_B1_monthly_land_2p5_36mo_v26qr_oxid33_pf0	
85	2050_B1_monthly_ocean_2p5_36mo_v26qr_oxid33_pf0	
86	2050_B1_monthly_reemission_2p5_36mo_v26qr_oxid33_pf0_int8	
87	2050_A1B_monthly_anthro_2p5_36mo_v26qr_oxid33_pf0_int8	2050 A1B future emissions scenario
88	2050_A1B_monthly_biomass_2p5_36mo_v26qr_oxid33_pf0_int8	
89	2050_A1B_monthly_land_2p5_36mo_v26qr_oxid33_pf0	
90	2050_A1B_monthly_ocean_2p5_36mo_v26qr_oxid33_pf0	
91	2050_A1B_monthly_reemission_2p5_36mo_v26qr_oxid33_pf0_int8	
92	2050_A1FI_monthly_anthro_2p5_36mo_v26qr_oxid33_pf0_int8	2050 A1FI future emissions scenario
93	2050_A1FI_monthly_biomass_2p5_36mo_v26qr_oxid33_pf0_int8	
94	2050_A1FI_monthly_land_2p5_36mo_v26qr_oxid33_pf0	
95	2050_A1FI_monthly_ocean_2p5_36mo_v26qr_oxid33_pf0	
96	2050_A1FI_monthly_reemission_2p5_36mo_v26qr_oxid33_pf0_int8	

The third part of the run-label text is a descriptor of the grid size used in the simulation. For essentially all of the runs presented in this report, a 2.5o x 2.5o grid was used, and this is indicated as "2p5" (for 2 point 5) in the run-label text, e.g., **2000_monthly_total_2p5_36mo_v26qr_oxid33_pf0_int8**.

The fourth part of the run-label text indicates the length of the simulation, and essentially all of the runs presented here is either 15 months ("15mo") or 36 months ("36mo"). All actual results shown are for the 12 months of 2005. In a 15-month run, 3 months of model spin-up were used, i.e., the simulation started in Oct 2004, but results were not "counted" until 2005 started. In a 36-month run, 24 months of model spin-up were used, i.e., the simulation started in Jan 2003, but results were not "counted" until 2005 started. Spin-up issues were discussed above in Section 3.3 (page 31). This descriptor is highlighted in yellow in this example: **2000_monthly_total_2p5_36mo_v26qr_oxid33_pf0_int8**.

The fifth part of the run-label text is a descriptor showing the model version used. In all runs presented in this report, version "v26qr" was used, e.g., **2000_monthly_total_2p5_36mo_v26qr_oxid33_pf0_int8**.

The sixth part of the run-label text is a descriptor indicating the scaling of the oxidation reaction rates used. In essentially all of the runs presented here, this is either 100% ("oxid100"), 50% ("oxid50"), or 33% ("oxid33"), e.g., **2000_monthly_total_2p5_36mo_v26qr_oxid33_pf0_int8**. The issue of reaction rate scaling is discussed above in Section 3.4 (page 36).

The seventh part of the run-label text is a descriptor indicating fraction of Hg(0) oxidation products of the O3, OH, and H2O2 reactions assumed to be Hg(p). In most cases, this is either 0% ("pf0") or 100% ("pf100"), e.g., **2000_monthly_total_2p5_36mo_v26qr_oxid33_pf0_int8**. The issue of oxidation products profile assumptions is discussed above in Section 3.4 (page 36).

The final part of the run-label text is an optional descriptor indicating the interpolation procedure that was used in the transformation of the emissions inventory to be used as input to the HYSPLIT-Hg model. Several iterations of this process were carried out, and the "final" method ("int8") was considered to be the most accurate. Accordingly, this approach was used in the relevant runs, and the "int8" descriptor is shown, e.g., **2000_monthly_total_2p5_36mo_v26qr_oxid33_pf0_int8**. For the L750_W1250 and LW2000 inventories, this transformation process was not needed, and so this descriptor is not present. Also, in the cases of the country-specific subsets of the anthropogenic emissions inventories, this descriptor was omitted. However, in these cases, the "int8" interpolation procedure was used, e.g., **2000_anthro_USA_2p5_36mo_v26qr_oxid33_pf0**. Additional information regarding the inventory transformation and interpolation procedures is included above in Section 2 (page 12).

The relatively involved, systematic set of run descriptors detailed above was utilized to keep accurate track of the configuration of any given run. Since 124 "final" runs were carried out – and hundreds more during testing and development – it was important to have clear, unambiguous run descriptors. Further, each simulation generated ~100 output files, and each run-output filename for a given run included the overall run name, for ease (and accuracy) in later use. This was particularly useful as many of the run-output files were used as input to various post-processing programs, and it was obviously essential to keep accurate track of which results belonged to which run. In this respect, these "complex" run labels served as an important QA/QC check on the results.

Table 10. Country-specific anthropogenic emissions inventory runs using the "oxid50, pf0" model configuration

Run Number	Run Name	Group
47	2000_anthro_USA_2p5_36mo_v26qr_oxid50_pf0	Country-specific anthropogenic emissions subsets for the 2000 baseline emissions inventory
48	2000_anthro_CAN_2p5_36mo_v26qr_oxid50_pf0	
49	2000_anthro_MEX_2p5_36mo_v26qr_oxid50_pf0	
50	2000_anthro_CHINA_2p5_36mo_v26qr_oxid50_pf0	
51	2000_anthro_INDIA_2p5_36mo_v26qr_oxid50_pf0	
52	2000_anthro_RUSSIA_2p5_36mo_v26qr_oxid50_pf0	
53	2000_anthro_OTHER_2p5_36mo_v26qr_oxid50_pf0	
54	2050B1_anthro_USA_2p5_36mo_v26qr_oxid50_pf0	Country-specific anthropogenic emissions subsets for the 2050 B1 future emissions scenario
55	2050B1_anthro_CAN_2p5_36mo_v26qr_oxid50_pf0	
56	2050B1_anthro_MEX_2p5_36mo_v26qr_oxid50_pf0	
57	2050B1_anthro_CHINA_2p5_36mo_v26qr_oxid50_pf0	
58	2050B1_anthro_INDIA_2p5_36mo_v26qr_oxid50_pf0	
59	2050B1_anthro_RUSSIA_2p5_36mo_v26qr_oxid50_pf0	
60	2050B1_anthro_OTHER_2p5_36mo_v26qr_oxid50_pf0	
61	2050A1B_anthro_USA_2p5_36mo_v26qr_oxid50_pf0	Country-specific anthropogenic emissions subsets for the 2050 A1B future emissions scenario
62	2050A1B_anthro_CAN_2p5_36mo_v26qr_oxid50_pf0	
63	2050A1B_anthro_MEX_2p5_36mo_v26qr_oxid50_pf0	
64	2050A1B_anthro_CHINA_2p5_36mo_v26qr_oxid50_pf0	
65	2050A1B_anthro_INDIA_2p5_36mo_v26qr_oxid50_pf0	
66	2050A1B_anthro_RUSSIA_2p5_36mo_v26qr_oxid50_pf0	
67	2050A1B_anthro_OTHER_2p5_36mo_v26qr_oxid50_pf0	
68	2050A1FI_anthro_USA_2p5_36mo_v26qr_oxid50_pf0	Country-specific anthropogenic emissions subsets for the 2050 A1FI future emissions scenario
69	2050A1FI_anthro_CAN_2p5_36mo_v26qr_oxid50_pf0	
70	2050A1FI_anthro_MEX_2p5_36mo_v26qr_oxid50_pf0	
71	2050A1FI_anthro_CHINA_2p5_36mo_v26qr_oxid50_pf0	
72	2050A1FI_anthro_INDIA_2p5_36mo_v26qr_oxid50_pf0	
73	2050A1FI_anthro_RUSSIA_2p5_36mo_v26qr_oxid50_pf0	
74	2050A1FI_anthro_OTHER_2p5_36mo_v26qr_oxid50_pf0	

Table 11. Country-specific anthropogenic emissions inventory runs using the "oxid33, pf0" model configuration

Run Number	Run Name	Group
97	2000_anthro_USA_2p5_36mo_v26qr_oxid33_pf0	Country-specific anthropogenic emissions subsets for the 2000 baseline emissions inventory
98	2000_anthro_CAN_2p5_36mo_v26qr_oxid33_pf0	
99	2000_anthro_MEX_2p5_36mo_v26qr_oxid33_pf0	
100	2000_anthro_CHINA_2p5_36mo_v26qr_oxid33_pf0	
101	2000_anthro_INDIA_2p5_36mo_v26qr_oxid33_pf0	
102	2000_anthro_RUSSIA_2p5_36mo_v26qr_oxid33_pf0	
103	2000_anthro_OTHER_2p5_36mo_v26qr_oxid33_pf0	
104	2050B1_anthro_USA_2p5_36mo_v26qr_oxid33_pf0	Country-specific anthropogenic emissions subsets for the 2050 B1 future emissions scenario
105	2050B1_anthro_CAN_2p5_36mo_v26qr_oxid33_pf0	
106	2050B1_anthro_MEX_2p5_36mo_v26qr_oxid33_pf0	
107	2050B1_anthro_CHINA_2p5_36mo_v26qr_oxid33_pf0	
108	2050B1_anthro_INDIA_2p5_36mo_v26qr_oxid33_pf0	
109	2050B1_anthro_RUSSIA_2p5_36mo_v26qr_oxid33_pf0	
110	2050B1_anthro_OTHER_2p5_36mo_v26qr_oxid33_pf0	
111	2050A1B_anthro_USA_2p5_36mo_v26qr_oxid33_pf0	Country-specific anthropogenic emissions subsets for the 2050 A1B future emissions scenario
112	2050A1B_anthro_CAN_2p5_36mo_v26qr_oxid33_pf0	
113	2050A1B_anthro_MEX_2p5_36mo_v26qr_oxid33_pf0	
114	2050A1B_anthro_CHINA_2p5_36mo_v26qr_oxid33_pf0	
115	2050A1B_anthro_INDIA_2p5_36mo_v26qr_oxid33_pf0	
116	2050A1B_anthro_RUSSIA_2p5_36mo_v26qr_oxid33_pf0	
117	2050A1B_anthro_OTHER_2p5_36mo_v26qr_oxid33_pf0	
118	2050A1FI_anthro_USA_2p5_36mo_v26qr_oxid33_pf0	Country-specific anthropogenic emissions subsets for the 2050 A1FI future emissions scenario
119	2050A1FI_anthro_CAN_2p5_36mo_v26qr_oxid33_pf0	
120	2050A1FI_anthro_MEX_2p5_36mo_v26qr_oxid33_pf0	
121	2050A1FI_anthro_CHINA_2p5_36mo_v26qr_oxid33_pf0	
122	2050A1FI_anthro_INDIA_2p5_36mo_v26qr_oxid33_pf0	
123	2050A1FI_anthro_RUSSIA_2p5_36mo_v26qr_oxid33_pf0	
124	2050A1FI_anthro_OTHER_2p5_36mo_v26qr_oxid33_pf0	

5. Model Evaluation

5.1. Some issues related to the comparison of model-estimated and measured atmospheric mercury concentrations and deposition

For ease in discussion, data from Figure 31 is reproduced below in Figure 32, along with some additional data that will now be discussed. In considering these results, it is important to note a few items.

First, for some of the sites, the measurements available for 2005 are very limited (as shown in Table 12). For example, the sampling periods for the Paradise and Gibbs Ranch sites (in Nevada) represent only a few percent of the entire year. For the 7 Canadian CAMNet sites shown, the sampling coverage ranges from 93-98%. The differing extents of data need to be considered in interpreting the comparison between annual, modeled, average concentrations and annual, measured, average concentrations. For each model configuration, two results are shown in the figure below: the average over all of 2005 and the average for the hours during 2005 during which measurements were reported.

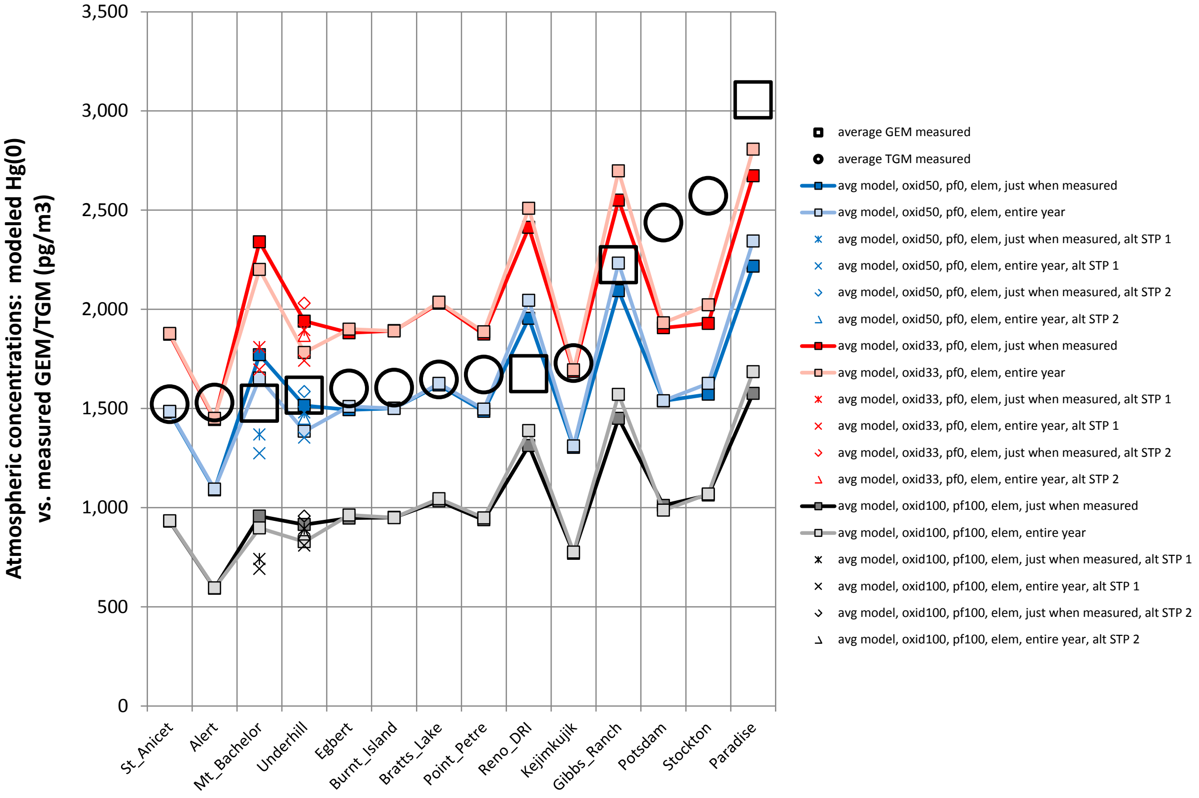

Figure 32. Comparison of modeled Hg(0) vs. measured GEM and TGM

Table 12. Sampling locations for comparison of modeled vs. measured Hg(0)

Site name	Average GEM or TGM Conc (ng/m^3)	Sample and/or Data Averaging Period (hours)	Number of Samples and/or Data Points	Approx. Percent of Year Covered by Samples	Measure -ment Quantity	Data Source[5]
St. Anicet	1.52	1	8428	96	TGM	CAMNet
Alert	1.53	1	8125	93	TGM	CAMNet
Kejimkujik	1.73	1	8158	93	TGM	CAMNet
Point Petre	1.67	1	8253	94	TGM	CAMNet
Egbert	1.60	1	8365	95	TGM	CAMNet
Burnt Island	1.61	1	8549	98	TGM	CAMNet
Bratt’s Lake	1.65	1	8132	93	TGM	CAMNet
Mt. Bachelor	1.53	1	1962	22	GEM	Seth Lyman and Dan Jaffe
Reno DRI	1.67	2	1521	35	GEM	Seth Lyman and Mae Gustin
Paradise	3.05	2	199	5	GEM	Seth Lyman and Mae Gustin
Gibbs Ranch	2.23	2	172	4	GEM	Seth Lyman and Mae Gustin
Underhill	1.57	2	1589	36	GEM	Eric Miller
Potsdam	2.44	24	68	19	TGM	Tom Holsen and Young-Ji Han
Stockton	2.57	24	43	12	TGM	Tom Holsen and Young-Ji Han

---

[5] Full references for the data sources are provided in the following sections in which each site is discussed

Second, there are inherent uncertainties in the modeling results relative to the elevation of the sampling site. In uniformly flat terrain within a given grid cell, the “ground level” specified in the meteorological model -- and therefore used in the Eulerian grid -- would be representative of all locations within the cell. In that simplistic case, the use of the average concentration in the lowest model layer (0-100 m) would be a reasonable choice to compare with ground-level measurements. However, in reality, the terrain is not uniform over many grid cells, and the use of a single height for the concentration results for that cell introduces uncertainty into the results. An example of this issue is the situation for Mt. Bachelor, one of the sites for which measurement data could be obtained for 2005. The actual elevation of the Mt. Bachelor sampling site, at the summit of Mt. Bachelor, is 2763 meters above mean sea level (m-msl).

The location of the site in relation to nearby Eulerian grid cells used in this modeling is shown in Figure 33. The grid cell centroids, spaced 2.5° x 2.5° apart, are shown, and the “grid square” that contains the Mt. Bachelor site is demarcated with a white dashed line. It is seen that the centroid of this grid square is at a substantial distance from the site (~130 km), and, the elevation at the grid centroid [~560m above mean sea level (msl)] is much lower than the elevation at the site (2763m-msl). The coarse grid of the model does not “see” the complex terrain in the grid square, but considers the entire grid cell as being “flat”. The terrain in the immediate vicinity of the site around the site is shown in Figure 34.

The 2005 time series of pressures and heights of the meteorological grid cells above Mt. Bachelor are shown in Figure 35, for the NCEP/NCAR Global Reanalysis data used in this analysis. The mandatory pressure at levels 1-5 are constant at 1000, 925, 850, 700, and 600 hPa, respectively (these are the horizontal lines shown in the figure). In this meteorological data set, the pressure levels are set at specified, fixed levels. The pressure at the “surface” of the grid cell (“PRSS_0_Mt_Bachelor”) is shown with yellow squares, and can be seen to on the order of 950 hPa, corresponding to somewhere between the 1st and 2nd layers (perhaps closest to the 2nd layer). So, in this case, the actual surface of the grid cell is somewhere between the 1st and 2nd layer heights. The first layer height (at 1000 hPa) is actually below the actual surface of the grid cell, but it is artificially computed and included in the dataset. Now, the height of the 2nd layer (shown with purple “+” symbols) is on the order of ~800 m-msl, while the height of 1st layer is on the order of ~200 m-msl.

So, the surface level height of the grid cell containing Mt. Bachelor is between ~200 -800 m-msl. This is consistent with the Google Earth derived elevation of 560 m-msl of the grid cell centroid, shown in Figure 33. As noted above, this can be interpreted as the “average” terrain height in this 2.5° x 2.5° grid cell. The actual terrain, of course, is complex, with Mt. Bachelor and other peaks and ranges within the cell at higher elevation, and other areas of the cell at lower elevation. For the modeled concentrations at Mt. Bachelor, we used the average concentration at a height layer 2000-3000 m above “ground level”, which for the grid cell in question, would be on the order of 2500 – 3500 m-msl. The basic idea here is that the coarseness of the grid – in this case, 2.5° x 2.5° -- introduces inherent uncertainties into the estimation of concentrations, particularly in grid cells that have highly uneven topography, like the grid cell containing Mt. Bachelor.

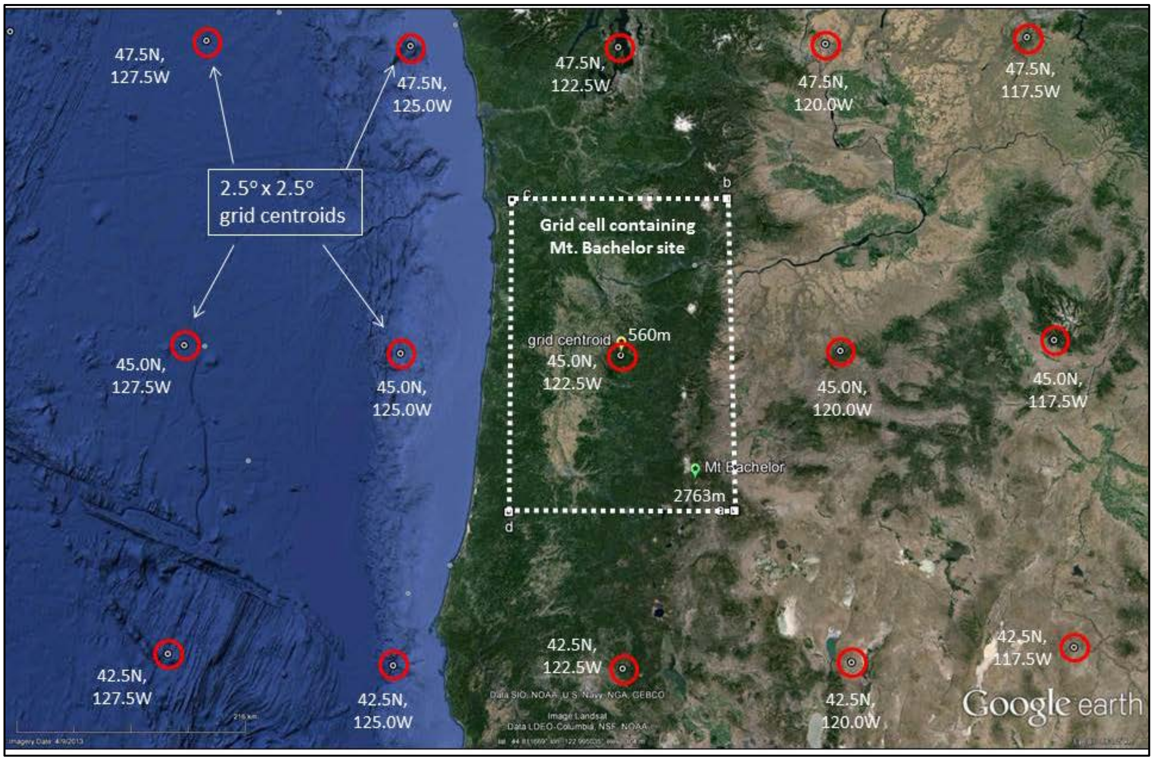

Figure 33. Eulerian grid centroids, cells, and the Mt. Bachelor site

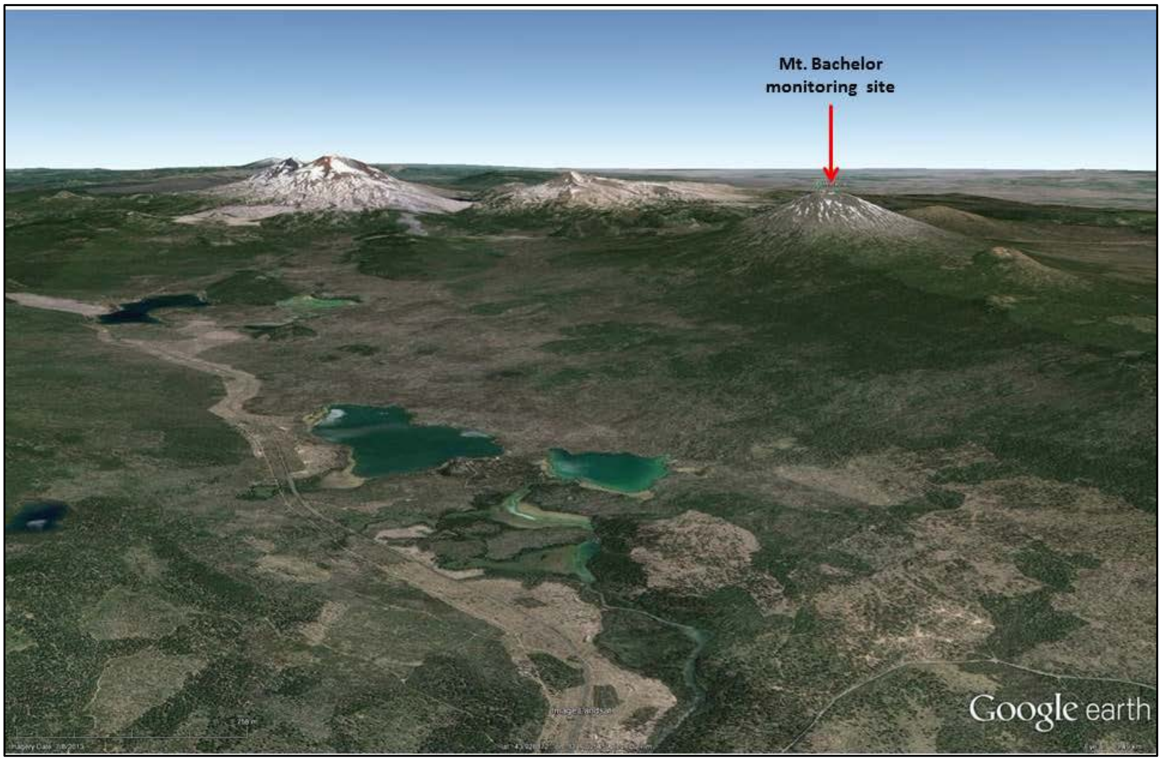

Figure 34. Terrain in the vicinity of the Mt. Bachelor site

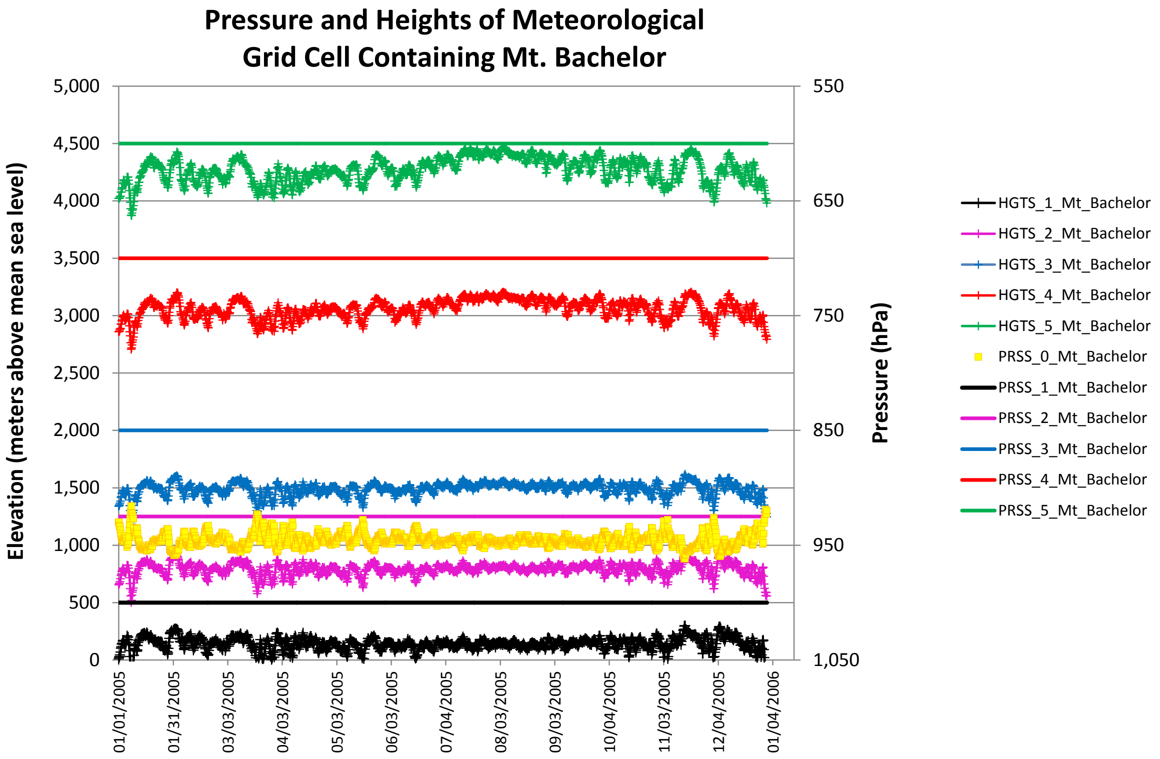

Figure 35. Pressure and heights of meteorological grid cell containing Mt. Bachelor

A closely related, inherent modeling uncertainty concerns the transformation of model results to *standard temperature and pressure* ("STP": 0 ^{o}C, 1 atm) in order to compare with measurement data. Mercury concentration data collected using the Tekran instrument suite, and comparable instrument suites, are generally reported transformed to STP. So, to properly compare modeled and measured concentration estimates, the modeled results must also be transformed to STP. The transformation can be carried out using the following equation:

$$C_{STP} = C_o * (P_{STP} / P_o) / (T_{STP} / T_o)$$

In which C_{STP} is the transformed concentration (at STP), e.g., in pg/m^3, C_o is the untransformed "model-native" concentration, e.g., in pg/m^3, P_{STP} is the "standard pressure" (1 atm), P_o is the "model-native" pressure, T_{STP} is the standard temperature (273.15 ^{o}K), and T_o is the "model-native" temperature (^{o}K). Now, while the temperature and pressures at the various model layers are "known", the exact elevation and layer to use for the conversion is complicated by the same factors as discussed above. In Figure 32, a plausible, alternative STP transformation is shown for Mt. Bachelor, and two plausible, alternative STP transformations are shown for Underhill. Underhill is also a site in region of complex terrain. It can be seen that these alternative transformations -- especially for Mt. Bachelor – introduce a potentially significant variation in the results.

Another issue that makes the comparison between modeled and measured concentrations and deposition challenging is directly related to the gridded nature of the emissions and the fate and transport modeling. The concentration and deposition results from the gridded model are averages for each entire grid cell – in this case 2.5^{o} x 2.5^{o} (approximately 250 km x 250 km) – but the comparable measurement data are for a specific location within that grid cell. In almost all cases, the actual concentrations or deposition will vary spatially within the cell. This implies that even if the model was perfect, its cell-average results should not actually match with the measurements at a specific location within the cell, unless that measurement site happened to fortuitously be located at a place that experienced the cell-average conditions. This inherent difficulty arises with all gridded (also called "Eulerian") models. The atmospheric concentration measurement sites in the immediate Great Lakes region used for model evaluation are shown in Figure 36 below.

A related issue concerns subgrid transport and dispersion phenomena. In reality, there are generally a number of significant point sources of mercury within a given grid cell. Each of these sources will have a greater or lesser impact on a given, nearby sampling site, depending on the detailed behavior of its downwind plume. With a gridded model, the emissions for all sources within a cell are combined together and uniformly distributed throughout the cell immediately after emission. This could result in overestimates or underestimates of concentration or deposition depending the locations and characteristics of the actual plumes from significant sources in the cell. The same atmospheric concentration model evaluation sites are shown in Figure 37 along with the gridded emissions of Hg(0) in the Great Lakes region, associated with the 2000-baseline inventory.

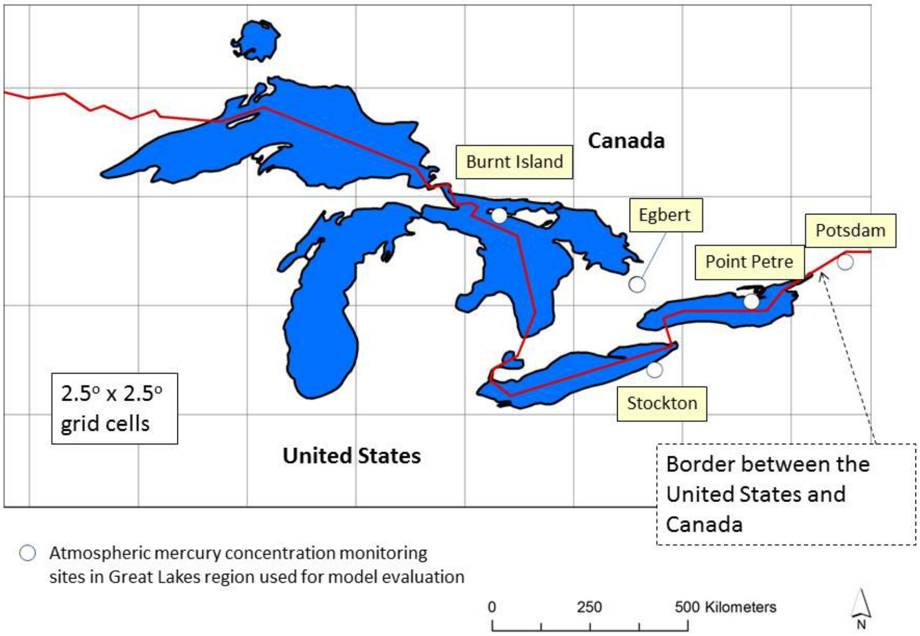

Figure 36. Grid cells and atmospheric concentration model evaluation sites in the immediate Great Lakes region

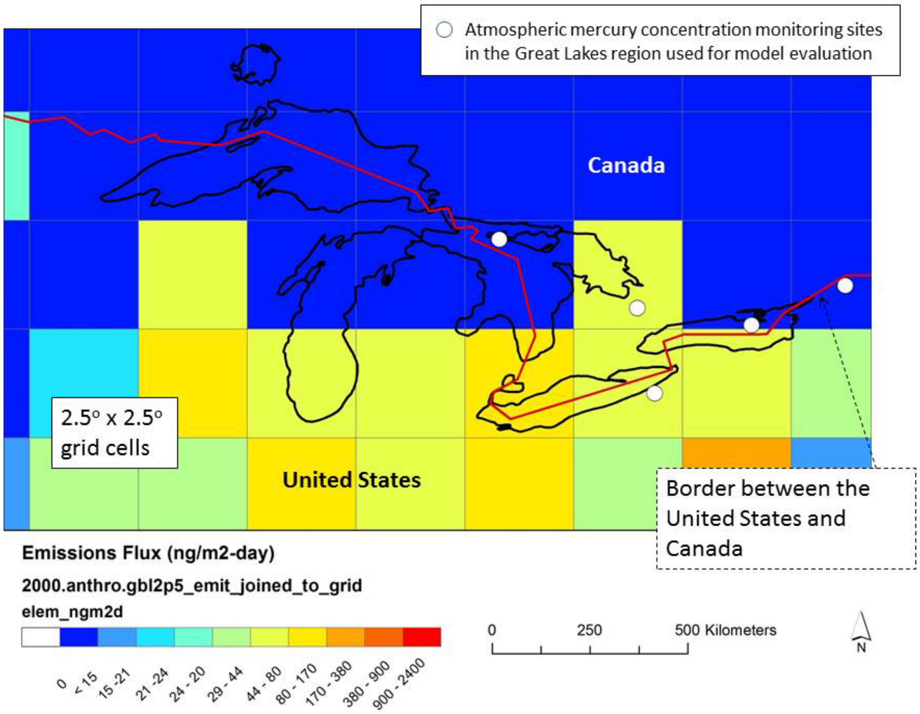

Figure 37. Grid cell emissions of Hg(0) and atmospheric concentration model evaluation sites in the immediate Great Lakes region

Next, it must be mentioned that the meteorological data used to drive the HYSPLIT-Hg model in this analysis is for 2005, as are the measurement data used for model evaluation. Ideally, the emissions used in the baseline modeling – used for the evaluation -- would also be for 2005. However, in this case, the year 2000 inventory of Lei *et al*. (2013, 2014) was used as the baseline, for model evaluation, as it was considered more methodologically consistent with the future emissions scenarios adapted from that work. Thus, again, even if the modeling was perfect, the modeled and measured concentrations and deposition would not be expected to match, as the emissions for the modeling and measurement periods are not for the same time frame. Mercury emissions are not believed to have changed dramatically between 2000 and 2005, but, there certainly were some changes that occurred. Overall, mercury emissions in the U.S. and Canada are believed to have declined moderately over that period, as discussed briefly in Section 2 above. But, emissions from some individual sources may have increased (e.g., new facilities were built) during this period, and the actual impact on a given measurement site of the mismatch between the emissions and measurement time periods is difficult to assess.

Finally, we note that for the purposes of the atmospheric concentration evaluations presented here, daily average model output concentrations were utilized. At some measurement sites, daily average measurements were collected, but at most sites, one-hour or two-hour measurements were reported. In some cases, these short-term measurements were collected throughout the day, and their average would represent a true daily average. But at some sites, the short-term measurements did not last throughout a given day, and so, the “average daily concentration” that could be estimated from these more sporadic measurements would not be expected to match the actual daily average concentration at the site.

With the above caveats in mind, model-estimated atmospheric concentrations and deposition of mercury are compared with measurements below. First, concentrations of Hg(0) are compared. Then, concentrations of Hg(II) and Hg(p) are compared. Finally model estimates of mercury wet deposition are compared against measurements. In light of all of the issues discussed above, perhaps the most that can be realistically hoped for is for the model estimates and measurements at any given site be approximately the same magnitude, and show roughly comparable variances.

5.2. Comparison of model-estimated and measured Hg(0) atmospheric concentrations

The universe of measurement sites considered for model evaluation is reproduced in Figure 38 below. 2005 data were not available for some of the sites and so they were not included. However, data for most of the sites were obtained – at least for Gaseous Elemental Mercury (GEM) or Total Gaseous Mercury (TGM). These measurements will be compared against model estimates of Hg(0).

It should be noted at the outset that while GEM and Hg(0) are the "same", TGM also likely includes other Hg species (e.g., some Hg(II) species) and so is not exactly comparable to Hg(0). In many cases, the levels of the non-Hg(0) mercury compounds in TGM are believed to be relatively small. Nevertheless, this introduces yet another difficulty in the interpretation of model evaluation results. TGM is expected to be greater than or equal to Hg(0) (aka GEM).

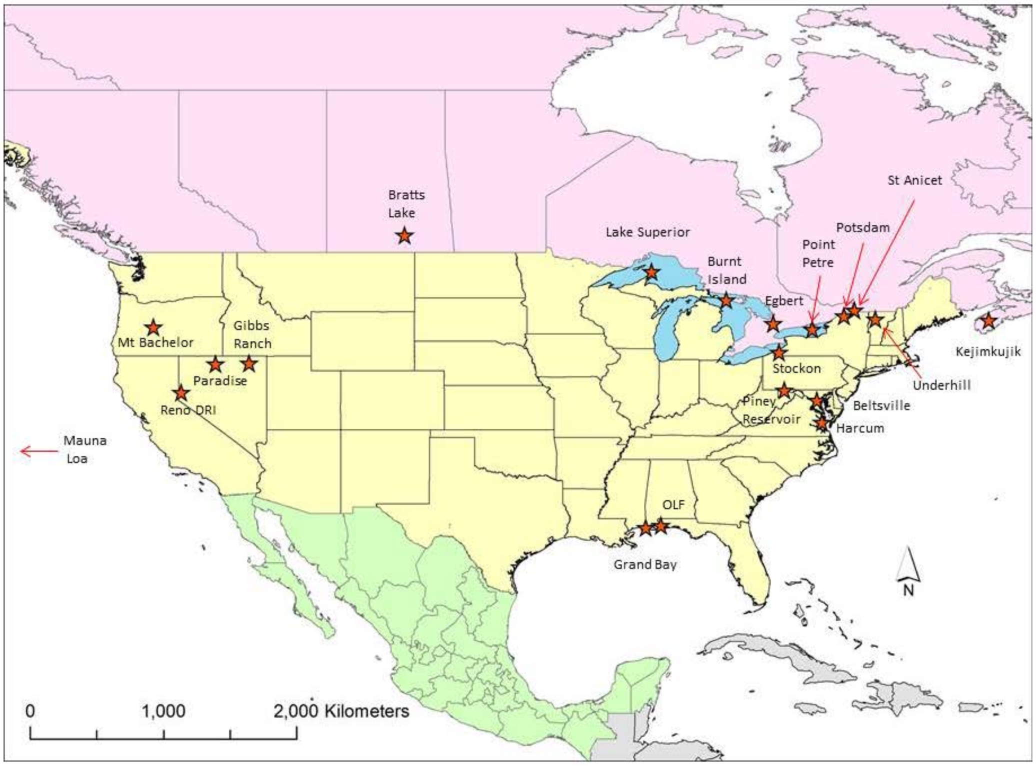

Figure 38. Measurement sites considered for atmospheric concentration model evaluation

5.2.1 **Underhill, Vermont, USA**

Mercury measurements collected in 2005 at Underhill, Vermont, were obtained from Eric Miller[6]. Measurements of GEM and RGM began in May 2005 at the site, and measurements of Hg(p) began in July 2005. The speciated mercury data collected at the site were generally 2-hour averages, taken every 3 hours. The Underhill site (Gratz *et al*., 2009) is located on the western slope of Mt. Mansfield at the Proctor Maple Research Center at an elevation of 399m above mean sea level. Like Mt. Bachelor, discussed in detail above, it is situated in somewhat complex terrain. As such, there are uncertainties regarding which model concentration level to use for comparison (i.e., level 02 = 0-100m vs. level 03 = 100-500m), and which meteorological data level to use for the correction to Standard Temperature and Pressure (STP).

Figure 39 shows daily average Hg(0) (aka Gaseous Elemental Mercury or “GEM”) measurements along with model-estimated daily average Hg(0) concentrations at concentration level 3 (100-500m above ground level). Four different model results are shown: one with no STP adjustment, and three with different STP adjustments, i.e., adjustments based on different meteorological data levels. In the model results in this figure, the “oxid50, pf0” model configuration was used. It can be seen that the alternative STP treatments do not introduce a dramatic change in the results, but the difference between the STP-adjusted model results and the non-STP-adjusted results is moderately significant in the summer months. Overall, it can also be seen that the model predictions are reasonably consistent with the measurements. During the first 3.5 months of measurements (May, June, July, and the first few weeks of August), and during October and November, the model shows quite good agreement with measurements. This level of agreement is perhaps even surprising, given challenges outlined in the previous section. There is a period of about a month, starting in late August 2005, with relatively low measured concentrations and systematic model overestimates. In addition, there is a 3-week period at the very end of 2005 with relatively high measured concentrations and systematic model underestimates. As discussed in the previous section, numerous factors are present that suggest that close agreement between these model results and the actual measurements is not at all expected. The reasons for the differences noted above would have to be investigated using a more highly resolved modeling approach, e.g., along the lines of the analysis carried out in earlier phases of this GLRI work.

Figure 40 shows a comparable comparison, but in this case, both the “oxid50, pf0” and “oxid33, pf0” configurations are shown, along with just two STP adjustment alternatives (no adjustment, and adjustment using the “surface” meteorological data (“STP Level 0”). It can be seen that the model predictions using the “oxid33, pf0” configuration are systematically higher than those using the “oxid50, pf0” configuration. This is an expected result, as the lower Hg(0) oxidation reaction rates in the “oxid33, pf0” configuration mean that more Hg(0) “survives” its transport after emissions and can contribute to atmospheric levels at a given site. It is also seen that the STP adjustment introduces a variation roughly comparable to the differences seen between the two oxidation rate treatments, especially in the

---

[6] Eric Miller, personal communication, 2012. Ecosystems Research Group, Norwich, VT

summer months. Overall, however, the figure shows that the “envelope” of model predictions is reasonably consistent with the measurements.

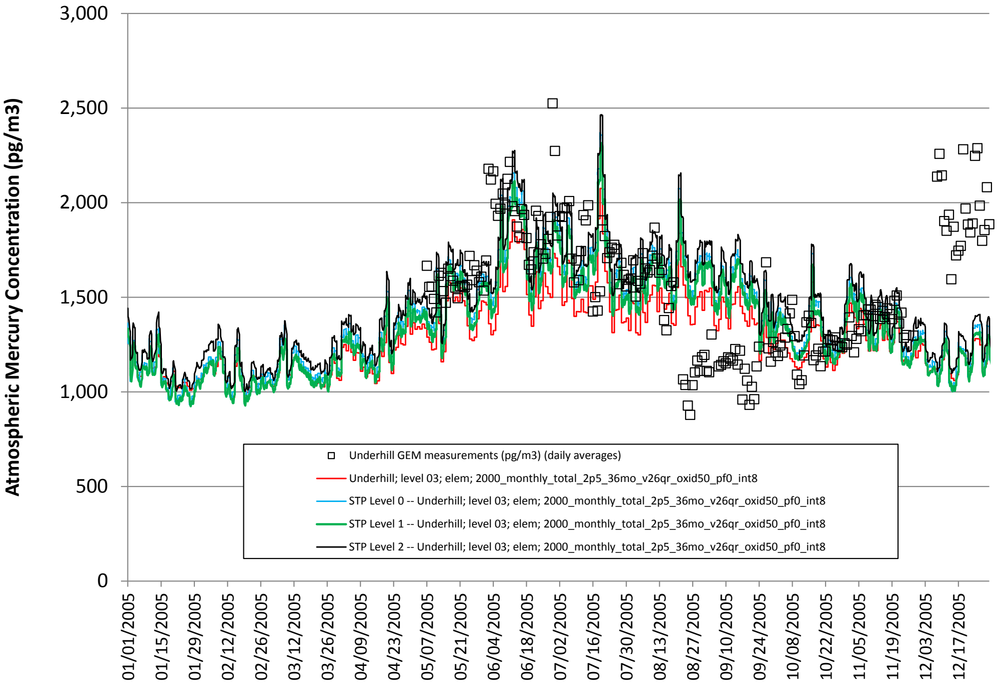

Figure 39. Measured Hg(0) at Underhill (Vermont) and model estimates using the "oxid50, pf0" configuration

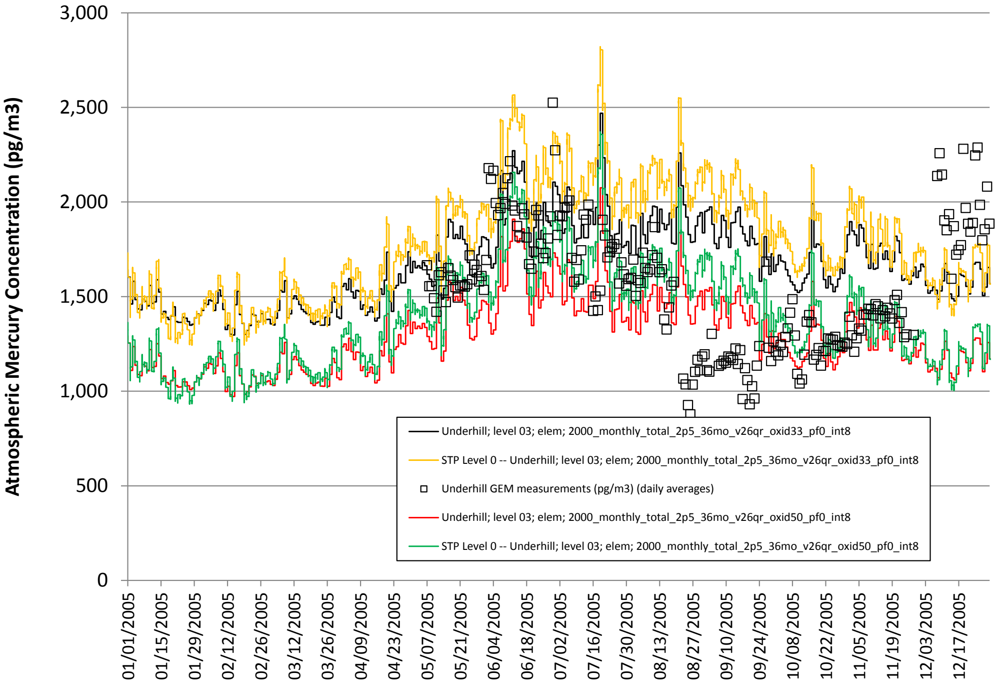

Figure 40. Measured Hg(0) at Underhill (Vermont) and model estimates using the “oxid50, pf0” and “oxid33, pf0” configurations, with and without STP adjustments

Given the uncertainties in comparing these modeling results to the measurements, this model evaluation exercise can be regarded as somewhat preliminary. Speciated ambient mercury concentration observations have continued at the Underhill site, under the direction of Eric Miller (e.g., Lan *et al*., 2012). In future collaborations, we hope to carry out analyses for more recent years, using a more highly resolved modeling approach. This would constitute a more complex model evaluation exercise, and the ability of the model to reproduce some of the actual temporal variations, e.g., specific episodic measurement peaks, could be investigated in more detail.

5.2.2 **St. Anicet, Quebec, Canada**

Total Gaseous Mercury (TGM) concentration measurement data for 2005 at the St. Anicet site in Quebec, part of the CAMNet monitoring network in Canada, were obtained from Environment Canada's *NAtChem* online chemical monitoring database (NAtChem, 2012). Laurier Poissant and Martin Pilote were the principal investigators collecting these TGM data at St. Anicet during 2005. Details about the site and its measurements are provided by Kellerhals *et al*. (2003), Poissant *et al*. (2005), Temme *et al*. (2007) and Cole *et al*. (2013). The St. Anicet site is 3km south of the St. Lawrence River between Cornwall Ontario and Montreal Quebec. It is a relatively level, rural location, surrounded by farms and wooded areas.

In Figure 41, the measured, daily average of the hourly measurements of TGM are shown along with model estimates, using the "oxid33, pf0" and the "oxid50, pf0" configurations, with and without an STP correction. In Figure 42, the same data are shown, just with the STP-corrected model results. In Figure 43, the hourly measurement data are added.

In these figures, it is seen that overall agreement between model results and measurements appears very reasonable. In some cases, the timing of "peaks" in the measurement data is matched very well by the model. Indeed, many of the broad "weekly-scale" temporal variations throughout the year appear to be relatively well captured by the model, even if the absolute magnitude of the concentration is not exactly matched. For example, both the measurements and the model results show a multi-day peak in the beginning of February 2005, although the magnitude of the observed peak is greater than that of the model-estimated peak. The high concentrations of mercury observed in this peak may have been caused by "direct" plume impacts from local and regional sources, the kind of impact that this coarse-grid modeling cannot easily capture.

During the first ~3 months of the year, the "oxid33, pf0" model predictions match the measurements more closely, but in most of the remainder of the year, the "oxid50, pf0" configuration results are closer to the measurements. During the last month of the year, the "oxid33, pf0" results again match more closely. It is interesting to note the low TGM concentrations for ~1 month starting in the latter half of August. This period of low concentrations is remarkably similar to that observed at the Underhill Vermont site, discussed above, suggesting that there may have been a common explanation for the low Hg(0) levels at the two sites during this period. The two sites are about 130 km apart.

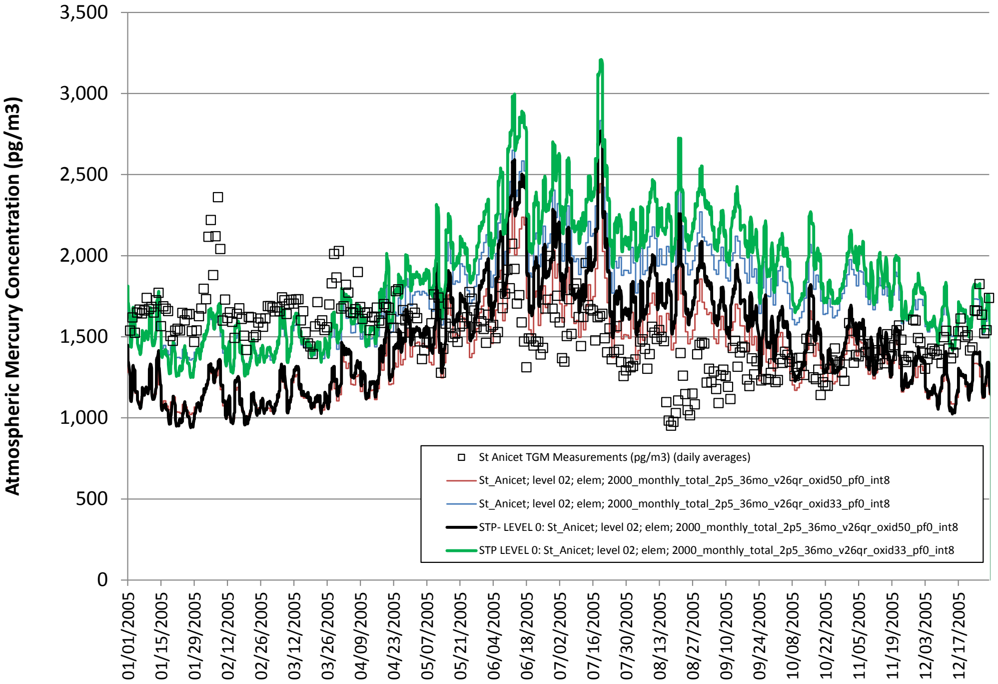

Figure 41. Measured TGM at St. Anicet (Quebec) and model estimates of Hg(0) using the "oxid50, pf0" and "oxid33, pf0" configurations, with and without STP adjustments

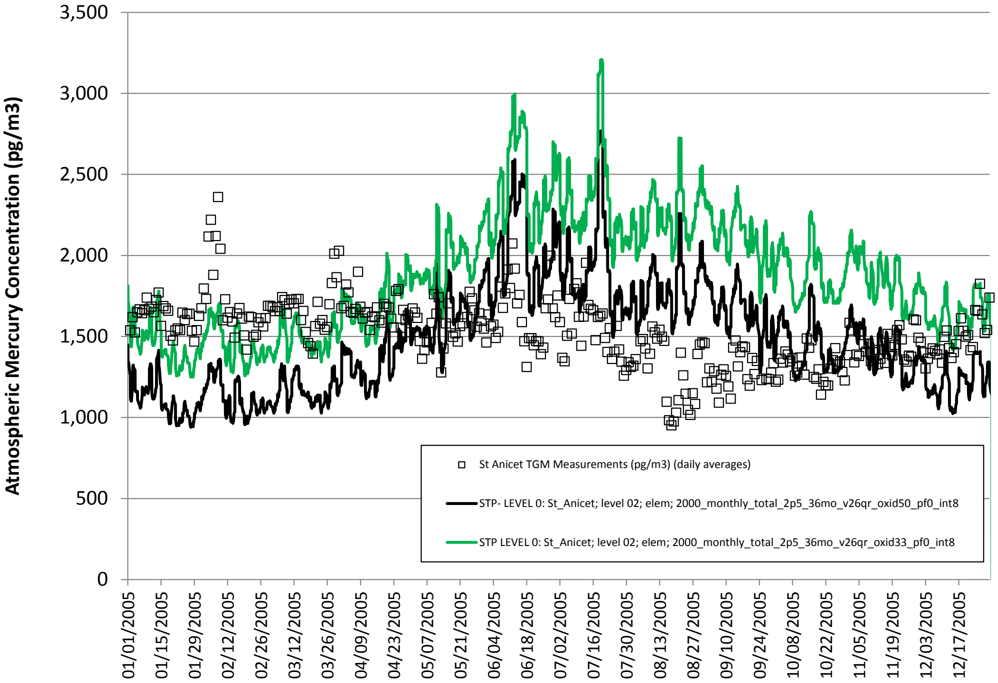

Figure 42. Measured TGM at St. Anicet (Quebec) and model estimates of Hg(0) using the "oxid50, pf0" and "oxid33, pf0" configurations

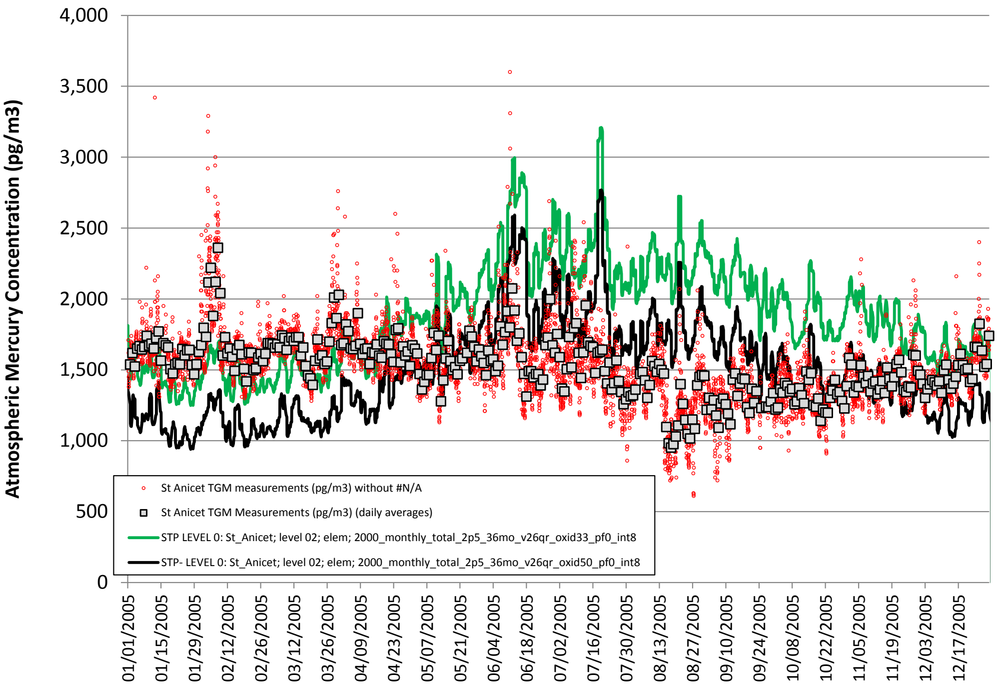

Figure 43. Measured TGM at St. Anicet (Quebec) (daily averages and hourly measurements) and model estimates of Hg(0) using the “oxid50, pf0” and “oxid33, pf0” configurations

5.2.3 **Reno (Desert Research Institute – DRI), Nevada, USA**

Mercury measurements collected in 2005 at the Desert Research Institute (DRI) in Reno, Nevada, were obtained from Seth Lyman[7]. The sampling methodology, data, and extensive analysis and interpretation are provided by Peterson *et al*. (2009). The speciated mercury data collected at the site were generally 2-hour averages, taken every 3 hours. The Reno-DRI site is ~5 km north of downtown Reno, Nevada. The elevation of the site is 1509m above sea level, located in a somewhat hilly region north of Reno, and is about 165m above the level of the city.

In Figure 45 and Figure 46, model estimates are compared against daily average measured concentrations, using model concentration level 02 (0-100 m above ground level) and model level 3 (100-500 m above ground level), respectively. In Figure 47 and Figure 48, the same data are plotted, along with the individual 2-hour measurements.

It is seen from these figures that for most of the dataset, the model results for concentration level 03 (100-500 m above ground level) are closer to the measurements, and within these results, the “oxid50, pf0” configuration appears to show the closest agreement with the measurements.

Interestingly, however, it can also be seen that for some of the highest measured values (e.g., the large peaks in Jan, Feb, Nov, and Dec), the model results for concentration level 02 (0 – 100 m above ground level) are more consistent with the measured values. Perhaps, this is because the site typically sees more elevated air masses, characteristic to a certain extent of the free troposphere, and so the elevated model concentration results (100-500 meters above ground level) are more realistic. But, in some cases, the site sees more local and/or “ground level” air masses, perhaps more heavily laden with mercury from surface emissions, and this leads to the higher measured concentrations. In these cases, the lower-model-concentration level would be considered more representative, and the data show this more consistent agreement for many of the peaks. In support of this possible explanation, Weiss-Penzias and co-workers (2014) suggest that the Reno DRI site (and Paradise site, discussed below) is somewhat influenced by local, surfaces sources. However, there are other potential explanations for the model vs. measurement findings presented here, and more investigation will need to be carried out to make any definitive statements.

On the whole, however, it can be seen that the model results are reasonably consistent with the measurements.

---

[7] Seth Lyman, personal communication, 2011, University of Washington-Bothell. Current affiliation: Utah State University, Vernal, Utah.

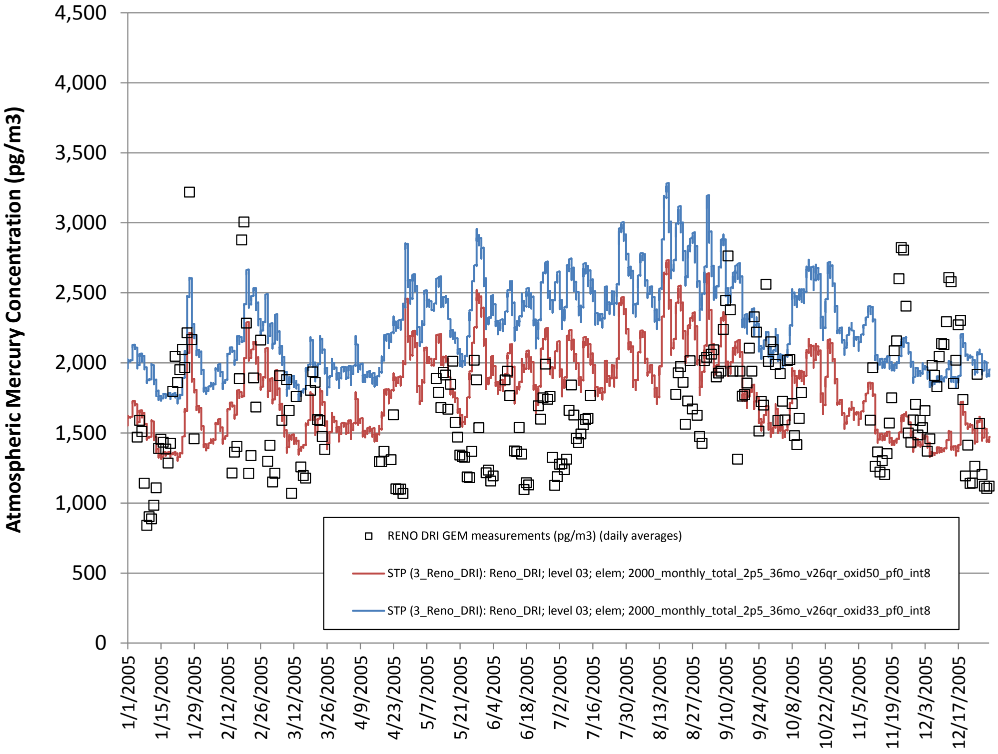

Figure 44. Measured Hg(0) at Reno (Nevada) and model estimates using the "oxid33, pf0" and "oxid50, pf0" configurations, in model concentration level 3 (100-500 m above ground level)

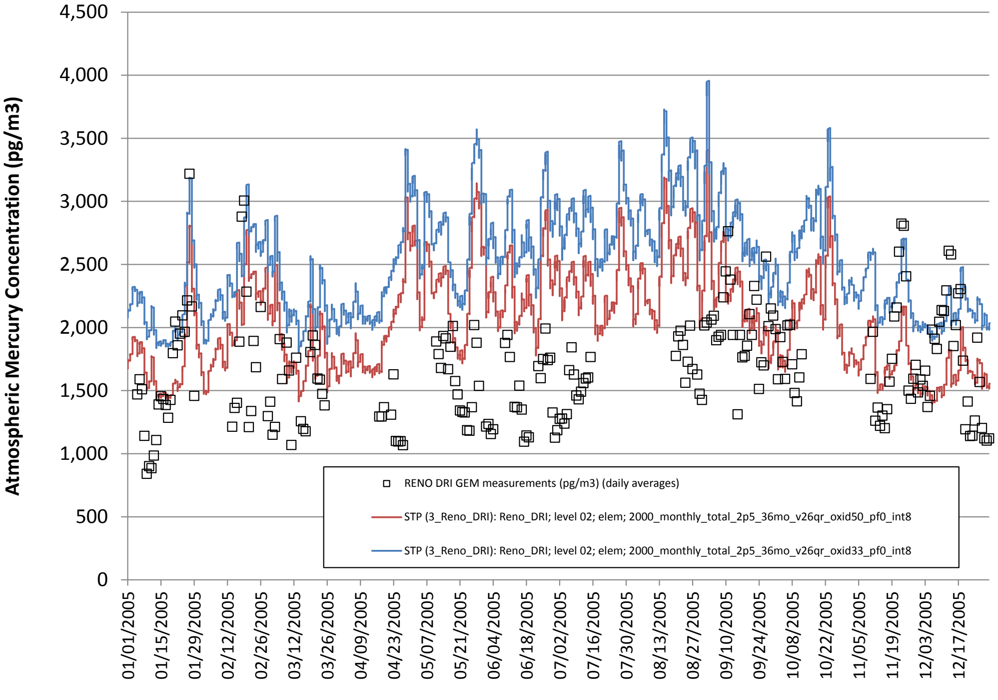

Figure 45. Measured Hg(0) at Reno (Nevada) and model estimates using the "oxid33, pf0" and "oxid50, pf0" configurations, in model concentration level 2 (0 - 100 m above ground level)

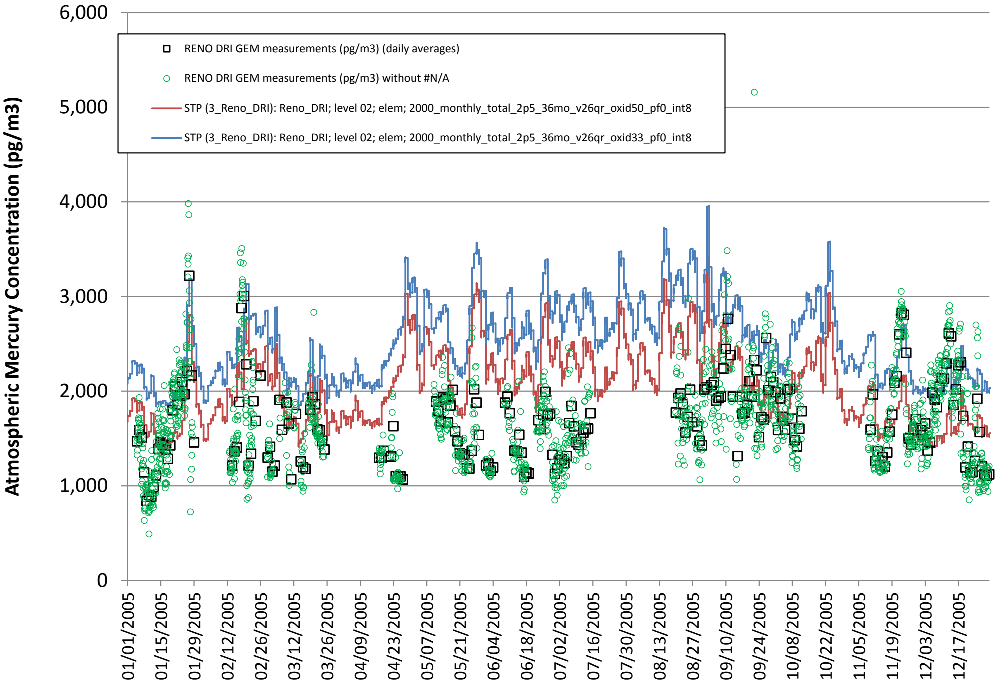

Figure 46. Measured Hg(0) at Reno (Nevada) (daily avgs and 2-hr measurements) and model estimates using the "oxid33, pf0" and "oxid50, pf0" configurations, in model concentration level 2 (0 - 100 m above ground level)

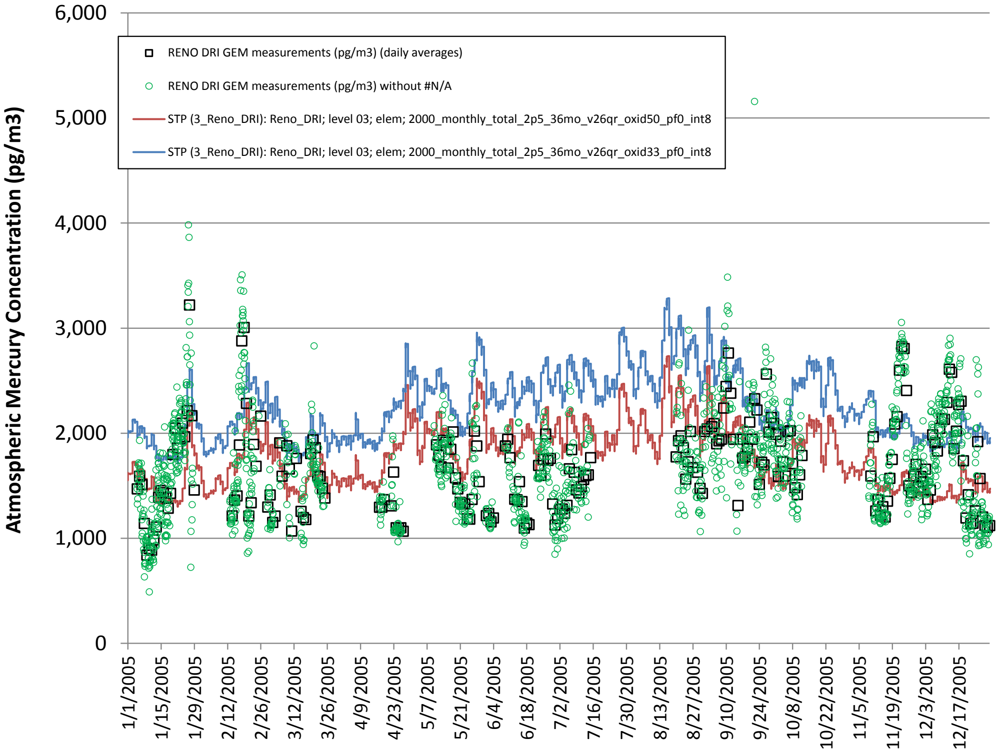

Figure 47. Measured Hg(0) at Reno (Nevada) (daily avgs and 2-hr measurements) and model estimates using the "oxid33, pf0" and "oxid50, pf0" configurations, in model concentration level 3 (100 -500 m above ground level)

5.2.4 **Mt. Bachelor, Oregon, USA**

Mercury measurements collected in 2005 at the Mount Bachelor Observatory (MBO) on the summit of Mt. Bachelor, Oregon, were obtained from Seth Lyman and Dan Jaffe[8]. The sampling methodology, data, and extensive analysis and interpretation regarding the Mt. Bachelor measurements are provided by Weiss-Penzias *et al*. (2006, 2007), Swartzendruber *et al*. (2006), and Finley *et al*. (2009). Gaseous elemental mercury (GEM) was measured continuously on 5-minute cycles, and when RGM and Hg(p) were measured, they were measured on a 3-hour cycle. Mount Bachelor Observatory is situated at the summit of Mt. Bachelor, a dormant volcano in the Cascade Mountain Range in central Oregon, at 2763 m above mean sea level. The site generally receives air masses from the west, and is considered to frequently sample "free tropospheric" air. The regional topography and the challenges of comparing the modeling results obtained in this analysis with the measurements at MBO are discussed in Section 5.1 above. Due to these model-based issues, it is not expected that the simulation results will closely match the measurements. Nevertheless, comparisons will be presented and discussed briefly here.

In Figure 48, model estimates are compared against daily average measured concentrations, using model concentration level 06 (2000-3000 m above ground level), for both the "oxid33, pf0" and "oxid50, pf0" configurations, using two alternative Standard Temperature and Pressure (STP) adjustments. In Figure 49, the same data are plotted, along with the individual hourly-average data points.

In one of the two different STP adjustments in these figures, data from meteorological level 4 (750 hPa) were used, denoted "*STP (4_Mt_Bachelor)*" in the figure legend. Since the atmospheric pressure measured at MBO is typically on the order of 735 hPa, the use of the 750 hPa level data is a reasonable choice. Data are also presented using the "surface-level" pressure, i.e., the surface level of the grid cell [denoted "*STP (0_Mt_Bachelor)*" in the figure legend]. It can be seen that there is a significant difference between the two STP adjustments, on the order of ~30%. This difference is the same order of magnitude as the differences between the "oxid33, pf0" and "oxid50, pf0" simulation results. In fact, as can be seen from the blue and green lines in the figure, the differences can "cancel" each other out, i.e., the reduction in Hg(0) concentration from using the higher oxidation rates in the "oxid50, pf0" configuration (green line) is matched by the increase in Hg(0) concentration with in using the STP-0 (surface-level) adjustment (blue line), as opposed to the STP-4 adjustment. It is seen from these figures that for most of the dataset, the envelope of model results appears to encompass the measurements. *If* the STP-4 adjustment is "correct", then the "oxid50, pf0" simulation results match the observations more closely than the "oxid33, pf0" configuration. It can also be seen that in some cases, the broad multi-week temporal patterns appear to be captured to a certain extent by the model, e.g., the overall rise and fall during August – September, and even including the modest reduction around the beginning of September. The timing of the observed peak in the two-week period beginning in late May also seems to be reproduced by the modeling.

---

[8] Seth Lyman, personal communication, 2011, University of Washington-Bothell. Current affiliation: Utah State University, Vernal, Utah

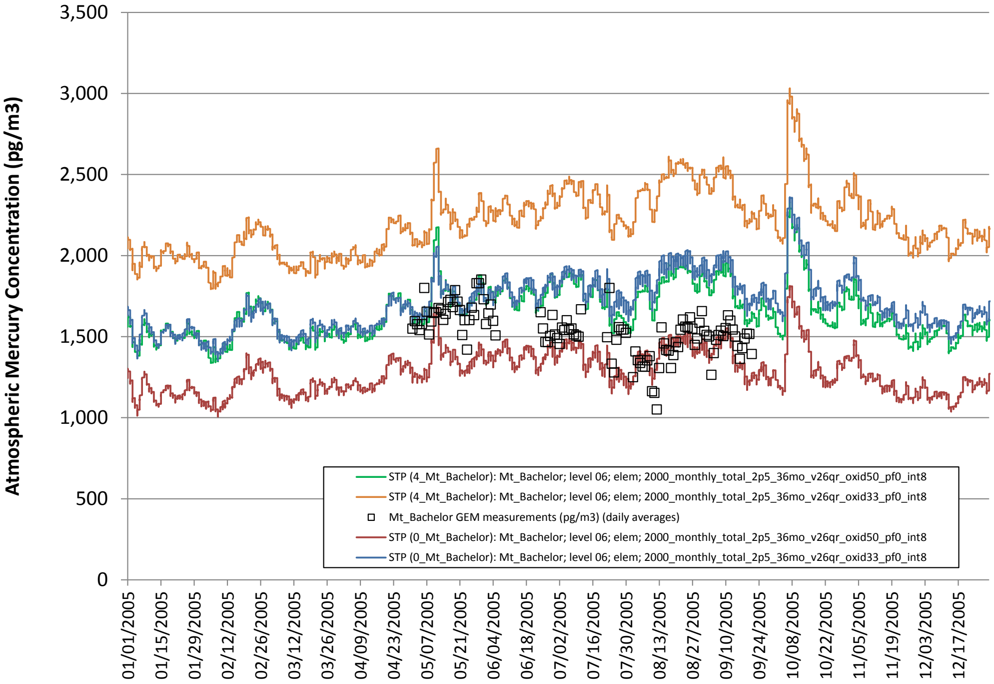

Figure 48. Measured Hg(0) at Mt. Bachelor (Oregon) and model estimates using the "oxid33, pf0" and "oxid50, pf0" configurations, with two different STP adjustments

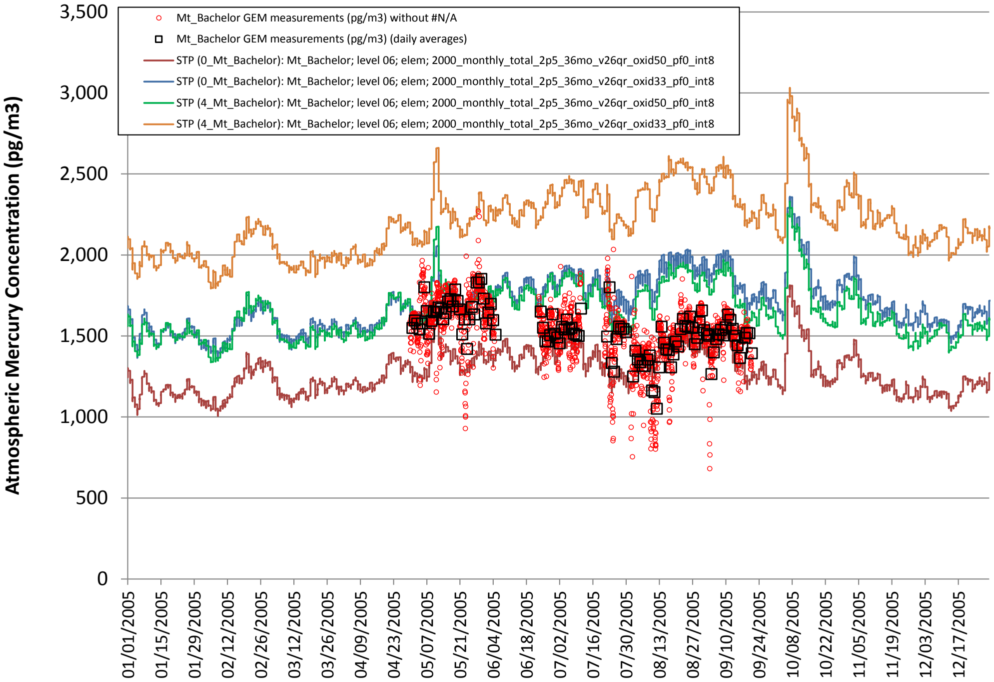

Figure 49. Measured Hg(0) at Mt. Bachelor (Oregon) (daily averages and hourly measurements) and model estimates using the "oxid33, pf0" and "oxid50, pf0" configurations, with two different STP adjustments

5.2.5 **Burnt Island, Ontario, Canada**

Total Gaseous Mercury (TGM) concentration measurement data for 2005 at the Burnt Island site in Ontario, part of the CAMNet monitoring network in Canada, were obtained from Environment Canada's *NAtChem* online chemical monitoring database (NAtChem, 2012). Frank Froude was the principal investigator collecting these TGM data at Burnt Island during 2005. Details about the site and its measurements are provided by Kellerhals *et al*. (2003) and Temme *et al*. (2007). The site is located near the southern shore of Burnt Island, a small island associated with Manitoulin Island in the northern Lake Huron. The terrain surrounding the site is relatively flat, and consists of shrubbery and dense mixed forest. This CAMNet relatively remote site is co-located with the Burnt Island Integrated Atmospheric Deposition Network (IADN) Canadian Master Station.

In Figure 50, the measured, daily average of the hourly TGM measurements are shown along with model estimates, using the "oxid33, pf0" and the "oxid50, pf0" configurations. In Figure 51, the hourly measurement data are added to the plot.

In these figures, it is seen that overall agreement between model results and measurements appears very reasonable. As has been seen with other sites, the timing of some of the "peaks" in the measurement data is matched very well by the model. Indeed, many of the broad "weekly-scale" temporal variations throughout the year appear to be relatively well captured by the model, even if the absolute magnitude of the concentration is not exactly matched. For example, like with the St. Anicet site discussed above, both the measurements and the model results show a multi-day peak in the beginning of February 2005, although the magnitude of the observed peak is greater than that of the model-estimated peak. The high concentrations of mercury observed in this peak may have been caused by "direct" plume impacts from local and regional sources, the kind of impact that this coarse-grid modeling cannot easily capture. Nevertheless, throughout the year, the timing of many of the observed measurement peaks appears to be matched by the model estimates.

Similar to the St. Anicet site discussed above, the "oxid33, pf0" model predictions match the measurements more closely during the first ~3-4 months of the year, but in most of the remainder of the year, the "oxid50, pf0" configuration results are closer to the measurements. As with St. Anicet, the "oxid33, pf0" configuration shows results more consistent with observations in December, 2005.

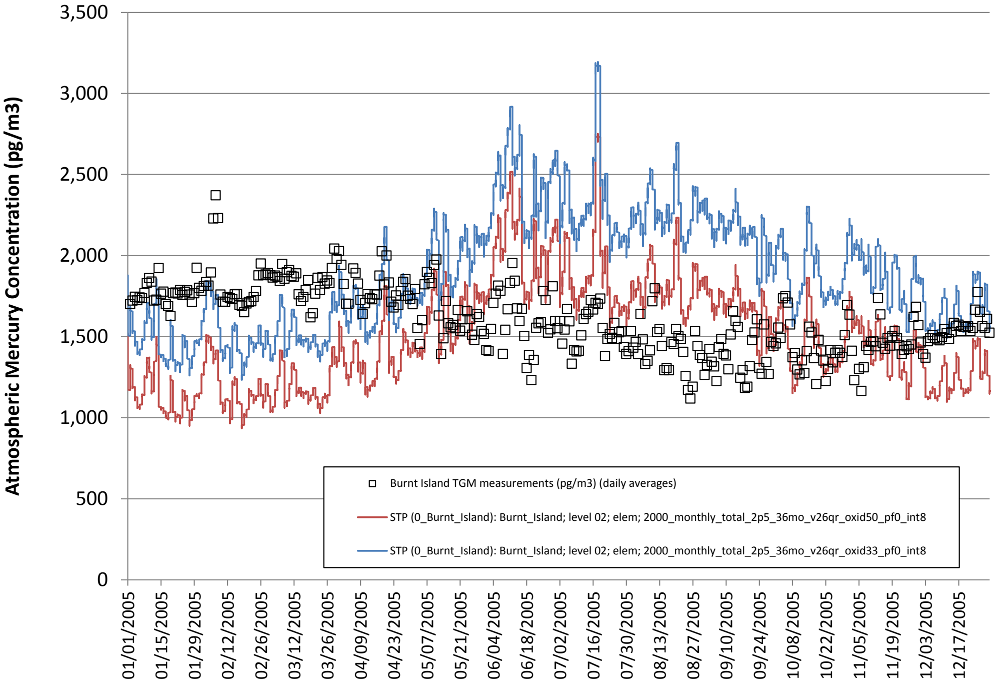

Figure 50. Measured TGM at Burnt Island (Ontario) and model estimates using the "oxid33, pf0" and "oxid50, pf0" configurations

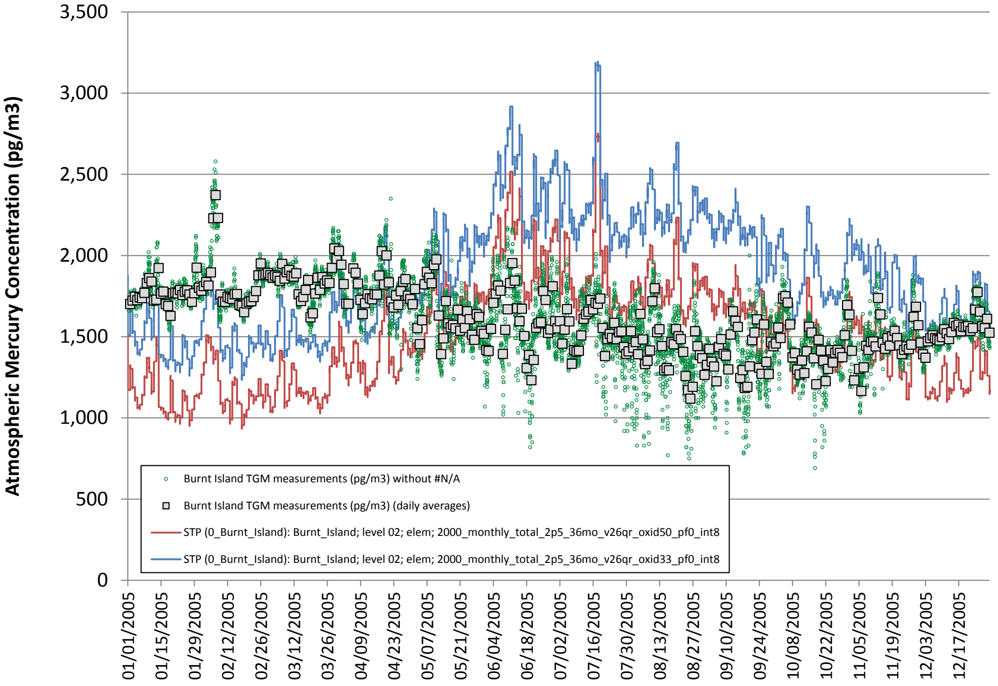

Figure 51. Measured TGM at Burnt Island (Ontario) (daily averages and hourly measurements) and model estimates using the "oxid33, pf0" and "oxid50, pf0" configurations

5.2.6 Egbert, Ontario, Canada

Total Gaseous Mercury (TGM) concentration measurement data for 2005 at the Center for Atmospheric Research (CARE) at Egbert, part of the CAMNet monitoring network in Canada, were obtained from Environment Canada's *NAtChem* online chemical monitoring database (NAtChem, 2012). The principal investigator collecting these TGM data at the Egbert site in 2005 was Frank Froude. Details about the site and its measurements are provided by Kellerhals *et al*. (2003) and Temme *et al*. (2007). The site is located in a semi-rural region about 70km north of Toronto and is situated in relatively flat terrain. The Egbert CAMNet site is co-located with a number of other the monitoring network sites.

In Figure 52, the measured, daily average of the hourly TGM measurements are shown along with model estimates, using the "oxid33, pf0" and the "oxid50, pf0" configurations. In Figure 53, the hourly measurement data are added to the plot.

As has been generally true with the other sites discussed, it is seen that overall agreement between model results and measurements is reasonable. And, has been seen with other sites, the timing of some of the "peaks" in the measurement data is well matched by the model, even if the magnitude of the peak concentration is not exactly matched. The high concentrations of mercury observed in many of these peaks may have been caused by more "direct" plume impacts from local and regional sources, the kind of impact that this coarse-grid modeling cannot easily capture. For example, like with the St. Anicet and Egbert sites discussed above, both the measurements and the model results show a multi-day peak in the beginning of February 2005, although the magnitude of the observed peak is greater than that of the model-estimated peak. It is noteworthy that the relatively high observed TGM concentrations in June and July are matched very well by the model estimates. Several other aspects of the temporal variations in the observations are reproduced by the model.

Similar to the St. Anicet and Burnt Island sites discussed above, the "oxid33, pf0" model predictions match the measurements more closely during the first ~3-4 months of the year, but in the remainder of the year (except for December), the "oxid50, pf0" configuration results are closer to the measurements.

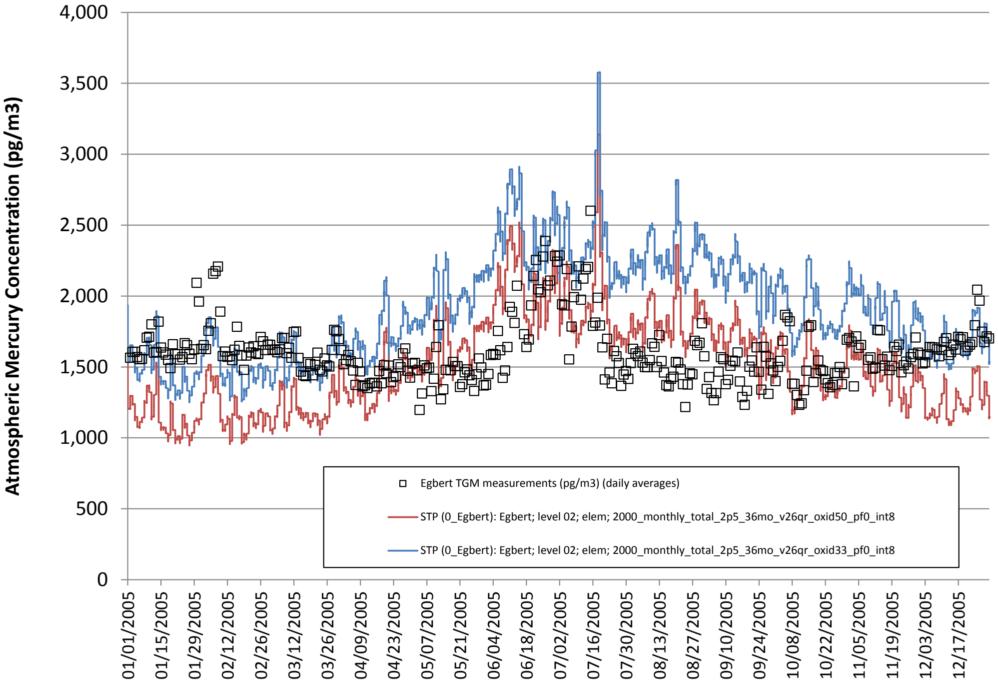

Figure 52. Measured TGM at Egbert (Ontario) and model estimates using the "oxid33, pf0" and "oxid50, pf0" configurations

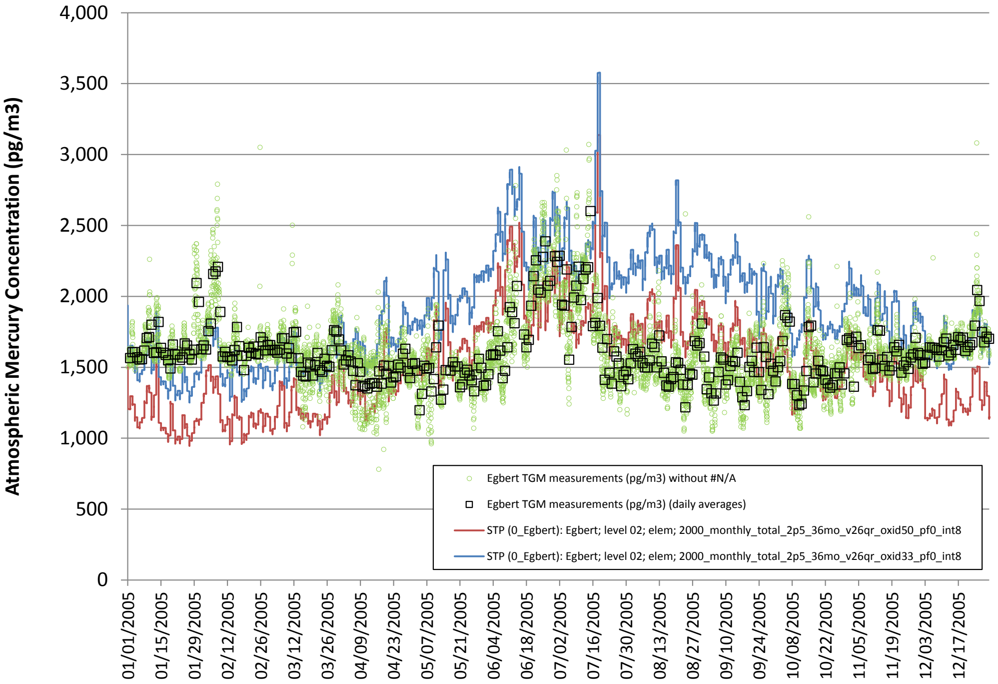

Figure 53. Measured TGM at Egbert (Ontario) (daily averages and hourly measurements) and model estimates using the "oxid33, pf0" and "oxid50, pf0" configurations

5.2.7 **Point Petre, Ontario, Canada**

Total Gaseous Mercury (TGM) concentration measurement data for 2005 at Point Petre, part of the CAMNet monitoring network in Canada, were obtained from Environment Canada's *NAtChem* online chemical monitoring database (NAtChem, 2012). The principal investigator collecting these TGM data at the Point Petre site during 2005 was Frank Froude. Details about the site and its measurements are provided by Kellerhals *et al*. (2003) and Temme *et al*. (2007). Point Petre is a small peninsula on the north-eastern shore of Lake Ontario, about 160 km east of Toronto and 85 km north of Rochester, NY. The site is relatively rural and is situated in flat terrain. The Point Petre CAMNet site is co-located with a number of other the monitoring network sites, including the Integrated Atmospheric Deposition Network (IADN) Canadian Master Station for Lake Ontario.

In Figure 54, the measured, daily average of the hourly TGM measurements are shown along with model estimates, using the "oxid33, pf0" and the "oxid50, pf0" configurations. In Figure 55, the hourly measurement data are added to the plot.

Similar to other sites, the overall agreement between model results and measurements appears reasonable. The timing of some of the "peaks" in the measurement data is well matched by the model, even if the magnitude of the peak concentration is not precisely matched. Similar to other sites in the region, for example, both the measurements and the model results show a multi-day peak in the beginning of February 2005, although the magnitude of the observed peak is greater than that of the model-estimated peak. There are other peaks in the observed concentrations that are also relatively well-matched by the model, at least insofar as their timing.

Similar to the other CAMNet sites discussed above (St. Anicet, Burnt Island, and Egbert), the "oxid33, pf0" model predictions match the measurements more closely during the first ~3-4 months of the year, but up until December, the "oxid50, pf0" configuration results are closer to the measurements. During the last month of the year, the "oxid33, pf0" results are more consistent with the observed concentrations.

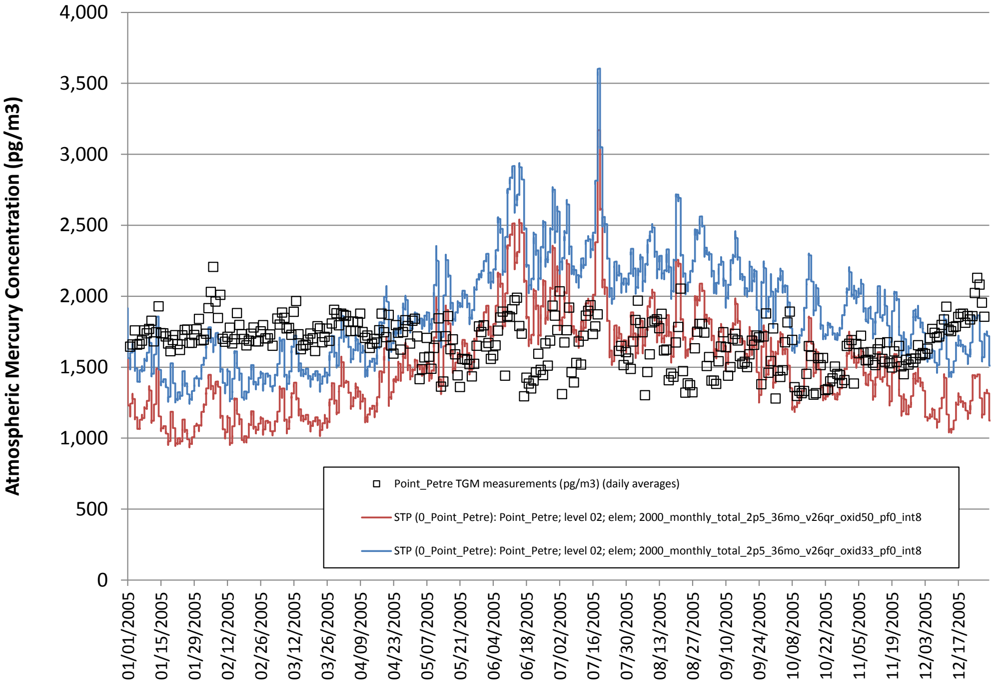

Figure 54. Measured TGM at Point Petre (Ontario) and model estimates using the "oxid33, pf0" and "oxid50, pf0" configurations

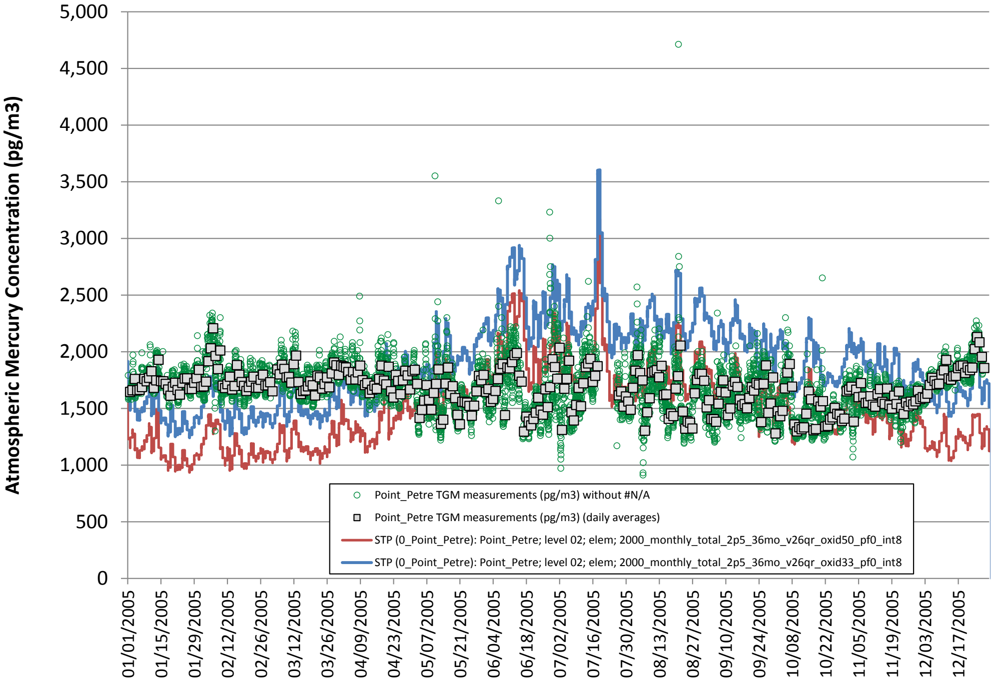

Figure 55. Measured TGM at Point Petre (Ontario) (daily averages and hourly measurements) and model estimates using the "oxid33, pf0" and "oxid50, pf0" configurations

5.2.8 Bratt's Lake, Saskatchewan, Canada

Total Gaseous Mercury (TGM) concentration measurement data for 2005 at the Bratt's Lake CAMNet site were obtained from Environment Canada's *NAtChem* online chemical monitoring database (NAtChem, 2012). The principal investigator collecting these TGM data at the Bratt's Lake site in 2005 was Brian Wiens. Details about the site and its measurements are provided by Temme *et al*. (2007). The Bratt's Lake site is located in a flat, rural area about 25 km south of Regina, in southern Saskatchewan. It is co-located with the SK12 Mercury Deposition Network site measuring wet deposition of mercury.

In Figure 56, the measured, daily average of the hourly TGM measurements are shown along with model estimates, using the "oxid33, pf0" and the "oxid50, pf0" configurations. In Figure 57, the hourly measurement data are added to the plot.

The overall agreement between model results and measurements appears reasonable. The timing of some of the "peaks" in the measurement data is well matched by the model, even if the magnitude of the peak concentration is not precisely matched. For example, both the observations and model results show two multi-day peaks in May and a moderate, broad peak during the March-April time frame (centered at approximately April 9).

Somewhat similarly to the other CAMNet sites discussed above (St. Anicet, Burnt Island, Egbert, and Point Petre), the "oxid33, pf0" model predictions match the measurements more closely during the first part of the year (in this case, through the first 5 months of the year), and then up until December, the "oxid50, pf0" configuration results are closer to the measurements.

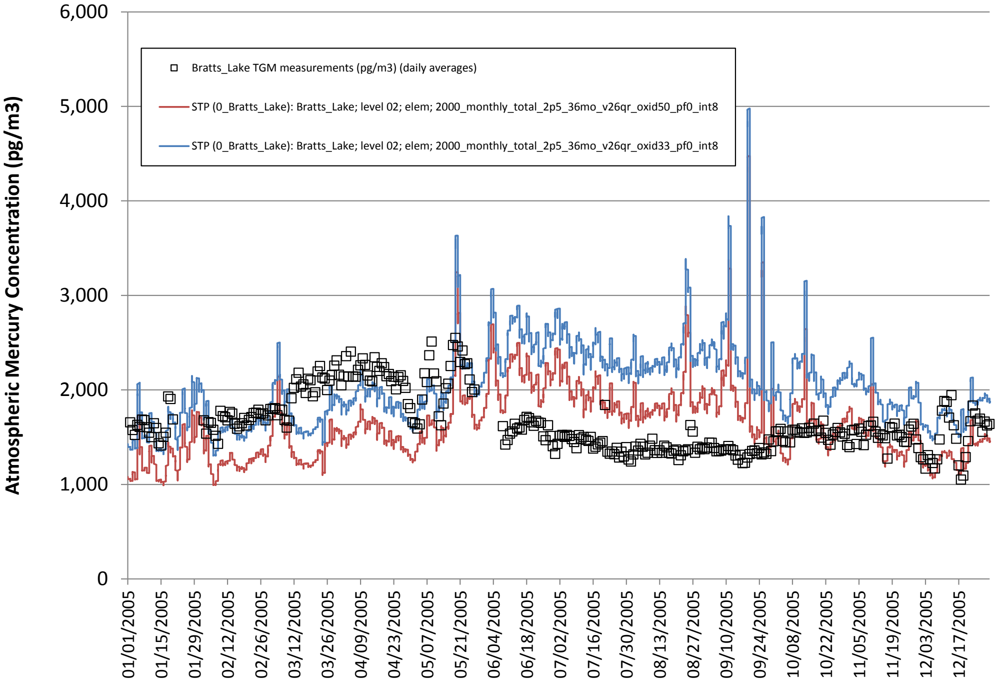

Figure 56. Measured TGM at Bratt's Lakes (Saskatchewan) and model estimates using the "oxid33, pf0" and "oxid50, pf0" configurations

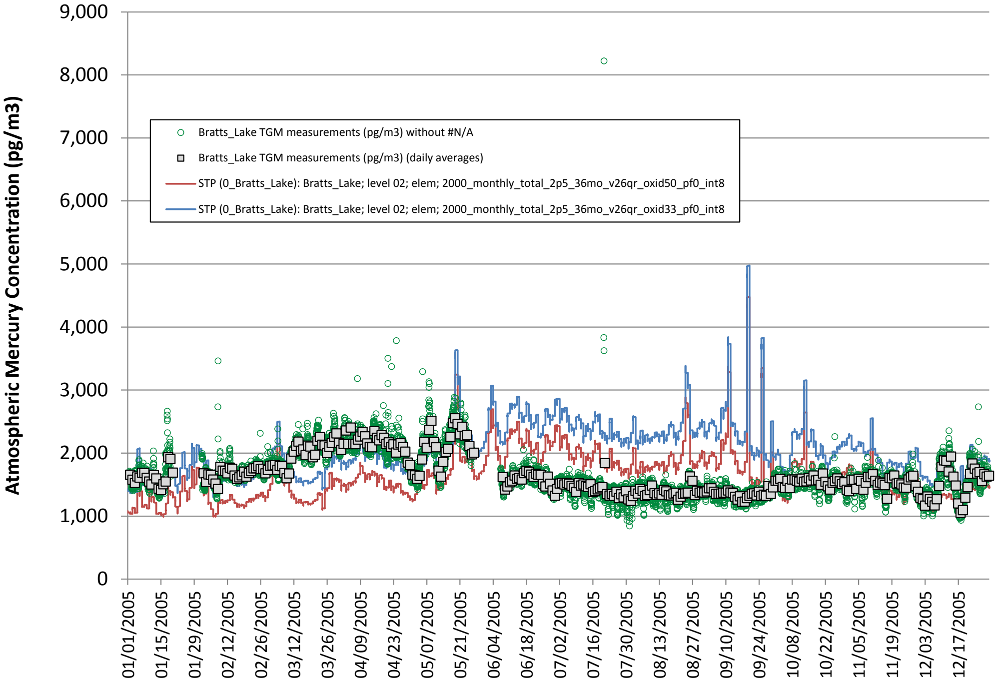

Figure 57. Measured TGM at Bratt's Lakes (Saskatchewan) (daily averages and individual hourly measurements) and model estimates using the "oxid33, pf0" and "oxid50, pf0" configurations

5.2.9 **Potsdam and Stockton, New York, USA**

Total Gaseous Mercury (TGM) concentrations were measured at Potsdam and Stockton, New York by principal investigators Thomas Holsen and Young-Ji Han of Clarkson University (Potsdam, NY), and they provided 2005 data for use in this study[9]. Details about the sites and their measurements, as well as extensive analysis and interpretation, e.g., using back-trajectory methods, are provided by Han *et al*. (2004, 2007).

The Potsdam site in northern New York and is characterized as relatively remote and rural and is situated in relatively flat terrain. The Stockton site is situated 19km south of Fredonia NY and about 10 km from the south-eastern shore of Lake Erie. It is also considered relatively rural and is situated in relatively flat terrain. During 2005, 24-hour samples were generally taken every 3 days from January through August at Potsdam, and January through July at Stockton. A total of 68 samples were collected during 2005 at the Potsdam site, and 43 samples were collected at the Stockton site

In Figure 58 Figure 59, the measured, daily average TGM measurements are shown along with model estimates, using the “oxid33, pf0” and the “oxid50, pf0” configurations, for the Potsdam and Stockton sites, respectively.

It is seen in these figures that the model tended to underestimate the observations during the first ~3 months of the year, with closer agreement during the remaining measurement period. In some cases, observed “peaks” in concentration are matched by the model, at least insofar as the timing of the peak is concerned.

Han *et al*. (2007) carried out an extensive source-receptor analysis of these measurement results, along with data from a site in Sterling New York, using several different back-trajectory-based methodologies. The analysis provided strong evidence that regional sources in Pennsylvania, Ohio, and Indiana, as well as more local sources (in southern New York) contributed significantly to the concentrations of TGM observed at the sites. Additional source regions were also identified. The geographic distribution of likely contributing regions was found to be reasonably consistent with the “known” (i.e., based on an emissions inventory) geographical pattern of emissions, lending substantial credibility to the analysis.

Overall, the modeling results show that the “oxid33, pf0” and “oxid50, pf0” configurations comparable consistency with the observations. That is, one of the approaches does not appear to be significantly “better” than the other in terms of matching the observations.

The modeling results show some relatively sharp peaks, e.g., that last 1-2 days. Since the measurements were made every 3 days, it’s possible that some of the peaks were “missed” in the observations. This could be investigated further with back-trajectories and/or other methodologies in future work.

---

[9] Thomas Holsen, Clarkson University, Potsdam, NY, Personal Communication, April, 2012.

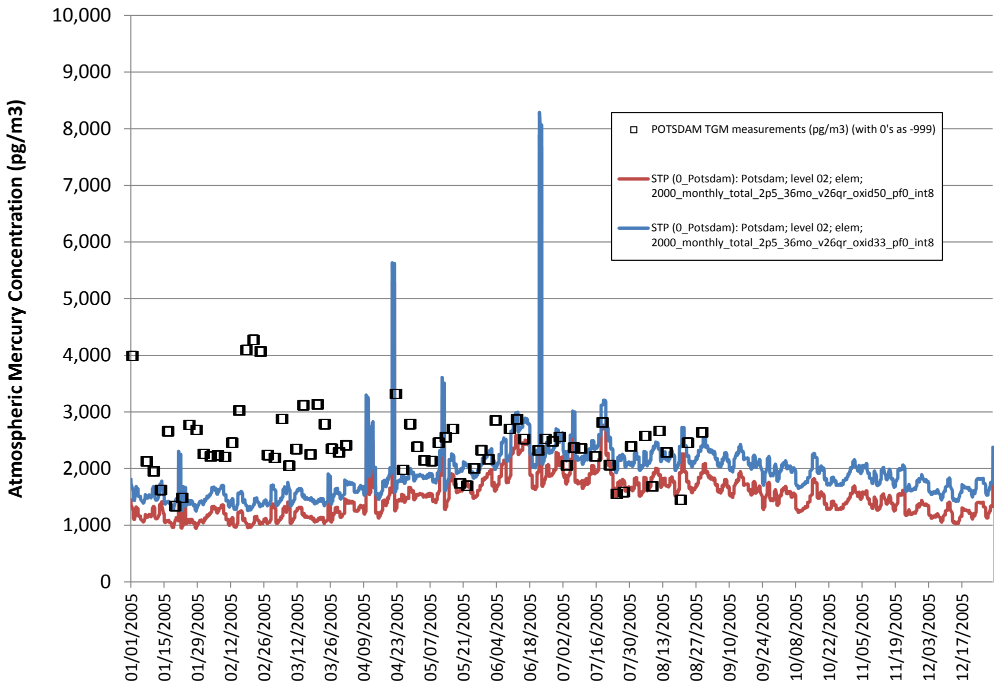

Figure 58. Measured TGM at Potsdam (New York) and model estimates using the "oxid33, pf0" and "oxid50, pf0" configurations

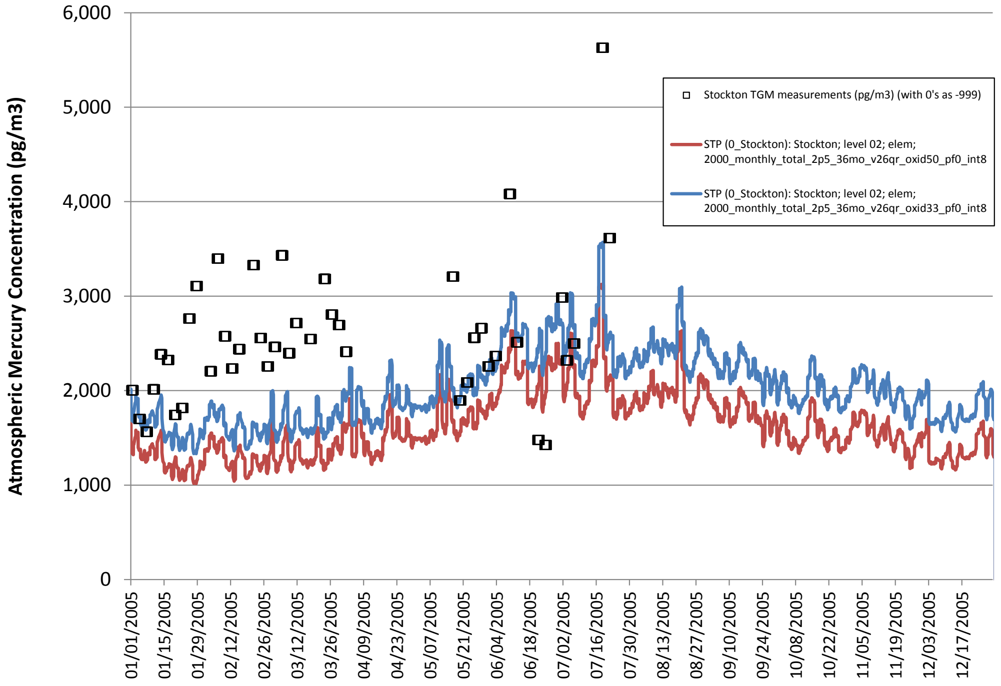

Figure 59. Measured TGM at Stockton (New York) and model estimates using the "oxid33, pf0" and "oxid50, pf0" configurations

5.2.10 **Paradise Valley and Gibbs Ranch, Nevada, USA**

Mercury measurements collected in 2005 at Paradise Valley and Gibbs Ranch, in Nevada, during several seasonal field intensive campaigns, were obtained from Seth Lyman[10]. Information about the sampling methodology, data, and extensive analysis and interpretation are provided by Lyman *et al*. (2007). The speciated mercury data collected at the site were generally 2-hour averages, taken every 3 hours. The mercury measurements were carried out in conjunction with a study of mercury dry deposition, estimated by direct and indirect methods (Lyman *et al*., 2007).

The Paradise Valley site is co-located with Mercury Deposition Network site NV02, at Lesperance Ranch, 70 km north of Winnemucca Nevada. The site lies in a broad valley at an elevation of 1388 m above sea level. There are mountains rising ~1000 m above the site to the southwest, west, and north, within about 10 km of the site. Thus, the terrain in the vicinity of the site is somewhat complex, at least from the perspective of the 2.5^o x 2.5^o grid used in this modeling (approximately 250 km x 250 km). The Gibbs Ranch site is co-located with Mercury Deposition Network site NV99, 80 km northwest of Wells, Nevada. The site lies on the eastern side of a narrow river valley, at an elevation of 1806 m above sea level. There are numerous mountains rising ~1000 m above the site within 10-30 km of the site, and so, like the Paradise Valley site, the terrain in the vicinity of the site is somewhat complex from the perspective of the relatively coarse grid used in this work.

For both of the sites, in comparing the modeling results with observations, the lowest model concentration level was used (0-100 meters above ground level), and the STP correction was based on the “surface” meteorological conditions as characterized in the 2.5^o x 2.5^o gridded meteorological data used in the modeling. Model estimates are compared against daily averaged measured concentrations at the Paradise Valley site in Figure 60 and in Figure 61 including individual 2-hr measurements. Analogous plots for the Gibbs Ranch site are shown in Figure 62 and Figure 63.

It can be seen that the model results are reasonably consistent with the measurements. As Lyman *et al*. (2007) have noted, there are numerous large mercury point sources (e.g., several gold-mining facilities) in the region surrounding these sites. Further, the region is characterized by relatively high geological levels of mercury, resulting in relatively high “geogenic” mercury emissions. These factors likely explain the relatively high levels of mercury observed at the sites. It is noteworthy that the modeling results also show relatively high concentrations.

Given the coarse-grid nature of the modeling, and given the proximity of significant sources to the sites, it is not expected that the modeling would be able to capture much if any of the timing or magnitudes of episodic peaks in the observations. Nevertheless, at least for some of the observations, the model results show reasonably consistent agreement with the timing and even the magnitude of such peaks.

---

[10] Seth Lyman, personal communication, 2011, University of Washington-Bothell. Current affiliation: Utah State University, Vernal, Utah.

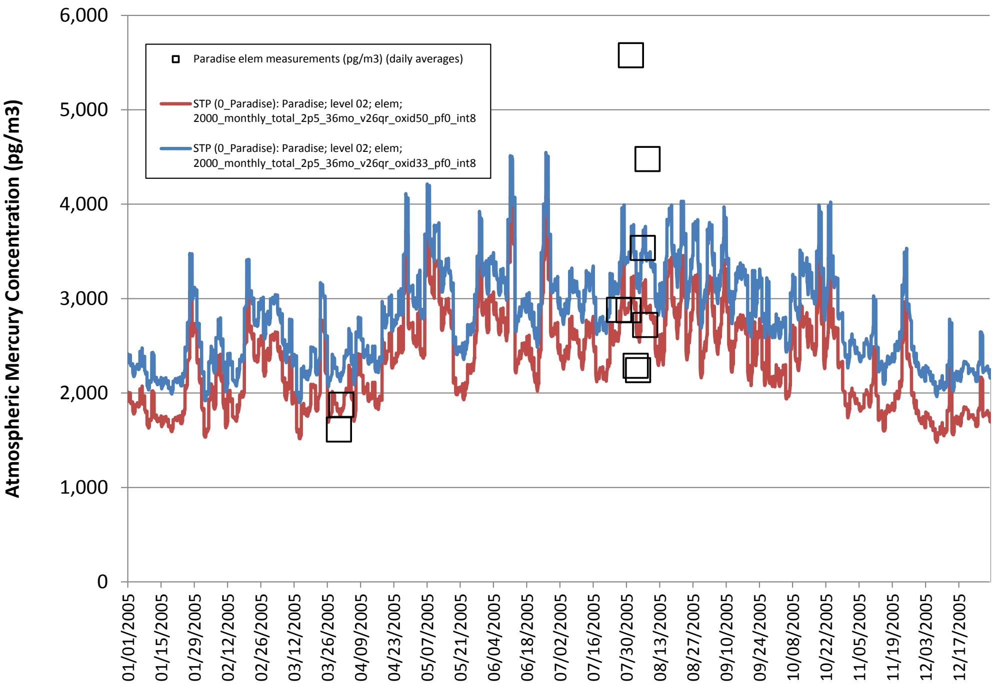

Figure 60. Measured Hg(0) at Paradise (Nevada) and model estimates using the "oxid33, pf0" and "oxid50, pf0" configurations

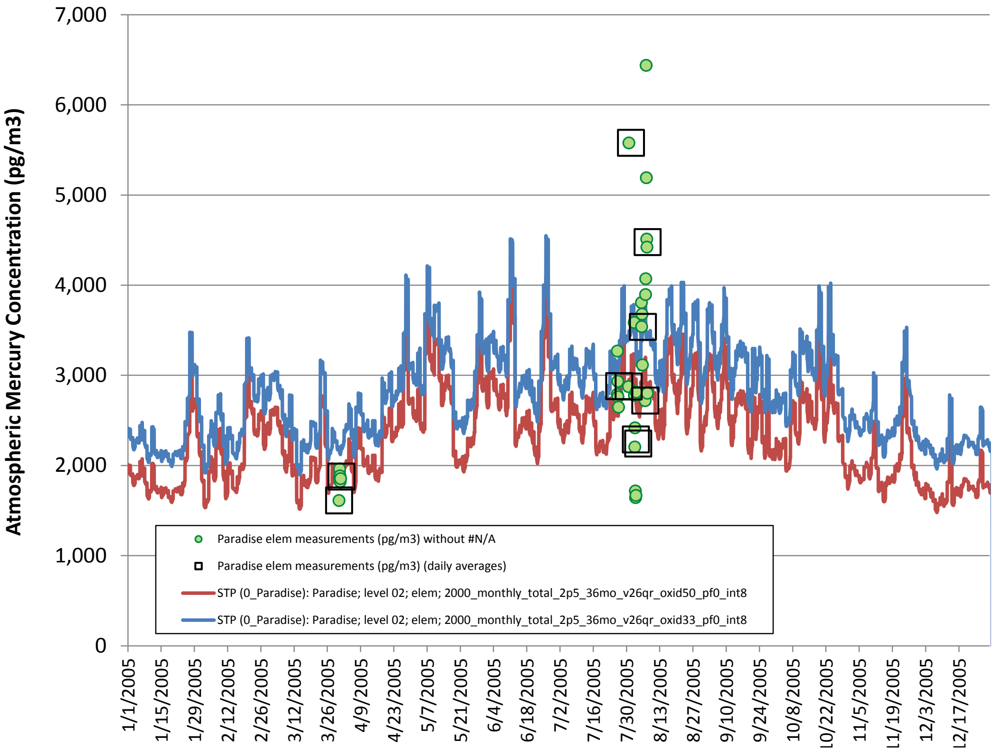

Figure 61. Measured Hg(0) at Paradise (Nevada)) (daily averages and individual 2-hr measurements) and model estimates using the "oxid33, pf0" and "oxid50, pf0" configurations

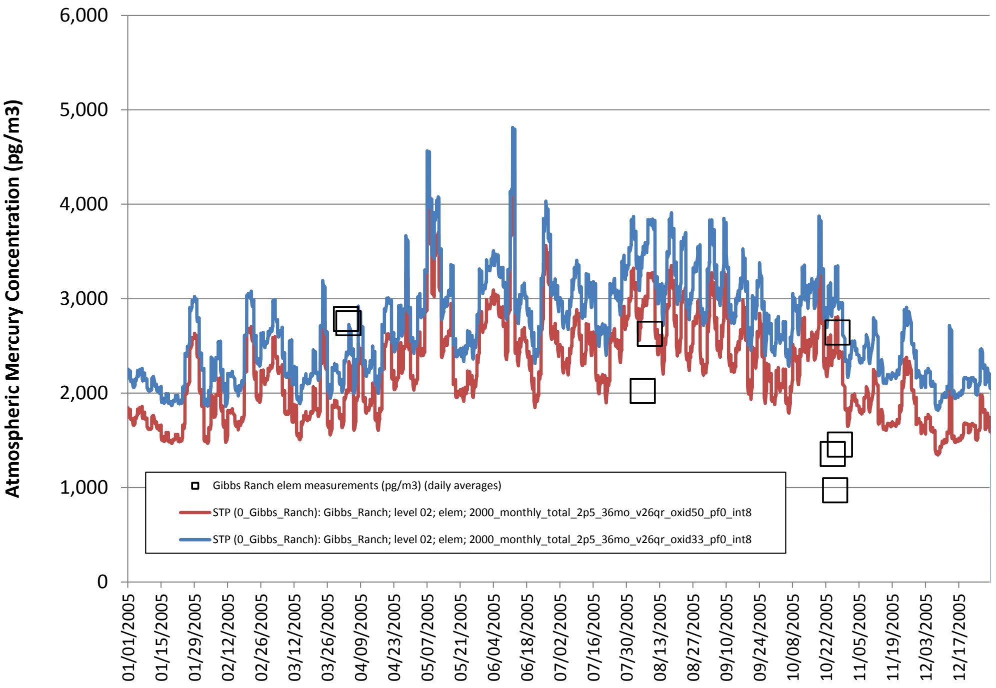

Figure 62. Measured Hg(0) at Gibbs Ranch (Nevada) and model estimates using the "oxid33, pf0" and "oxid50, pf0" configurations

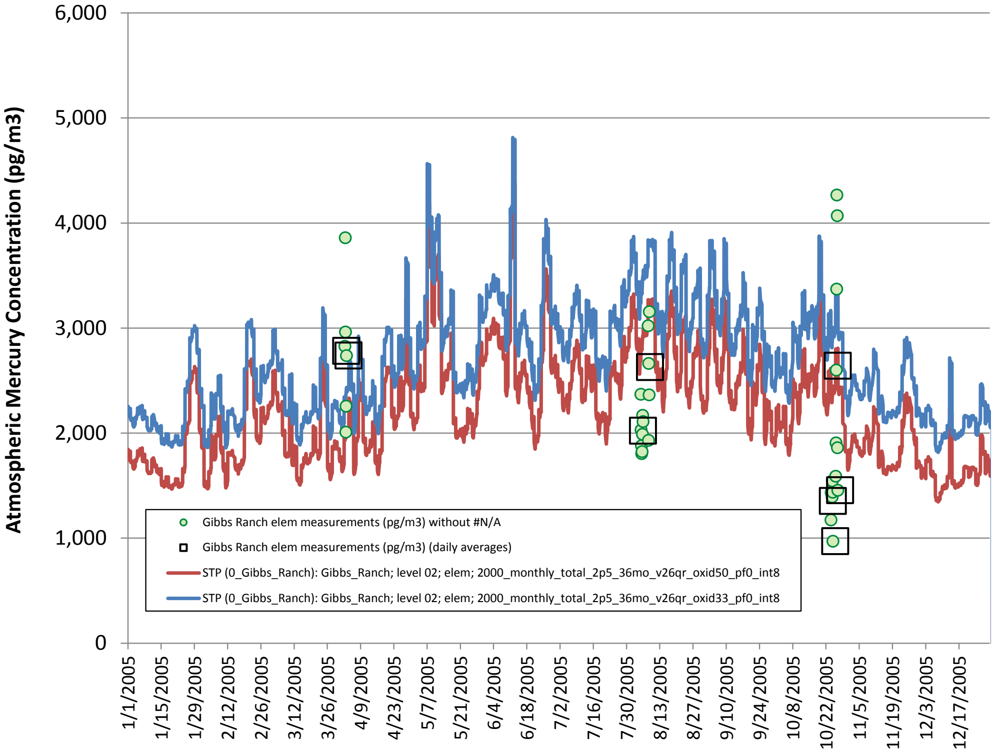

Figure 63. Measured Hg(0) (daily averages and individual 2-hr measurements) at Gibbs Ranch (Nevada) and model estimates using the "oxid33, pf0" and "oxid50, pf0" configurations

5.2.11 Alert, Nunavut

Total Gaseous Mercury (TGM) concentration measurement data for 2005 at the Alert CAMNet site in Nunavut were obtained from Environment Canada's *NAtChem* online chemical monitoring database (NAtChem, 2012). The principal investigators collecting these TGM data at Alert in 2005 were Alexandra Steffen and Cathy Banic. Details about the site and its measurements are provided by Kellerhals *et al*., (2003), Temme *et al*. (2007) and Cole *et al*. (2013). The Alert site is located in the high, remote Arctic on the northern tip of Ellesmere Island on a plateau approximately 7 kilometers from the shore of the Lincoln Sea.

Mercury in the Arctic is subject to "Atmospheric Mercury Depletion Events" (AMDE's) occurring during Polar spring in which elemental mercury is rapidly converted to Hg(II) and/or Hg(p) via bromine-mediated chemical reactions and subsequently deposited (e.g., Schroeder *et al*., 1998; Berg *et al*., 2003; Brooks *et al*., 2006; Steffen *et al*., 2008; Cole *et al*., 2013). During an AMDE, the concentration of Hg(0) in the atmosphere can be dramatically decreased.

However, bromine chemistry is not included in the modeling carried out here, nor is a description of the complex process by which reactive bromine species are generated in the Arctic air, in some regions – e.g., in the vicinity of sea ice leads -- under certain conditions. Thus, the model is not expected to be able to capture these Arctic AMDE's in any way.

In Figure 64, the measured, daily average of the hourly TGM measurements are shown along with model estimates, using the "oxid33, pf0" and the "oxid50, pf0" configurations. Significant depletion of TGM can clearly be seen in March-May, during the polar spring, when the TGM concentration falls in some cases below 500 pg/m^3.

As noted above, the model cannot reproduce these depletions. However, during other periods of the year, the agreement between modeled and observed concentrations is relatively good, especially for the "oxid33, pf0" configuration. Notably, the observed, broad elevation of concentration during the summer months is well reproduced by the model.

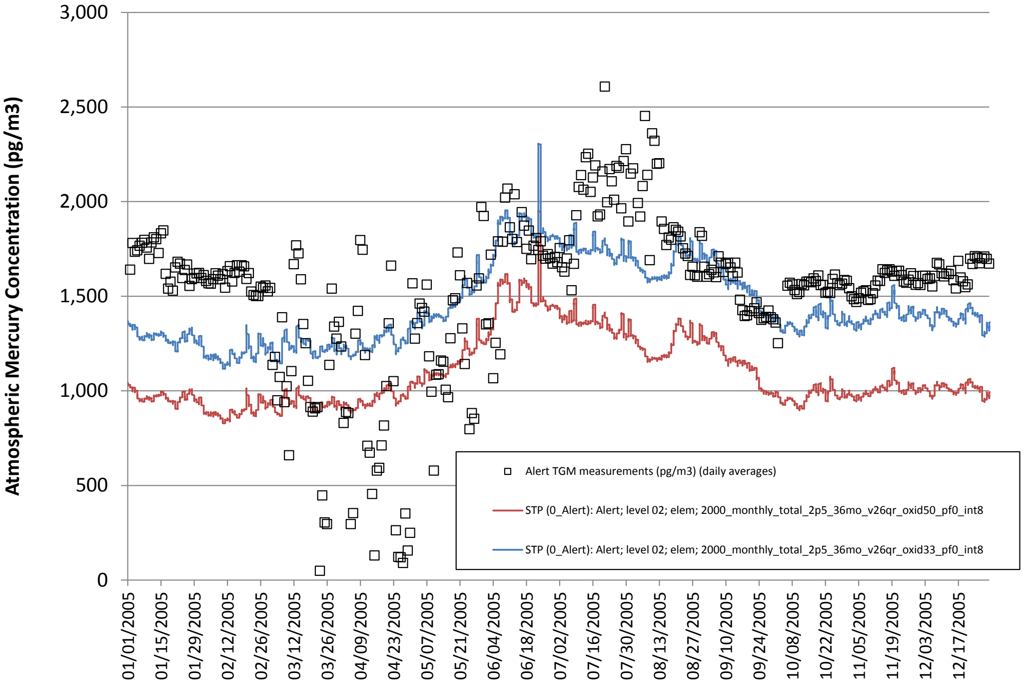

Figure 64. Measured TGM at Alert (Nunavut) and model estimates using the "oxid33, pf0" and "oxid50, pf0" configurations

5.3. Comparison of model-estimated and measured atmospheric concentrations of Hg(II) and Hg(p)

5.3.1 Potsdam and Stockton, New York, USA

Reactive Gaseous Mercury (RGM) concentrations were measured at Potsdam and Stockton, New York by principal investigators Thomas Holsen and Young-Ji Han[11] of Clarkson University (Potsdam, NY), and they provided 2005 data for use in this study[12]. Details about the sites and their measurements, as well as extensive analysis and interpretation, e.g., using back-trajectory methods, are provided by Han *et al*. (2004, 2005, and 2007).

As discussed above in Section 5.2.9 (page72), the Potsdam site in northern New York and is characterized as relatively remote and rural and is situated in relatively flat terrain. The Stockton site is situated 19km south of Fredonia NY and about 10 km from the south-eastern shore of Lake Erie. It is also considered relatively rural and is situated in relatively flat terrain. During 2005, 24-hour samples were generally taken every 3 days from January through August at Potsdam, and January through July at Stockton. A total of 58 day-long RGM samples were collected during 2005 at the Potsdam site, and 25 day-long RGM samples were collected at the Stockton site.

In Figure 65, measured, 24-hr RGM measurements are shown along with model estimates of Hg(II), using the “oxid33, pf0” and the “oxid50, pf0” configurations, for the Potsdam site. In Figure 66, the same data are plotted using a logarithmic scale. In Figure 67, an analogous plot comparing observations and measurements is presented for the Stockton sites.

It is seen in these figures that the model estimates are reasonably consistent with the observations for both sites. Observed “peaks” in concentration appear to be relatively well matched by the model in some cases, at least insofar as the timing of the peak is concerned. Overall, the modeling results show that as far as Hg(II) concentrations are concerned there is little difference between the “oxid33, pf0” and “oxid50, pf0” configurations. .As with TGM, the modeling results show some relatively sharp peaks, e.g., that last 1-2 days. Since the measurements were made every 3 days, it’s possible that some of the peaks were “missed” in the observations. This could be investigated further with back-trajectories and/or other methodologies in future work.

Han *et al*. (2005) carried out an extensive source-receptor analysis of observations at these sites collected in 2002-2003, along with data from a site in Sterling New York, using several different back-trajectory-based methodologies. Similar to a comparable TGM analysis discussed above, the analysis suggested that regional sources in Pennsylvania, Ohio, and Indiana, as well as more local sources (in southern New York) were important contributors to the concentrations of RGM observed at the sites. Additional source regions were also identified. The geographic distribution of likely contributing regions was found to be reasonably consistent with the “known” (i.e., based on an emissions inventory) geographical pattern of emissions.

---

[11] Current affiliation: Kangwon National University, Kangwon Do, South Korea

[12] Thomas Holsen, Clarkson University, Potsdam, NY, Personal Communication, April, 2012.

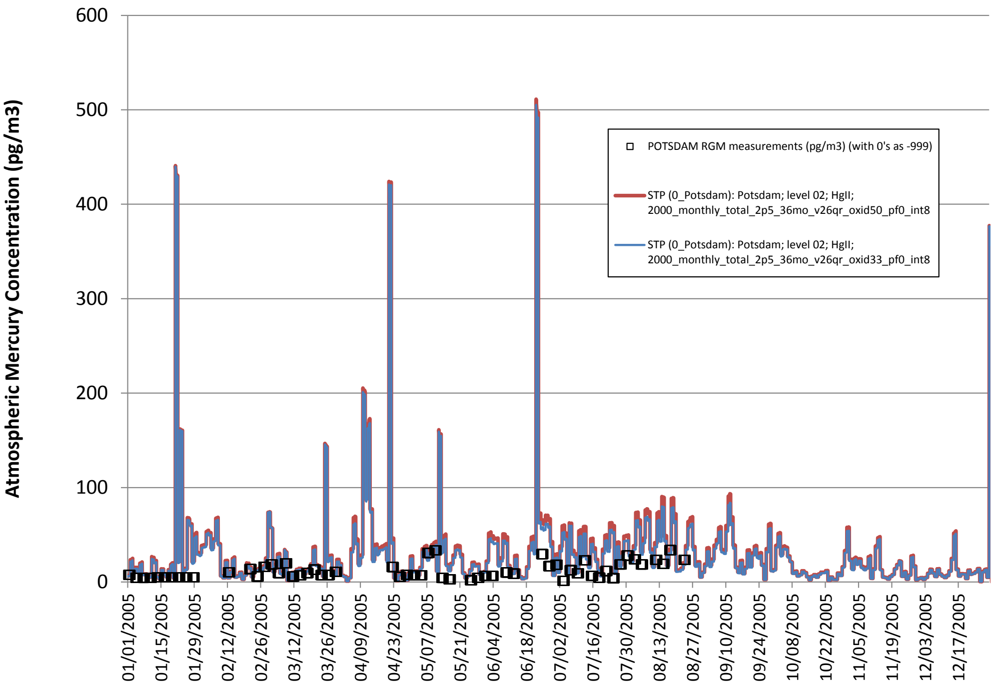

Figure 65. Measured RGM at Potsdam (New York) and model estimates of Hg(II) using the "oxid33, pf0" and "oxid50, pf0" configurations

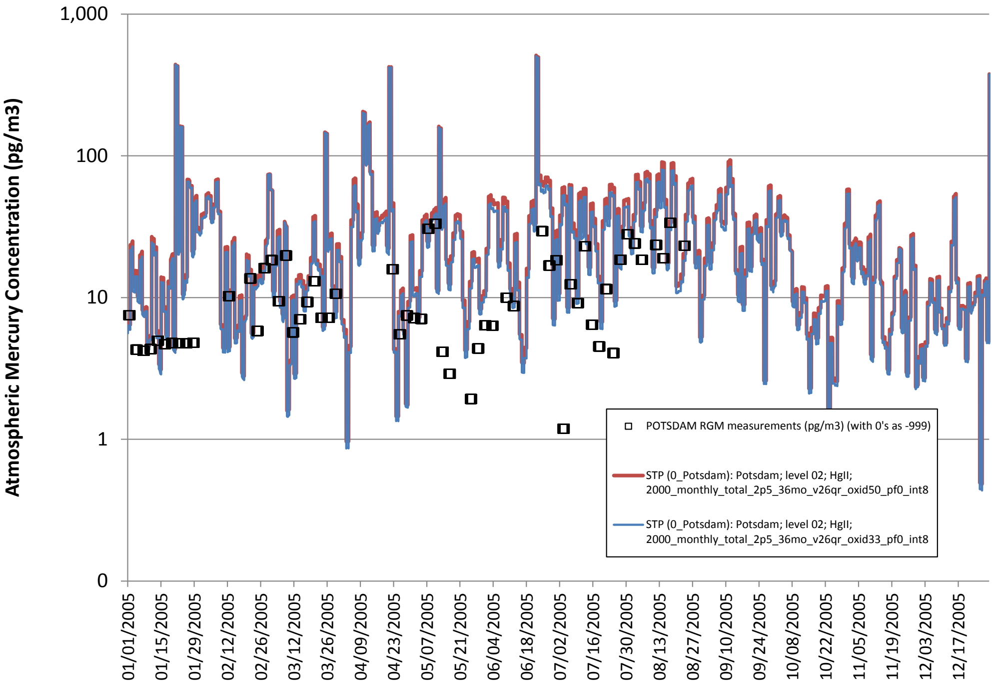

Figure 66. Measured RGM at Potsdam (New York) and model estimates of Hg(II) using the "oxid33, pf0" and "oxid50, pf0" configurations (logarithmic scale)

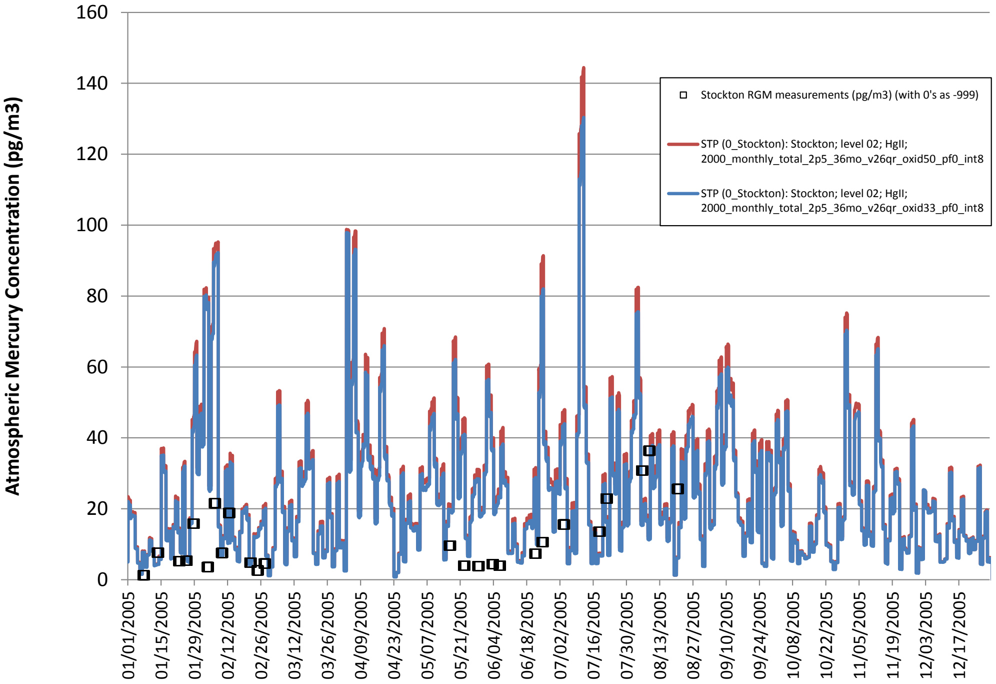

Figure 67. Measured RGM at Stockton (New York) and model estimates of Hg(II) using the "oxid33, pf0" and "oxid50, pf0" configurations

5.3.2 Reno (Desert Research Institute – DRI), Nevada, USA

Reactive Gaseous Mercury (RGM) and particulate mercury (Hg(p)) measurements collected in 2005 at the Desert Research Institute (DRI) in Reno, Nevada, were obtained from Seth Lyman[13]. The sampling methodology, data, and extensive analysis and interpretation are provided by Peterson *et al*. (2009). The speciated mercury data collected at the site were generally 2-hour averages, taken every 3 hours. As noted above in Section 5.2.3, The Reno-DRI site is ~5 km north of downtown Reno, Nevada. The elevation of the site is 1509m above sea level, located in a somewhat hilly region north of Reno, and is about 165m above the level of the city.

In Figure 68, model estimates of Hg(II) concentrations are compared against daily average measured RGM concentrations, using model concentration level 02 (0-100 m above ground level, "agl"), along with the individual 2-hour measurements. In Figure 69, an analogous comparison is presented in which results using model concentration level 3 (100-500 m-agl) is used. As noted in Section 5.2.3 above, it appears possible that both of these levels may be relevant to the observed concentrations at the site.

In Figure 70 and Figure 71, corresponding comparisons are made for Hg(p) modeling results and observations. In these latter two figures, model results for "Hg2s" concentrations are also shown. As discussed in Section 3.4 (page 36), Hg2s refers to Hg(II) absorbed reversibly to soot in the model. There

---

[13] Seth Lyman, personal communication, 2011, University of Washington-Bothell.

is some uncertainty as to how Hg2s will interact with the measurement systems, e.g., will it end up being quantified as RGM or Hg(p)? It seems plausible that it may be "measured" as Hg(p), and this is why the Hg2s model predictions are included.

In examining these RGM and Hg(p) figures, the following can be noted:

- The model results are reasonably consistent with the measurements.
- As was seen in the previous section, the results using the "oxid33, pf0" and "oxid50, pf0" configurations are very similar.
- In some cases, particularly for RGM, the model appears able to reproduce the timing and approximate magnitude of peak concentrations, e.g., the multi-day episodes in the ~2nd week of March and the ~3rd week of November.
- Comparison of the relative agreement between Figure 68 and Figure 69, it appears that the results for model level 02 (0-100 m-agl) are closer, overall, to the observations than those for model level 03 (100-500 m-agl). However, for the highest RGM measured concentrations, the results for model concentration level 03 provide a better match. It is possible that these tendencies reflect some of the fate and transport phenomena occurring for RGM, but they could also be due to a "simple" non-physical reason, e.g., if the model underpredicts the RGM concentration at a given time, then using a model concentration level that gives higher values will be closer to the observations.
- Contrary to the Hg(0) modeling results discussed in Section 5.2.3, the RGM predictions in model concentration level 03 (100-500 m-agl) are higher than those in model concentration level 02 (0-100 m-agl). This is likely due at least in part to the much higher tendency of RGM to be dry deposited and thus removed from the lowest model layer. For the Hg(p) and Hg2s results, there is not much difference between the model results for the two levels. This can at least partly be understood as a result of the lower dry deposition velocity of particles as compared to RGM.
- Measured and modeled concentrations of Hg(p) are relatively low, generally on the order of ~10 pg/m^3 or lower, with the exception of a few observed peaks.
- Modeled concentrations of Hg2s are much higher than the modeled concentrations of Hg(p).
- For much of the year, the modeled concentrations of Hg2s appear to be greater than the observed Hg(p) concentrations. However, for observed, episodic peak Hg(p) concentration levels, the model estimated Hg2s concentration (or the sum of the Hg2s and Hg(p) concentrations) is often relatively consistent.
- The measurement of Hg(p) generally includes a "cut-off" or threshold particle size above which particles are excluded from the sampler. This particle size is typically 2.5 – 3 um, and this was the case for these Hg(p) measurements (Lyman *et al.*, 2007). This means that only a fraction of the Hg(p) is actually measured in the field. Thus, all things being equal, one would expect that the "total modeled Hg(p)" would be somewhat greater than the size-limited Hg(p) observations, depending on the size distribution of Hg(p) in the atmosphere.

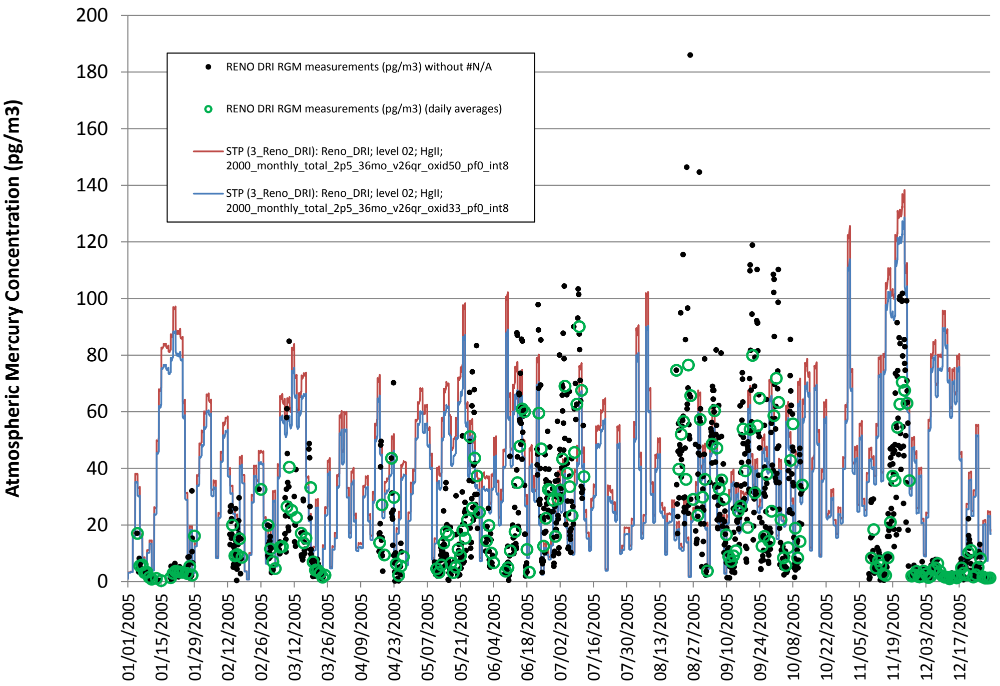

Figure 68. Measured RGM at Reno (Nevada) (daily averages and 2-hr measurements) and model estimates of Hg(II) using the "oxid33, pf0" and "oxid50, pf0" configurations, at model level 02 (0-100 m above ground level)

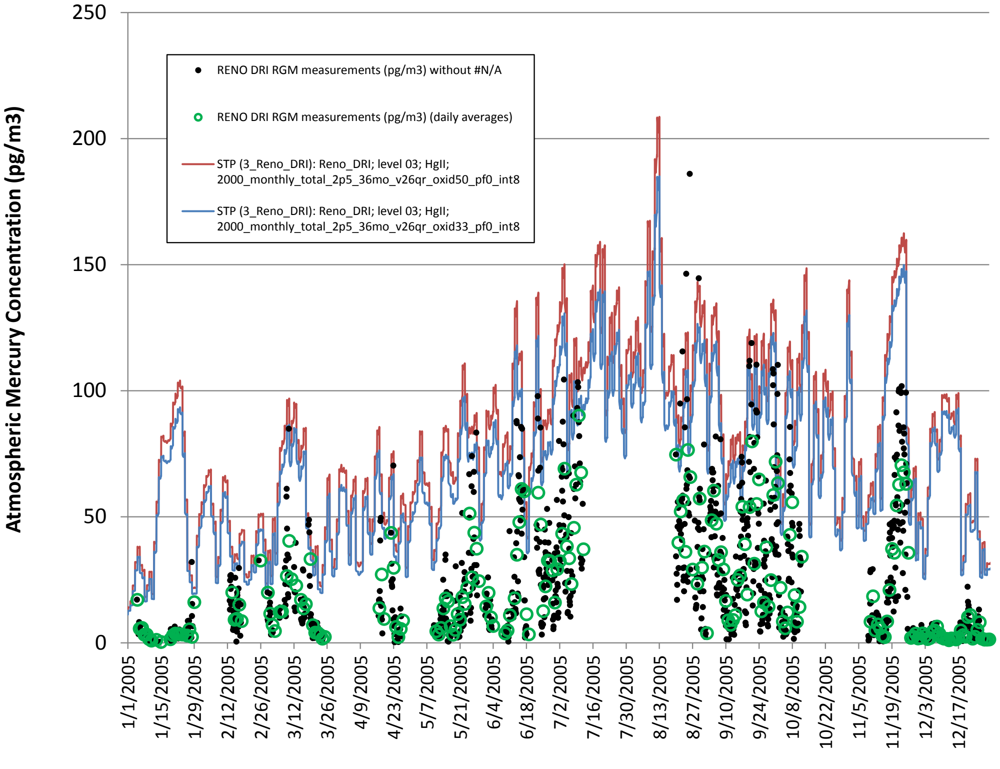

Figure 69. Measured RGM at Reno (daily averages and 2-hr measurements) and model estimates of Hg(II) using the "oxid33, pf0" and "oxid50, pf0" configurations, at model level 03 (100-500 m above ground level)

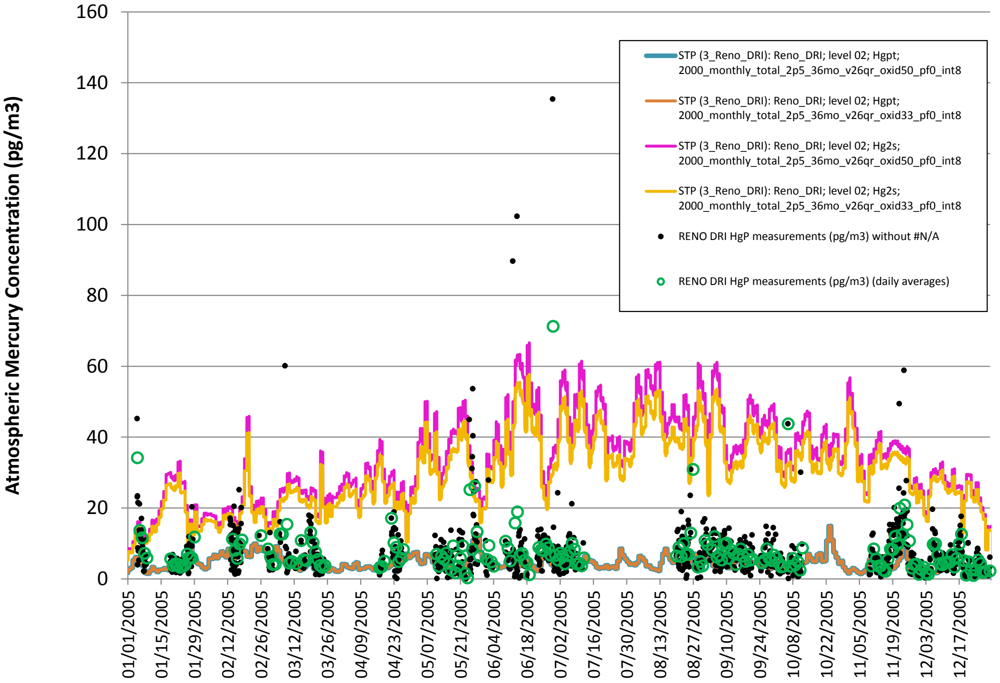

Figure 70. Measured Hg(p) at Reno (daily averages and 2-hr measurements) and model estimates of Hg(p) and Hg2s using the "oxid33, pf0" and "oxid50, pf0" configurations, at model level 02 (0-100 m above ground level)

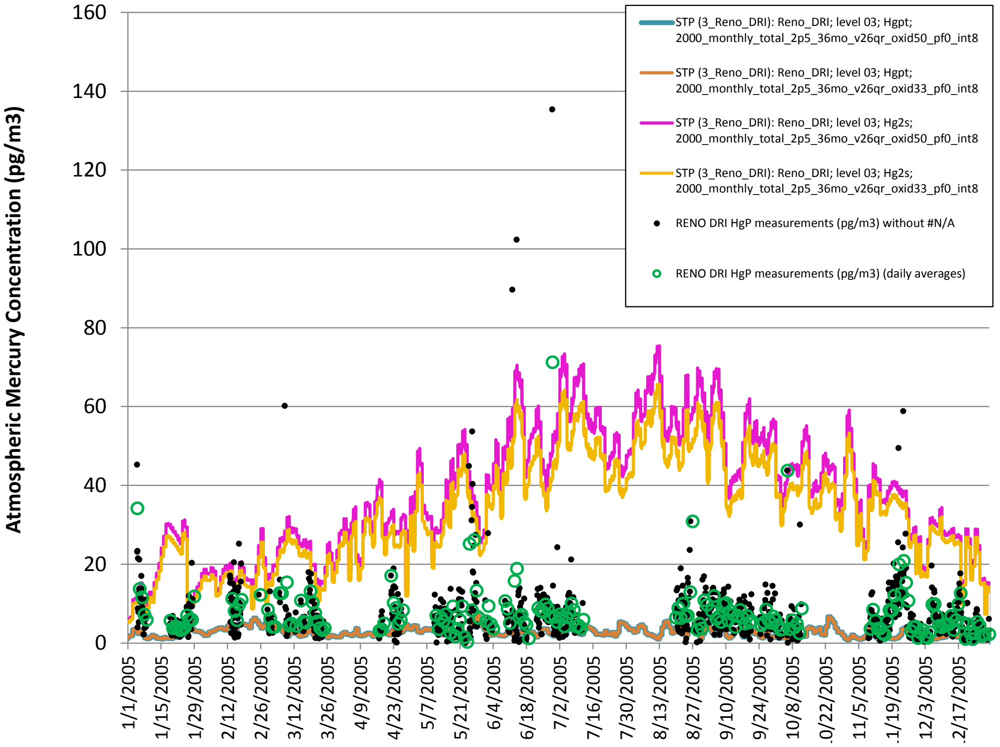

Figure 71. Measured Hg(p) at Reno (daily averages and 2-hr measurements) and model estimates of Hg(p) and Hg2s using the "oxid33, pf0" and "oxid50, pf0" configurations, at model level 03 (100-500 m above ground level)

5.3.3 Paradise Valley and Gibbs Ranch, Nevada, USA

Reactive Gaseous Mercury (RGM) and particulate mercury (Hg(p)) measurements collected in 2005 at the Paradise Valley and Gibbs Ranch sites in Nevada were obtained from Seth Lyman[14]. The sampling methodology, data, and extensive analysis and interpretation are provided by Lyman *et al*. (2007). The speciated mercury data collected at the site were generally 2-hour averages, taken every 3 hours. As noted above in Section 5.2.10, these sites are both in valleys surrounded by relatively complex terrain. These measurements were taken as part of seasonal short-term field intensive campaigns, and so there are limited periods of data.

In Figure 72 and Figure 73, model estimates of Hg(II) concentrations are compared against daily average measured RGM concentrations, using model concentration level 02 (0-100 m above ground level, “agl”), along with the individual 2-hour measurements for Paradise Valley and Gibbs Ranch, respectively. In Figure 74 and Figure 75, analogous comparisons are presented for Hg(p) modeling results and observations. In these latter two figures, model results for “Hg2s” concentrations are also shown. As discussed in relation to the Reno data above and Section 3.4 (page 36), Hg2s refers to Hg(II) absorbed reversibly to soot in the model. It seems plausible that Hg2s may be “measured” as Hg(p), and this is why the Hg2s model predictions are included.

In examining these RGM and Hg(p) figures, the following can be noted:

- The model results are reasonably consistent with the measurements. But, given the limited “campaign” nature of the measurements, caution must be exercised in drawing conclusions from the model vs. observations comparisons.
- As was seen in the previous sections, the results using the “oxid33, pf0” and “oxid50, pf0” configurations are very similar.
- In some cases, the model appears able to reproduce the timing and approximate magnitude of peak concentrations and the non-peak (e.g., “trough”, or very low concentrations).
- Modeled concentrations of Hg2s are much higher than the modeled concentrations of Hg(p).
- In most of the limited cases, the modeling results for Hg(p), Hg2s, and the total of the two seem to more or less envelope the observed concentrations.

---

[14] Seth Lyman, personal communication, 2011, University of Washington-Bothell.

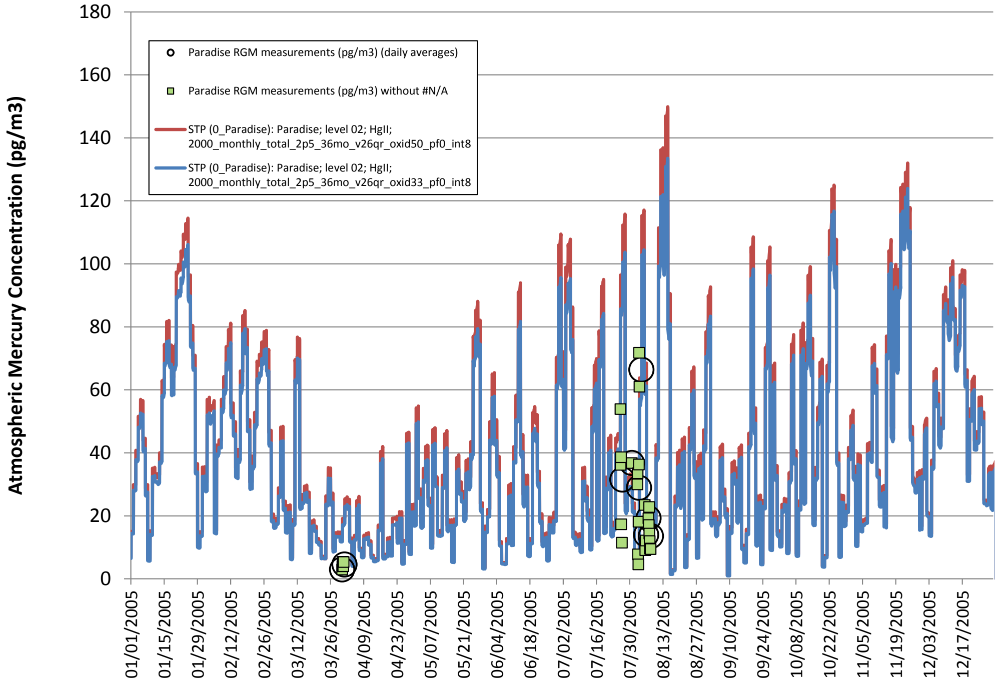

Figure 72. Measured RGM at Paradise (Nevada) (daily averages and 2-hour measurements) and model estimates of Hg(II) using the "oxid33, pf0" and "oxid50, pf0" configurations

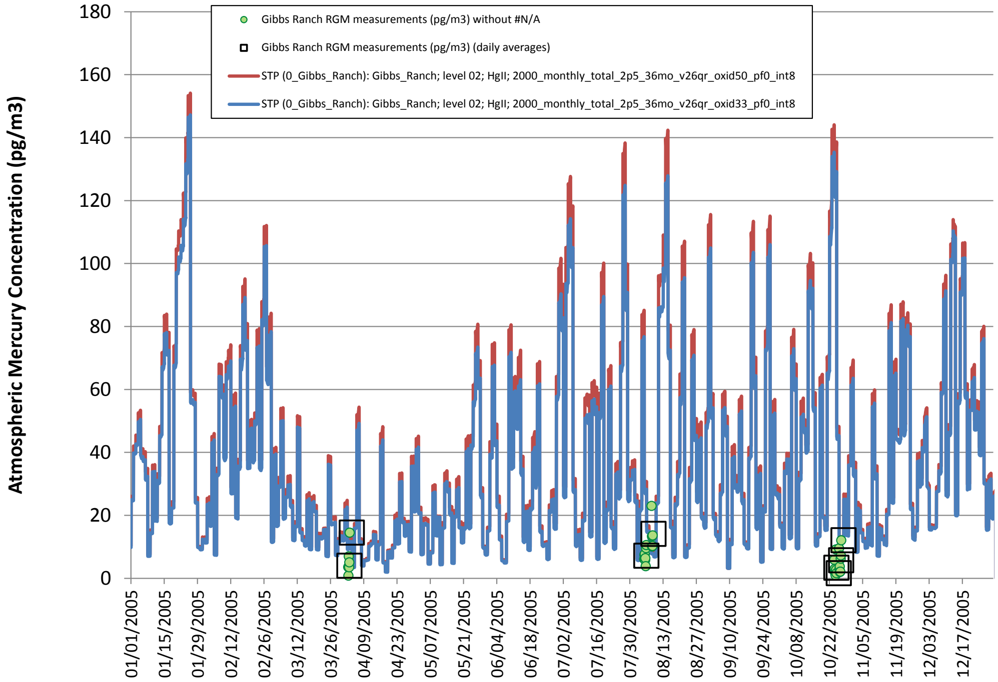

Figure 73. Measured RGM at Gibbs Ranch (Nevada) (daily averages and 2-hour measurements) and model estimates of Hg(II) using the "oxid33, pf0" and "oxid50, pf0" configurations

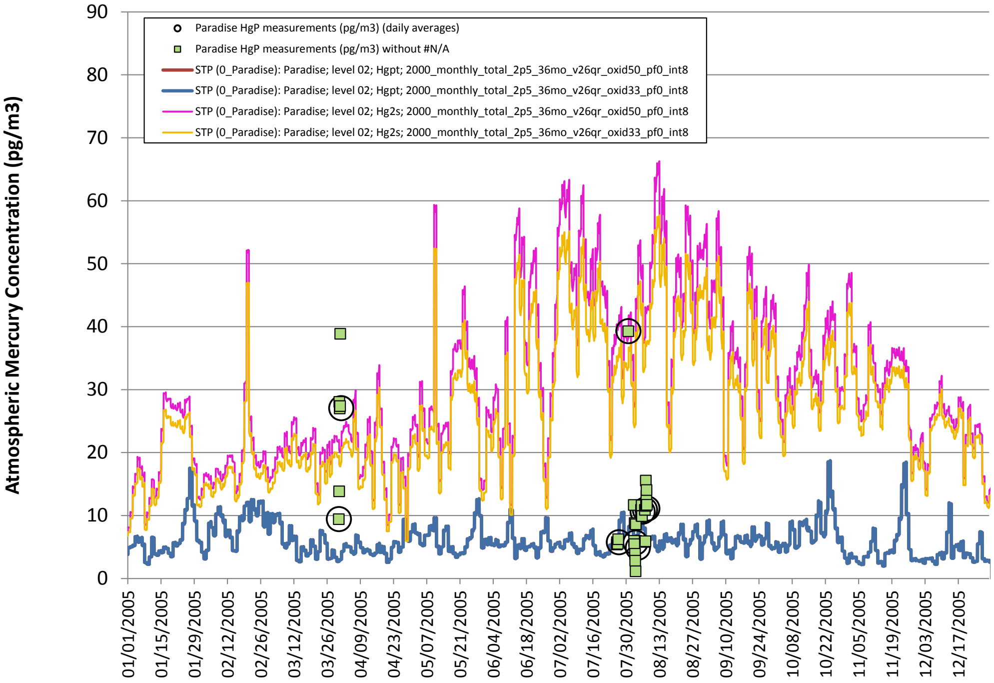

Figure 74. Measured Hg(p) (daily averages and 2-hour measurements) at Paradise Valley (NV) and model estimates of Hg(p) and Hg2s using the "oxid33, pf0" and "oxid50, pf0" configurations

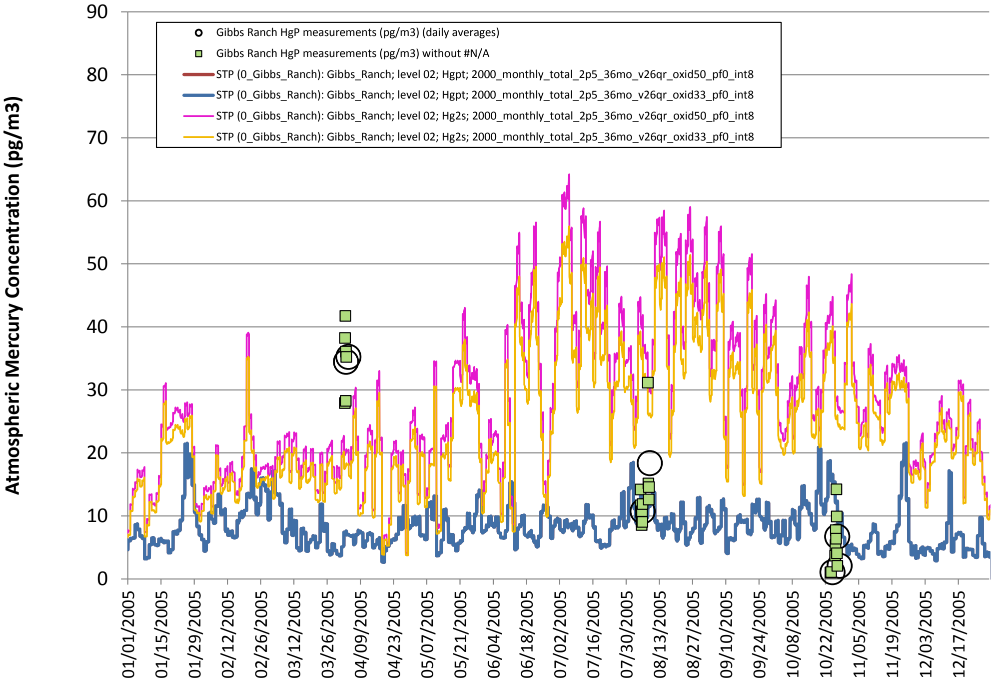

Figure 75. Measured Hg(p) (daily averages and 2-hour measurements) at Gibbs Ranch (NV) and model estimates of Hg(p) and Hg2s using the "oxid33, pf0" and "oxid50, pf0" configurations

5.3.4 Underhill, Vermont, USA

Mercury measurements collected in 2005 at Underhill, Vermont, were obtained from Eric Miller[15]. Measurements of GEM (discussed above in Section 5.2.1) and RGM began in May 2005 at the site, and measurements of Hg(p) began in July 2005. The speciated mercury data collected at the site were generally 2-hour averages, taken every 3 hours. The Underhill site (Gratz *et al.*, 2009) is located on the western slope of Mt. Mansfield at the Proctor Maple Research Center at an elevation of 399m above mean sea level. Like Mt. Bachelor and the Nevada sites, it is situated in relatively complex terrain. As such, there are uncertainties regarding which model concentration level to use for comparison (i.e., level 02 = 0-100m vs. level 03 = 100-500m), and which meteorological data level to use for the correction to Standard Temperature and Pressure (STP).

In Figure 76 and Figure 77, model estimates of Hg(II) concentrations are compared against daily average measured RGM concentrations, along with the individual 2-hour measurements, using results for model level 02 (0-100 m-agl) and model level 03 (100-500 m-agl), respectively. In Figure 78, daily averages of measured Hg(p) are compared against model results for concentration level 03 (100-500 m-agl). In Figure 79, the same Hg(p) data is plotted, with the addition of the individual 2-hr measurements, and with the addition of model estimated Hg2s concentrations.

In considering these RGM and Hg(p) model vs. measurement comparisons, the following can be noted:

- The model estimated Hg(II) concentrations are generally higher than the observed RGM concentrations. The concentration level 02 results for Hg(II), showing lower modeled values, are thus closer to the measured values. It is not clear if there is a physical basis for this, i.e., that the site is “seeing” this lower elevation air more than the higher elevation air.
- As was seen in previous comparisons, the model results using the “oxid33, pf0” and “oxid50, pf0” configurations are very similar for Hg(II), Hg(p), and Hg2s.
- In some cases, especially for RGM, the model appears able to reproduce the timing and approximate magnitude of peak concentrations and the non-peak (e.g., “trough”, or very low concentrations).
- The data for Hg(p) is more limited. However, the modeled and measured concentrations of Hg(p) are both generally very low, less than 10 pg/m^3. The model tends to underestimate the observed values.
- Modeled concentrations of Hg2s are much higher than the modeled concentrations of Hg(p). In most of the limited cases, the modeling results for Hg(p) and Hg2s (and, the total of the two) seem to more or less envelope the observed concentrations.

---

[15] Eric Miller, personal communication, 2012. Ecosystems Research Group, Norwich, VT

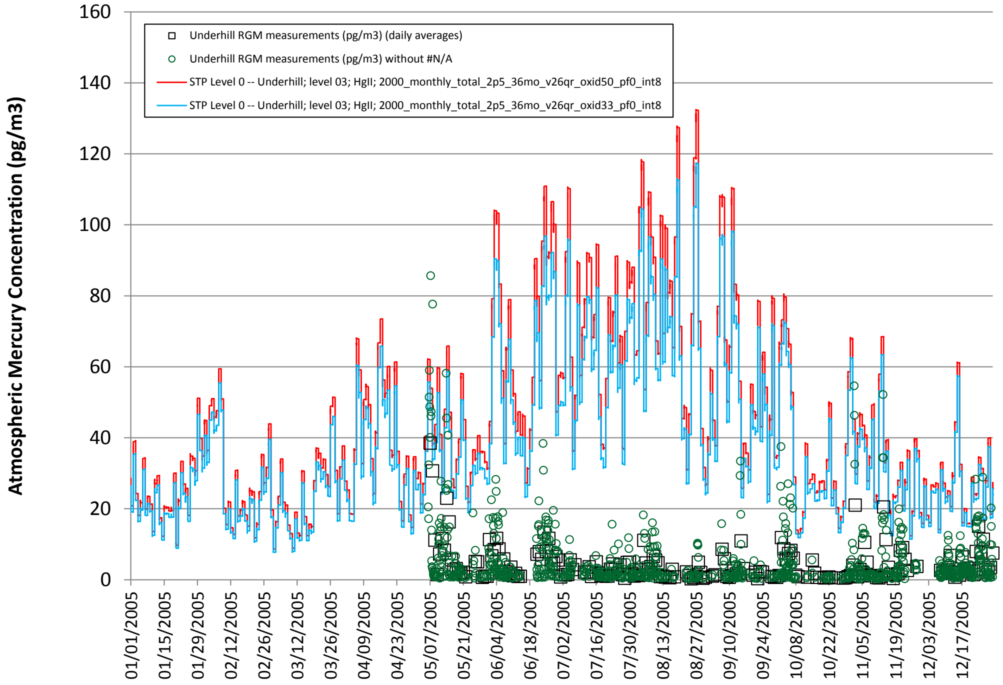

Figure 76. Measured RGM at Underhill (Vermont) (daily averages and 2-hour measurements) and model estimates of Hg(II) using the "oxid33, pf0" and "oxid50, pf0" configurations, at model concentration level 03

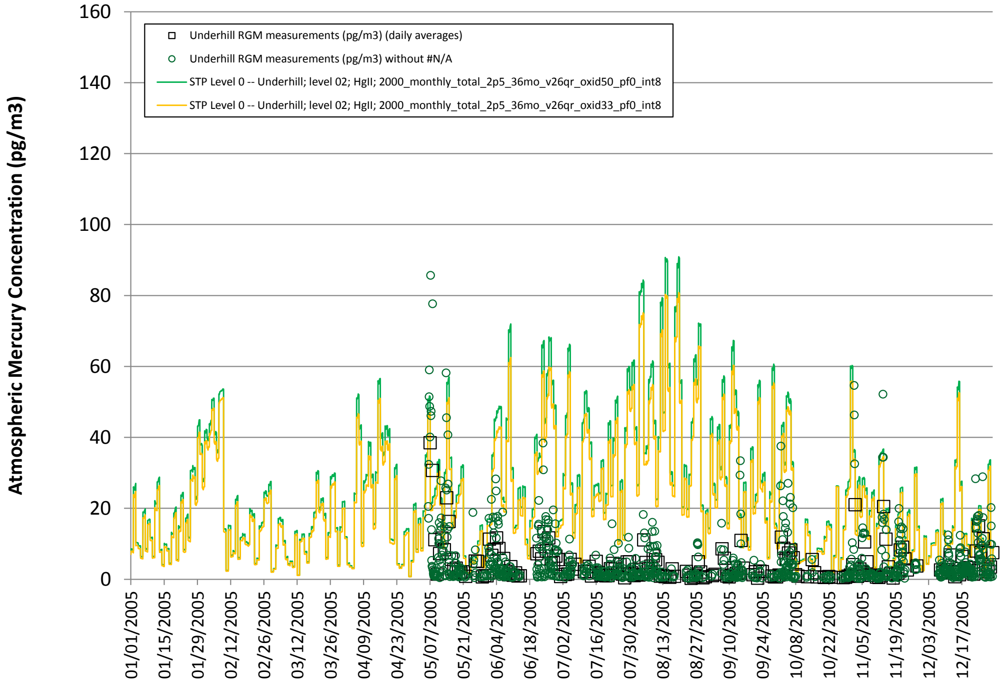

Figure 77. Measured RGM at Underhill (Vermont) (daily averages and 2-hour measurements) and model estimates of Hg(II) using the "oxid33, pf0" and "oxid50, pf0" configurations, at model concentration level 02

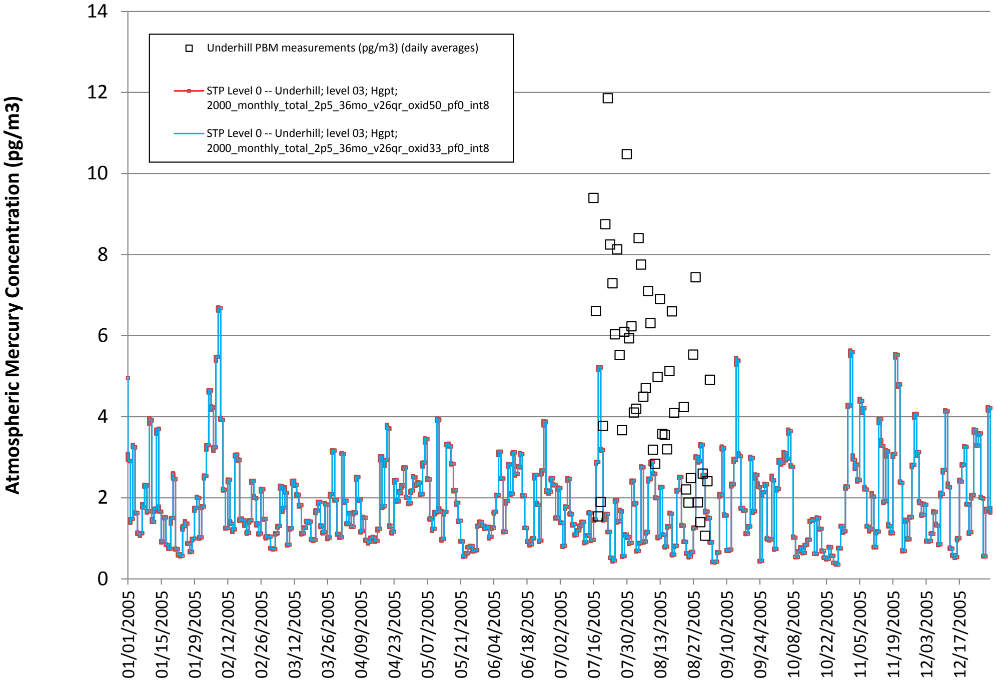

Figure 78. Measured Hg(p) at Underhill (Vermont) and model estimates of Hg(p) using the "oxid33, pf0" and "oxid50, pf0" configurations

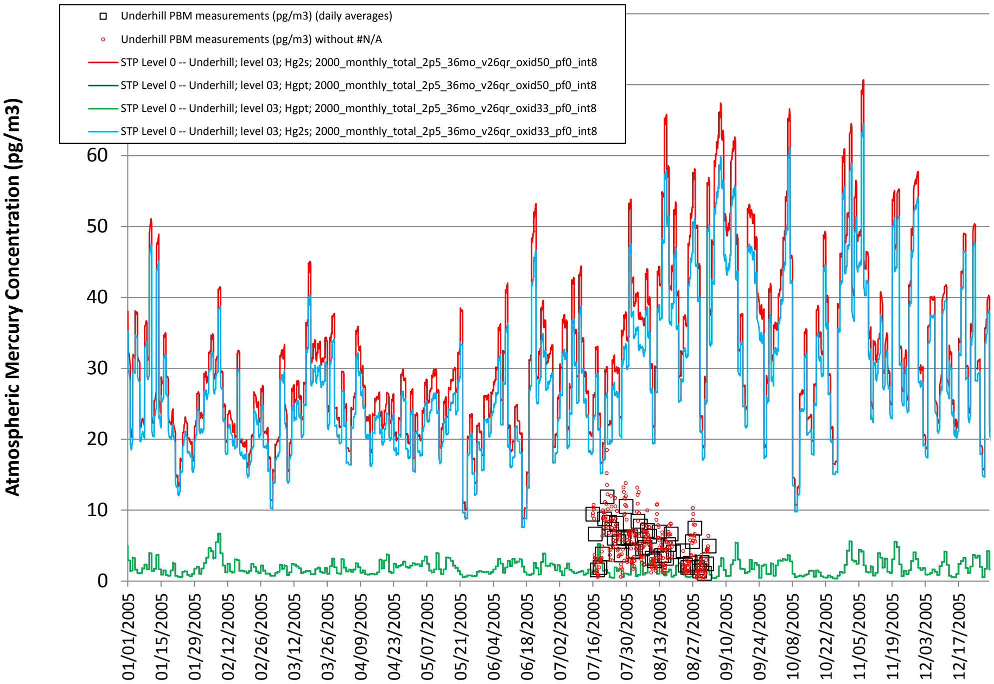

Figure 79. Measured Hg(p) at Underhill (Vermont) (daily averages and 2-hour measurements) and model estimates of Hg(p) and Hg2s using the "oxid33, pf0" and "oxid50, pf0" configurations

5.3.5 Mt. Bachelor, Oregon, USA

Mercury measurements -- including GEM, RGM, Hg(p) and total-Hg ("Hgtot") -- collected in 2005 at the Mount Bachelor Observatory (MBO) on the summit of Mt. Bachelor, Oregon, were obtained from Seth Lyman and Dan Jaffe[16]. The GEM data have been discussed above in Section 5.2.4 (page 62). The sampling methodology, data, and extensive analysis and interpretation regarding the Mt. Bachelor measurements are provided by Weiss-Penzias *et al*. (2006, 2007), Swartzendruber *et al*. (2006), and Finley *et al*. (2009). When RGM and Hg(p) were measured (~May-September), they were measured on a 3-hour cycle. When Hgtot was measured (~January-March), it was measured on a 1-hour cycle. As described earlier, MBO is at the summit of Mt. Bachelor, 2763 m above mean sea level. The site generally receives air masses from the west, and is believed to frequently encounter free tropospheric air masses. The complex terrain and the related difficulties in comparing the modeling results with measurements at MBO are discussed above (Section 5.1). Due to these model-related challenges, it is not expected that the modeling will closely reproduce the observations. Nevertheless, comparisons of the RGM, Hg(p) and Hgtot measurements with model results will be presented and discussed here.

In Figure 80, model estimates of Hg(II) are compared against measured concentrations of RGM (daily averages, and individual 3-hr measurements), using model concentration level 06 (2000-3000 m-agl), for both the "oxid33, pf0" and "oxid50, pf0" configurations, using two alternative STP adjustments.

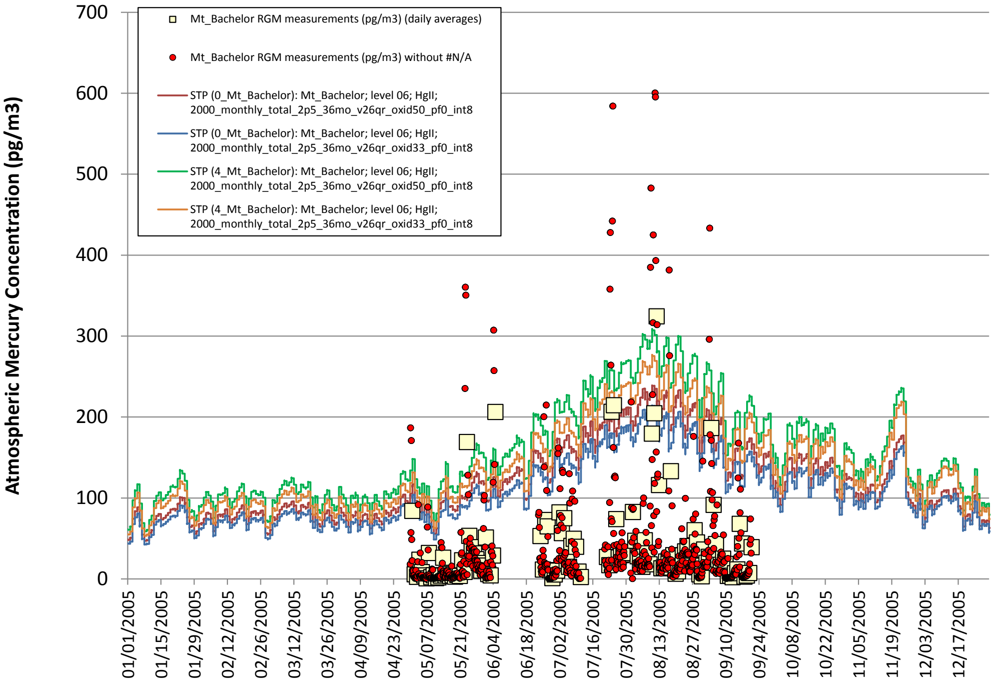

Figure 80. Measured RGM at Mt. Bachelor (Oregon) (daily averages and 3-hr measurements) and model estimates of Hg(II) using the "oxid33, pf0" and "oxid50, pf0" configurations, with two different STP adjustments

---

[16] Seth Lyman, personal communication, 2011, Univ.of Wash. Current affiliation: Utah State University, Vernal, Utah

It can be seen that on the scale of the measurement and modeled concentration range shown, the differences between the different model configurations and STP adjustment are not dramatic. During some periods, the modeled concentrations appear to match the measurements very well. During other periods, the model tends to over-predict the daily average concentration. The Jaffe research group has recently carried out an evaluation of the standard denuder-based RGM measurement technique (McClure, Jaffe, and Edgerton, 2014) using $HgBr_2$ as an RGM surrogate. They found that in some cases, the measured $HgBr_2$ appears to be artificially lowered due to release of mercury from the denuder. The efficiency of $HgBr_2$ capture by the measurement system fell to 20-54% under conditions of elevated humidity and ozone. Given these recent findings, it is possible that the at least some of the model over-prediction may be due to measurement under-prediction.

In Figure 81, model estimates of Hg(p) and Hg2s are compared against measured concentrations of Hg(p) (daily averages, and individual 3-hr measurements), using model concentration level 06 (2000-3000 m-agl), for both the “oxid33, pf0” and “oxid50, pf0” configurations, using two alternative Standard Temperature and Pressure (STP) adjustments. These same data are plotted using a logarithmic scale in Figure 82, in order to “see” the very low modeled concentrations of Hg(p) (~1 pg/m^3). The measured Hg(p) concentrations are generally in the range ~1 – 20 pg/m^3. The modeled Hg2s concentrations are relatively higher, in the range from ~20 – 120 pg/m^3. It can be seen that on the scale of the measurement and modeled concentration range shown, the differences between the different model configurations and STP adjustment are not dramatic, for Hg(p) or for Hg2s. In general, the observed concentrations of Hg(p) appear to be bracketed by the Hg2s model results and Hg(p) model results.

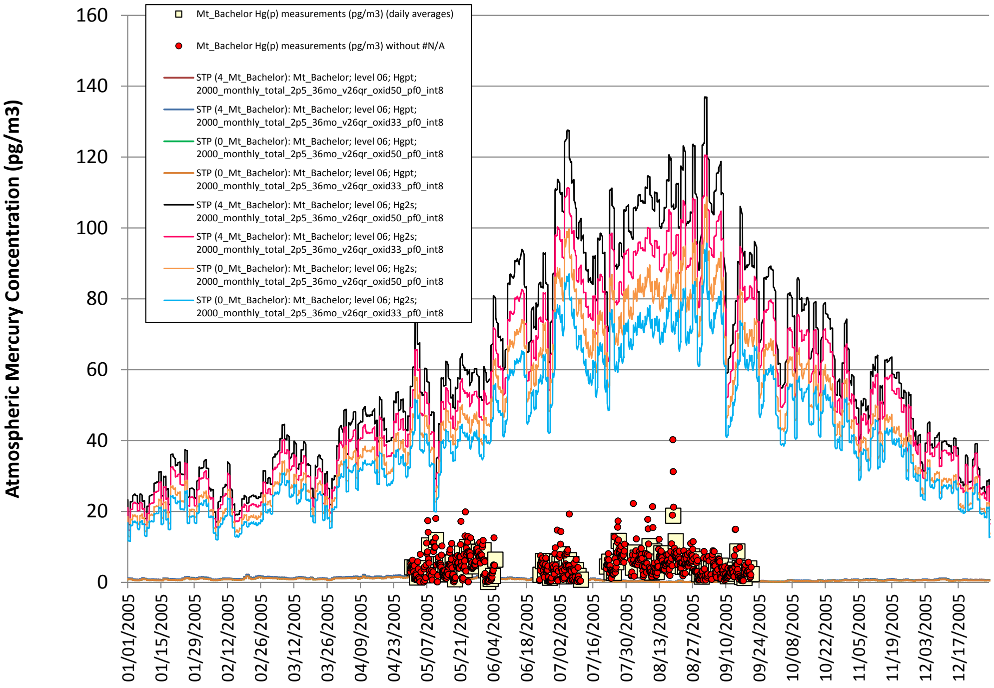

Figure 81. Measured Hg(p) at Mt. Bachelor (Oregon) (daily averages and 3-hr measurements) and model estimates of Hg(p) and Hg2s using the "oxid33, pf0" and "oxid50, pf0" configurations, with two different STP adjustments

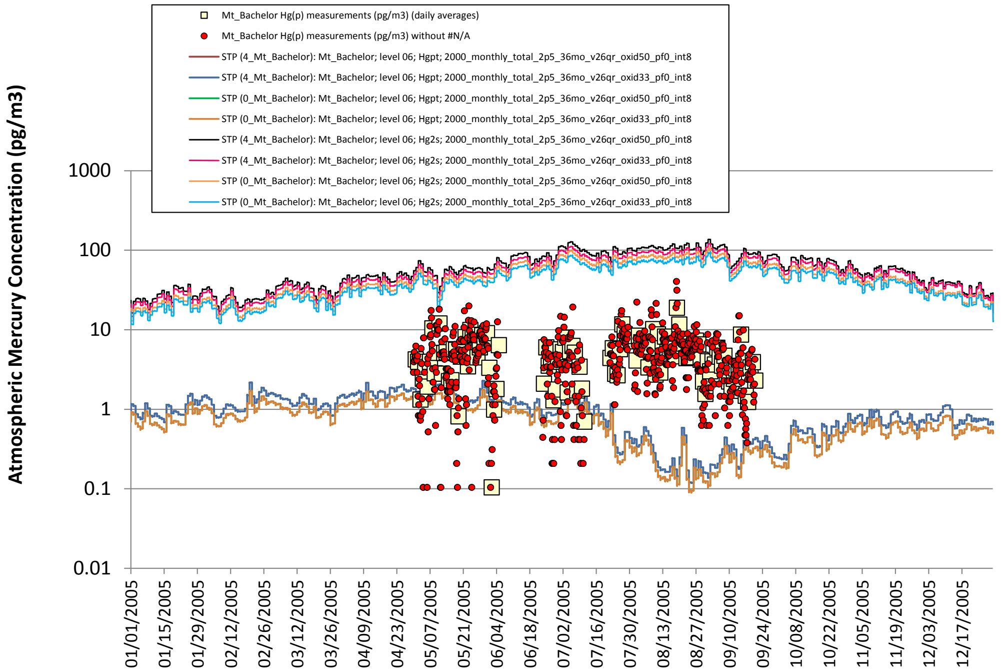

Figure 82. Logarithmic axis: Measured Hg(p) at Mt. Bachelor (daily avgs & 3-hr measurements) and model estimates of Hg(p) & Hg2s using the "oxid33, pf0" & "oxid50, pf0" configurations, with two STP adjustments

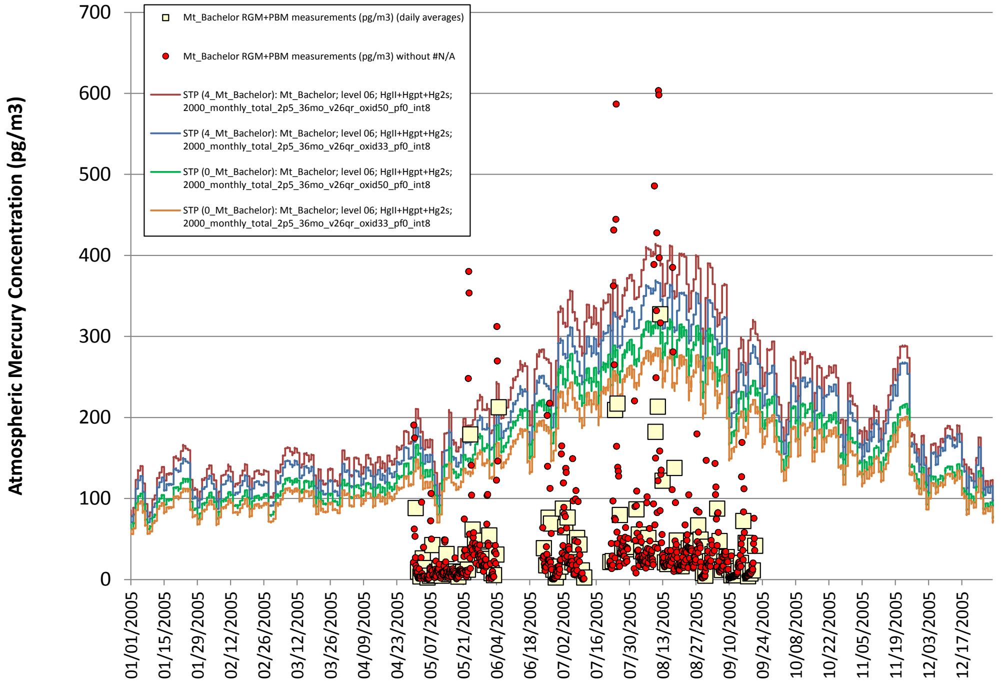

Figure 83. Measured total of Hg(Ii)+Hg(p) (i.e., all non Hg(0) measured mercury) at Mt. Bachelor (Oregon) (daily averages and 3-hr measurements) and model estimates of Hg(p)+Hg(II)+Hg2s (i.e., all non Hg(0) modeled mercury) using the "oxid33, pf0" and "oxid50, pf0" configurations, with two different STP adjustments

In Figure 83, model estimates of the total non-Hg(0) mercury forms (i.e., modeled Hg(p)+Hg(II)+Hg2s) are compared against the measured sum of the concentrations of Hg(p) and RGM, when both were measured. As above, model concentration level 06 (2000-3000 m-agl) is used, and results for both the “oxid33, pf0” and “oxid50, pf0” configurations are presented, using two alternative STP adjustments. It can be seen that on the scale of the measurement and modeled concentration range shown, the differences between the different model configurations and STP adjustment are not dramatic. Like with the RGM results discussed above, the modeled concentrations are sometimes consistent but often overestimate the observations. The potential issues of measurement under-prediction discussed above would also apply here, at least to the RGM component of the non-Hg(0) total.

In Figure 84, model estimates of the total mercury concentration (i.e., modeled Hg(0) + Hg(p) + Hg(II) + Hg2s) are compared against the measured Hgtot, when it was measured (Jan-March) and the sum of the concentrations of GEM, Hg(p) and RGM, when these were measured, during May-Sept. It can be seen that the model predictions are reasonably consistent with the measured total mercury concentrations.

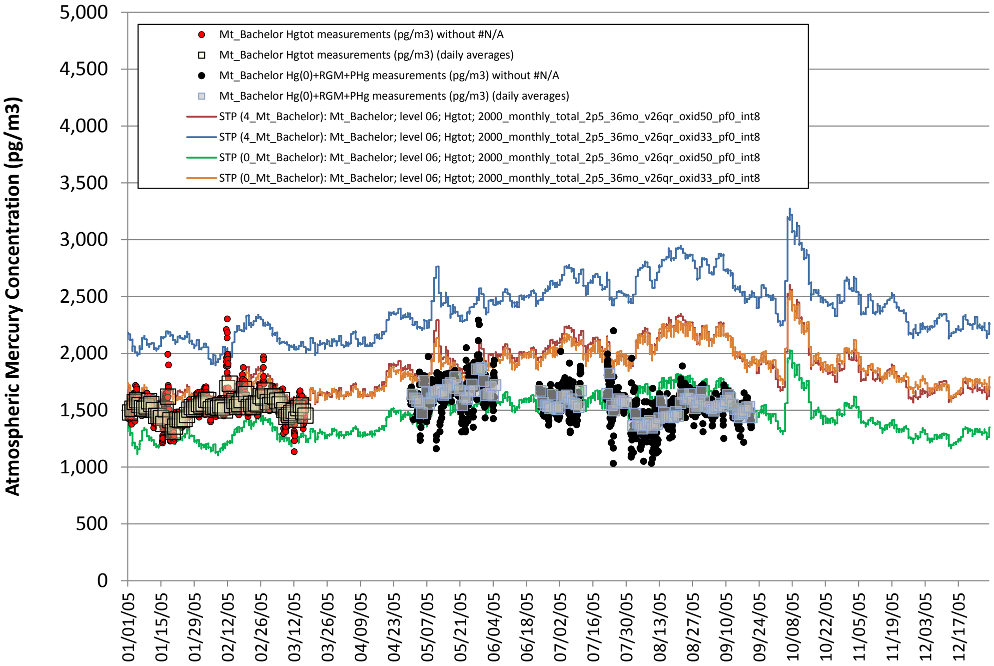

Figure 84. Measured Hgtot at Mt. Bachelor (daily averages and individual measurements) and model estimates of Hgtot using the "oxid33, pf0" and "oxid50, pf0" configurations, with two different STP adjustments

5.4. Comparison of model-estimated and measured mercury wet deposition at sites in the Great Lakes region

In addition to evaluating the model results by comparison against ambient concentration measurements, comparisons of modeled and measured wet deposition for sites in the Great Lakes region will be presented here. This was primary model evaluation approach used in the earlier phases of this GLRI modeling project (Cohen *et al*., 2011, 2013).

Weekly measurements of total mercury wet deposition from the Mercury Deposition Network (MDN) were obtained for 2005 for site in the Great Lakes region (NADP, 2011). A total of 32 sites with data for 2005 were used, including 20 in the western Great Lakes region and 12 in the eastern Great Lakes region, many of which are generally downwind of the Great Lakes (Figure 85).

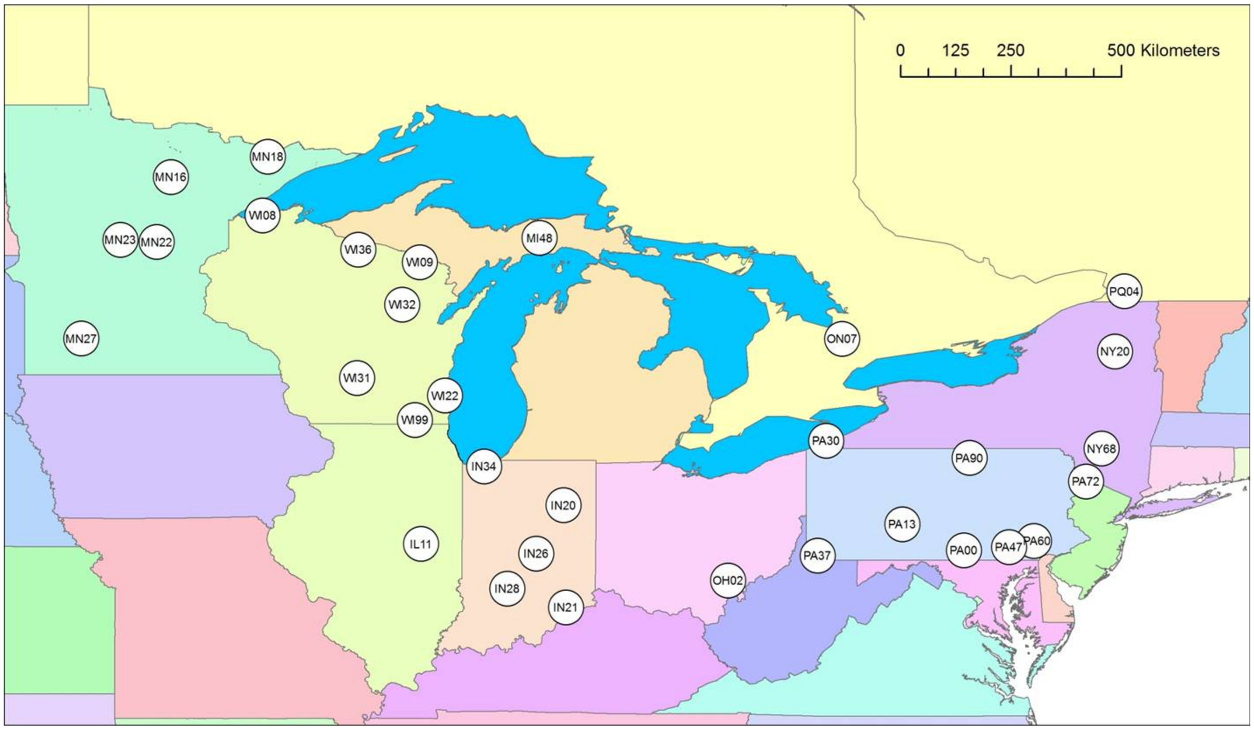

Figure 85. Mercury Deposition Network Sites in the Great Lakes Region with 2005 data

As discussed in Section 3.2 above (page 29), the grid-cell average precipitation amounts in the NCEP/NCAR Global Reanalysis meteorological data used in this work did not exactly match the precipitation measured at individual MDN sites located with a given grid cell. This is to be expected, of course, as precipitation at a specific location within a grid cell would not generally be the same as the grid cell average, even if both the model and measurements were "perfect".

As in the earlier phases of this work, we have used different approaches for dealing with this inherent uncertainty in comparing the model predictions with the wet deposition measurements. In one method, no adjustment was made to any of the model-predicted wet deposition estimates. In another, the wet deposition estimates at the MDN sites were adjusted proportionally to balance out the precipitation "error" in the meteorological. We also considered variations introduced by basing the adjustment on the precipitation measured at the MDN site by the rain-gauge, versus basing the adjustment on maximum value of the precipitation measured by the rain gauge and the mercury collector itself.

It is recognized that the impact of the precipitation "errors" in the meteorological datasets will introduce complex, non-linear deviations in the simulations. So, the approaches described above involving the measured/model-input precipitation ratio at any given site are clearly oversimplifications. This methodology provides an approximate estimate of the order of magnitude of the uncertainty introduced by the inherent grid-related precipitation issues in the input meteorological data.

The essential evaluation comparison is shown in Figure 86 for the "oxid33, pf0" model configuration and Figure 87 for the "oxid50, pf0" configuration. These same data are presented, for the two configurations, in Figure 88 and Figure 89, with the sites in the western and eastern Great Lakes region differentiated.

In the model evaluation figures below, the values and "error bars" shown are the average and range, respectively, of the estimates made using the various adjustment methods discussed above. In the figures, best-fit linear regressions are shown, along with the "slope", and "R^2" of the regression in each case. If the modeled data matched the measurements perfectly, the slope would be "1" and the R^2 would be "1".

It can be seen that the agreement between modeled and measured values tends to be somewhat better for the "oxid33, pf0" configuration than the "oxid50, pf0" configuration. It can also be seen that the model tends to overestimate the wet deposition at the sites in the eastern Great Lakes region (generally downwind of the Great Lakes). However, the modeling results for the western sites more closely match the measurements. For most western sites, the "range" in the model estimates includes the measured value. These findings are similar to those in the earlier phases of this work.

Other modeling efforts have encountered this over-prediction of wet deposition in the eastern Great Lakes region (e.g., Grant *et al*., 2014). To address the issue, some analyses have assumed that a significant portion (~75%) of emitted Hg(II) is reduced to Hg(0) immediately after emission (e.g., Zhang *et al*., 2012, Chen *et al*., 2014). With this assumption, modeled wet deposition in the eastern Great Lakes region is reduced to be closer to observations. The validity of this assumption and its impact on the model evaluation results of this HYSPLIT-Hg modeling will be examined in future work.

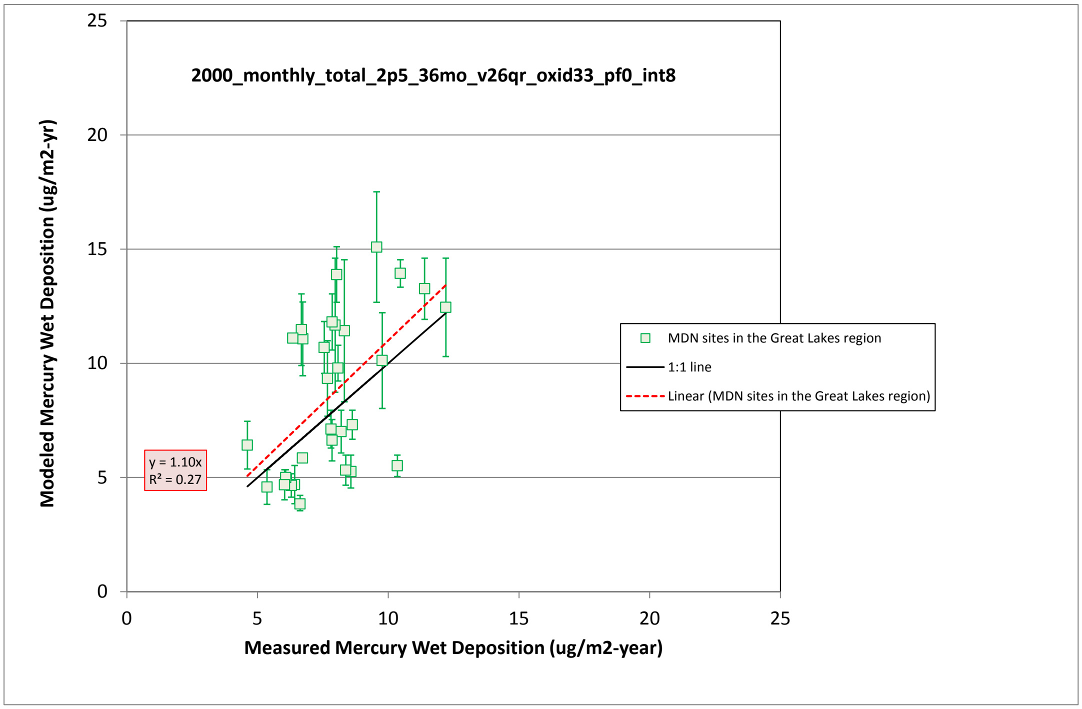

Figure 86. Measured mercury wet deposition compared with model estimates at MDN sites in the Great Lakes region, for the "oxid33, pf0" model configuration

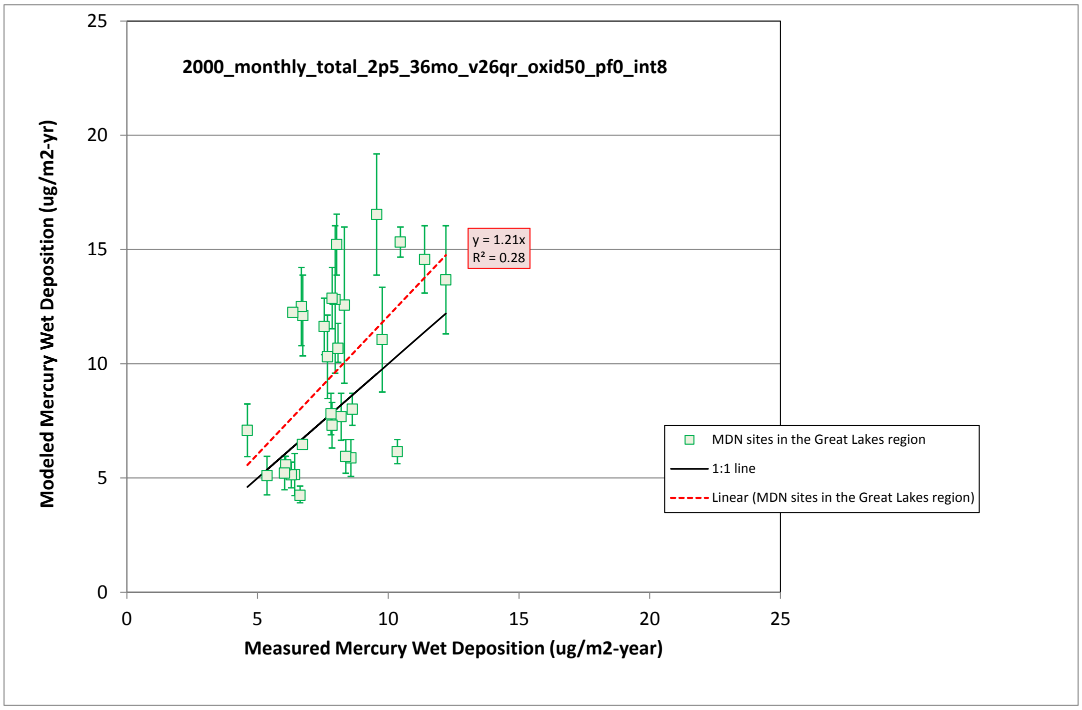

Figure 87. Measured mercury wet deposition compared with model estimates at MDN sites in the Great Lakes region, for the "oxid50, pf0" model configuration

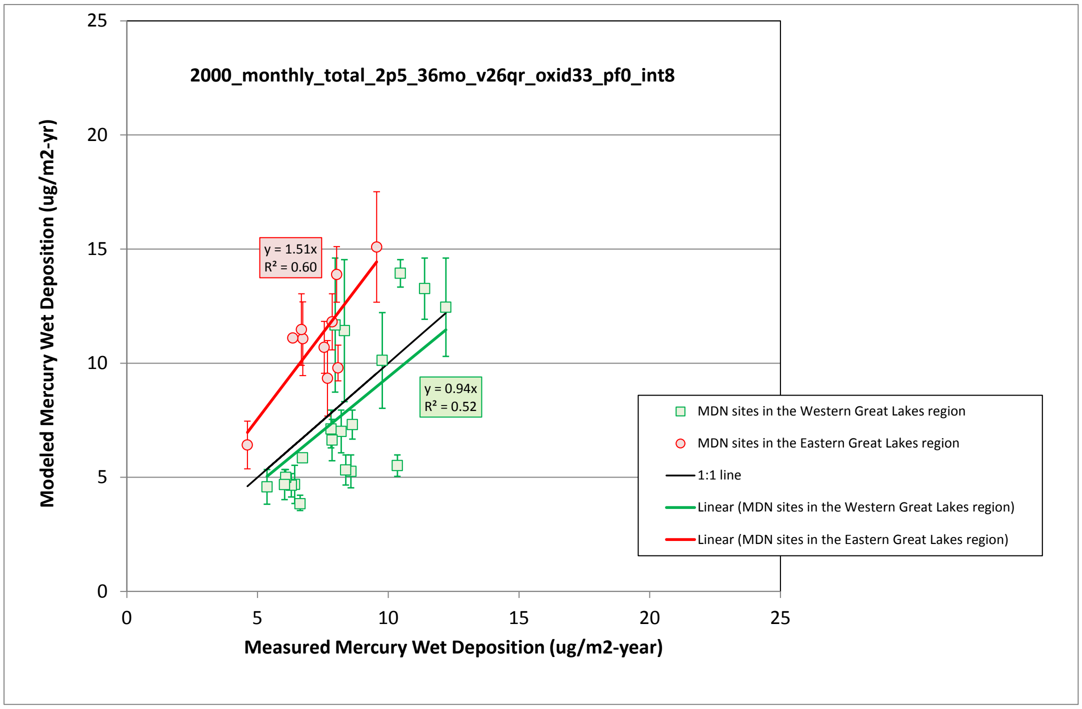

Figure 88. Measured mercury wet deposition compared with model estimates at MDN sites in the Western and Eastern Great Lakes region, for the "oxid33, pf0" model configuration

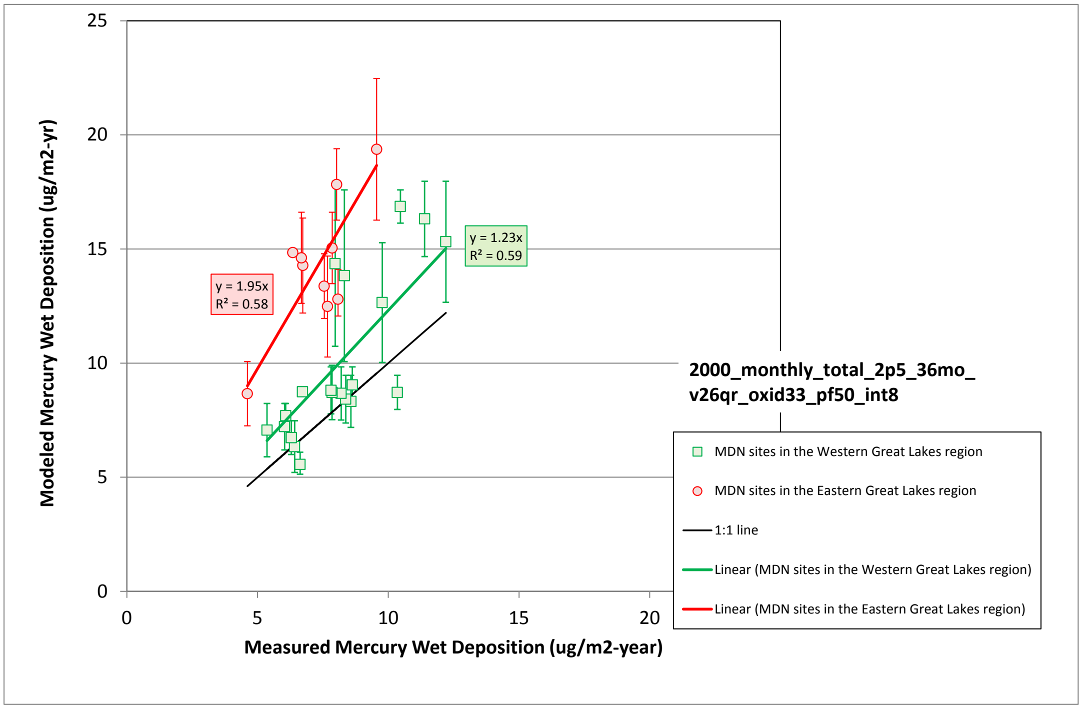

Figure 89. Measured mercury wet deposition compared with model estimates at MDN sites in the Western and Eastern Great Lakes region, for the "oxid50, pf0" model configuration

5.5. Comparison of model-estimated and measured mercury wet deposition at all Mercury Deposition Network sites with 2005 data

In addition to the 32 MDN sites in the Great Lakes region, there were 54 additional MDN sites with complete or nearly complete data coverage for 2005 (NADP, 2011). These 54 additional sites include 17 in the Gulf of Mexico region and 37 elsewhere in the U.S. and Canada. In this section, the results for these additional sites are presented, along with the overall results for all 86 MDN sites with 2005 data.

The same approaches outlined in the previous section were used to deal with the inherent uncertainty in comparing the model predictions with the wet deposition measurements. In the model evaluation figures below, the values and "error bars" shown are the average and range, respectively, of the estimates made using these various adjustment methods. In the figures, best-fit linear regressions are shown, along with the equation of the regression line and the "R^2" of the regression in each case.

A comparison of modeled vs. measured wet deposition at all 86 MDN sites is shown in Figure 90 for the "oxid33, pf0" model configuration and Figure 91 for the "oxid50, pf0" configuration. In these figures, two different regression lines are shown. One forces the intercept to be "0", and one allows the intercept to be determined from the regression. In Figure 92 and Figure 93, analogous comparisons for the 17 MDN sites in the Gulf of Mexico region are shown. In Figure 94 and Figure 95, an analogous set of comparisons is presented for the 37 MDN sites not in the Great Lakes or Gulf of Mexico region.

The overall agreement between modeled and measured values appears very reasonable, and there is not a clear "winner" between the "oxid33, pf0" and "oxid50, pf0" configurations. The model tends to underestimate wet deposition at sites in the Gulf of Mexico region, and the moderately higher wet deposition estimates in the "oxid50, pf0" results are therefore closer to the observations. For the 37 "other" MDN sites (not in the Great Lakes or Gulf of Mexico regions) the model appears to perform very well (Figure 94 and Figure 95).

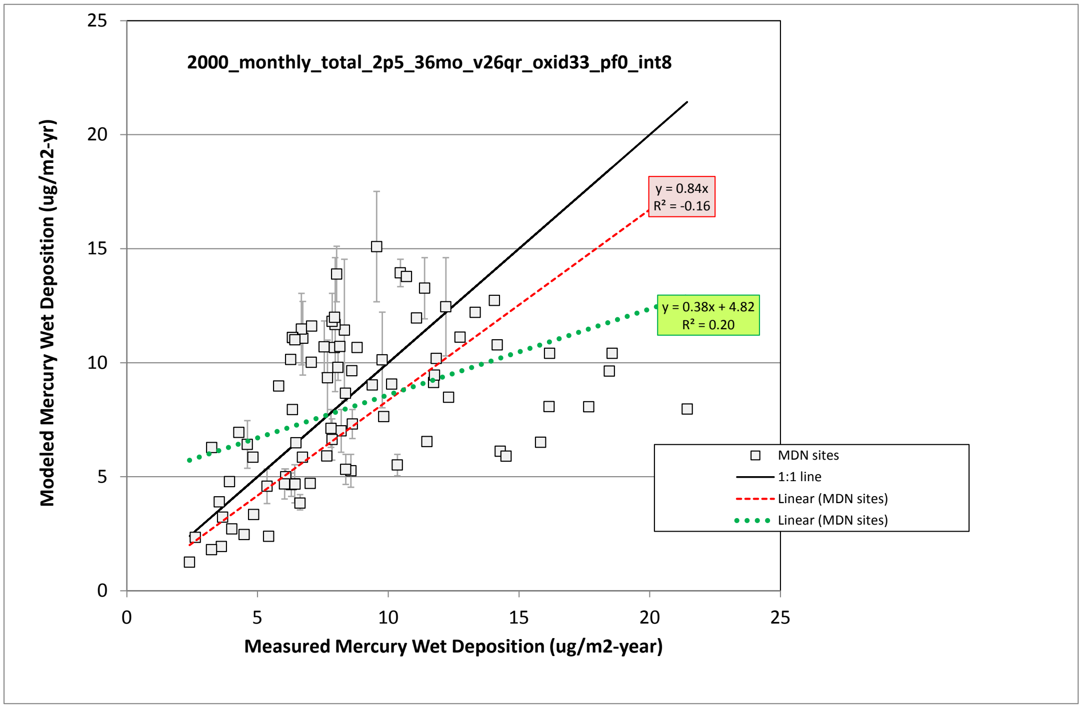

Figure 90. Measured mercury wet deposition compared with model estimates at all MDN sites with 2005 data, for the “oxid33, pf0” model configuration

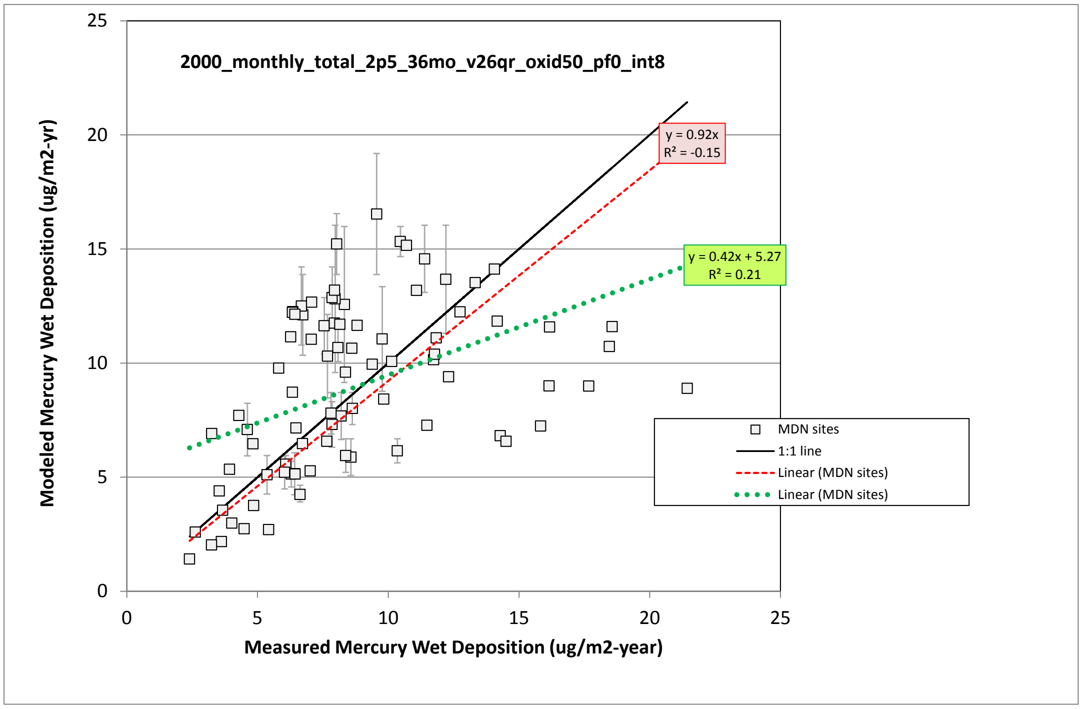

Figure 91. Measured mercury wet deposition compared with model estimates at all MDN sites with 2005 data, for the “oxid50, pf0” model configuration

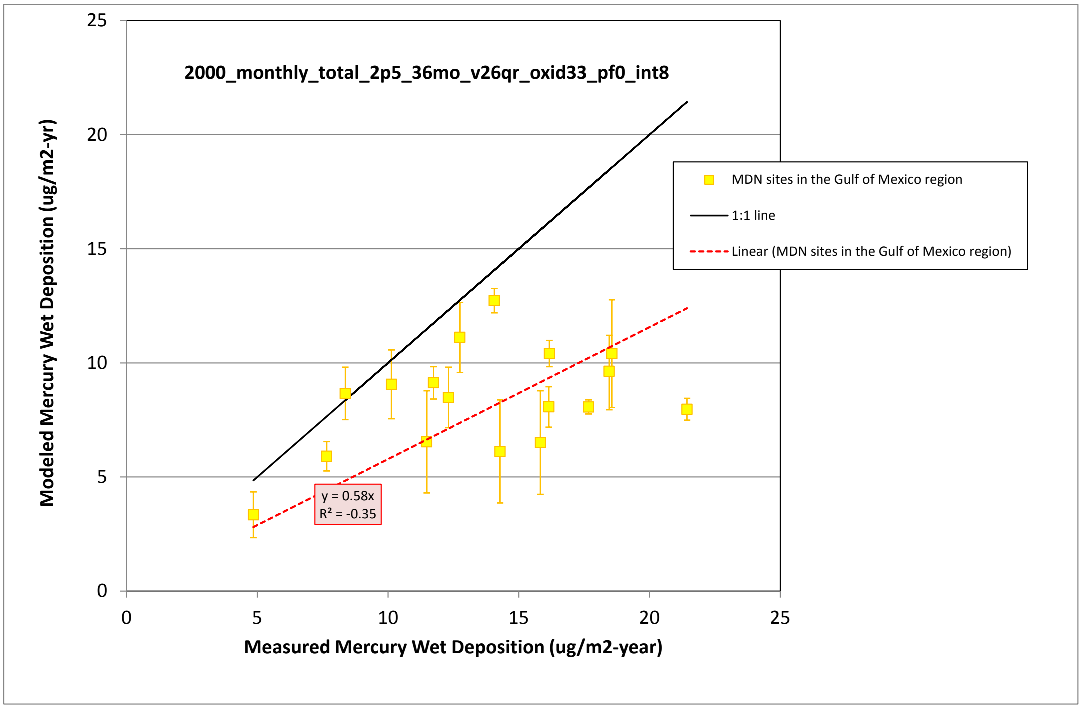

Figure 92. Measured mercury wet deposition compared with model estimates at all MDN sites in the Gulf of Mexico region, for the “oxid33, pf0” model configuration

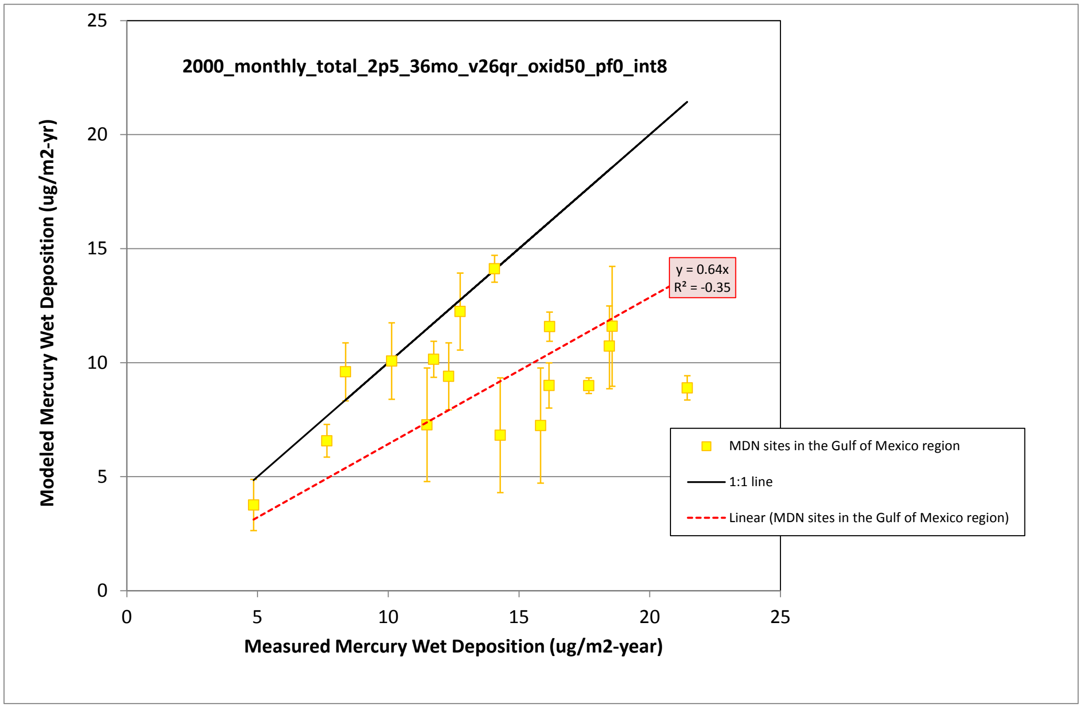

Figure 93. Measured mercury wet deposition compared with model estimates at all MDN sites in the Gulf of Mexico region, for the “oxid50, pf0” model configuration

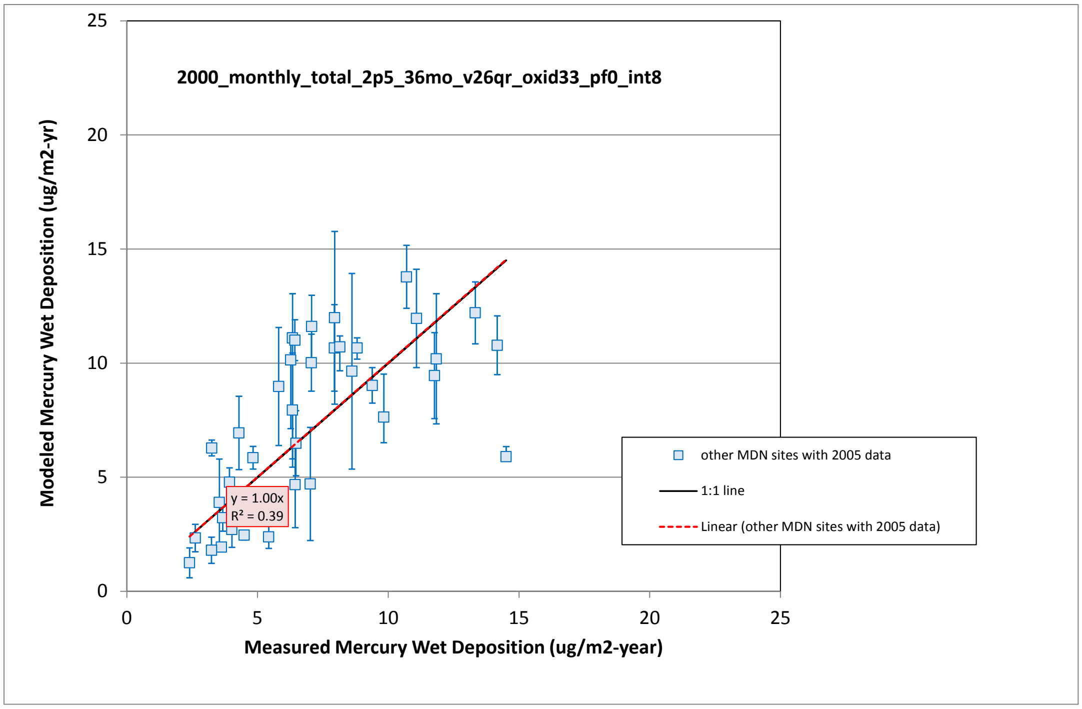

Figure 94. Measured mercury wet deposition compared with model estimates at all MDN sites with 2005 data other than those in the Great Lakes and Gulf of Mexico regions, for the “oxid33, pf0” model configuration

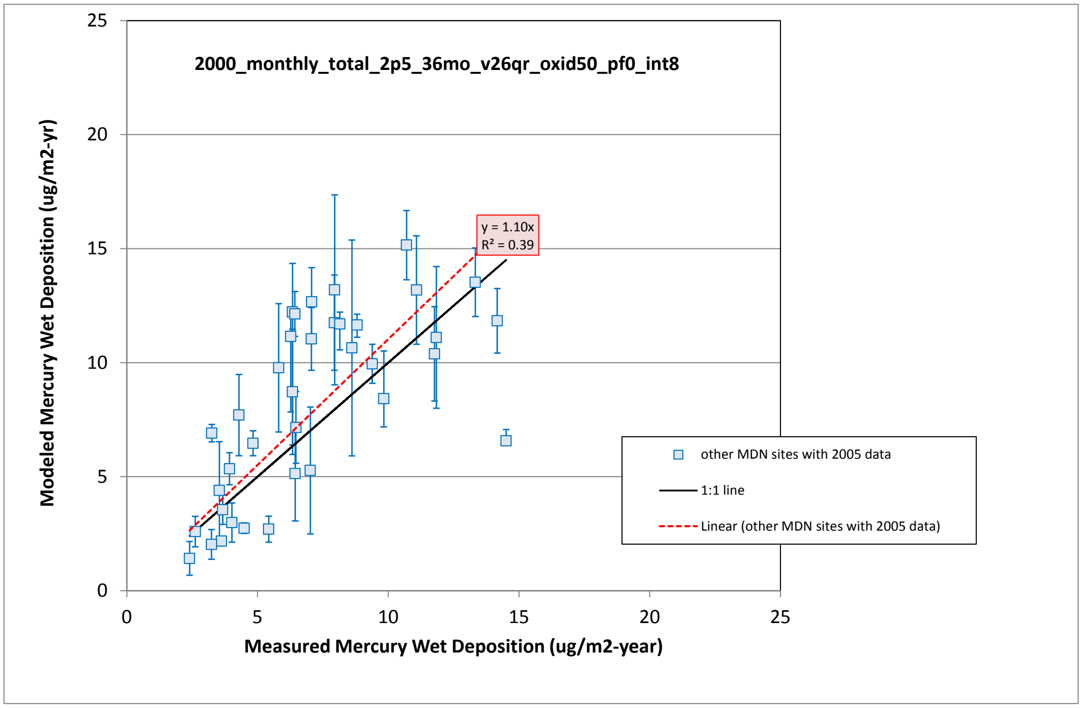

Figure 95. Measured mercury wet deposition compared with model estimates at all MDN sites with 2005 data other than those in the Great Lakes and Gulf of Mexico regions, for the “oxid50, pf0” model configuration

6. Simulation Results

6.1. Total inventory results for the Great Lakes

As noted above, 23 different “total inventory” simulations were carried out, shown in Table 6. Total model-estimated deposition flux values for each of the Great Lakes and their watersheds are shown in Figure 96 through Figure 102, below.

To begin, in considering the results shown in Figure 96 for Lake Erie, several observations can be made.

First, it is noted that the “oxid100, pf100” configuration shows approximately 10% higher deposition fluxes than the “oxid33, pf0” configuration, for comparable runs, i.e., [01] > [02], [03] > [04], [05] > [06], [07] > [08], [09] > [11], [10] > [12]. As discussed above in Section 3.4 (page 36), the “oxid100, pf100” configuration resulted in unrealistically low Hg(0) concentrations, and unrealistically high Hg(p) concentrations, compared to the “oxid33, pf0” and “oxid50, pf0” configurations. Despite large differences in estimated concentrations, though, the estimated deposition fluxes are only modestly increased

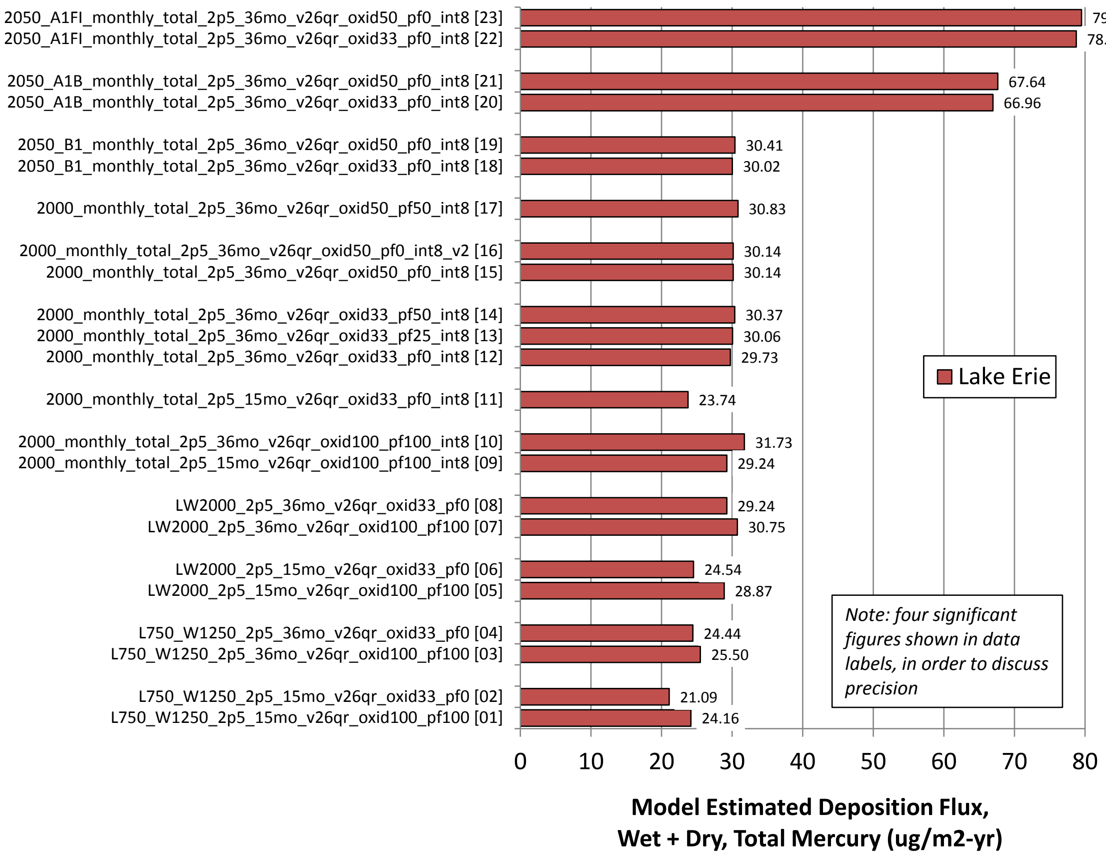

Note: four significant figures shown in data labels, in order to discuss precision

Figure 96. Total mercury inventory deposition results for Lake Erie

Second, for any set of comparable runs, the results with the "oxid50, pf0" and "oxid33, pf0" configurations are *very* similar, with the "oxid50, pf0" configuration showing a slightly larger deposition, on the order of 1% higher than the "oxid33, pf0" configuration.

Third, it is seen that for comparable simulations, i.e., all other factors held constant, the deposition arising from the different emissions inventories displays the following pattern:

L750_W1250 < LW2000 < 2000 ~ 2050B1 < 2050A1B < 2050A1FI

This pattern is entirely consistent with the overall magnitudes of the emissions inventories, as summarized in Table 7 above (page 40).

Fourth, the deposition increases shown for the 2050A1B and 2050A1FI future emissions scenarios are somewhat disproportional to the overall inventory emissions, however. That is, the estimated deposition arising from those inventories [runs 20-23] are more than twice that arising from comparable simulations using the 2000 and 2050B1 inventories [runs 12-19], even though the emissions are only about 25% to 40% higher.

Fifth, it is seen from Figure 96 that for comparable simulations, the 15 month runs (i.e., 3-month spin-up, before the 12 months of 2005) show lower deposition results than the 36 month runs (i.e., 24-month spin-up, before the 12 months of 2005). The difference for the "oxid100, pf100" configuration, e.g., between runs [1] and [3], and between [5] and [7], are generally only on the order of a few percent, whereas the differences for the "oxid33, pf0" configuration – e.g., between runs [2] and [4], and between runs [6] and [8] -- are somewhat larger, on the order of 15%-20%. The relatively small deposition differences with the "oxid100, pf100" configuration, used in earlier analyses (e.g., Cohen *et al*. 2011, 2013), was part of the rationale employed in that earlier work to limit the spin-up to 3 months.

Sixth, there are only small differences between comparable runs in which the "particle fraction" ["pf"] of Hg(0) oxidation products are varied. For example, in the series of runs [12], [13], [14], the particle fraction is varied from 0%, to 25%, to 50% (all with "oxid33"), but the model estimated deposition flux to Lake Erie only changes by about 1-2%. The same can be said for an analogous comparison for "oxid50", runs [15] and [17], which show a similar small difference.

Finally, one example of a particular QA/QC check is shown in this figure, for runs [15] and [16]. These runs were designed to be identical, but were carried out on two different computational workstations at different times. The results of the two runs were identical, as expected.

Upon inspection of the remaining comparable figures in this section (Figure 97 through Figure 102), it can be seen that the above findings generally hold for the other Great Lakes and their watersheds. One overarching finding emerging from this analysis is that the differences in model-estimated deposition arise primarily due to emissions amounts, and much less due to chemical mechanism variations. This suggests that the deposition results are more robust than might be expected due to uncertainties in the atmospheric chemistry of mercury.

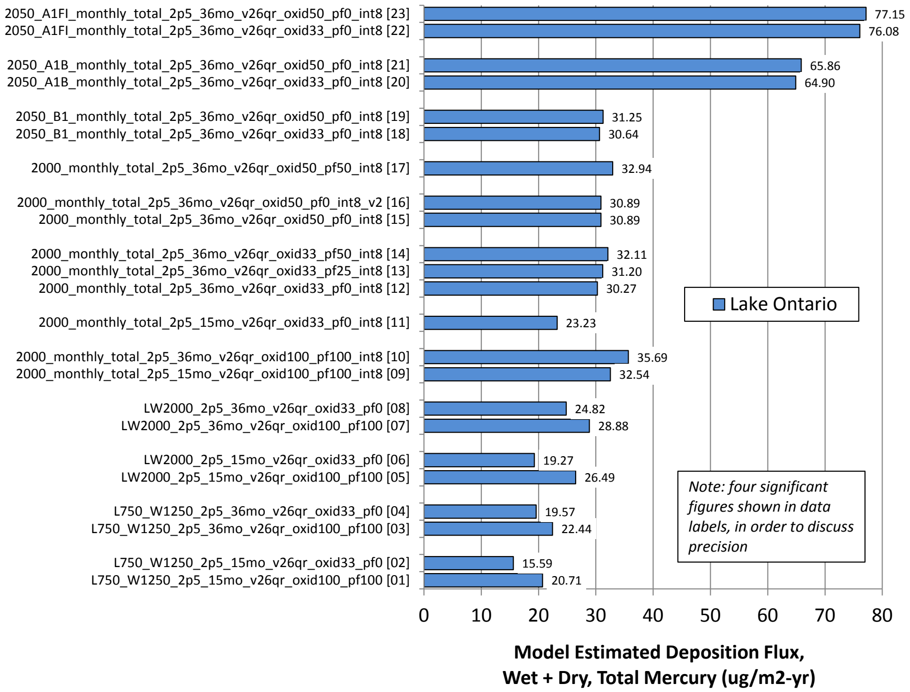

Note: four significant figures shown in data labels, in order to discuss precision

Figure 97.Total mercury inventory deposition results for Lake Ontario

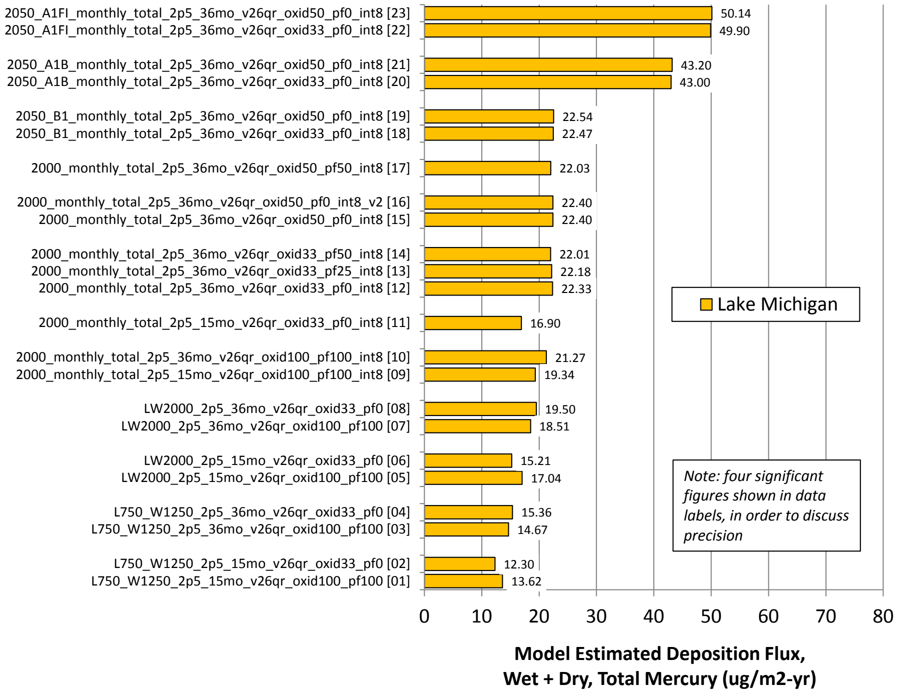

Note: four significant figures shown in data labels, in order to discuss precision

Figure 98. Total mercury inventory deposition results for Lake Michigan

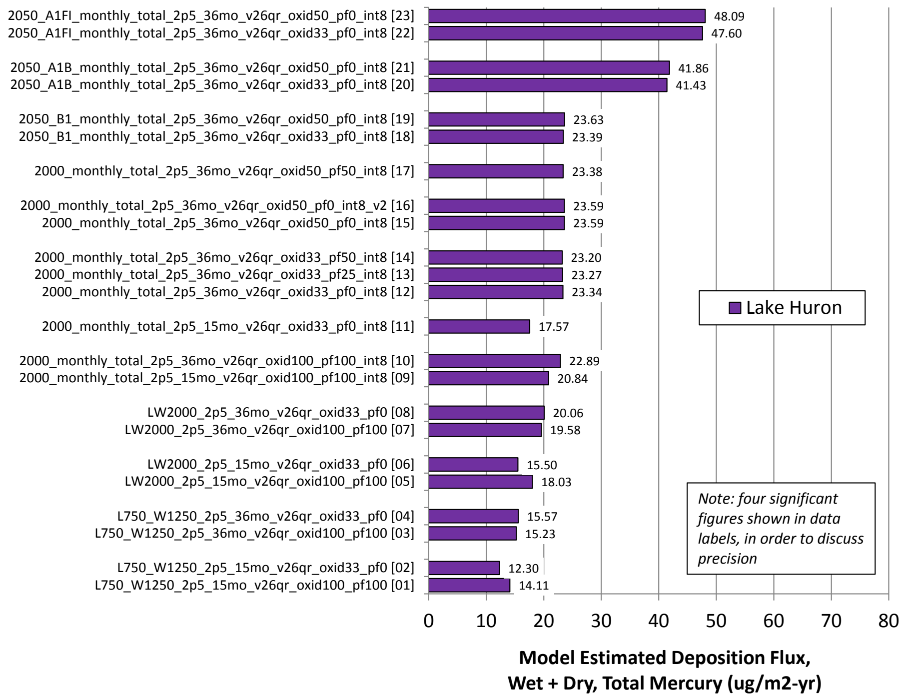

Note: four significant figures shown in data labels, in order to discuss precision

Figure 99. Total mercury inventory deposition results for Lake Huron

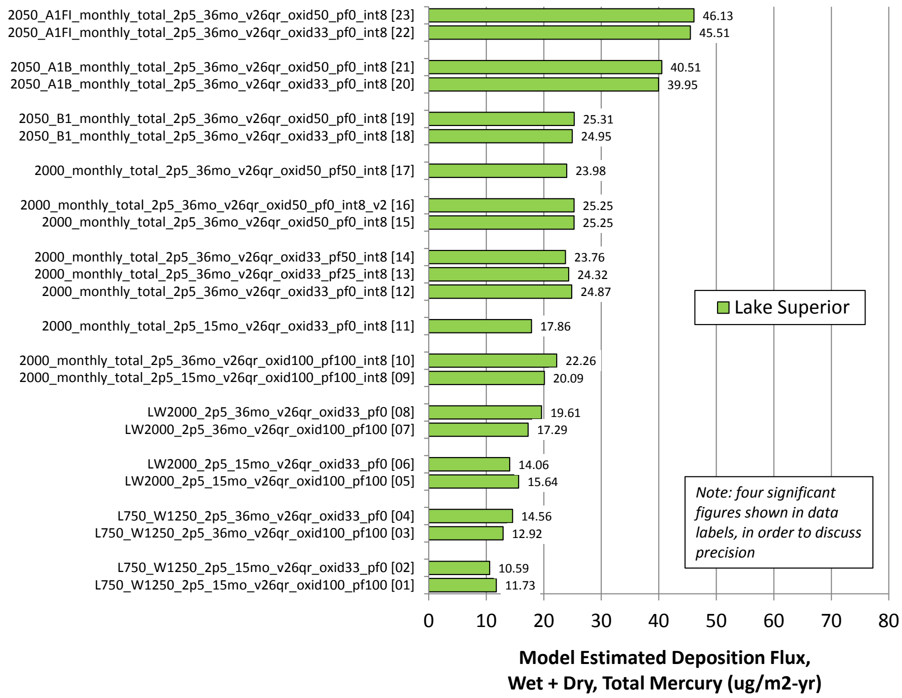

Note: four significant figures shown in data labels, in order to discuss precision

Figure 100. Total mercury inventory deposition results for Lake Superior

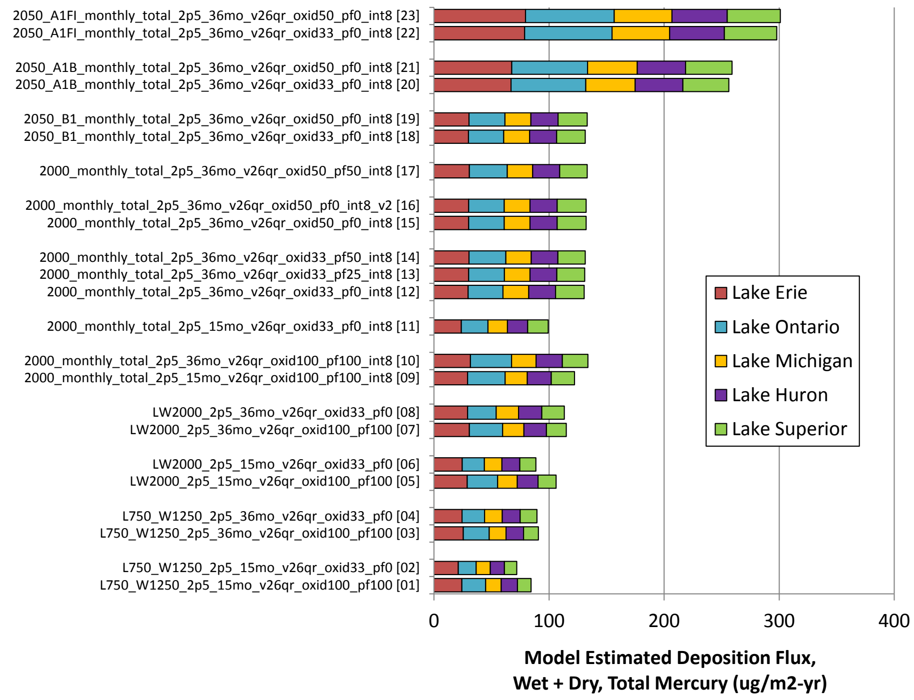

Figure 101. Total mercury inventory deposition results for all Great Lakes

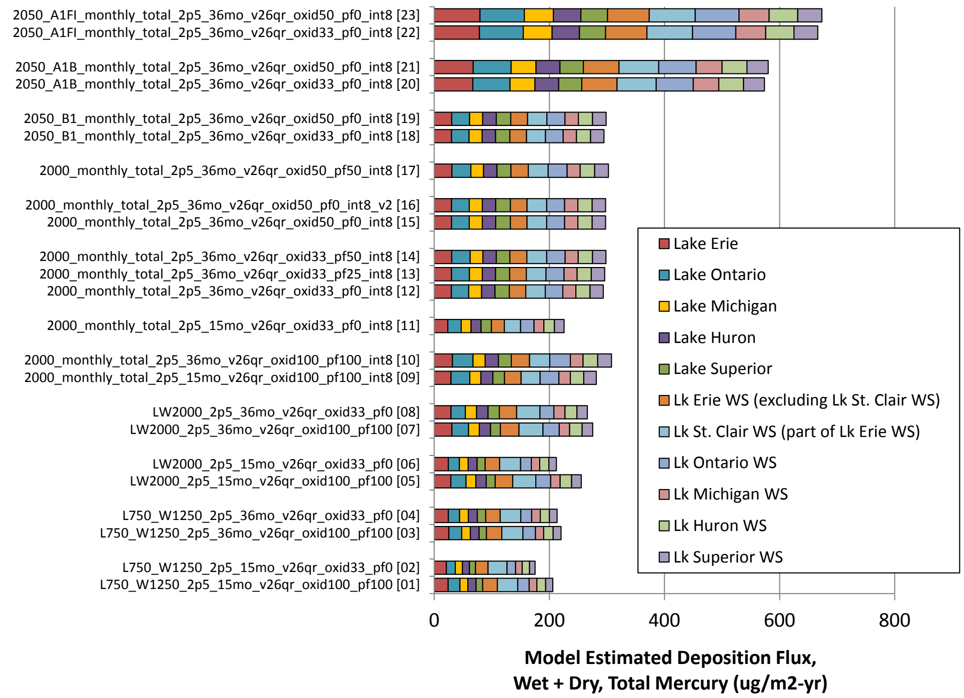

Figure 102. Total mercury inventory deposition results for all Great Lakes and their watersheds

A modeling analysis using the CMAQ model has recently been carried out by Grant *et al*. (2014), in which mercury deposition estimates for the Great Lakes were developed. This alternative analysis used a 2005 inventory, as opposed to the 2000 inventory used here, and so the results are not strictly comparable. Nevertheless, a comparison between the results of the two analyses is shown in Figure 103. Considering the difference in inventory years, numerous methodological differences between the two analyses (e.g., grid size, atmospheric chemistry, meteorology, deposition schemes, etc.) and uncertainties in the atmospheric chemistry and physics of mercury, the results are encouragingly consistent. Consistency between HYSPLIT-Hg and CMAQ model results for Great Lakes atmospheric mercury deposition has been found in earlier work (Cohen *et al*. 2007).

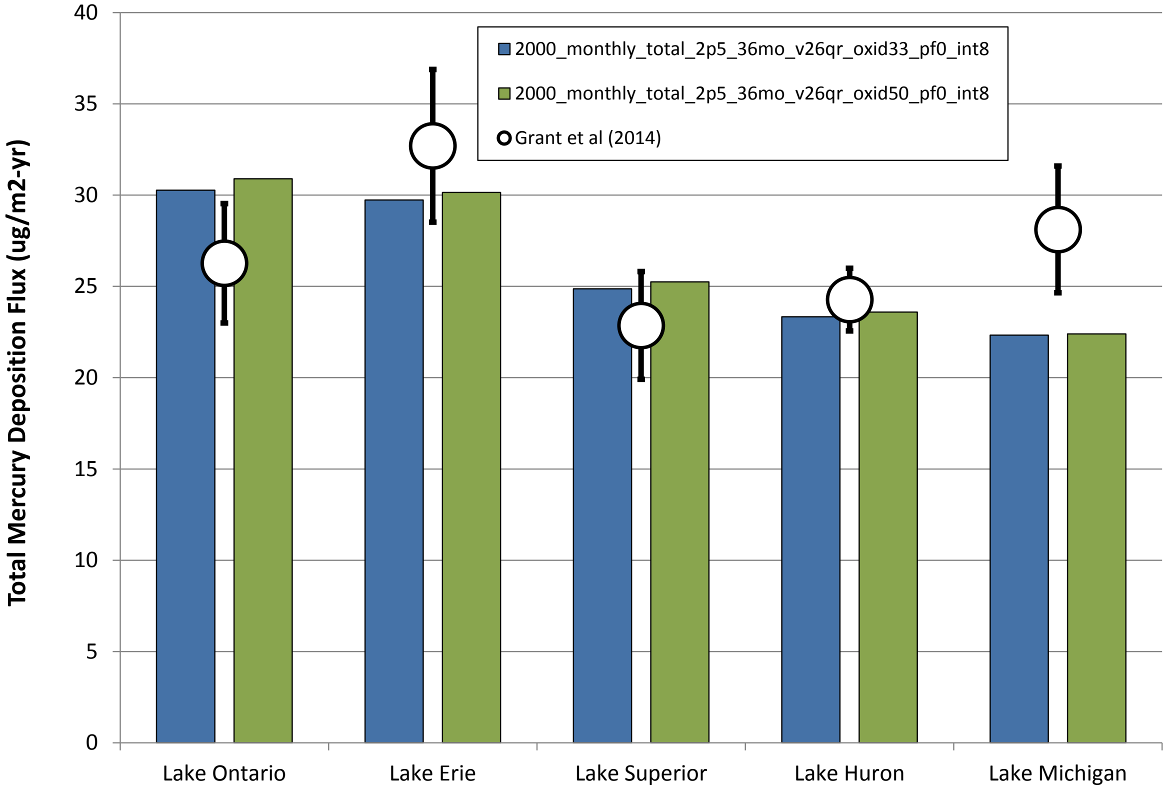

Figure 103. Comparison of modeling results with those of Grant *et al*. (2014) for Great Lakes mercury deposition

6.2. Inventory subset contributions to Great Lakes mercury deposition

As discussed above, independent simulations were carried out using the primary emissions inventory subsets -- anthropogenic, biomass, land, ocean, reemissions, and volcano – for the 2000 baseline and three 2050 future emissions scenarios, for both the “oxid33, pf0” and “oxid50, pf0” model configurations. This allows the contribution to Great Lakes mercury deposition from each of the different inventory subsets to be estimated. Figure 104 shows an example of these results for Lake Erie.

As a QA/QC check, the figure also shows the total deposition estimated from the comparable total-inventory simulation. The totals should match, and it can be seen that they indeed do match.

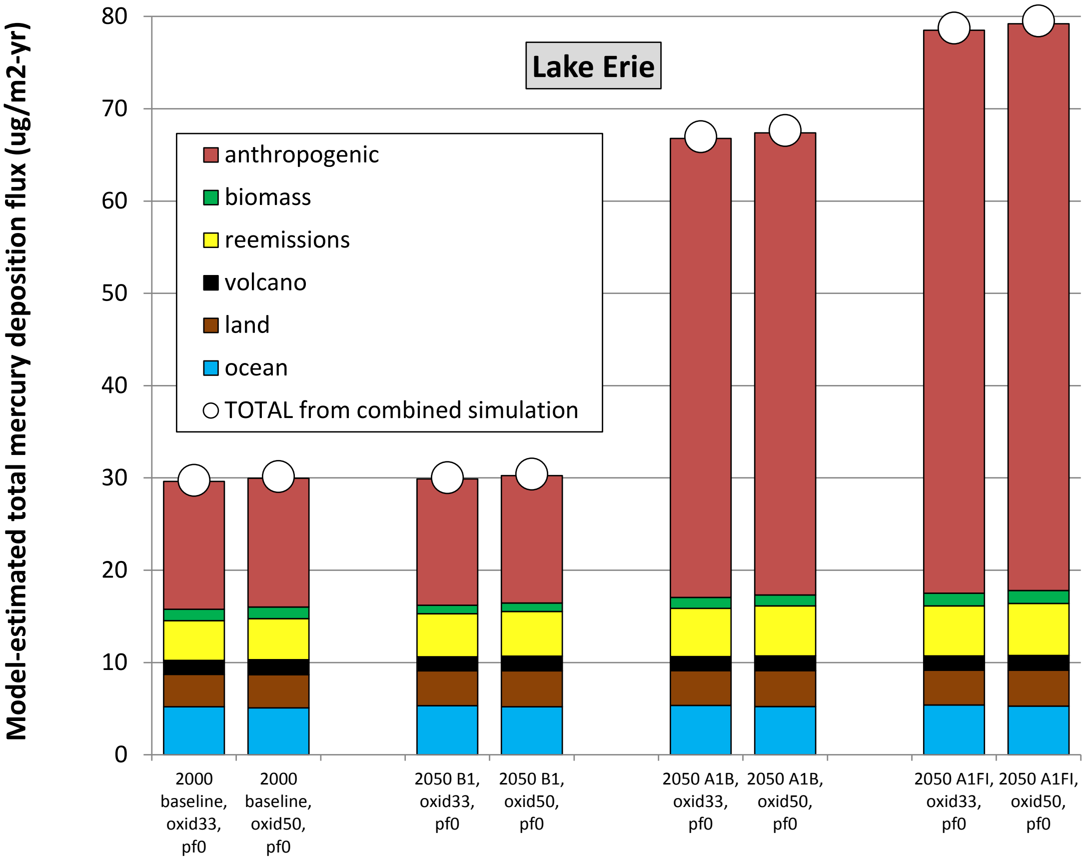

Figure 104. Inventory subset contributions to model-estimated mercury deposition to Lake Erie, compared with the results of the total-inventory simulation

Inventory subset contribution results for each of the Great Lakes are presented in Figure 105, Figure 107, Figure 109, Figure 111, and Figure 113. In addition, the percent of total modeled deposition contributed by each inventory subset are presented in Figure 106, Figure 108, Figure 110, Figure 112, and Figure 114, for each of the Great Lakes.

Several observations can be made regarding these results.

First, there is little difference between the results using the “oxid33, pf0” and the “oxid50, pf0” configurations, for any given inventory, for any inventory subset, for any lake. This is important, as it means that the uncertainty in atmospheric mercury’s chemical mechanism does not appear to introduce significant uncertainties in the source-attribution of deposition.

Second, the amounts contributed by the biomass, land, ocean, reemissions, and volcano subsets are very similar for all of the baseline and future scenario simulations carried out. This is not surprising given that the emissions in these subsets did not change significantly, as can be seen in Figure 5 (page 14) and Table 2 (page 13).

Third, the contribution from direct anthropogenic emissions did not change significantly between the 2000 baseline and the 2050 B1 future emissions scenario. This is expected, as the anthropogenic emissions in the two inventories are similar.

Fourth, the contributions from direct anthropogenic emissions increased dramatically, both in amount and percentage, for the 2050 A1B and 2050 A1FI future emissions scenarios, relative to the 2000 baseline and 2050 B1 scenario. This is expected, given the significant increase in anthropogenic emissions in these two scenarios, but the relative deposition contribution increase is disproportionally large, relative to the emissions increases. For example, anthropogenic emissions increased by a factor of ~2.0 and ~2.5, respectively, for the 2050 A1B and 2050 A1FI scenarios, relative to the 2000 baseline scenario, but, the model-estimated amounts contributed to Lake Erie increased by a factor of ~3.5 and ~4.5, respectively. This disproportionate impact is likely the result of two different factors: (a) the spatial distribution of emissions are increased disproportionately in the industrial regions surrounding the Great Lakes, and, (b) the fraction of Hg(II) emissions increases in the estimated A1B and A1FI anthropogenic inventories. Emitted Hg(II) has a greater local and regional impact than emissions of other mercury forms.

Fifth, the contribution from direct anthropogenic emissions, as a fraction of total model-estimated deposition, increased dramatically in the 2050 A1B and 2050 A1FI future scenarios relative to the 2000 baseline and 2050 B1 scenario. For Lake Erie, for example, the fraction increased from ~45% to ~75%. Even for the lake with the smallest contribution from direct anthropogenic emissions, Lake Superior, the fraction increased from ~28% to more than 50%. Other lakes showed increases in between those exhibited for Lake Erie and Lake Superior.

The overarching conclusion that can be drawn from the results presented in this section is that the future course of anthropogenic mercury emissions may have a very large impact on the atmospheric deposition of mercury to the Great Lakes.

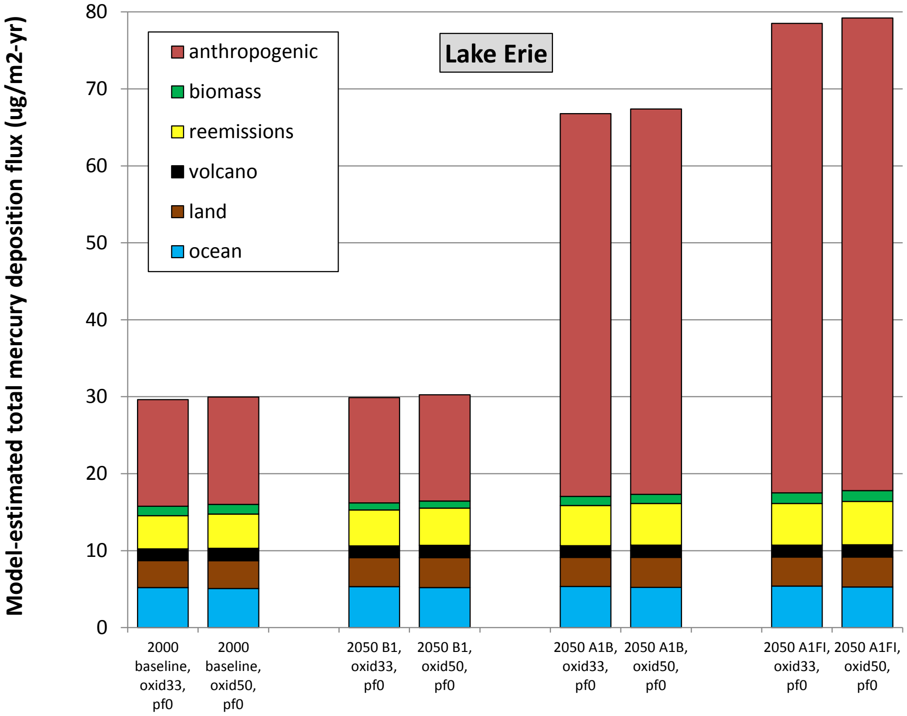

Figure 105. Inventory subset contributions to model-estimated mercury deposition to Lake Erie

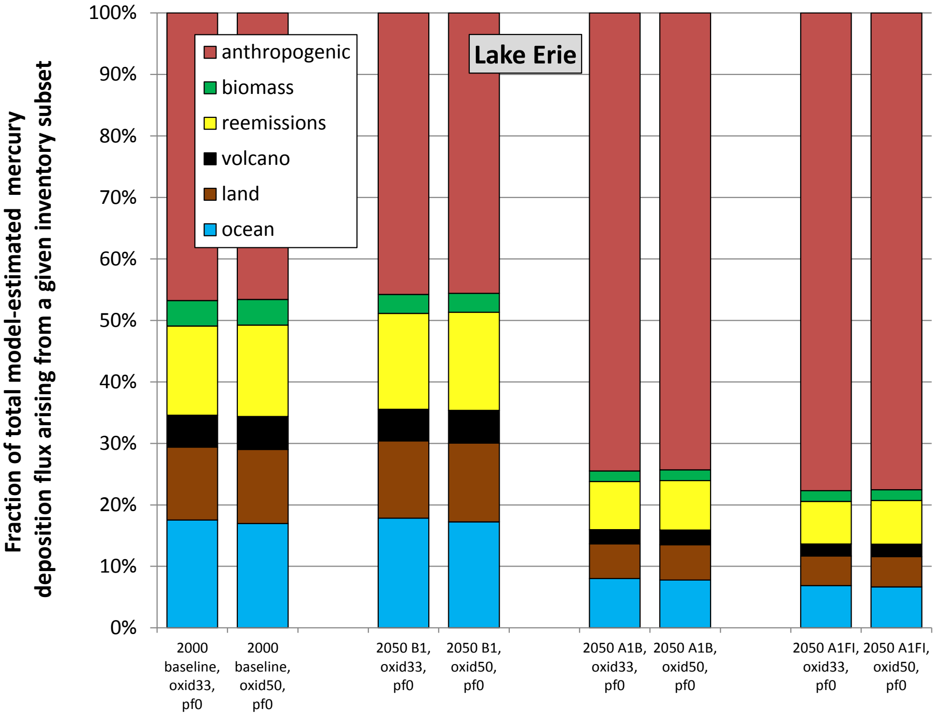

Figure 106. Percent of total deposition contributed by each Inventory subset to model-estimated mercury deposition to Lake Erie

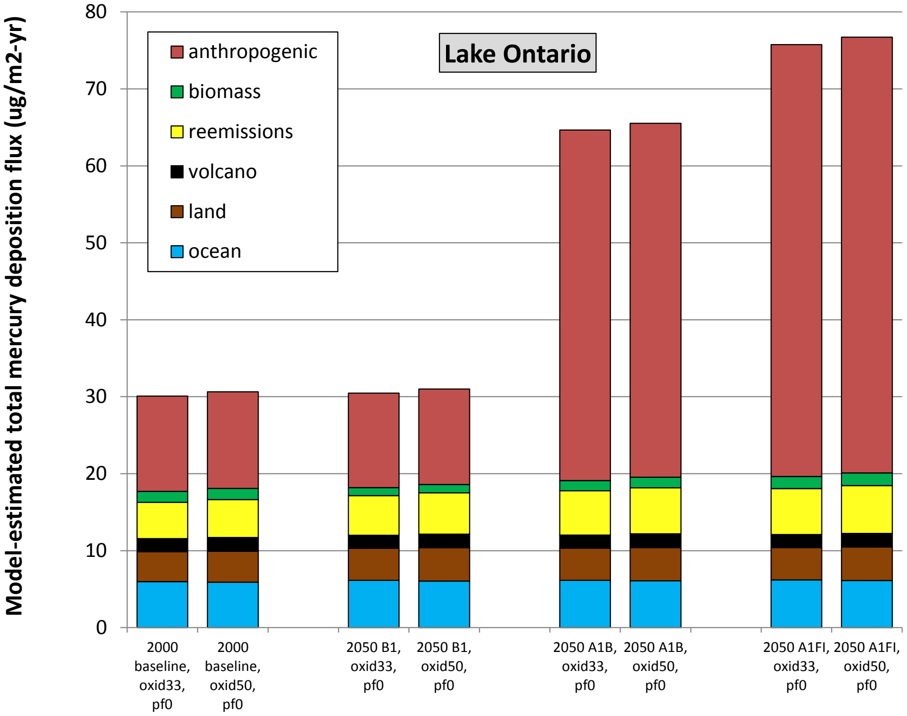

Figure 107. Inventory subset contributions to model-estimated mercury deposition to Lake Ontario

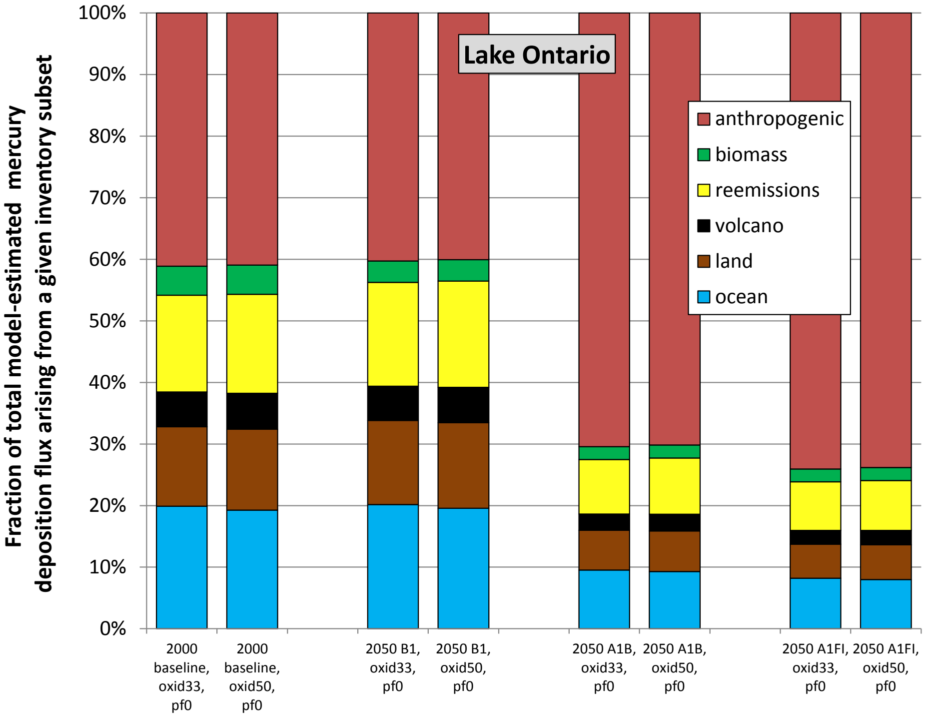

Figure 108. Percent of total deposition contributed by each Inventory subset to model-estimated mercury deposition to Lake Ontario

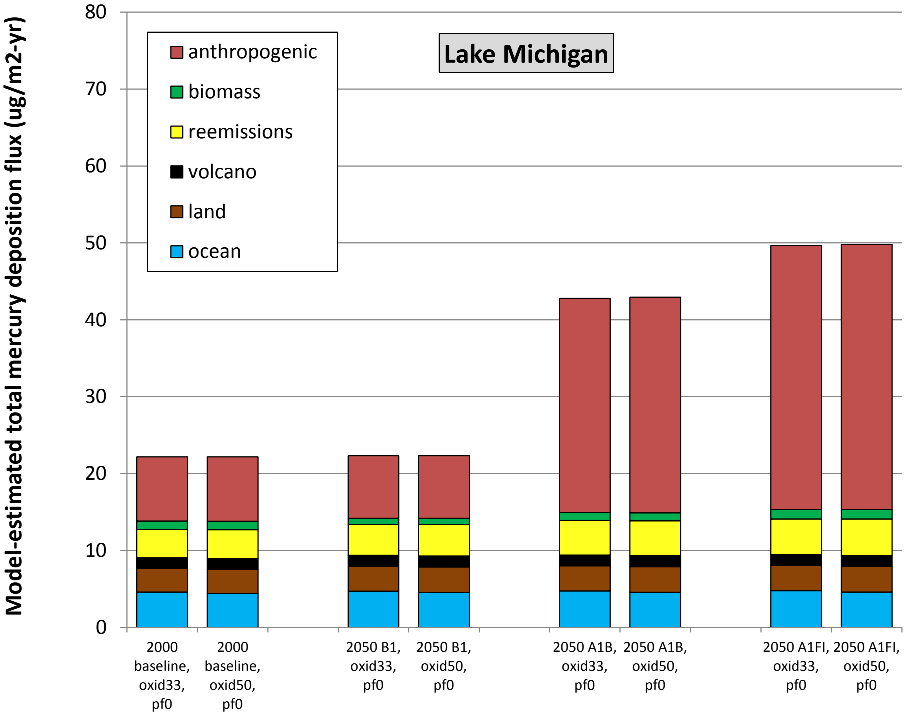

Figure 109. Inventory subset contributions to model-estimated mercury deposition to Lake Michigan

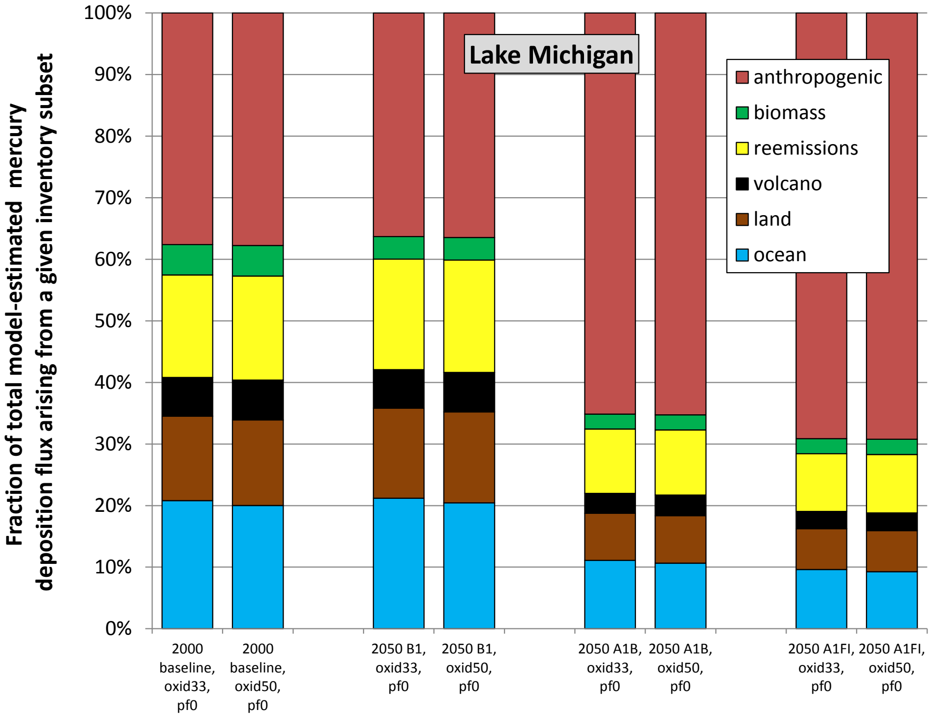

Figure 110. Percent of total deposition contributed by each Inventory subset to model-estimated mercury deposition to Lake Michigan

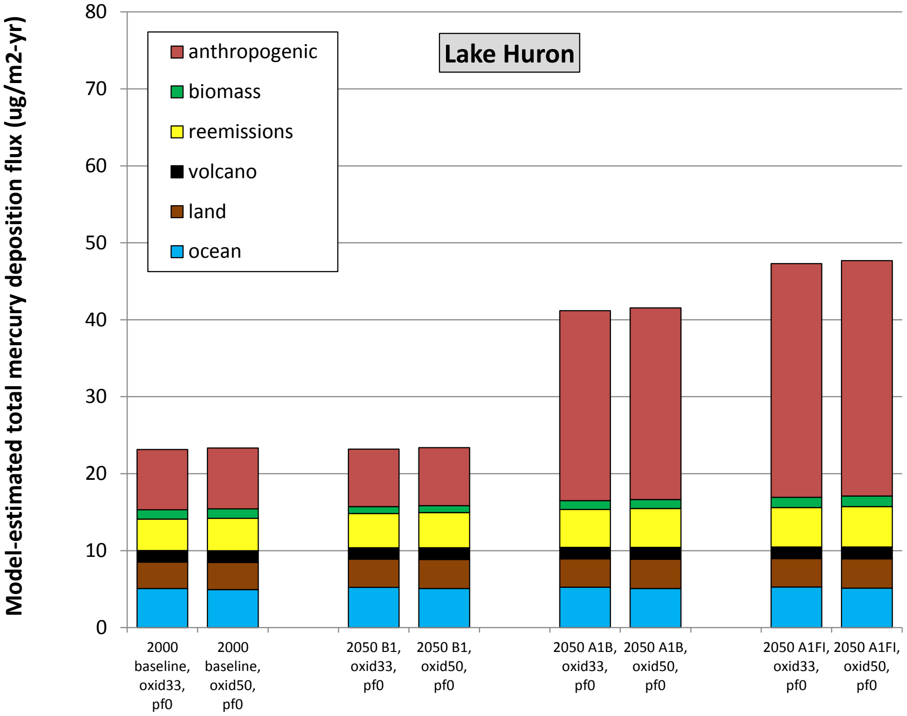

Figure 111. Inventory subset contributions to model-estimated mercury deposition to Lake Huron

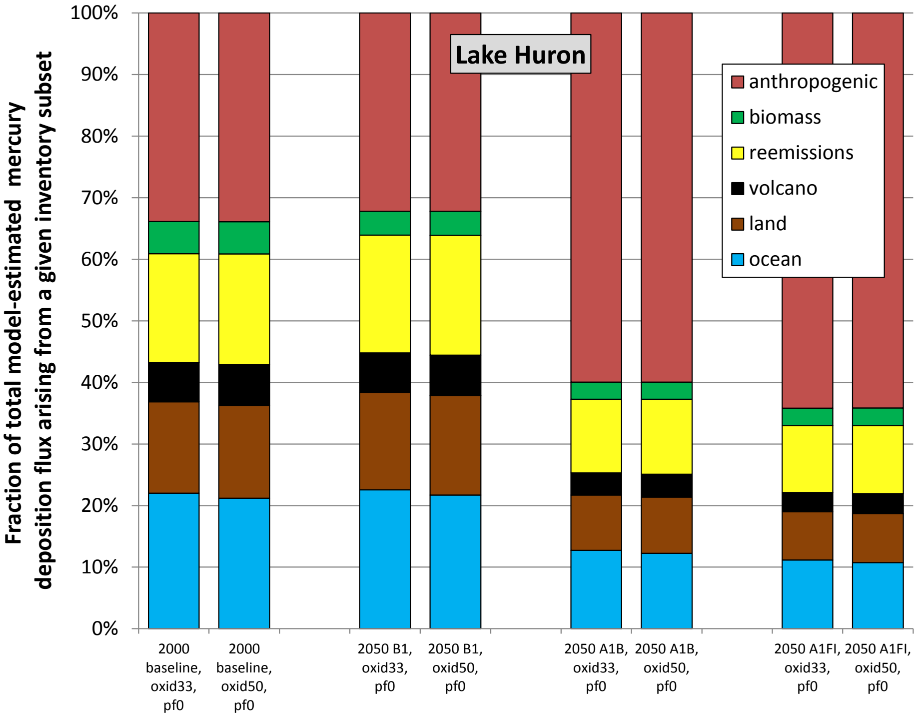

Figure 112. Percent of total deposition contributed by each Inventory subset to model-estimated mercury deposition to Lake Huron

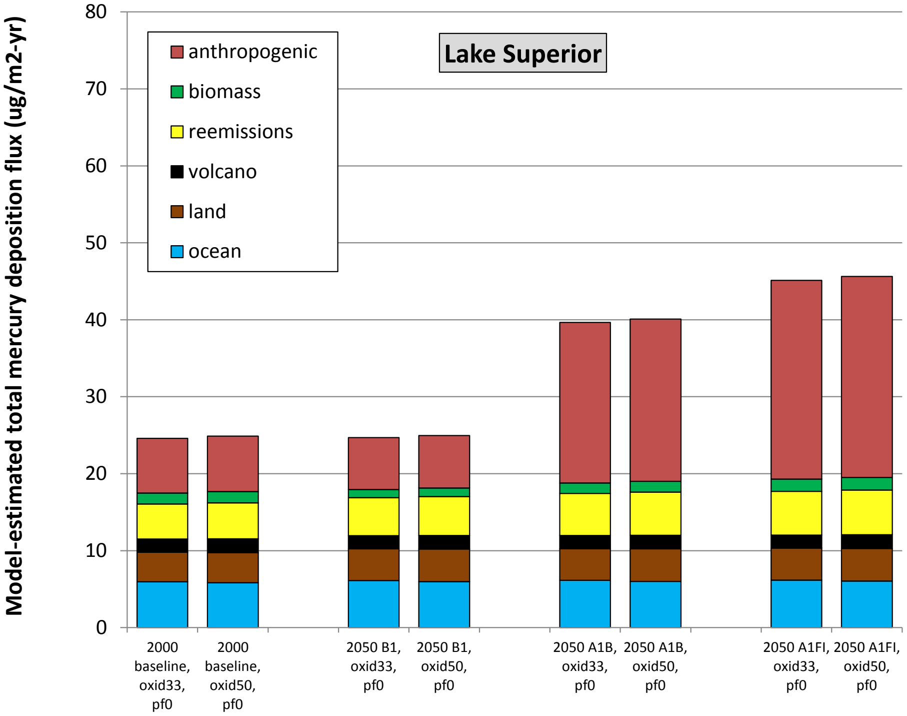

Figure 113. Inventory subset contributions to model-estimated mercury deposition to Lake Superior

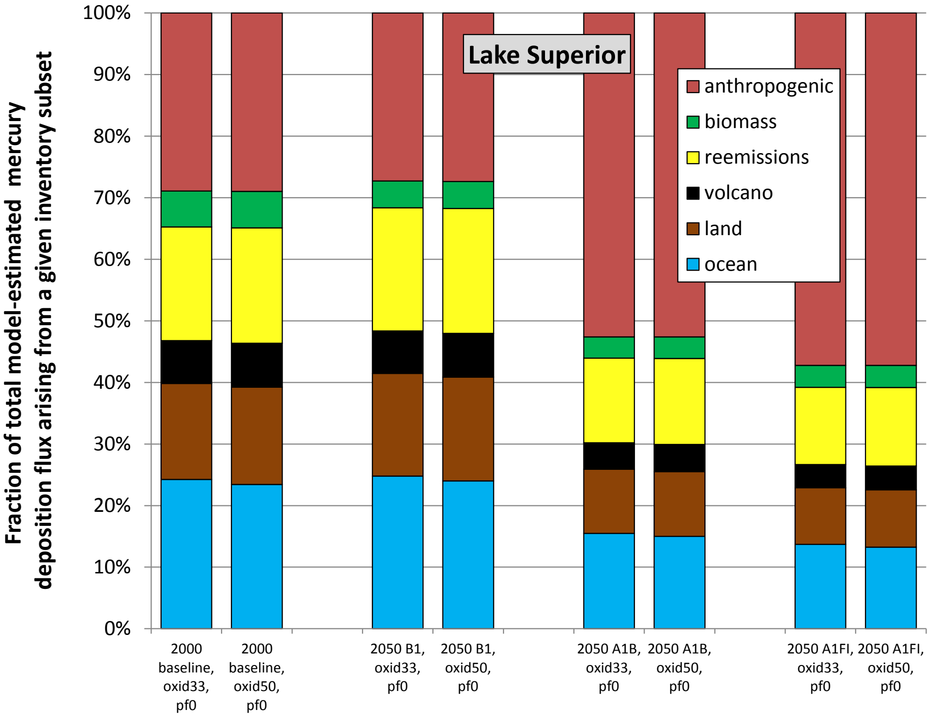

Figure 114. Percent of total deposition contributed by each Inventory subset to model-estimated mercury deposition to Lake Superior

6.3. Contributions to Great Lakes mercury deposition arising from country-specific direct anthropogenic emissions

As discussed above, independent simulations were carried out using country-specific subsets of the direct-anthropogenic emissions component of the 2000-baseline and future scenario emissions inventories. Separate simulations were carried out for such emissions from the United States, Canada, Mexico, China, India, Russia, and the “rest of the world” (“Other”).

Before presenting the results, it must be acknowledged that a number of uncertainties in these source-attribution results for the Great Lakes derive from the use of a relatively coarse 2.5° x 2.5° grid throughout the analysis. For perspective, the grid cells (Figure 115) and some examples of the gridded emissions in the Great Lakes region are shown below for Hg(0) (Figure 116) and Hg(II) (Figure 117 -- Figure 120).

One grid-related uncertainty is inherent in the assignment of anthropogenic emissions in a given cell to a given country, if the cell is on the border between two or more countries. As noted in in Section 2, an approximate apportionment procedure was employed that based the split in such cases on the comparable split between anthropogenic emissions in the much-finer-resolution 2005 inventory used in earlier phases of this project (Cohen *et al*., 2011, 2013).

Another grid-related uncertainty is associated with the fate and transport modeling itself being carried out on the coarse grid. Even if a grid cell’s emissions were “perfectly” apportioned between countries, a given country’s emissions for that grid cell would still be uniformly emitted over the entire cell. Put another way, the emitted mercury in any grid cell is immediately diluted over the entire grid cell after emission. This could lead to overestimates or underestimates of a given, real source’s impact, depending on whether the actual plume from the actual source would have impacted one or more of the Great Lakes or not. Examination of the gridded emissions figures below gives an initial sense of the potential significance of this issue.

These uncertainties are expected to be greatest in vicinity of the Great Lakes, as the scale discrepancies are greatest. Small uncertainties in the emissions location for a distant source, e.g., in China, would not be expected to have a big impact on the source’s impact on the Great Lakes. However, in the Great Lakes region, these locational uncertainties could have a big influence on the modeling results. For example, a source on the generally upwind side of a given lake would have a much different impact than the same source on the prevailing downwind side of the same lake. Since the countries bordering the Great Lakes are the USA and Canada, it must be recognized that the uncertainties introduced by the coarse-grid nature of the emissions apportionment and modeling are most significant for the estimates of source-attribution for these two countries.

The coarseness of the grid chosen was dictated in large part by limitations in the computational resources available for this project. In the future, it is hoped that sufficient computational resources will be available to employ a finer grid (e.g., 1° x 1°).

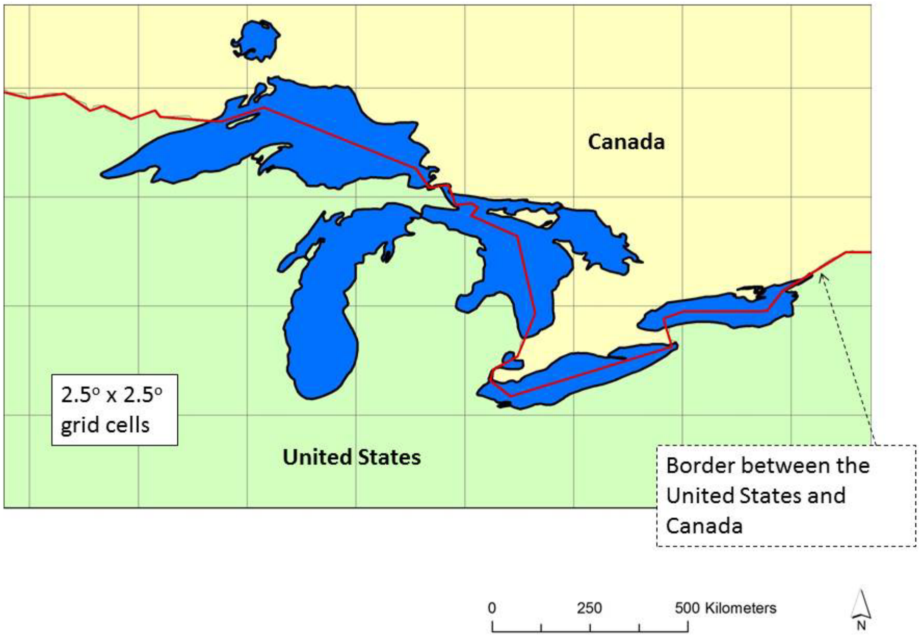

Figure 115. Grid cells in the Great Lakes region

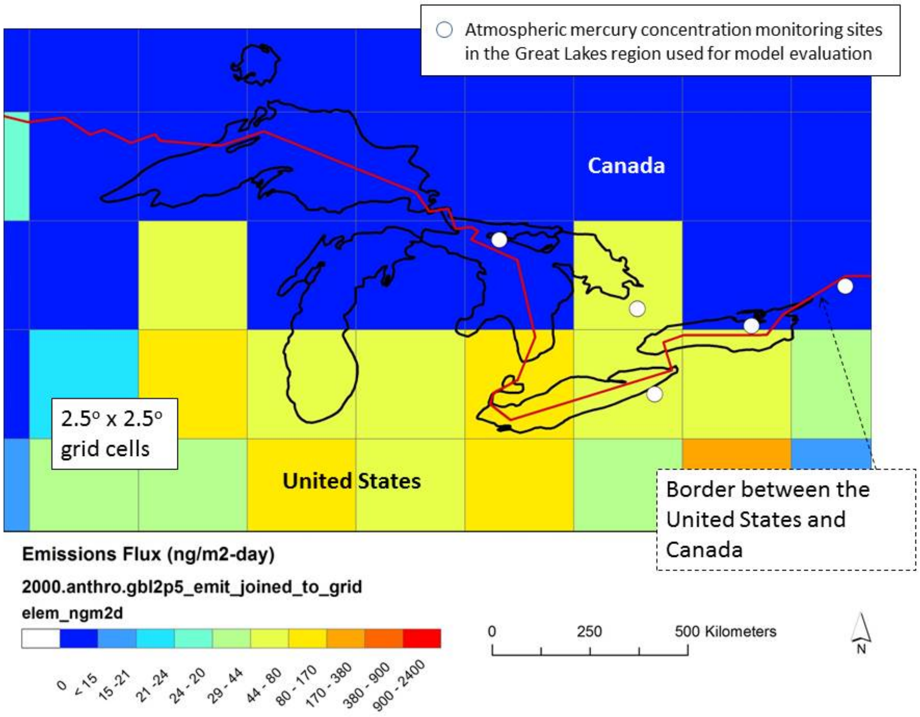

Figure 116. Emissions of Hg(0) in the 2000-baseline inventory from grid cells in the Great Lakes region

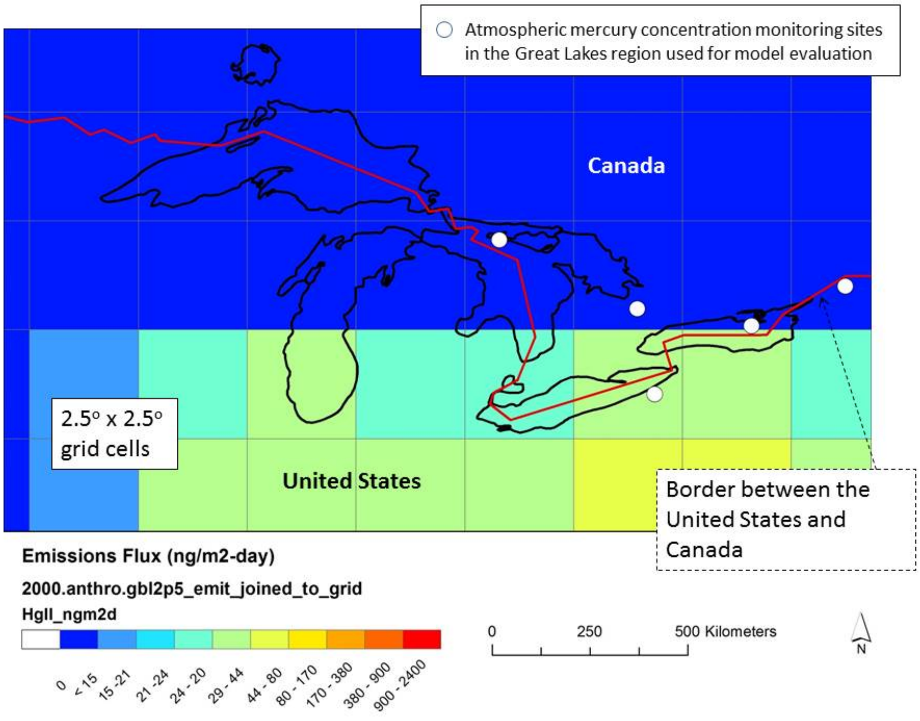

Figure 117. Emissions of Hg(II) in the 2000-baseline inventory from grid cells in the Great Lakes region

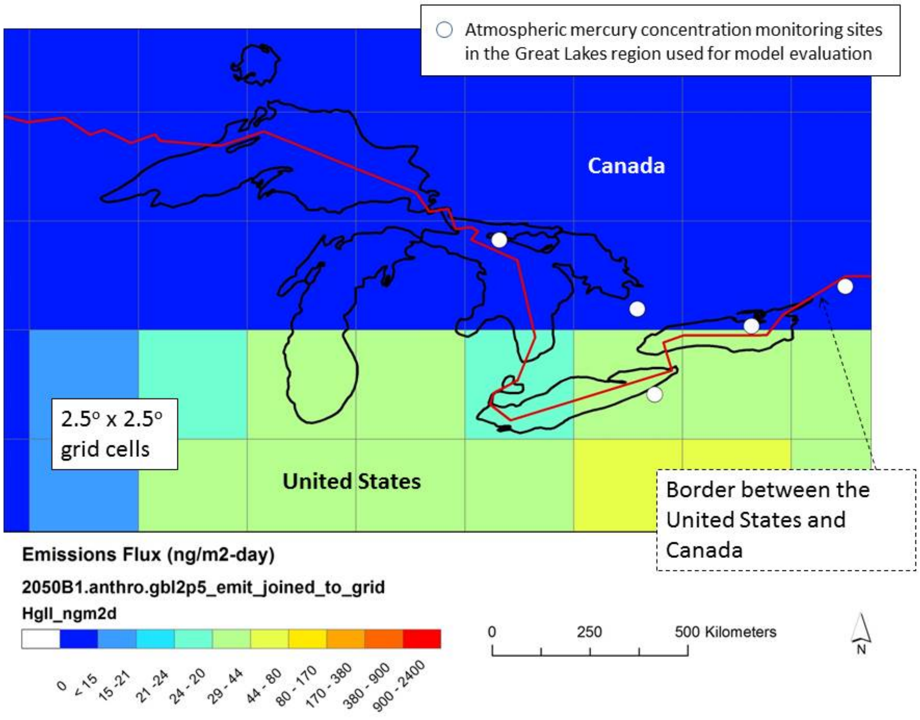

Figure 118. Emissions of Hg(II) in the 2050 B1 scenario inventory from grid cells in the Great Lakes region

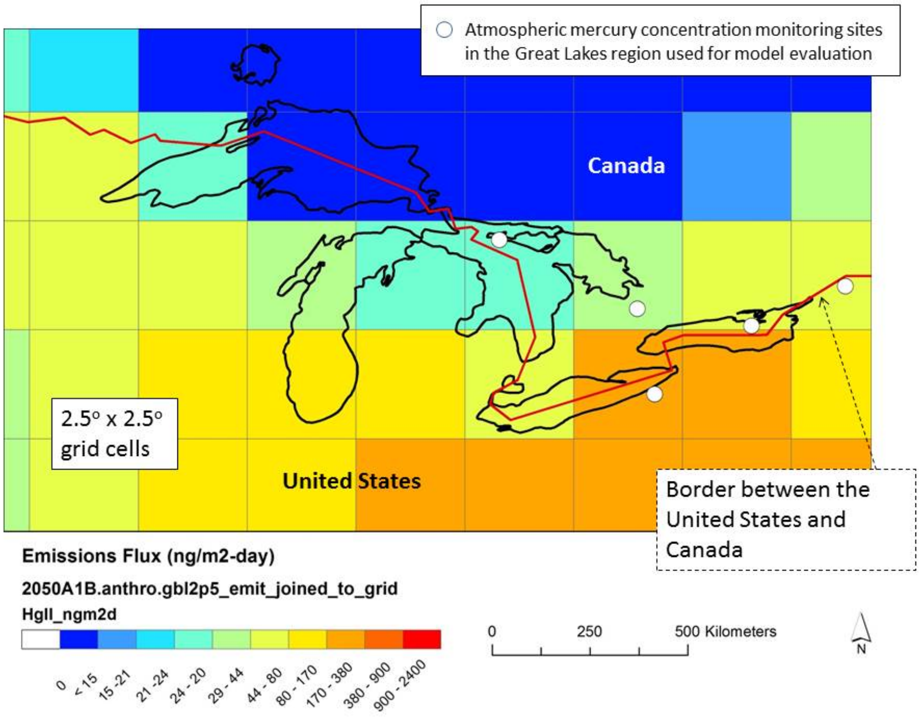

Figure 119. Emissions of Hg(II) in the 2050 A1B scenario inventory from grid cells in the Great Lakes region

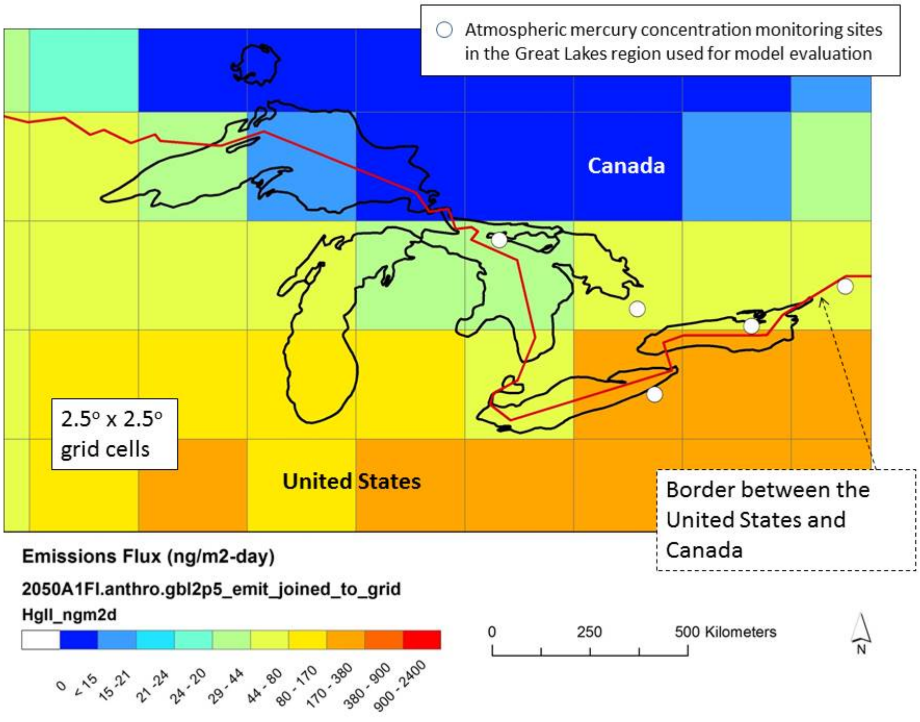

Figure 120. Emissions of Hg(II) in the 2050 A1FI scenario inventory from grid cells in the Great Lakes region

Subject to the above limitations, these country-specific simulations were carried out for the 2000 baseline and three 2050 future emissions scenarios, for both the “oxid33, pf0” and “oxid50, pf0” model configurations. This allows the contribution to Great Lakes mercury deposition from different countries to be compared. Figure 121 shows an example of these results for Lake Erie. As a QA/QC check, the figure also shows the total deposition estimated from the comparable total-direct-anthropogenic inventory simulation, i.e., the “anthropogenic” subset results presented in the previous section. The totals should match, and it can be seen that they indeed do match.

As an alternative to the “stacked bar” plot shown in Figure 121, individual bars for each selected country are shown in Figure 122, using a linear scale. In order to see the details of the lower-contributing countries, the same data are shown with a logarithmic scale in Figure 123. Comparable graphs are shown for the other Great Lakes in Figure 124, Figure 125, Figure 126, and Figure 127.

Several observations can be made regarding these results.

First, there is little difference between the results using the “oxid33, pf0” and the “oxid50, pf0” configurations, for any given inventory, for any country, for any lake. This is important, as it means that the uncertainty in atmospheric mercury’s chemical mechanism does not appear to introduce significant uncertainties in the source-attribution of deposition.

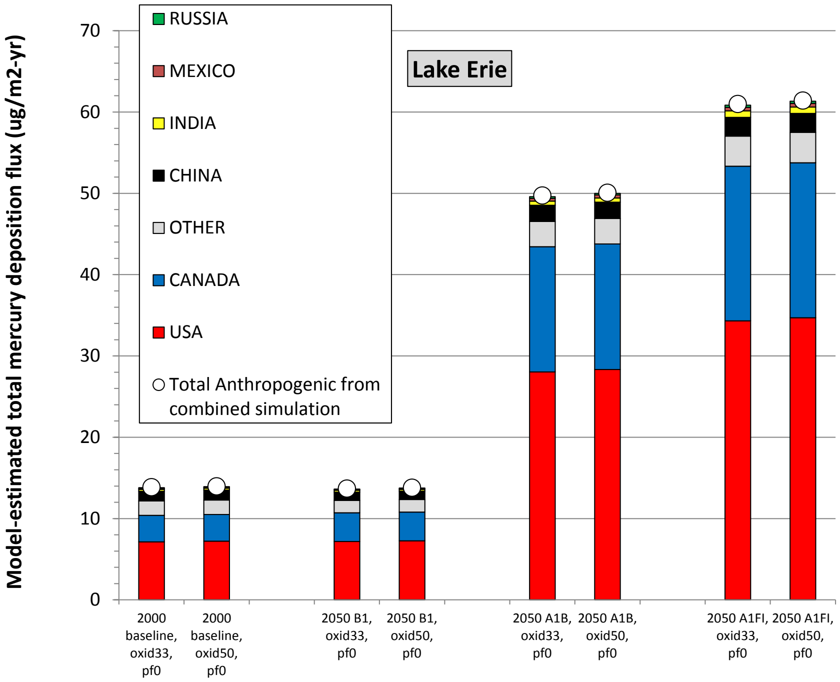

Figure 121. Contribution to Lake Erie mercury deposition arising from country-specific direct anthropogenic emissions, compared to deposition with a comparable, combined direct-anthropogenic emissions inventory

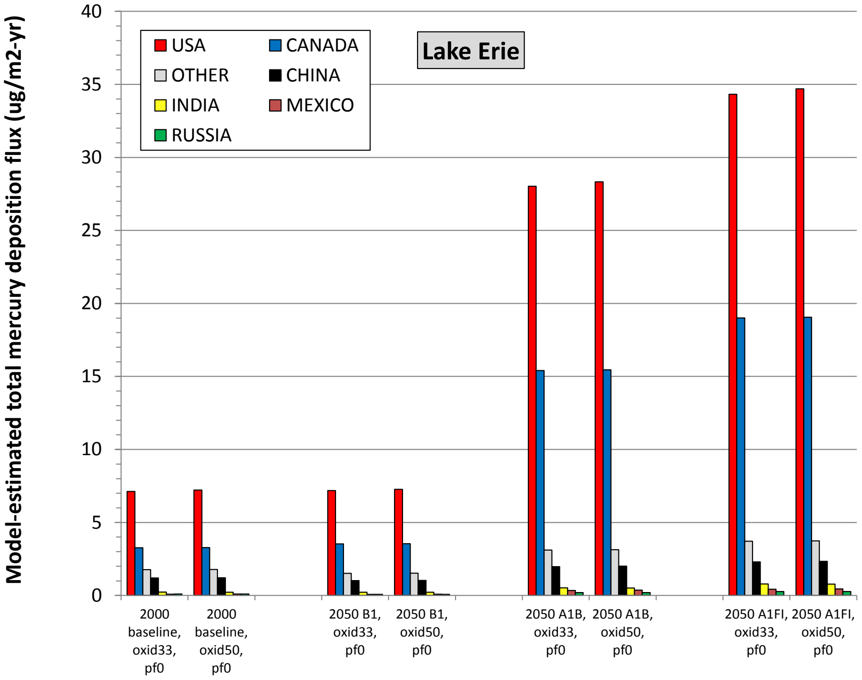

Figure 122. Contribution to Lake Erie mercury deposition arising from country-specific direct anthropogenic emissions (linear scale)

Second, the contribution from direct anthropogenic emissions did not change significantly between the 2000 baseline and the 2050 B1 future emissions scenario for any given country. This is expected, as the anthropogenic emissions in the two inventories are similar.

Third, as could be anticipated from the combined direct-anthropogenic results discussed in the previous section, the contributions from direct anthropogenic emissions for each country increased dramatically, both in amount and percentage, for the 2050 A1B and 2050 A1FI future emissions scenarios, relative to the 2000 baseline and 2050 B1 scenario.

Fourth, according to this model analysis, the United States appears to generally contribute the largest fraction of atmospheric deposition arising from direct anthropogenic emissions. The fractional amounts for each of the Great Lakes and for each configuration and country are presented in Figure 128, Figure 129, Figure 130, Figure 131, and Figure 132. It can be seen, for example, that according to these model estimates, the USA contributes on the order of 50-60% of this deposition to Lake Erie, Lake Ontario, and Lake Huron, about 60-75% to Lake Michigan, and about 40-55% to Lake Superior. The fractions attributable to the USA generally increase with the higher-emission future scenarios (2050 A1B and 2050 A1FI), i.e., are at the high end of these ranges, compared to the 2000 baseline and 2050 B1 emissions, with USA-attributable fractions at the low end of these ranges.

Fifth, according to this model analysis, Canada contributes the second largest fraction of atmospheric deposition arising from direct anthropogenic emissions, to Lake Erie and Lake Ontario (contributing from 15-30%), while China contributes the 2nd largest fraction to Lake Michigan and Lake Superior. For Lake Huron, the contributions from Canada and China are mixed: China contributes more with the 2000 baseline and 2050 B1 inventories, but Canada contributes a higher fraction with the 2050 A1B and 2050 A1FI scenarios. The higher relative contribution of Canada to Lakes Erie and Ontario is consistent with the spatial distribution of emissions in Canada, with a higher emissions density in the region of these two Great Lakes. Analysis by Temme *et al*. (2007) of mercury air concentration data in Canada over the 10-year period from 1996-2005 found that atmospheric concentrations of Total Gaseous Mercury (TGM) declined at several sites in Canada. It was found that the largest decreases occurred at sites closest to large urban areas: Point Petre, near Toronto, where TGM levels declined by 17% and St. Anicet, near Montreal, where TGM levels fell by 13%. Emissions in Canada (and the USA) declined significantly over this time period, while emissions in China and other regions in Asia are believed to have increased significantly (e.g., Pirrone *et al*., 2010). This supports the finding here that Canadian emissions may make a significant contribution to mercury levels in the Great Lakes region, potentially even larger than the impact from China for Lakes Ontario and Erie, the lakes closest to the largest industrial and population centers in Canada.

India generally contributes on the order of ~2%, Russia about ~1%, and Mexico about ~1%. The “other” category, i.e., all other countries besides those with explicit estimates, generally accounts for about 20% of the direct anthropogenic deposition arising from the 2000 baseline and the 2050 B1 inventories, but only about 10% of that arising from the 2050 A1B and 2050 A1FI inventories. The decrease in the higher-emissions future inventories is a direct result of the significant increases attributable to the USA and Canada in those higher-emissions inventories. The higher relative contributions of the USA and Canada in those higher-emissions future scenarios is due to the increased emissions of Hg(II) in those scenarios, which has a larger local and regional deposition impact.

The overarching conclusion that can be drawn from the results presented in this section is that the USA has the largest impact on the Great Lakes, while Canada and China also have significant impacts, with the relative importance varying among different lakes and emissions scenarios.

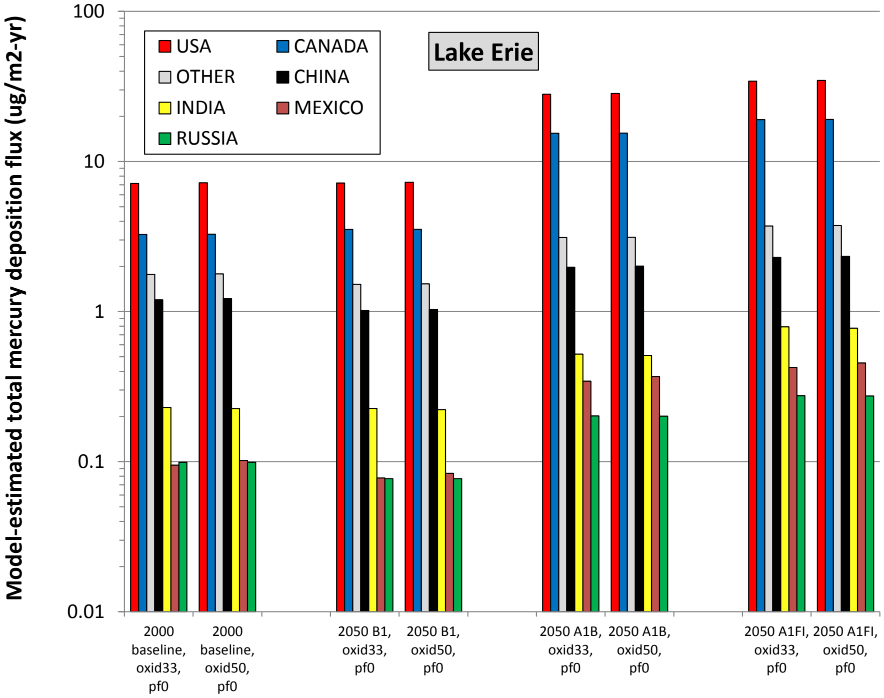

Figure 123. Contribution to Lake Erie mercury deposition arising from country-specific direct anthropogenic emissions (logarithmic scale)

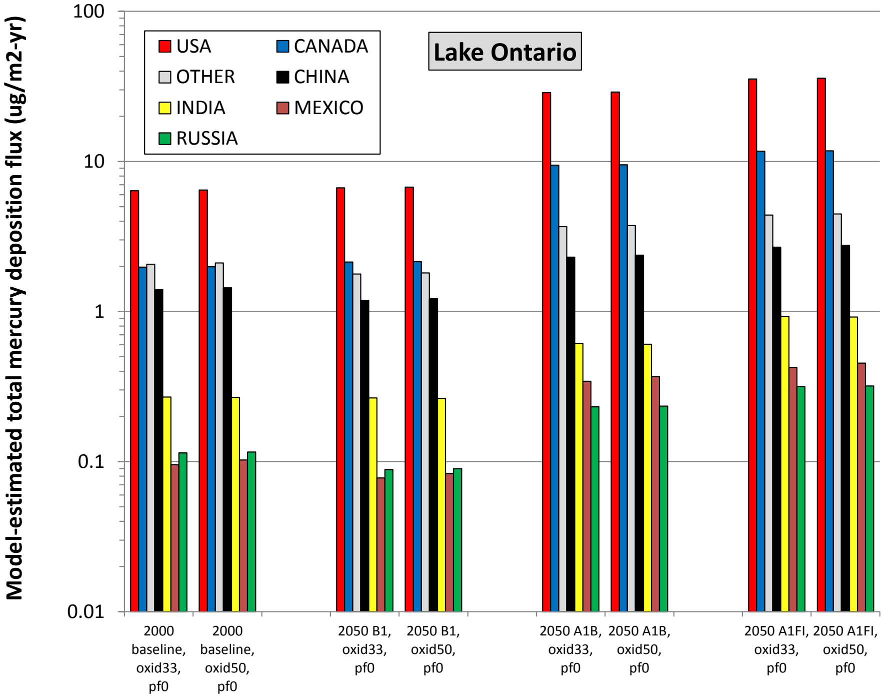

Figure 124. Contribution to Lake Ontario mercury deposition arising from country-specific direct anthropogenic emissions

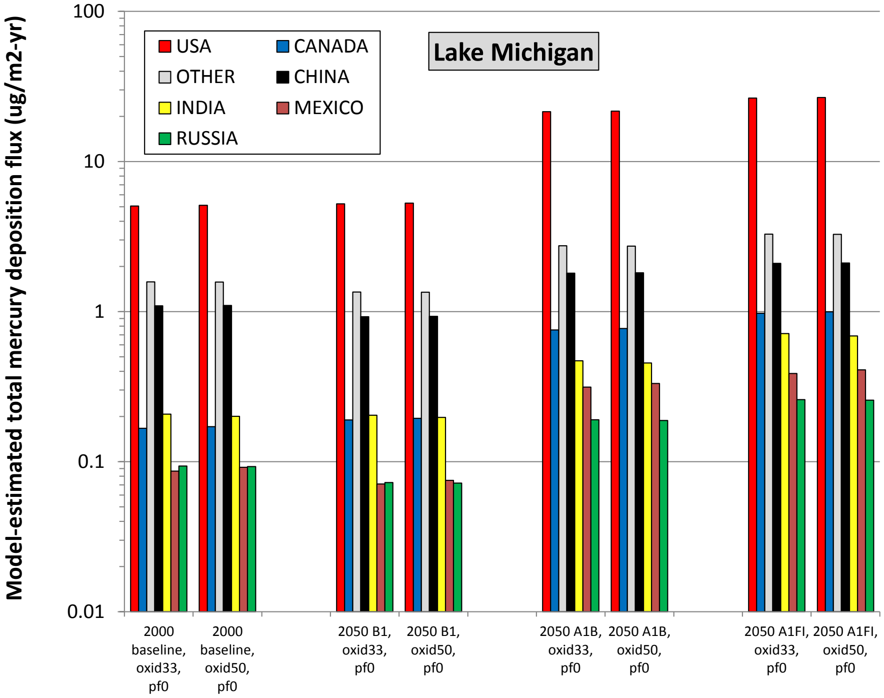

Figure 125. Contribution to Lake Michigan mercury deposition arising from country-specific direct anthropogenic emissions

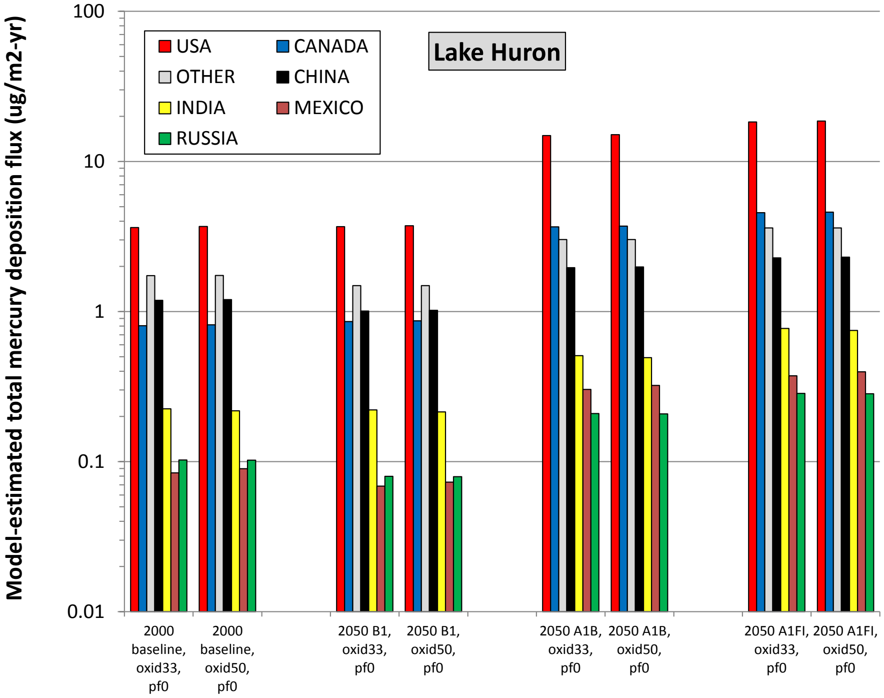

Figure 126. Contribution to Lake Huron mercury deposition arising from country-specific direct anthropogenic emissions

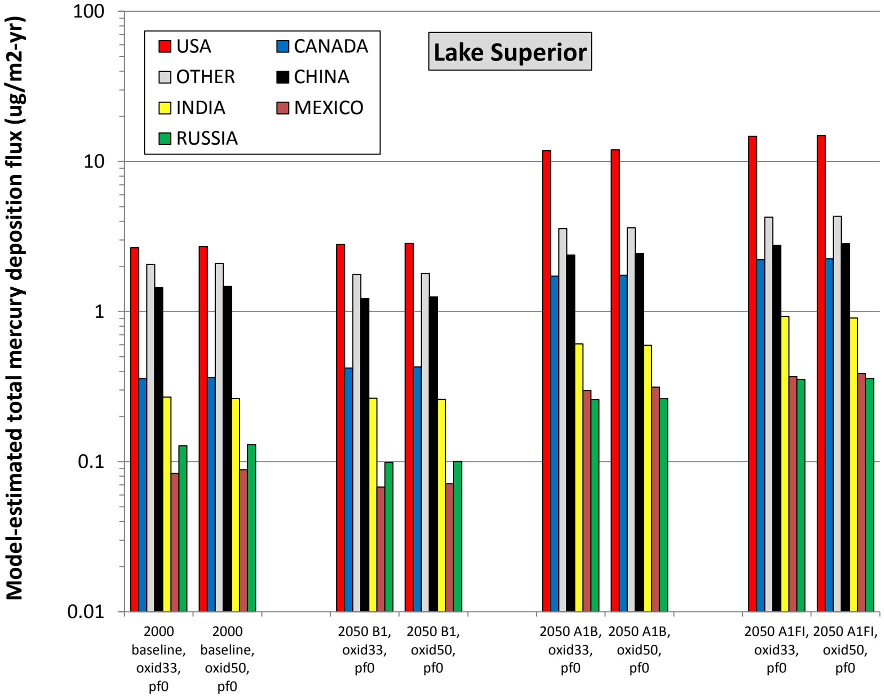

Figure 127. Contribution to Lake Superior mercury deposition arising from country-specific direct anthropogenic emissions

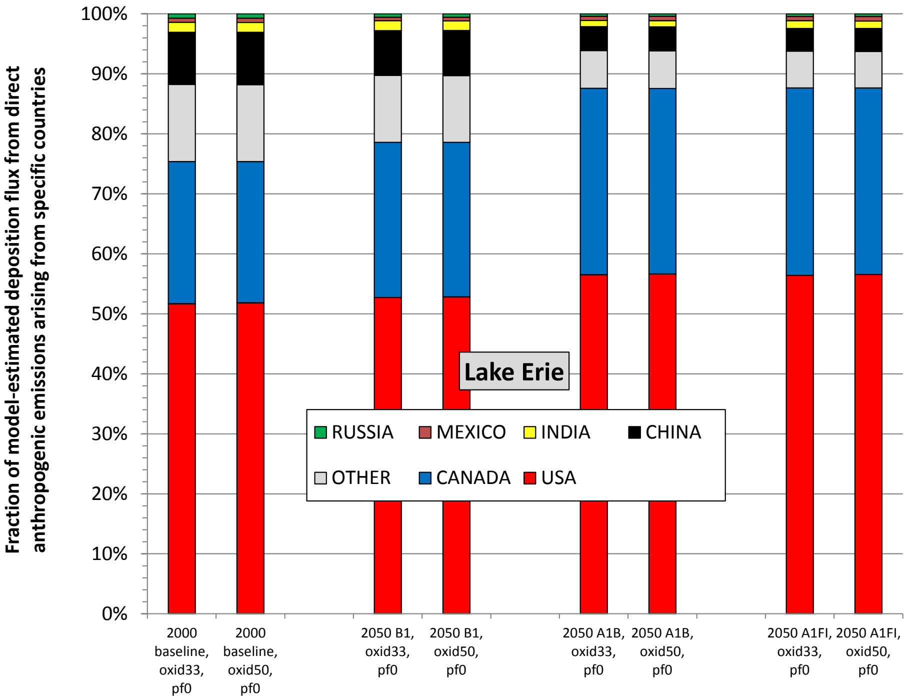

Figure 128. Fraction of model-estimated deposition flux to Lake Erie from direct anthropogenic emissions arising from specific countries

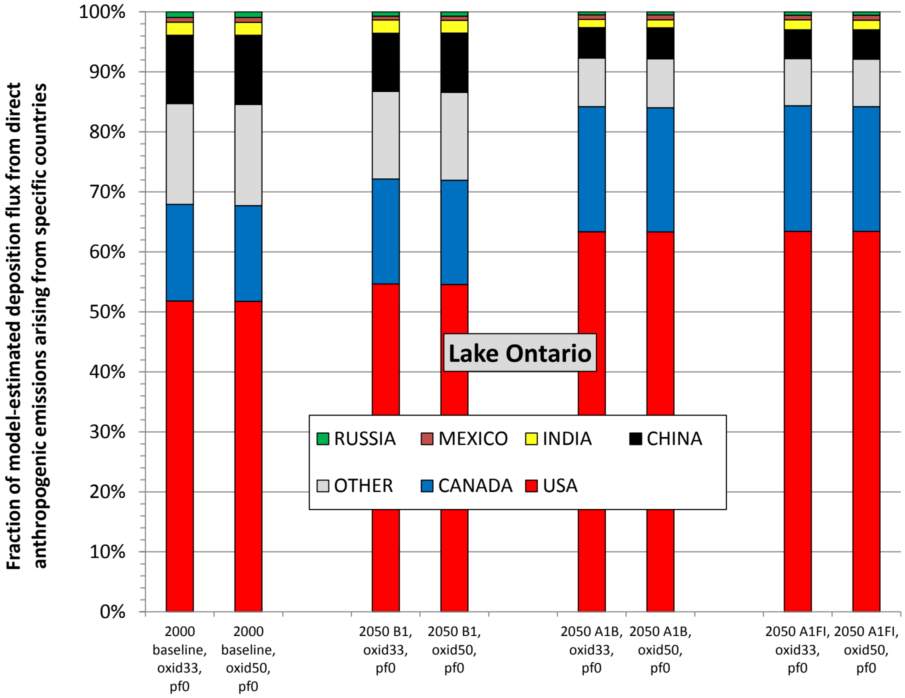

Figure 129. Fraction of model-estimated deposition flux to Lake Ontario from direct anthropogenic emissions arising from specific countries

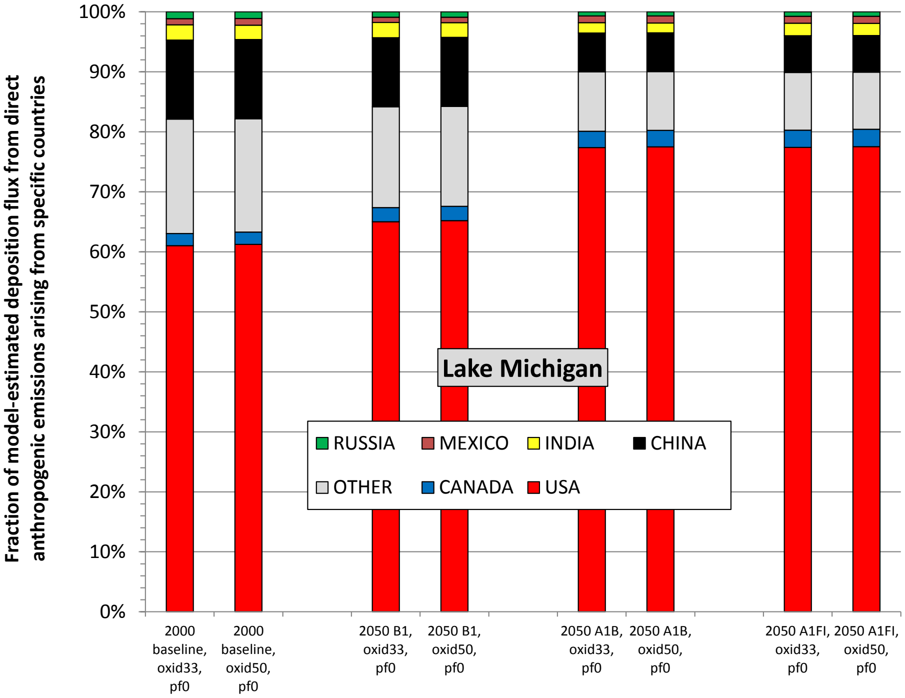

Figure 130. Fraction of model-estimated deposition flux to Lake Michigan from direct anthropogenic emissions arising from specific countries

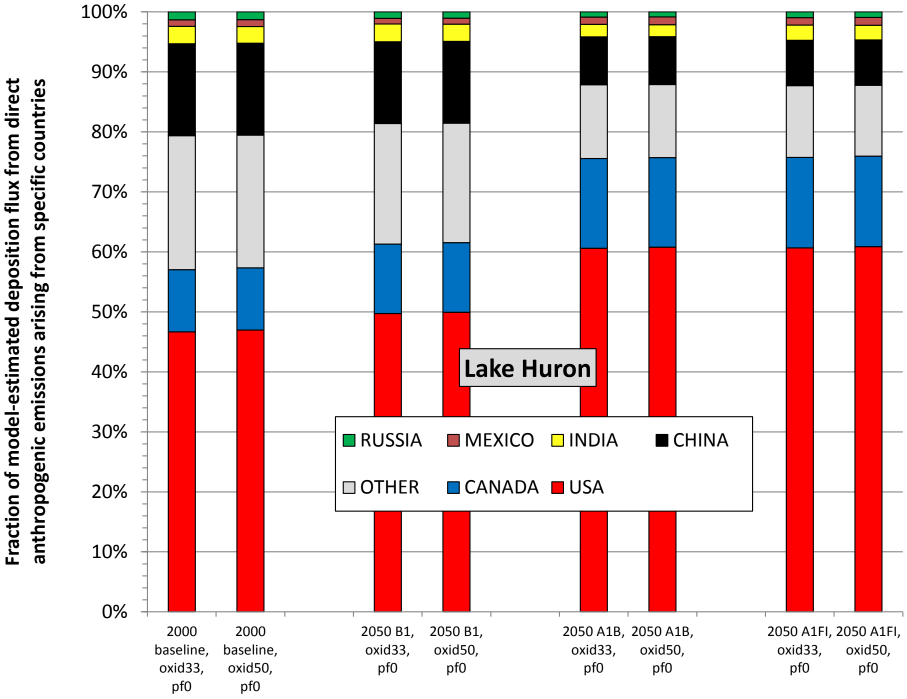

Figure 131. Fraction of model-estimated deposition flux to Lake Huron from direct anthropogenic emissions arising from specific countries

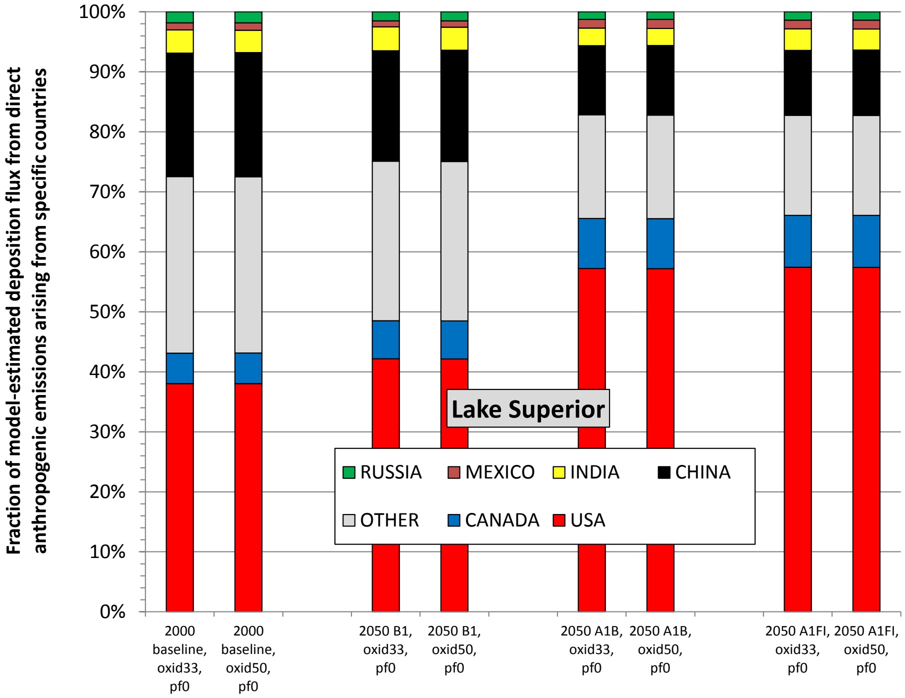

Figure 132. Fraction of model-estimated deposition flux to Lake Superior from direct anthropogenic emissions arising from specific countries

6.4. Synthesis of deposition and source-attribution results for atmospheric mercury deposition to the Great Lakes

The results presented in the previous sections have been combined to produce an overall synthesis of these modeling estimates. Since the contributions from three of the explicitly modeled countries (India, Russia, and Mexico) were relatively small compared to that from the USA, Canada, and China, they have been lumped together with the "Other" direct anthropogenic emissions. So, in the results presented in this section, there are explicit results for the USA, Canada, and China, and for the "rest of the world". These country-specific results are combined with the earlier inventory subset results for biomass burning, land, ocean, reemissions, and volcano to create an overall picture of source-attribution for atmospheric mercury deposition to the Great Lakes.

These combined results are presented for each of the Great Lakes in the figures below, in two different ways. For each lake, there is one plot showing the model-estimated source-attribution results for the deposition amount (μg/m^2-yr), e.g., Figure 133 for Lake Erie, and one plot showing the same results as a percentage of the total model estimated deposition for any particular overall configuration, e.g., Figure 134 for Lake Erie.

The observations that can be made about these results are of course similar to those made in the sections above. The value in these figures is that they show the relative importance of country-specific emissions – for the USA, Canada, and China – compared to other sources of atmospheric mercury deposition to the Great Lakes.

For Lake Erie, Lake Ontario, and Lake Michigan, these model-based estimates show that that direct anthropogenic emissions from the USA contribute the largest amount of atmospheric mercury deposition, on the order of ~20% of the total for the 2000 baseline and 2050 B1 inventories, and on the order of ~40% for the 2050 A1B and 2050 A1FI scenarios. For Lake Huron and Lake Superior, the contribution from direct anthropogenic emissions in the USA are smaller, on the order of 10-15% in the 2000 baseline and 2050 B1 inventories, and on the order of ~30% in the 2050 A1B and 2050 A1FI inventories. For these last two scenarios, USA's contribution was the highest of all the tabulated contributions.

These results suggest that the contribution of Canadian emissions to Great Lakes atmospheric mercury deposition may be higher than that of China for Lake Ontario and Lake Erie, but less than China's contribution for Lake Michigan and Lake Superior. For Lake Huron, the relative contributions are mixed, depending on the scenario. For the 2000 and 2050 B1 scenarios, they have roughly equal contribution. However, the significantly increased emissions in the 2050 A1B and 2050 A1FI scenarios, including increased Hg(II) emissions in the Great Lake region, result in a higher relative impact of Canadian emissions compared the other Great Lakes.

It is important remember that these source-attribution results for the USA and Canada are likely more uncertain than those for other countries, due to the grid-related uncertainties discussed in the previous section.

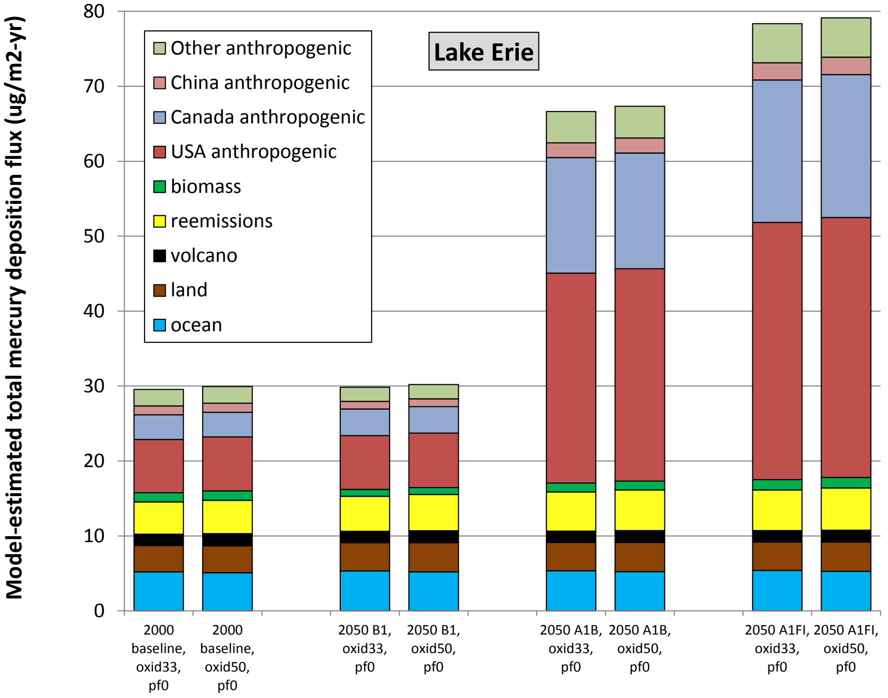

Figure 133. Overall source-attribution synthesis for deposition flux amounts for Lake Erie

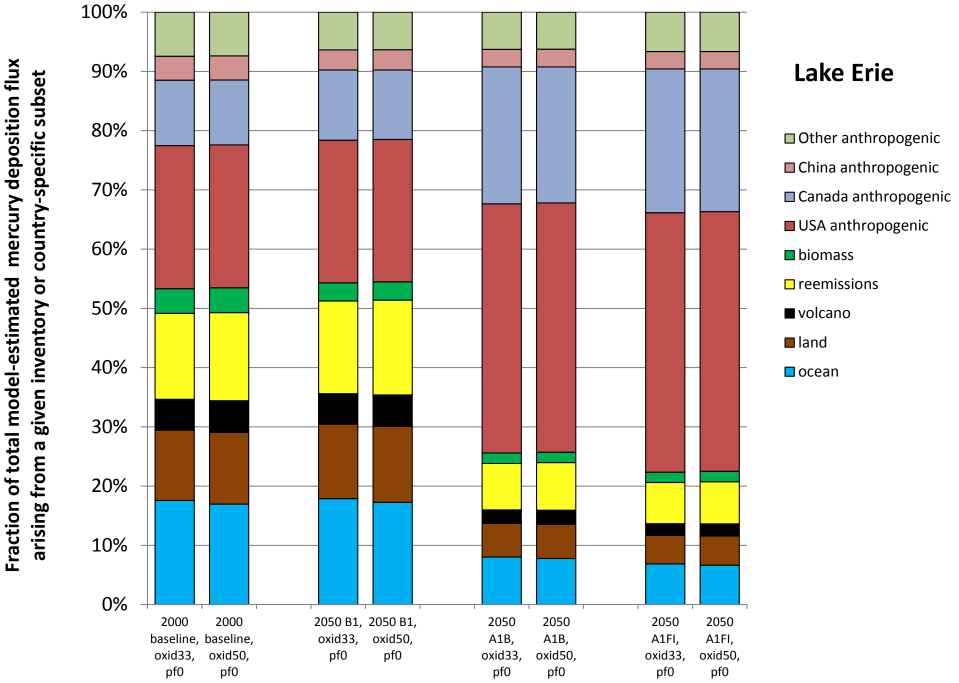

Figure 134. Overall source-attribution synthesis for deposition flux percentages for Lake Erie

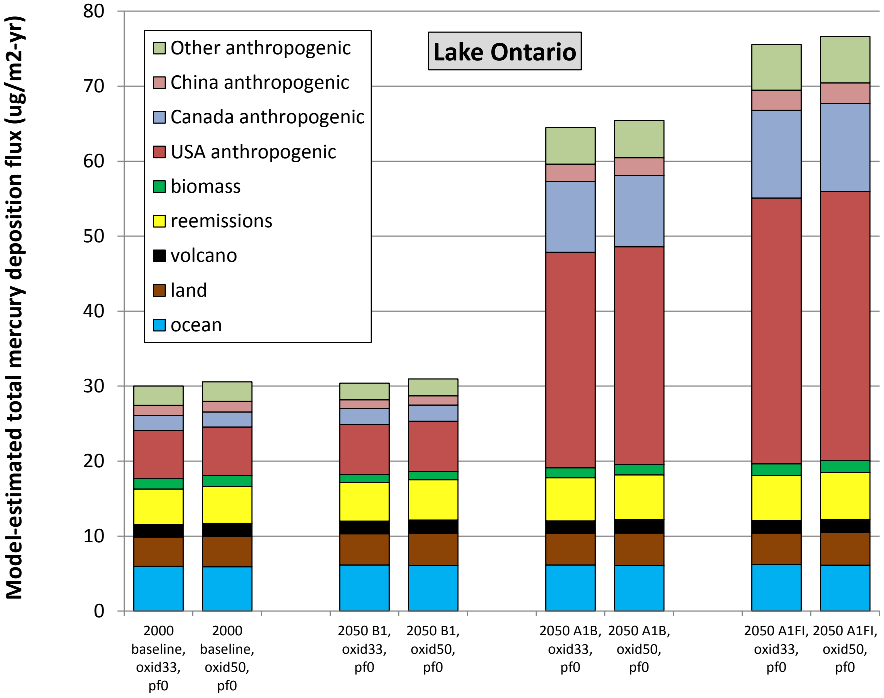

Figure 135. Overall source-attribution synthesis for deposition flux amounts for Lake Ontario

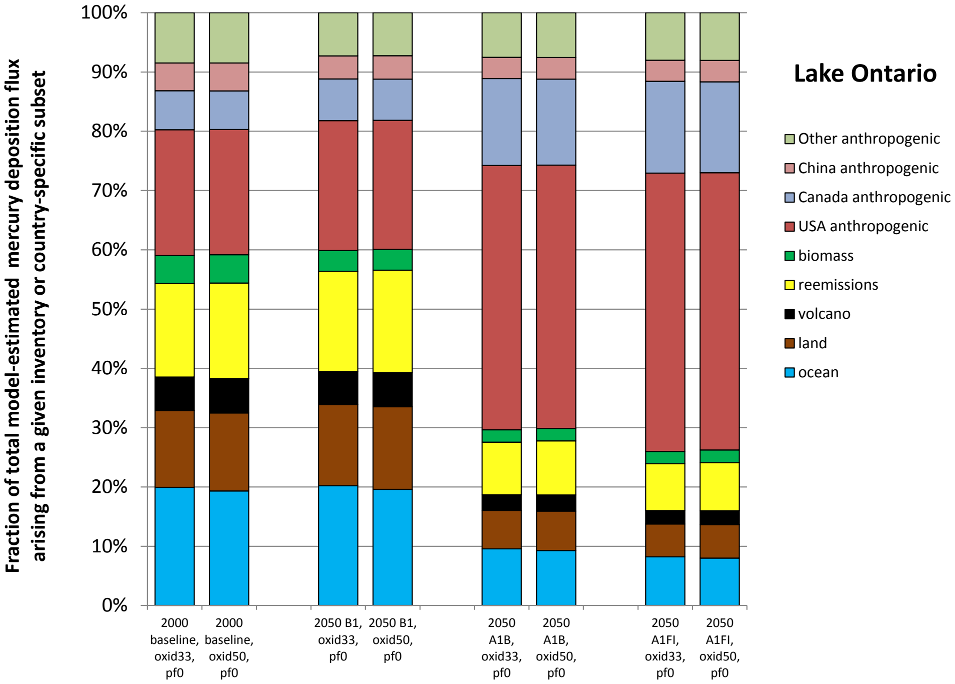

Figure 136. Overall source-attribution synthesis for deposition flux percentages for Lake Ontario

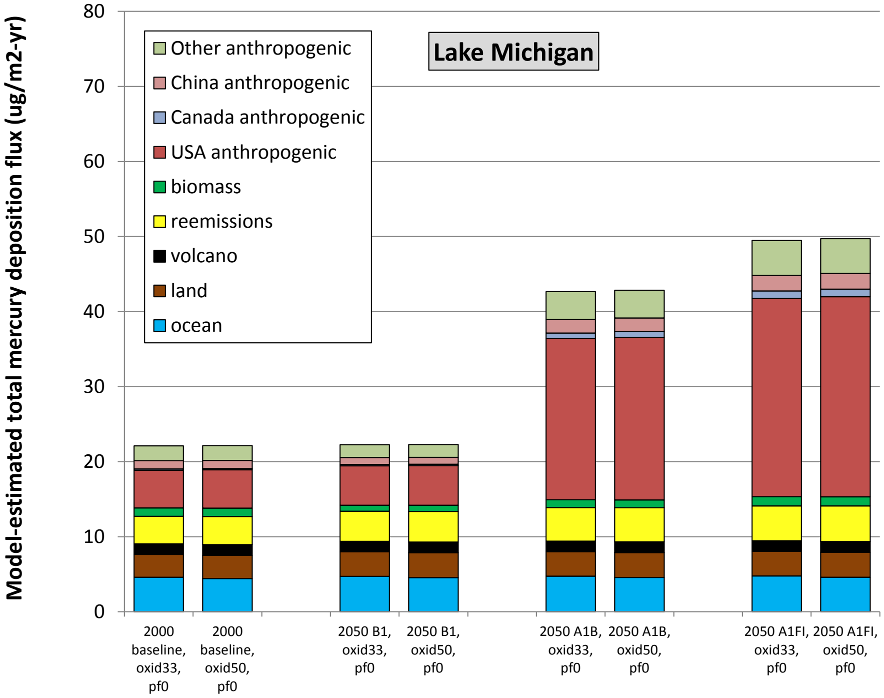

Figure 137. Overall source-attribution synthesis for deposition flux amounts for Lake Michigan

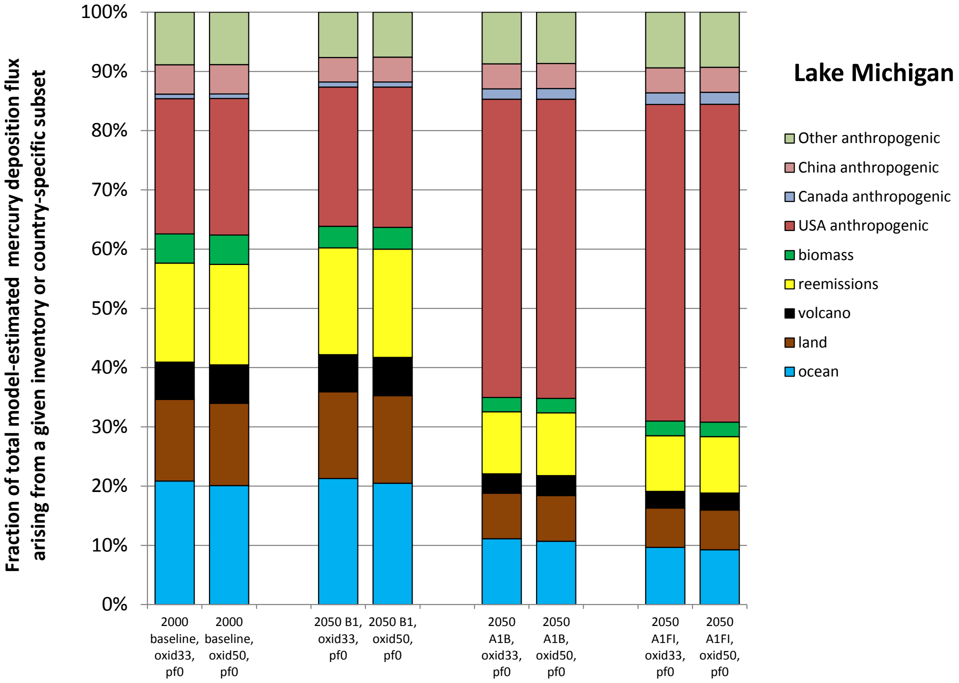

Figure 138. Overall source-attribution synthesis for deposition flux percentages for Lake Michigan

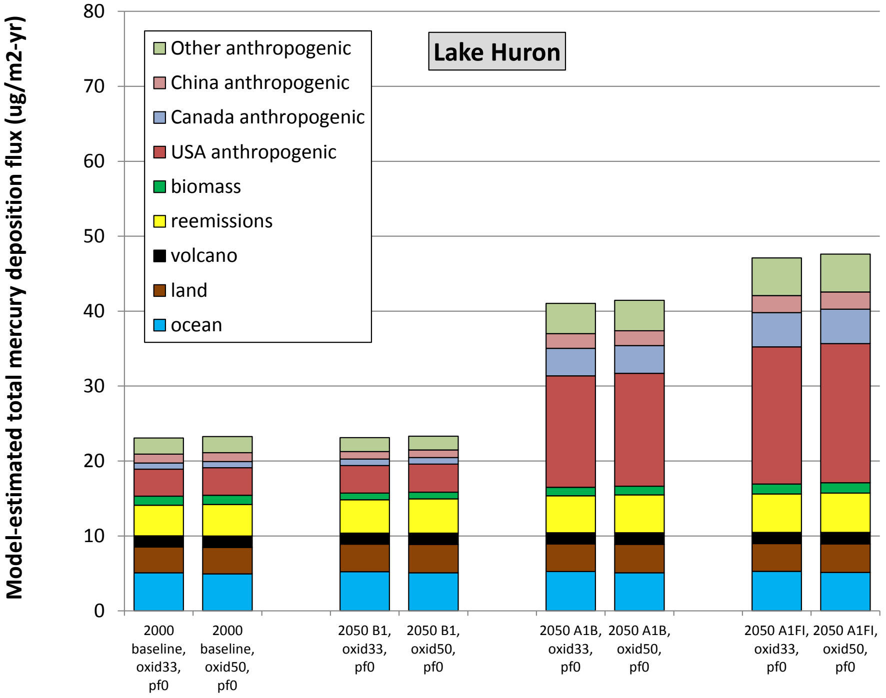

Figure 139. Overall source-attribution synthesis for deposition flux amounts for Lake Huron

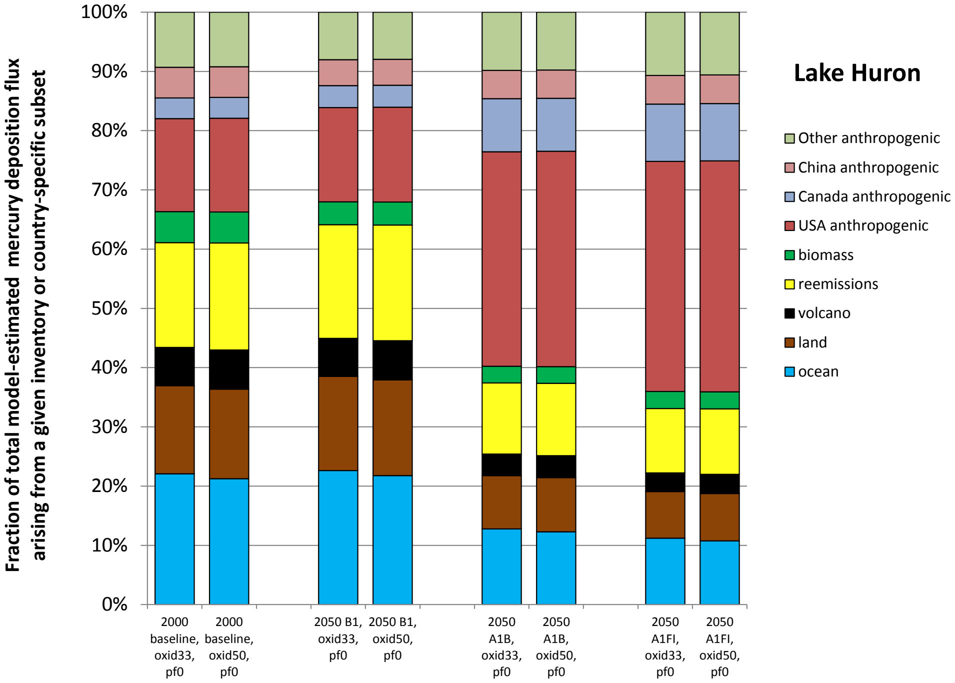

Figure 140. Overall source-attribution synthesis for deposition flux percentages for Lake Huron

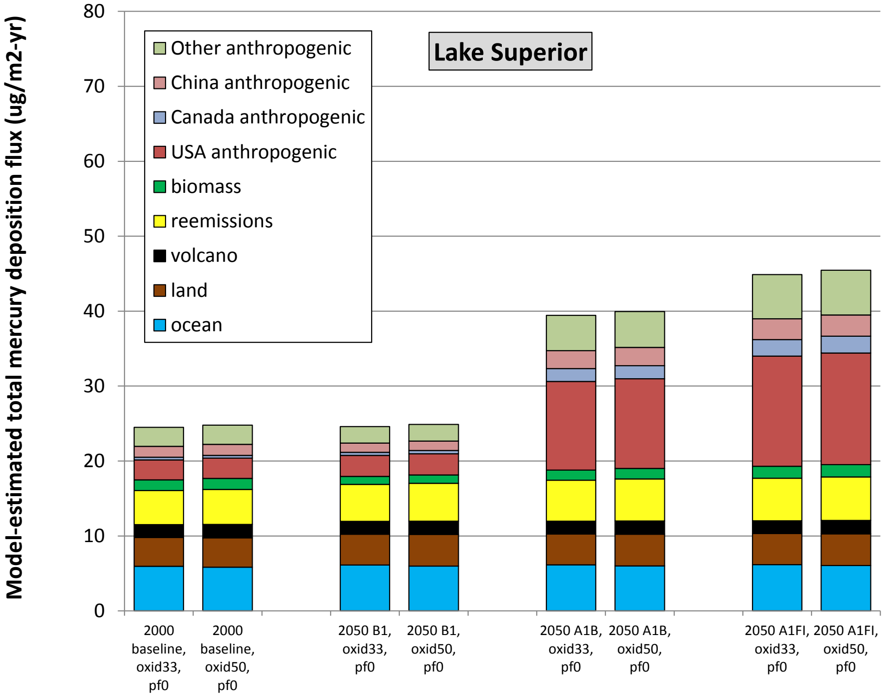

Figure 141. Overall source-attribution synthesis for deposition flux amounts for Lake Superior

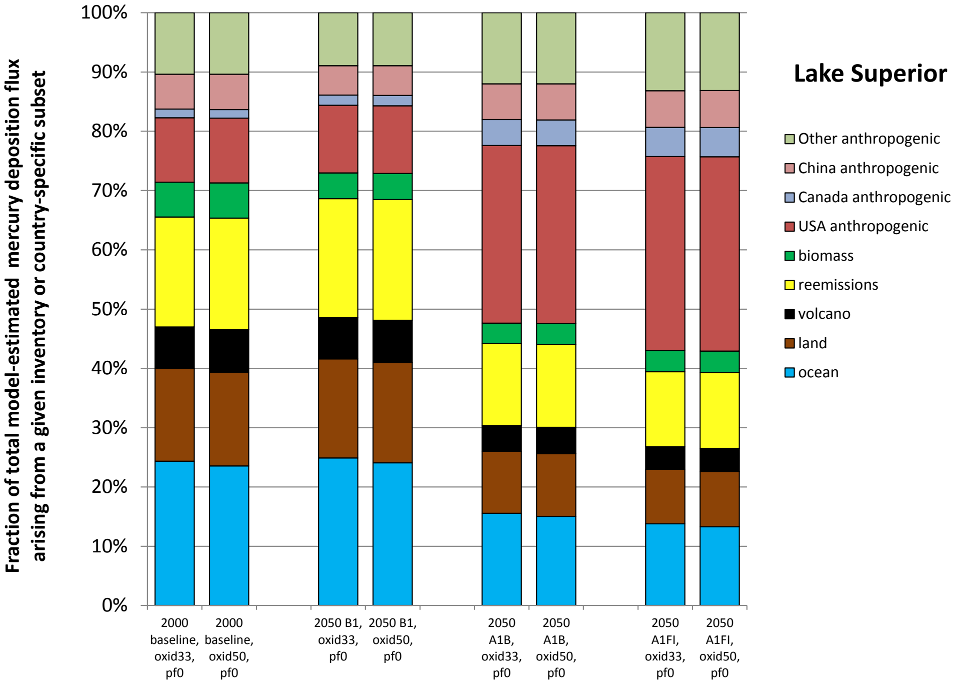

Figure 142. Overall source-attribution synthesis for deposition flux percentages for Lake Superior

7. References

AMAP / Wilson *et al*. (2010). Updating Historical Global Inventories of Anthropogenic Mercury Emissions to Air. AMAP Technical Report No. 3 (2010), Arctic Monitoring and Assessment Programme (AMAP), Oslo, Norway.

Berg, T., *et al*. (2003). Springtime depletion of mercury in the European Arctic as observed at Svalbard. Science of the Total Environment 304: 43-51.

Bhavsar, S. P., S. B. Gewurtz, D. J. McGoldrick, M. J. Keir and S. M. Backus (2010). Changes in Mercury Levels in Great Lakes Fish Between 1970s and 2007. Environmental Science & Technology 44(9): 3273-3279.

Brooks, S. B., A. Saiz-Lopez, H. Skov, S. E. Lindberg, J. M. C. Plane, and M. E. Goodsite (2006). The mass balance of mercury in the springtime arctic environment. Geophys. Res. Lett., 33, L13812

Bullock, O.R., and Brehme, K. (2002). Atmospheric mercury simulation using the CMAQ model: formulation description and analysis of wet deposition results. *Atmos. Environ.* **36**, 2135-2146.

Calhoun, J., and Prestbo, E. (2001). Kinetic study of the gas phase oxidation of elemental mercury by molecular chlorine. Frontier Geosciences, Inc., Seattle, WA (as cited by Bullock and Brehme, 2002).

Chen, L., H.H. Wang, J.F. Liu, Y.D. Tong, L.B. Ou, W. Zhang, D. Hu, C. Chen, and X.J. Wang (2014). Intercontinental transport and deposition patterns of atmospheric mercury from anthropogenic emissions. Atmos. Chem. Phys., 14, 10163–10176.

Cohen, M., R. Artz, R. Draxler, P. Miller, L. Poissant, D. Niemi, D. Ratte, M. Deslauriers, R. Duval, R. Laurin, J. Slotnick, T. Nettesheim and J. McDonald (2004). Modeling the atmospheric transport and deposition of mercury to the Great Lakes. Environmental Research 95(3): 247-265.

Cohen, M., Artz, R., Draxler, R. (2007). *NOAA Report to Congress: Mercury Contamination in the Great Lakes*. Silver Spring, MD, NOAA Air Resources Laboratory: 162 pages. Available at: http://www.arl.noaa.gov/documents/reports/NOAA_GL_Hg.pdf

Cohen, M., R. Draxler, R. Artz (2011). *Modeling Atmospheric Mercury Deposition to the Great Lakes. Final Report for work conducted with FY2010 funding from the Great Lakes Restoration Initiative.* NOAA Air Resources Laboratory, Silver Spring, MD. Dec 16, 2011. 160 pages. Available at: http://www.arl.noaa.gov/documents/reports/GLRI_FY2010_Atmospheric_Mercury_Final_Report_2011_Dec_16.pdf

Cohen, M., R. Draxler, R. Artz (2013). *Modeling Atmospheric Mercury Deposition to the Great Lakes: Examination of the Influence of Variations in Model Inputs, Parameters, and Algorithms on*

Model Results. Final Report for work conducted with FY2011 funding from the Great Lakes Restoration Initiative. NOAA Air Resources Laboratory, Silver Spring, MD. June 30, 2013. 157 pages. Available at: http://www.arl.noaa.gov/documents/reports/GLRI_FY2011_Atmospheric_Mercury_Final_Report_2013_June_30.pdf

Cole, A. S., A. Steffen, K. A. Pfaffhuber, T. Berg, M. Pilote, L. Poissant, R. Tordon and H. Hung (2013). Ten-year trends of atmospheric mercury in the high Arctic compared to Canadian sub-Arctic and mid-latitude sites. Atmospheric Chemistry and Physics 13(3): 1535-1545.

Evers, D., J. Wiener, *et al*. (2011a). Mercury in the Great Lakes region: bioaccumulation, spatiotemporal patterns, ecological risks, and policy. *Ecotoxicology* 20(7): 1487-1499.

Evers, D.C., Wiener, J.G., Driscoll, C.T., Gay, D.A., Basu, N., Monson, B.A., Lambert, K.F., Morrison, H.A., Morgan, J.T., Williams, K.A., Soehl, A.G. (2011b). *Great Lakes Mercury Connections: The Extent and Effects of Mercury Pollution in the Great Lakes Region*. Biodiversity Research Institute. Gorham, Maine. Report BRI 2011-18. 44 pages. http://www.briloon.org/mercuryconnections/greatlakes

Finley, B. D., P. C. Swartzendruber and D. A. Jaffe (2009). Particulate mercury emissions in regional wildfire plumes observed at the Mount Bachelor Observatory. Atmospheric Environment 43(38): 6074-6083.

Gandhi, N., R. W. K. Tang, S. P. Bhavsar and G. B. Arhonditsis (2014). Fish Mercury Levels Appear to Be Increasing Lately: A Report from 40 Years of Monitoring in the Province of Ontario, Canada. Environmental Science & Technology 48(10): 5404-5414.

Gardfeldt, K. and Jonnson, M. (2003). Is bimolecular reduction of Hg(II)-complexes possible in aqueous systems of environmental importance? *J. Phys. Chem. A* **107**, 4478-4482.

Grant, S. L., M. Kim, P. Lin, K. C. Crist, S. Ghosh and V. R. Kotamarthi (2014). A simulation study of atmospheric mercury and its deposition in the Great Lakes. Atmospheric Environment 94: 164-172.

Gratz, L., Keeler, G., and Miller, E. (2009). Long Term Relationships between Mercury Wet Deposition and Meteorology. *Atmospheric Environment* **43**: 6218-6229.

Hall, B., and Bloom, N.S. (1993). Report to the Electric Power Research Institute, Palo Alto, CA. As cited in Seigneur *et al*., 1994.

Hall, B. (1995). The gas phase oxidation of elemental mercury by ozone. *Water, Air, and Soil Pollution* **80**, 301-315.

Han, Y.J., Holsen, T., Lai, S.O., Hopke, P., Yi, S.M., Lie, W., Pagano, J., Falanga, L., Milligan, M., and Andolina, C. (2004). Atmospheric gaseous mercury concentrations in New York State:

relationships with meteorological data and other pollutants. Atmospheric Environment 38: 6431-6446.

Han, Y.J., Holsen, T., Hopke, P., Yi, S.M. (2005). Comparison between back-trajectory based modeling and Lagrangian backward dispersion modeling for locating sources of reactive gaseous mercury. Environmental Science and Technology 39: 1715-1723.

Han, Y.J., Holsen, T., and Hopke, P. (2007). Estimation of source locations of total gaseous mercury measured in New York State using trajectory-based models. Atmospheric Environment 41: 6033-6047.

IPCC (2000). IPCC Special Report, Emissions Scenarios, Summary for Policymakers. A Special Report of IPCC Working Group III. Published for the Intergovernmental Panel on Climate Change, WMO, UNEP. ISBN: 92-9169-113-5. Available at: https://www.ipcc.ch/pdf/special-reports/spm/sres-en.pdf

Kellerhals, M., S. Beauchamp, W. Belzer, P. Blanchard, F. Froude, B. Harvey, K. McDonald, M. Pilote, L. Poissant, K. Puckett, B. Schroeder, A. Steffen and R. Tordon (2003). Temporal and spatial variability of total gaseous mercury in Canada: results from the Canadian Atmospheric Mercury Measurement Network (CAMNet). Atmospheric Environment 37(7): 1003-1011.

Lan, X., Talbot, R., Castor, M., Perry, K., and Luke, W. (2012). Seasonal and diurnal variations of atmospheric mercury across the US determined from AMNet monitoring data. *Atmos Chem Phys* **12**: 10569-10582.

Lei, H., Liang, X.-Z., Wuebbles, D.J., Tao, Z. (2013). Model analyses of atmospheric mercury: present air quality and effects of transpacific transport on the United States. *Atmos Chem Phys* **13**: 10807-10825.

Lei, H., Wuebbles, D.J., Liang, X.-Z., Tao, Z., Olsen, S., Artz, R., Ren, X., and Cohen, M. (2014). Projections of atmospheric mercury levels and their effect on air quality in the United States. *Atmos Chem Phys* **14**: 783-795.

Lin, C. and Pehkonen, S. (1997). The chemistry of atmospheric mercury: a review. *Atmos. Environ.* **33**, 2067-2079.

Lin, C., and Pehkonen, S. (1998). Oxidation of elemental mercury by aqueous chlorine (HOCl/OCl-): implications for tropospheric mercury chemistry. *J. Geophys. Res.* **103 (D21)** 28093-28102.

Lyman, S., Gustin, M., Prestbo, E., and Marsik, F. (2007). Estimation of dry deposition of atmospheric mercury in Nevada by direct and indirect methods. Environmental Science and Technology 41: 1970-1976.

McClure, C.D., Jaffe, D.A., Edgerton, E.S. (2014). Evaluation of the KCl Denuder Method for Gaseous Oxidized Mercury using HgBr2 at an In-Service AMNet Site. *Environmental Science & Technology* Article ASAP (in press).

Munthe, J. (1992). The aqueous oxidation of elemental mercury by ozone. *Atmos. Environ.* **26A**, 1461-1468.

NADP (2011). National Atmospheric Deposition Program Office, Illinois State Water Survey, 2204 Griffith Dr., Champaign, IL 61820. 2005 data for mercury wet deposition at sites in the NADP's Mercury Deposition Network were downloaded Aug 11, 2011 from: http://nadp.sws.uiuc.edu/

NAtChem (2012). Canadian National Atmospheric Chemistry Toxics Database. Environment Canada, Science and Technology Branch, 4905 Dufferin Street, Toronto, Ontario, Canada M3H 5T4. Total Gaseous Mercury (TGM) data at several monitoring sites for 2005 downloaded October 25, 2012, from http://www.ec.gc.ca/natchem

NCAR/NWS (1994…). National Centers for Environmental Prediction/National Weather Service/NOAA/U.S. Department of Commerce. 1994, updated monthly. NCEP/NCAR Global Reanalysis Products, 1948-continuing. Research Data Archive at the National Center for Atmospheric Research, Computational and Information Systems Laboratory. http://rda.ucar.edu/datasets/ds090.0/

NOAA ARL (2003…) Updated annually. Data from the NCAR/NWS Global Reanalysis Project (CDAS, Climate Data Assimilation System) is converted to and archived in HYSPLIT format at the NOAA ARL Ready website: https://ready.arl.noaa.gov/gbl_reanalysis.php. Additional information at: http://www.cpc.ncep.noaa.gov/products/wesley/reanalysis.html

Parsons, M. T., D. McLennan, M. Lapalme, C. Mooney, C. Watt and R. Mintz (2013). Total Gaseous Mercury Concentration Measurements at Fort McMurray, Alberta, Canada. Atmosphere 4(4): 472-493.

Peterson, C., Gustin, M., Lyman, S. (2009). Atmospheric mercury concentrations and speciation measured from 2004-2007 in Reno, Nevada, USA. *Atmospheric Environment* **43**: 4646-4654.

Pirrone, N., S. Cinnirella, X. Feng, R. B. Finkelman, H. R. Friedli, J. Leaner, R. Mason, A. B. Mukherjee, G. B. Stracher, D. G. Streets and K. Telmer (2010). Global mercury emissions to the atmosphere from anthropogenic and natural sources. Atmospheric Chemistry and Physics 10(13): 5951-5964.

Poissant, L., M. Pilote, C. Beauvais, P. Constant and H. H. Zhang (2005). A year of continuous measurements of three atmospheric mercury species (GEM, RGM and Hg-p) in southern Quebec, Canada. Atmospheric Environment 39(7): 1275-1287.

Schroeder, W., *et al*. (1998). Arctic springtime depletion of mercury. Nature 394: 331-332

Seigneur, C., Wrobel, J., and Constantinou, E. (1994). A chemical kinetic mechanism for atmospheric inorganic mercury. *Environ Sci Technol* **28**, 1589-1597.

Seigneur, C., Abeck, H., Chia, G., Reinhard, M., Bloom, N., Prestbo, E., and Saxena, P. (1998). Mercury adsorption to elemental carbon (soot) particles and atmospheric particulate matter. *Atmos. Environ.* **32**, 2649-2657.

Sommar, J., Gardfeldt, K., Stromberg, D., and Feng, X. (2001). A kinetic study of the gas-phase reaction between the hydroxyl radical and atomic mercury. *Atmos. Environ.* **35**, 3049-3054.

Steffen, A., *et al*. (2008). A synthesis of atmospheric mercury depletion event chemistry in the atmosphere and snow. Atmospheric Chemistry and Physics 8: 1445-1482.

Streets, D.G., Zhang, Q., Wu, Y. (2009). Projections of Global Mercury Emissions in 2050. *Environmental Science and Technology* **43**: 2983-2988.

Swartzendruber, P. C., D. A. Jaffe, E. M. Prestbo, P. Weiss-Penzias, N. E. Selin, R. Park, D. J. Jacob, S. Strode and L. Jaegle (2006). Observations of reactive gaseous mercury in the free troposphere at the Mount Bachelor Observatory. Journal of Geophysical Research-Atmospheres 111(D24).

Temme, C., P. Blanchard, A. Steffen, C. Banic, S. Beauchamp, L. Poissant, R. Tordon and B. Wiens (2007). Trend, seasonal and multivariate analysis study of total gaseous mercury data from the Canadian atmospheric mercury measurement network (CAMNet). Atmospheric Environment 41(26): 5423-5441.

Tokos, J., Hall, B., Calhoun, J., and Prestbo, E. (1998). Homogeneous gas-phase reaction of Hg0 with H2O2, O3, CH3I, and (CH3)3 S: implications for atmospheric Hg cycling. *Atmos. Environ.* **32**, 823-827.

Van Loon, L., Mader, E., and Scott, S. (2000). Reduction of the aqueous mercuric ion by sulfite: UV spectrum of HgSO3 and its intramolecular redox reaction. *J. Phys. Chem. A* **104**, 1621-1626.

Weiss-Penzias, P., D. A. Jaffe, P. Swartzendruber, J. B. Dennison, D. Chand, W. Hafner and E. Prestbo (2006). Observations of Asian air pollution in the free troposphere at Mount Bachelor Observatory during the spring of 2004. Journal of Geophysical Research-Atmospheres 111(D10).

Weiss-Penzias, P., D. Jaffe, P. Swartzendruber, W. Hafner, D. Chand and E. Prestbo (2007). Quantifying Asian and biomass burning sources of mercury using the Hg/CO ratio in pollution plumes observed at the Mount Bachelor Observatory. Atmospheric Environment 41(21): 4366-4379.

Weiss-Penzias, P., *et al*. (2014). Use of a global model to understand speciated atmospheric mercury observations at five high-elevation sites. *Atmospheric Chemistry and Physics Discussions* **14**: 22763-22792.

Xiao, Z.F., Munthe, J., Stromberg, D., and Lindqvist, O. (1994). Photochemical Behavior of Inorganic Mercury Compounds in Aqueous Solution. Chapter VI-6, pages 581-592, in *Mercury Pollution Integration and Synthesis*, edited by Watras, C.J., CRC Press, Boca Raton, FL.

Zhang, Y., L. Jaegle, A. van Donkelaar, R. V. Martin, C. D. Holmes, H. M. Amos, Q. Wang, R. Talbot, R. Artz, S. Brooks, W. Luke, T. M. Holsen, D. Felton, E. K. Miller, K. D. Perry, D. Schmeltz, A. Steffen, R. Tordon, P. Weiss-Penzias and R. Zsolway (2012). Nested-grid simulation of mercury over North America. Atmospheric Chemistry and Physics 12(14): 6095-6111.

8. Appendix: Emissions Maps

8.1. Anthropogenic, Hg(0)

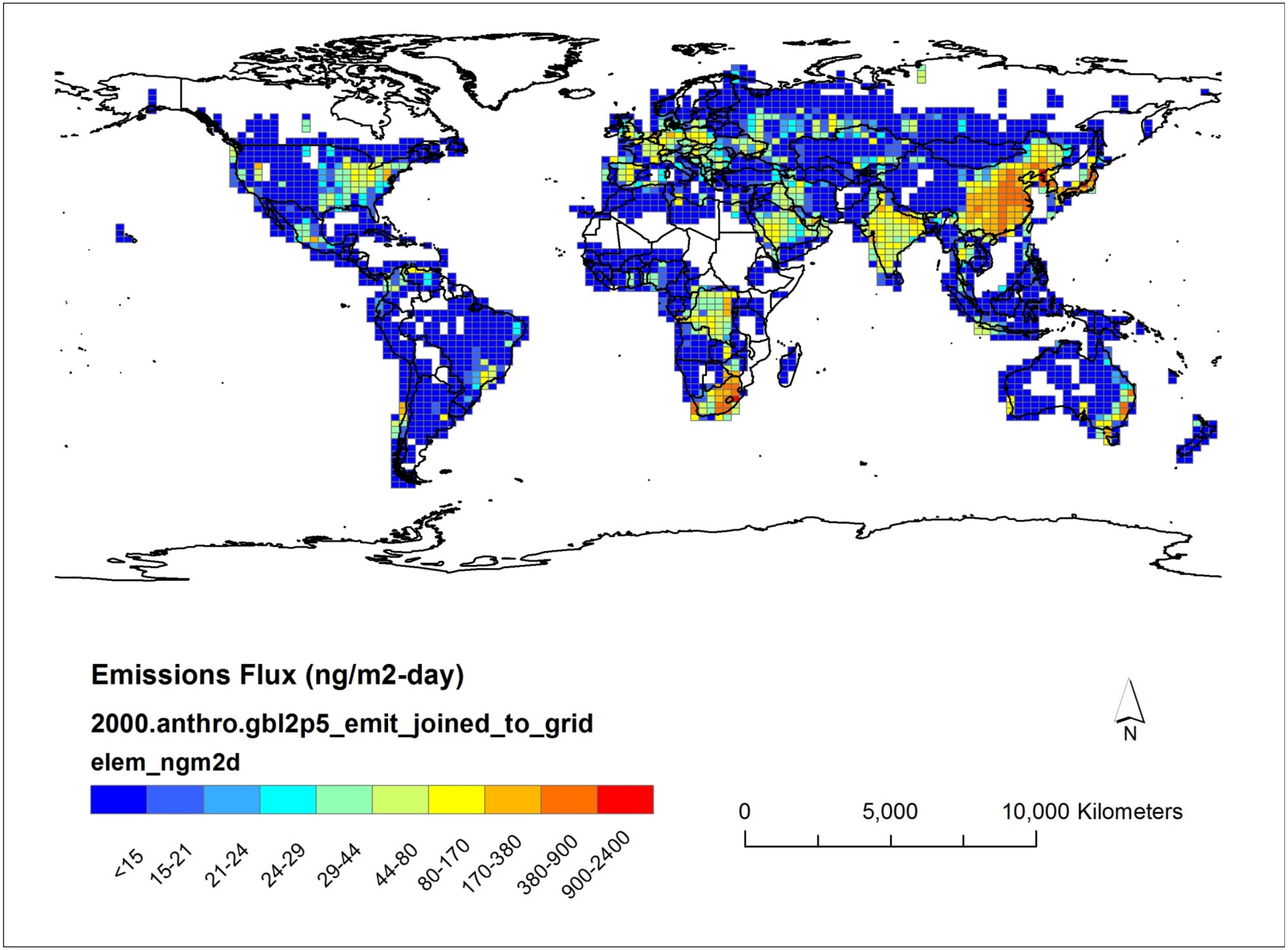
Emissions Flux (ng/m2-day)
2000.anthro.gbl2p5_emit_joined_to_grid
elem_ngm2d
<15
15-21
21-24
24-29
29-44
44-80
80-170
170-380
380-900
900-2400
0
5,000
10,000 Kilometers
N

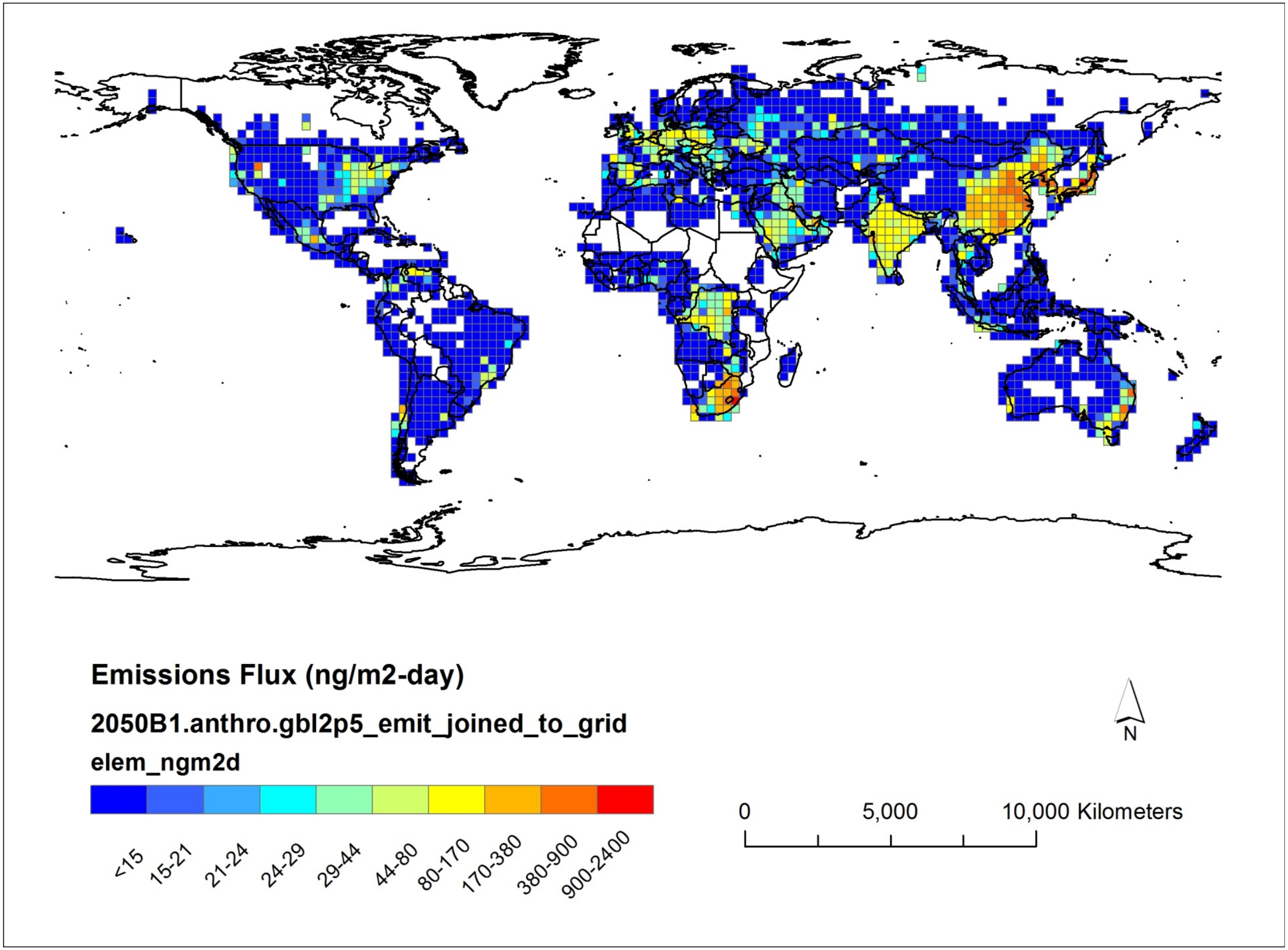
Emissions Flux (ng/m2-day)
2050B1.anthro.gbl2p5_emit_joined_to_grid
elem_ngm2d
<15
15-21
21-24
24-29
29-44
44-80
80-170
170-380
380-900
900-2400
N
0
5,000
10,000 Kilometers

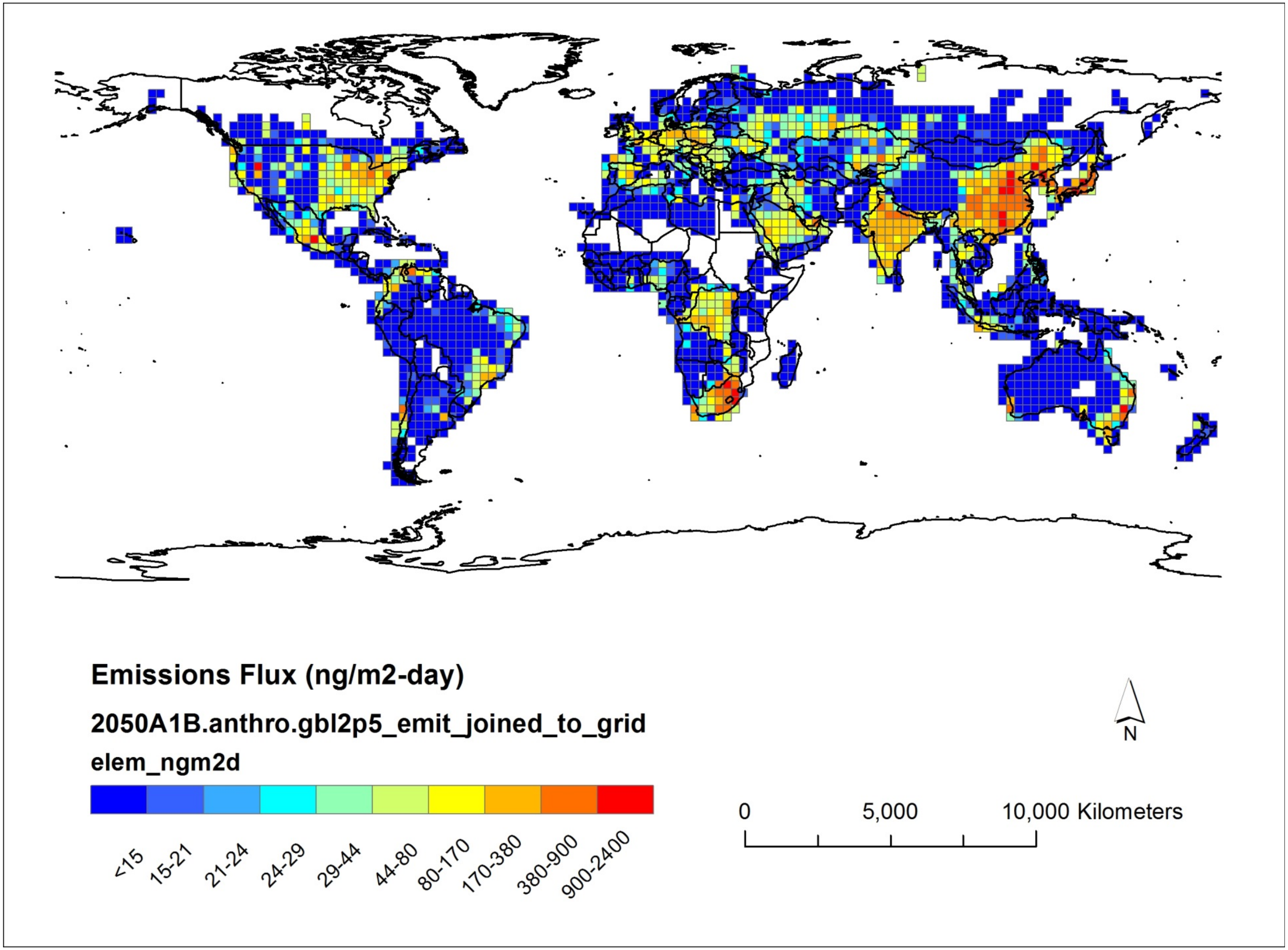
Emissions Flux (ng/m2-day)
2050A1B.anthro.gbl2p5_emit_joined_to_grid
elem_ngm2d
<15
15-21
21-24
24-29
29-44
44-80
80-170
170-380
380-900
900-2400
N
0
5,000
10,000 Kilometers

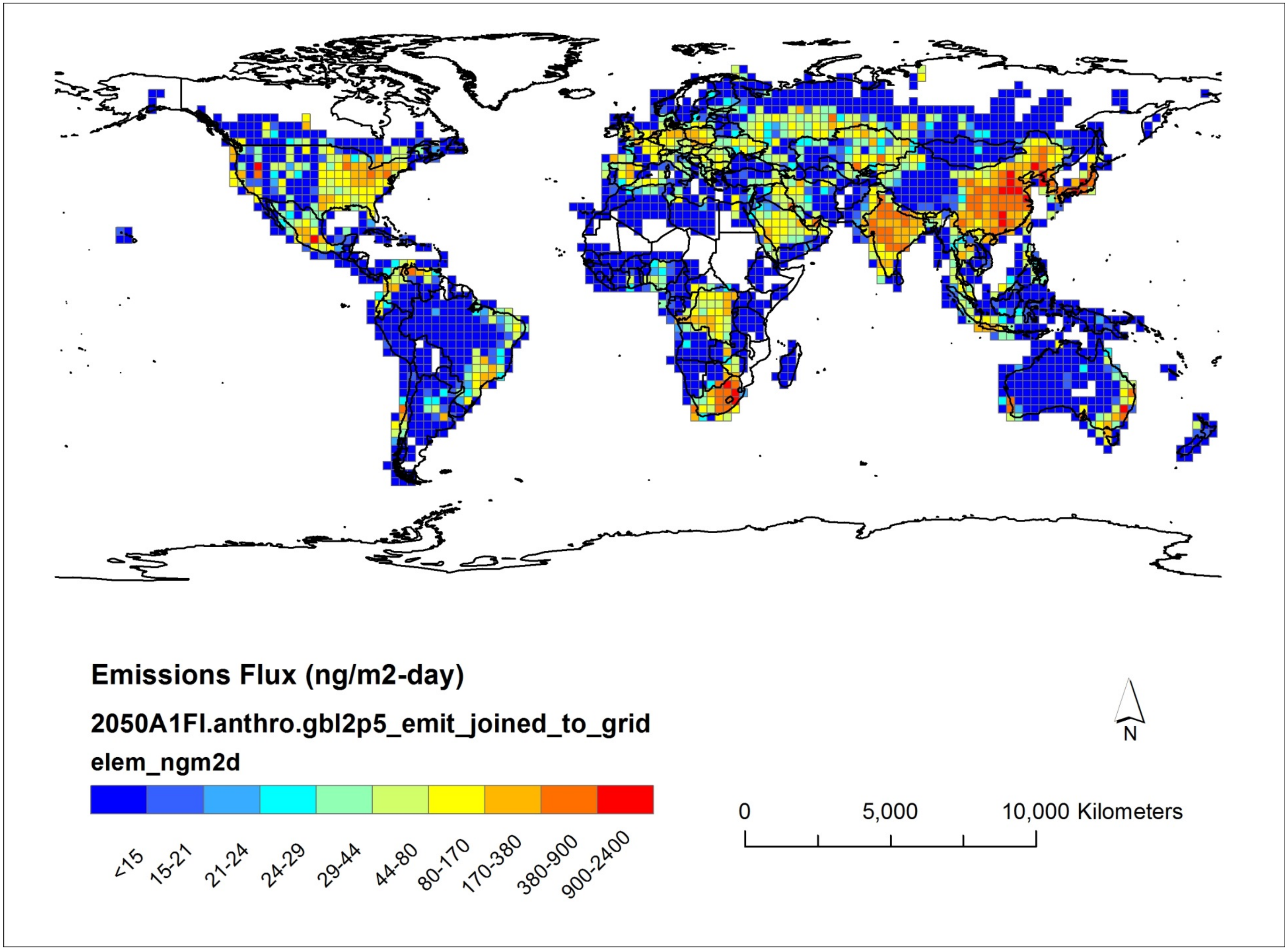
Emissions Flux (ng/m2-day)
2050A1FI.anthro.gbl2p5_emit_joined_to_grid
elem_ngm2d
<15
15-21
21-24
24-29
29-44
44-80
80-170
170-380
380-900
900-2400
0
5,000
10,000 Kilometers
N

8.2. Anthropogenic, Hg(II)

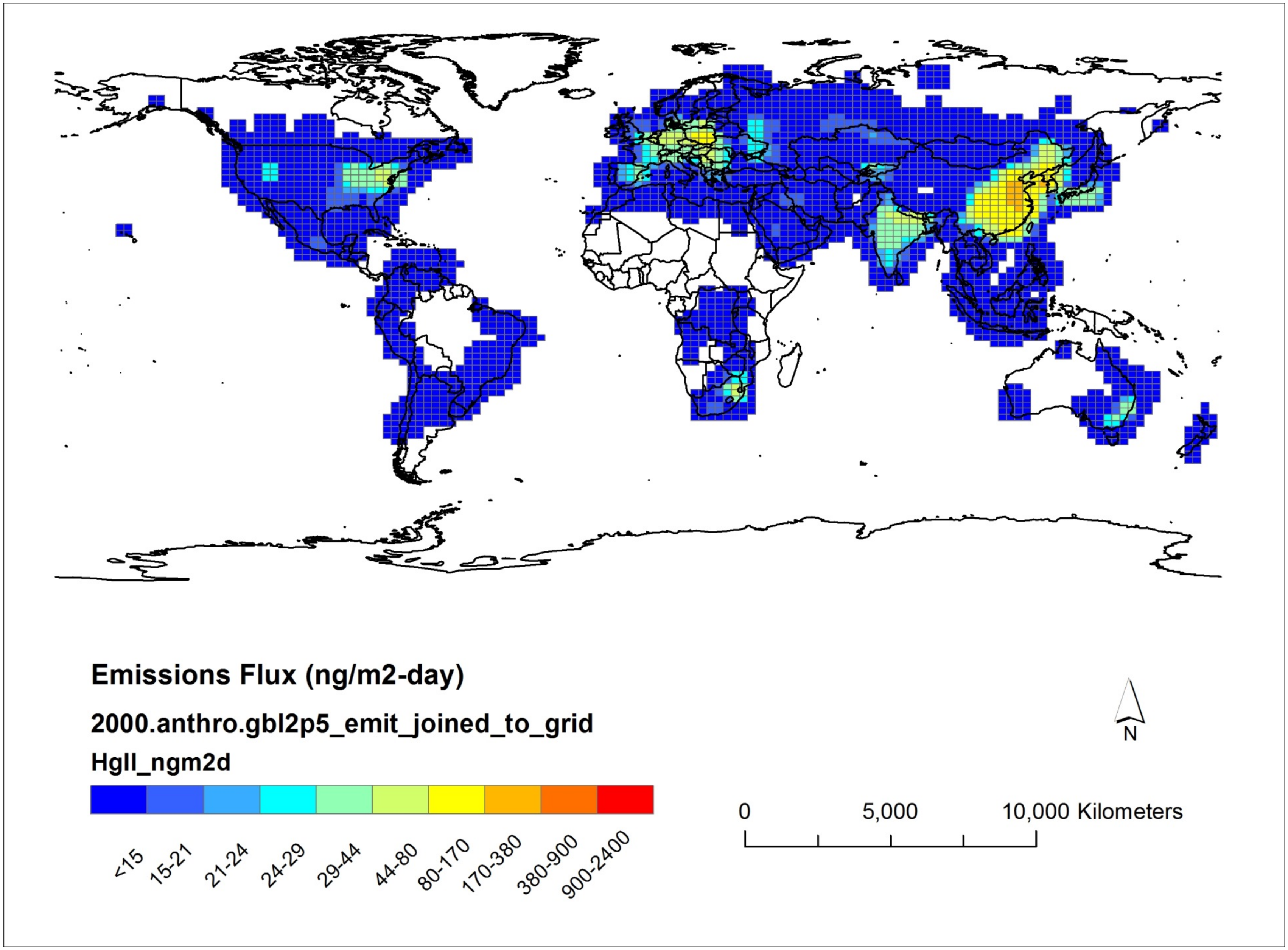
Emissions Flux (ng/m2-day)
2000.anthro.gbl2p5_emit_joined_to_grid
HgII_ngm2d
<15
15-21
21-24
24-29
29-44
44-80
80-170
170-380
380-900
900-2400
N
0
5,000
10,000 Kilometers

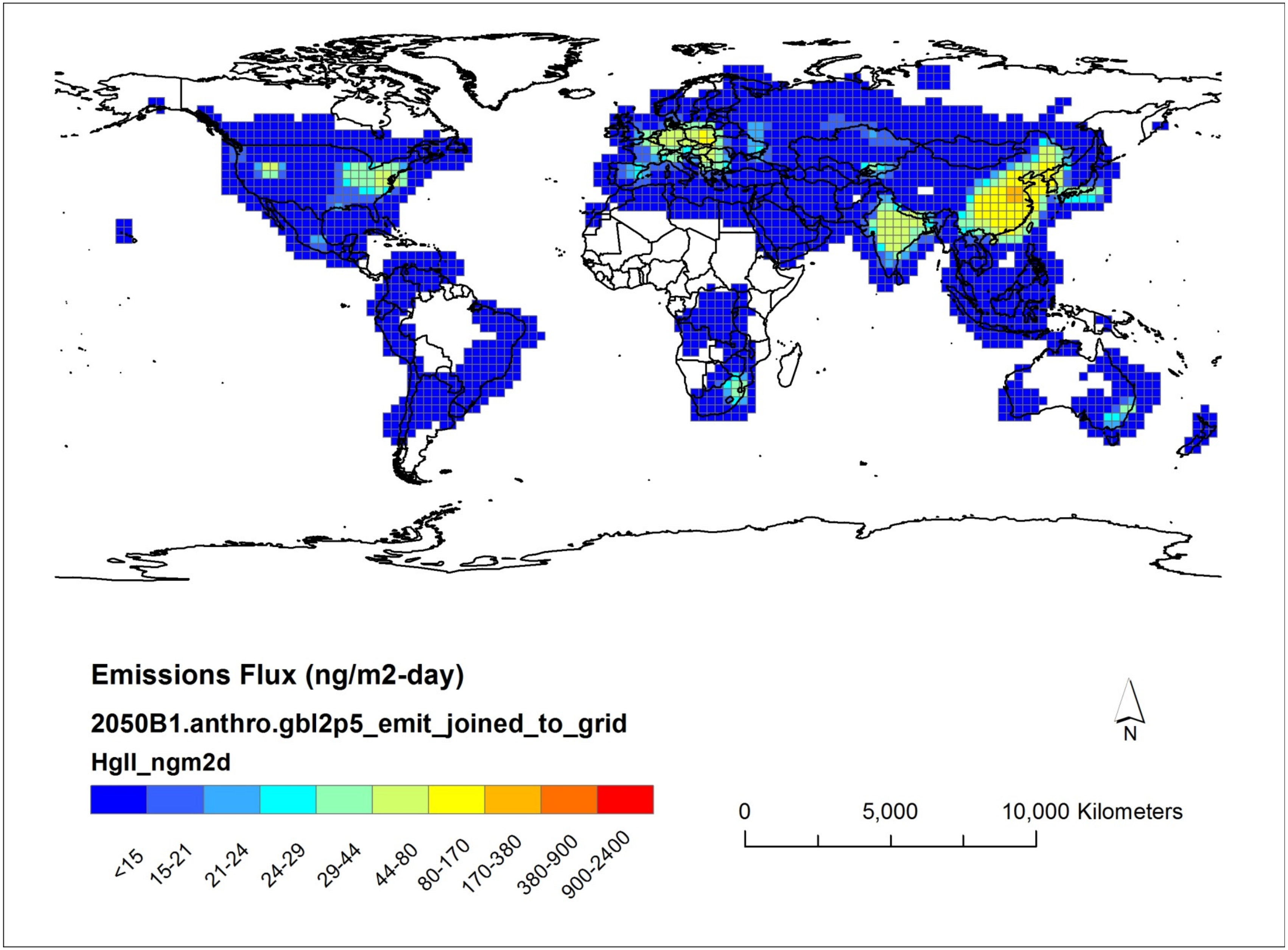
Emissions Flux (ng/m2-day)
2050B1.anthro.gbl2p5_emit_joined_to_grid
HgII_ngm2d
<15
15-21
21-24
24-29
29-44
44-80
80-170
170-380
380-900
900-2400
0
5,000
10,000 Kilometers
N

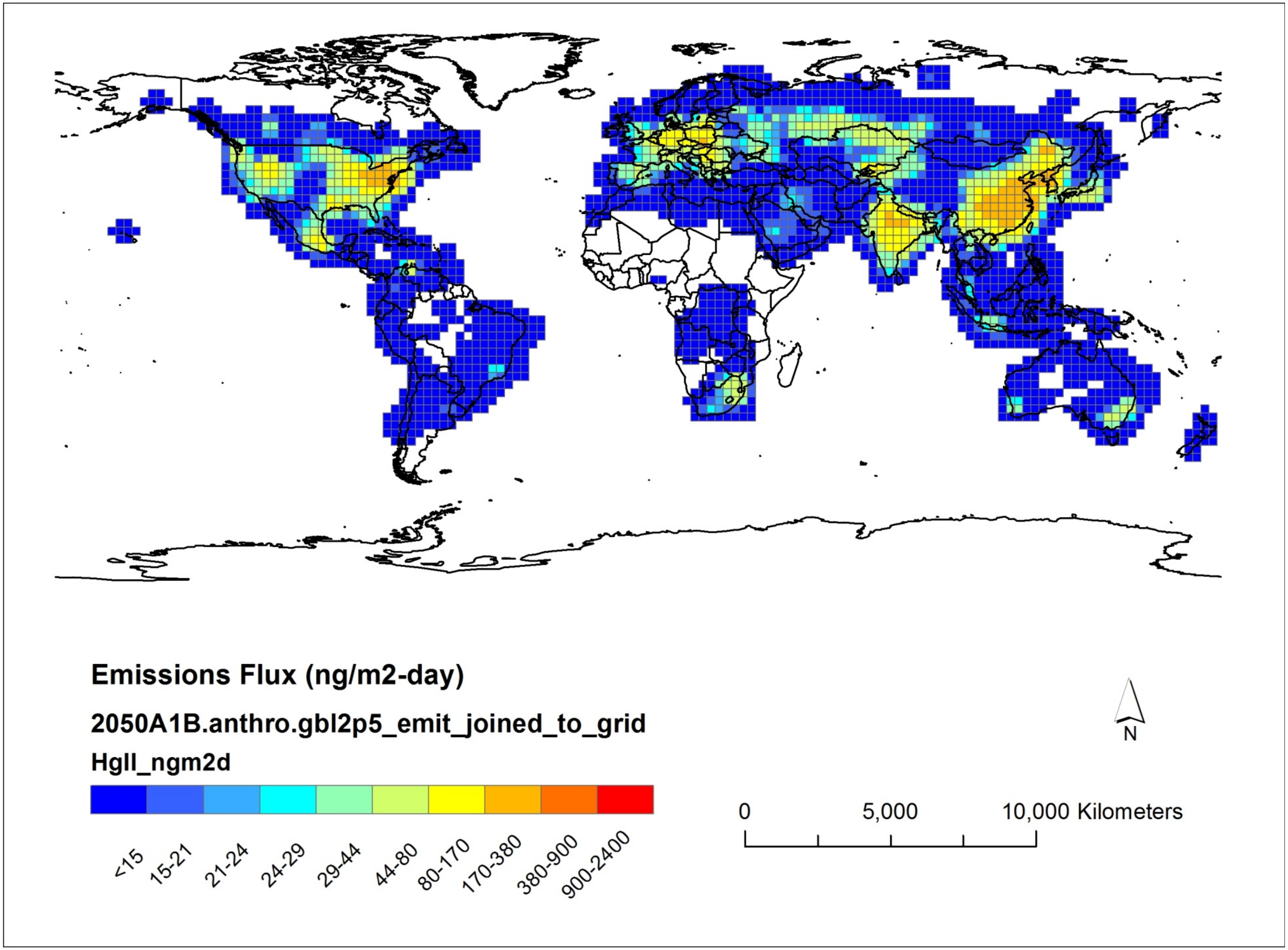
Emissions Flux (ng/m2-day)
2050A1B.anthro.gbl2p5_emit_joined_to_grid
HgII_ngm2d
<15
15-21
21-24
24-29
29-44
44-80
80-170
170-380
380-900
900-2400
0
5,000
10,000 Kilometers
N

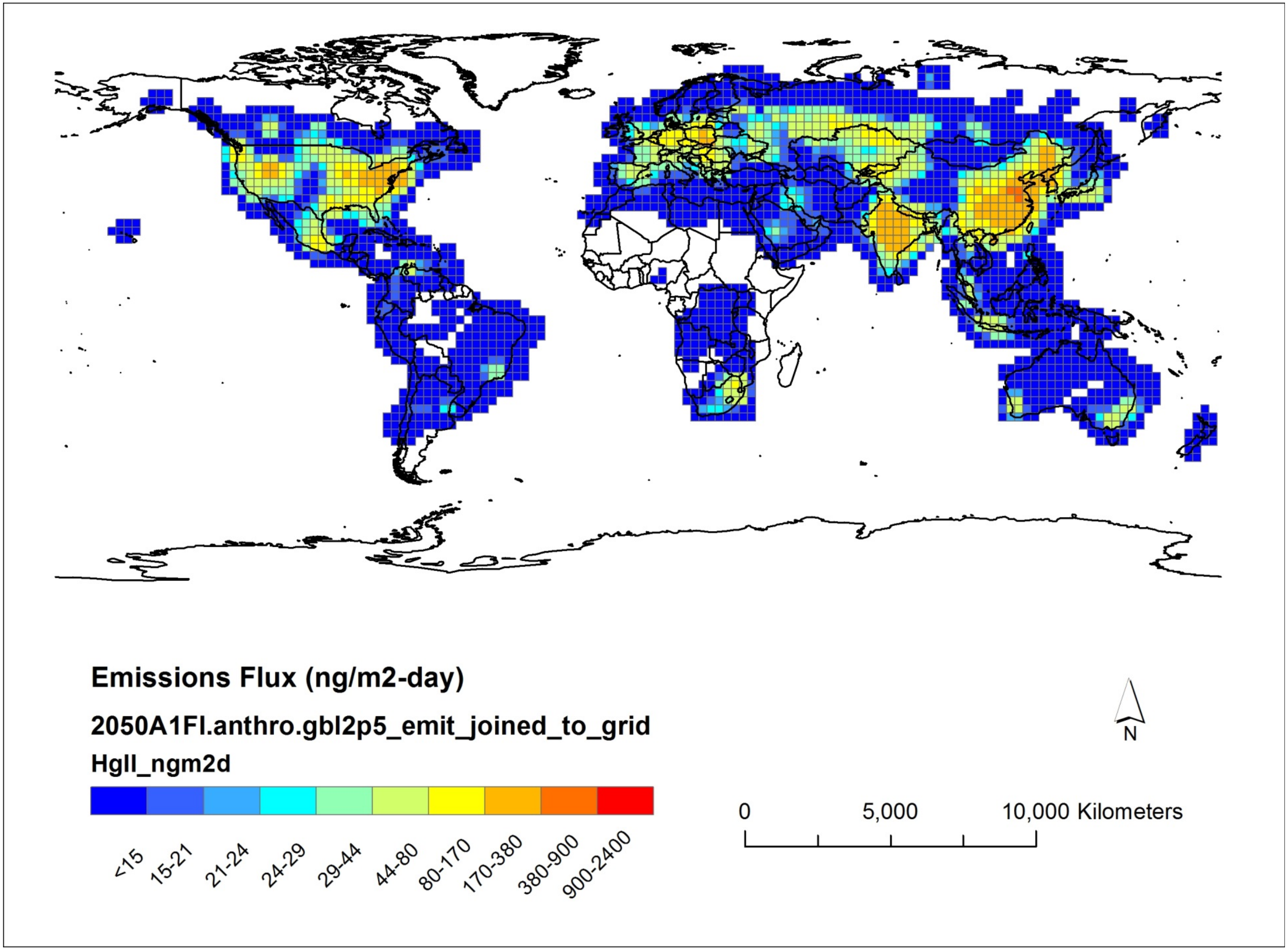
Emissions Flux (ng/m2-day)
2050A1FI.anthro.gbl2p5_emit_joined_to_grid
HgII_ngm2d
<15
15-21
21-24
24-29
29-44
44-80
80-170
170-380
380-900
900-2400
0
5,000
10,000 Kilometers
N

8.3. Anthropogenic, Hg(p)

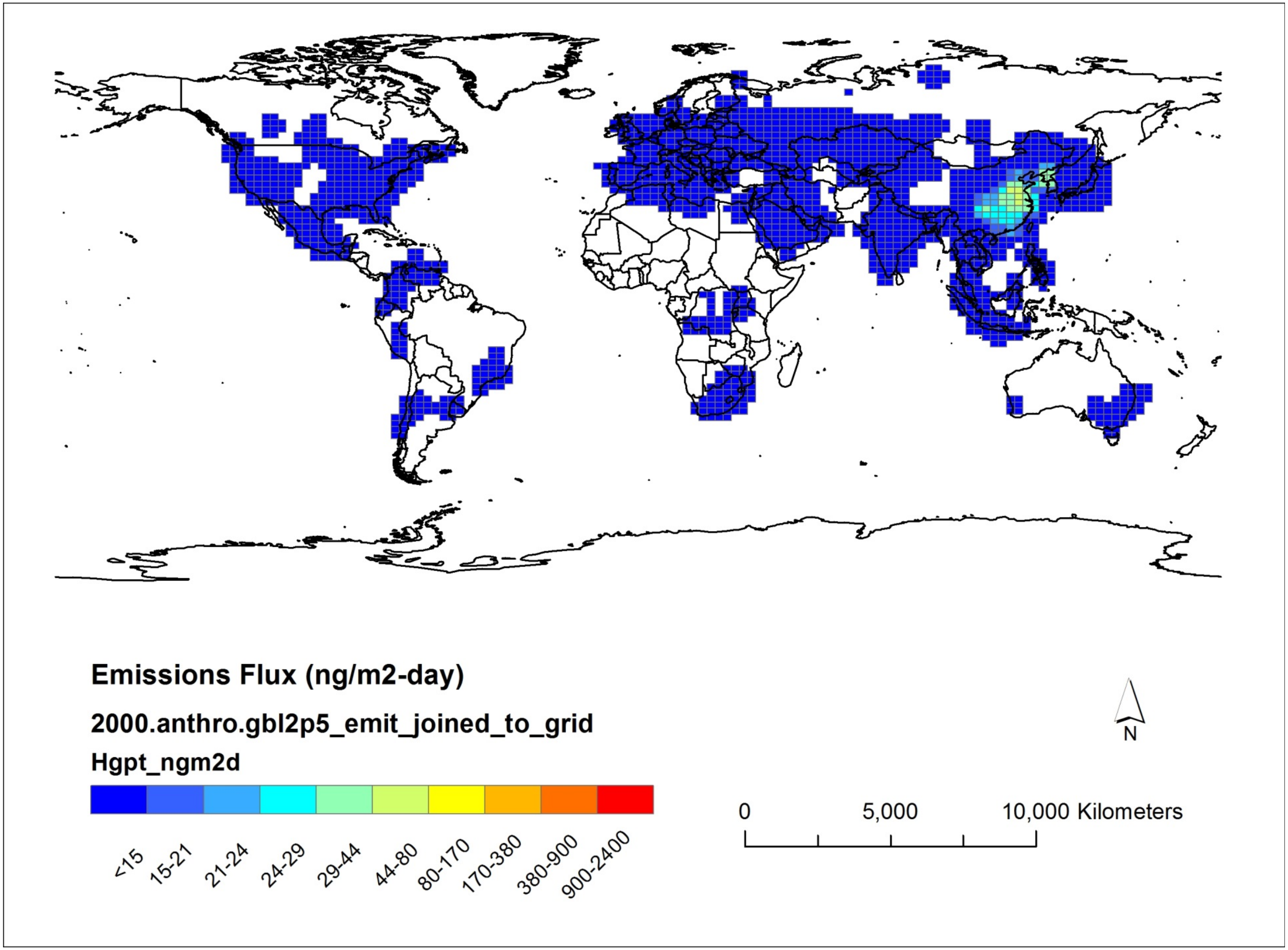
Emissions Flux (ng/m2-day)
2000.anthro.gbl2p5_emit_joined_to_grid
Hgpt_ngm2d
<15
15-21
21-24
24-29
29-44
44-80
80-170
170-380
380-900
900-2400
0
5,000
10,000 Kilometers
N

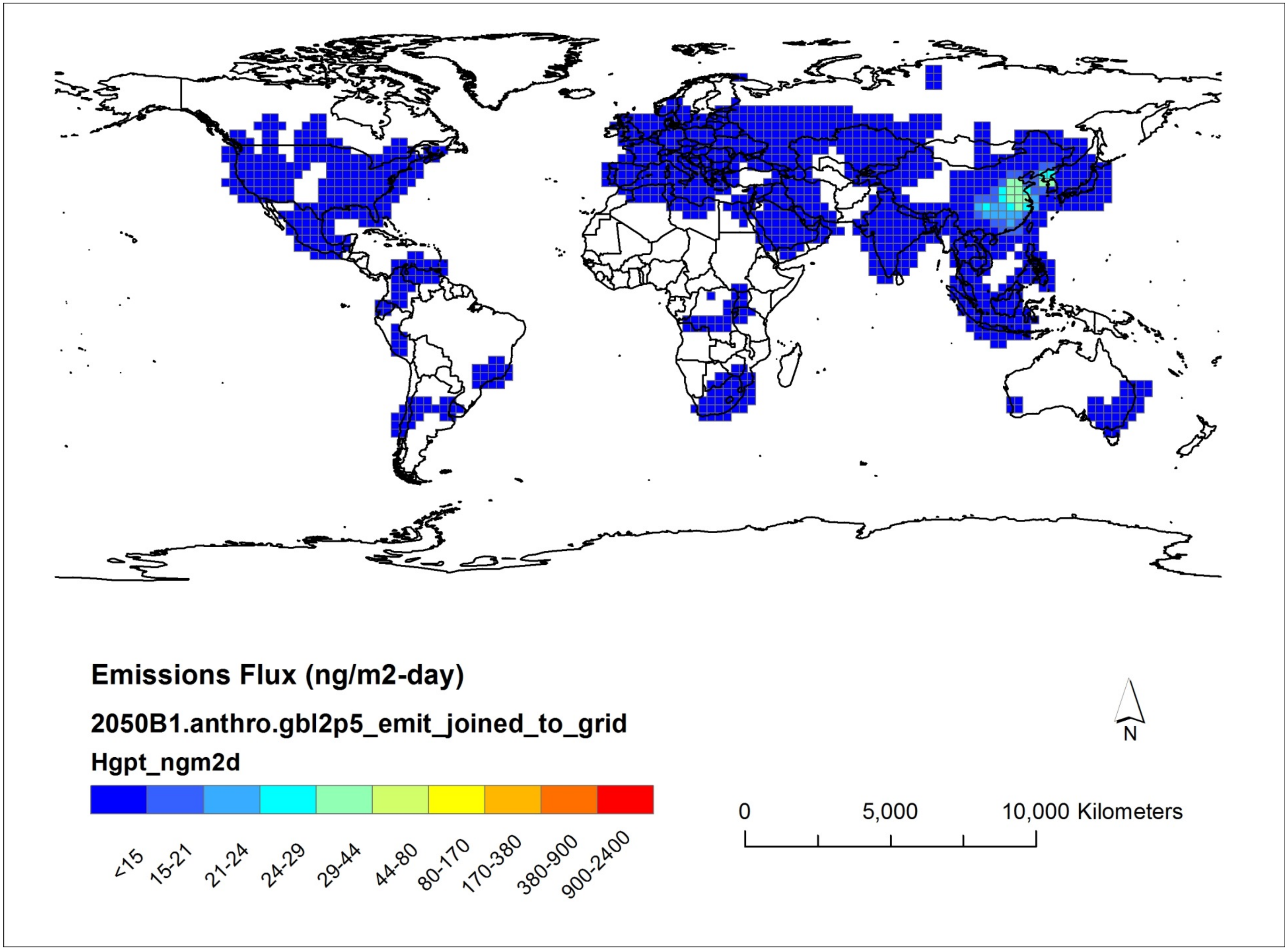
Emissions Flux (ng/m2-day)
2050B1.anthro.gbl2p5_emit_joined_to_grid
Hgpt_ngm2d
<15
15-21
21-24
24-29
29-44
44-80
80-170
170-380
380-900
900-2400
0
5,000
10,000 Kilometers
N

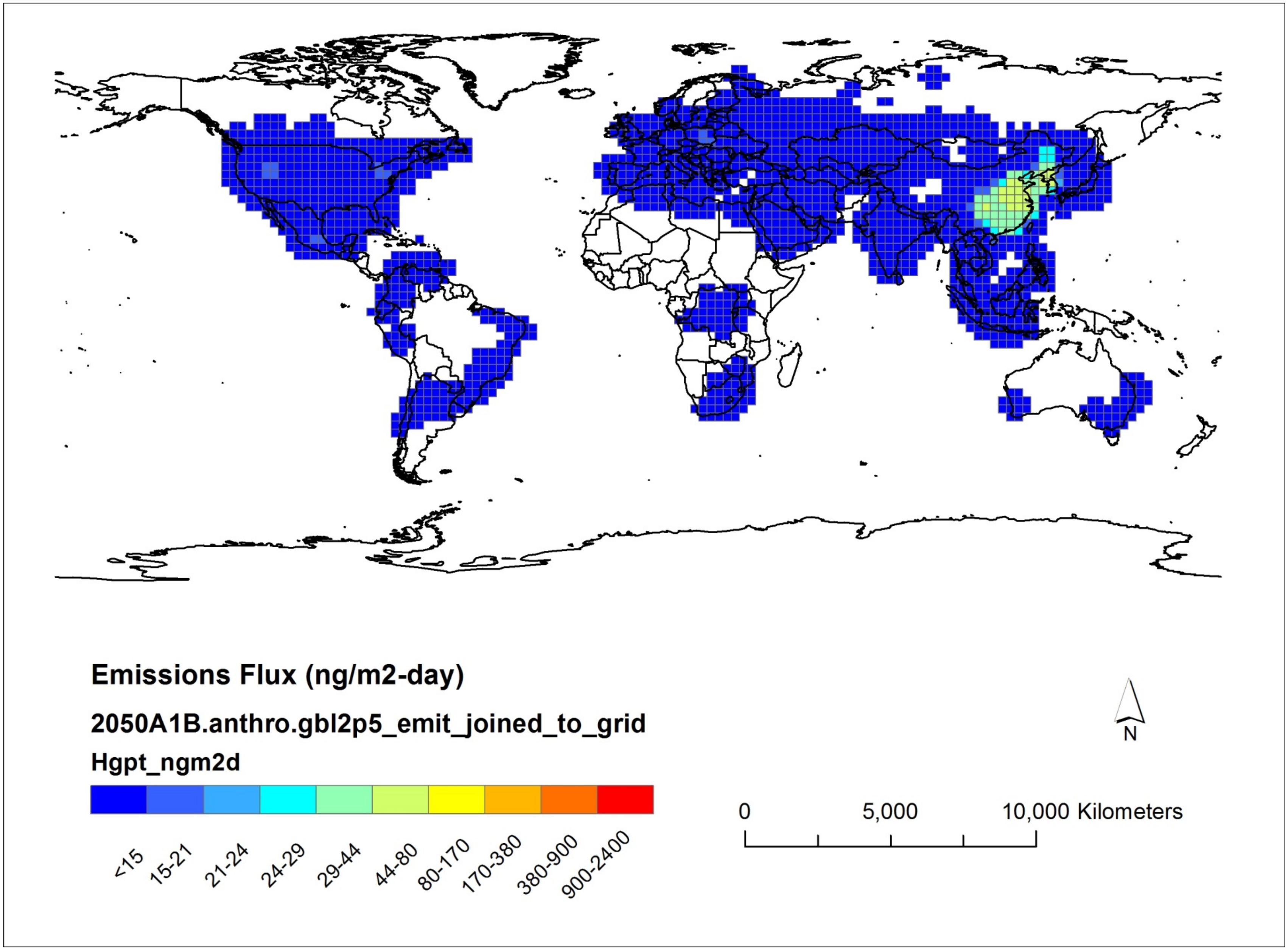
Emissions Flux (ng/m2-day)
2050A1B.anthro.gbl2p5_emit_joined_to_grid
Hgpt_ngm2d
<15
15-21
21-24
24-29
29-44
44-80
80-170
170-380
380-900
900-2400
0
5,000
10,000 Kilometers
N

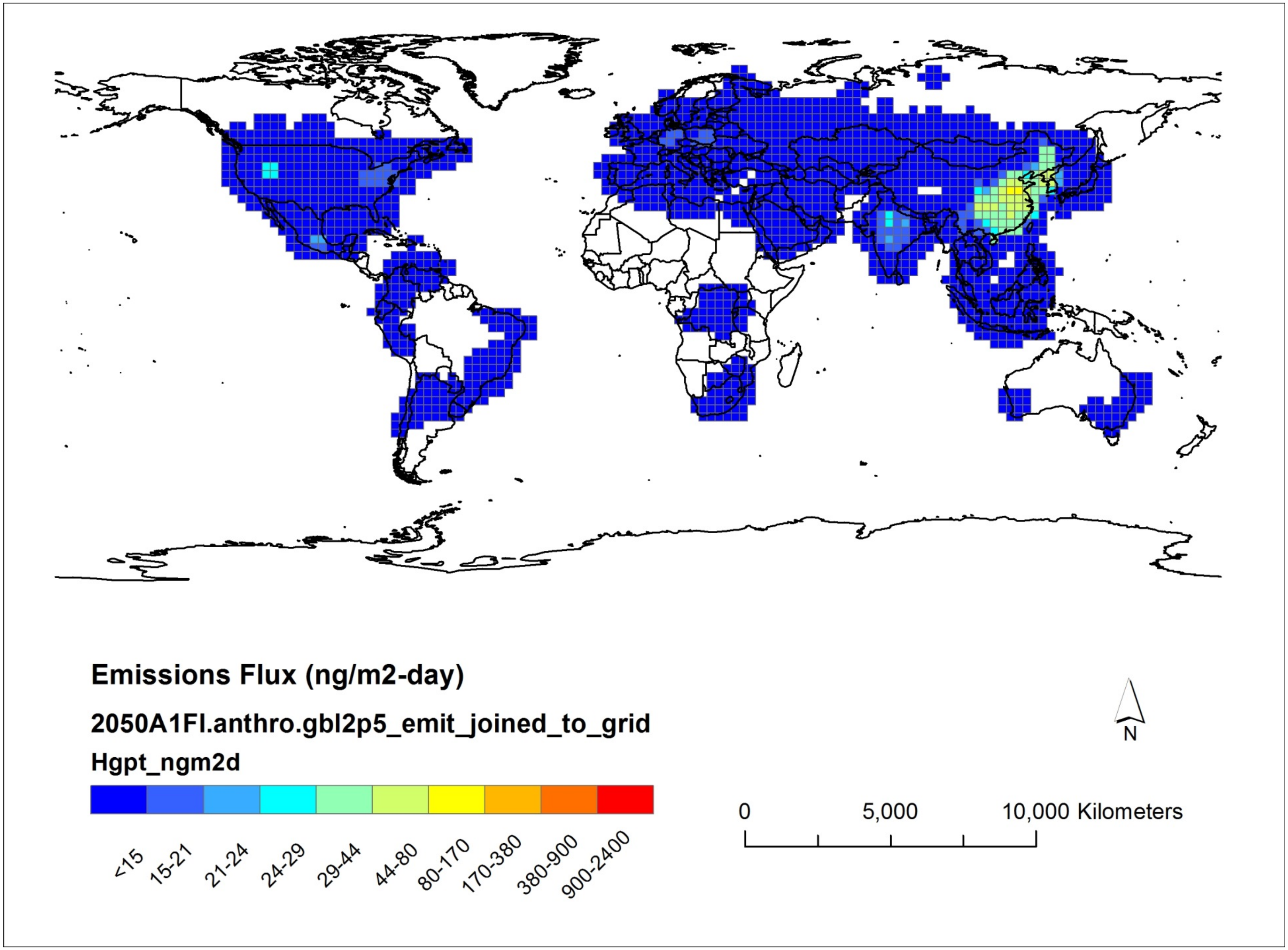
Emissions Flux (ng/m2-day)
2050A1FI.anthro.gbl2p5_emit_joined_to_grid
Hgpt_ngm2d
<15
15-21
21-24
24-29
29-44
44-80
80-170
170-380
380-900
900-2400
0
5,000
10,000 Kilometers
N

8.4. Anthropogenic, Hg(total)

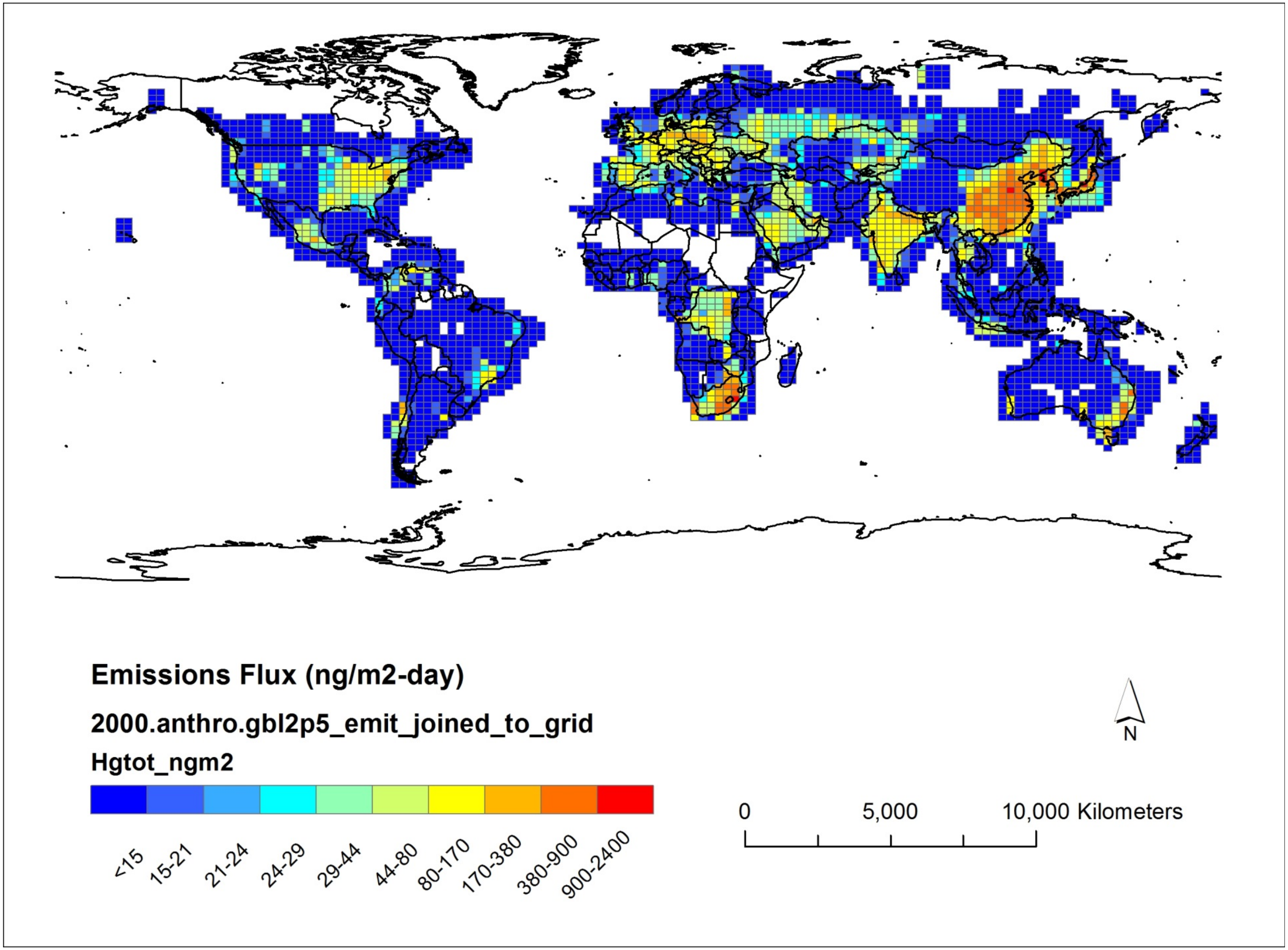
Emissions Flux (ng/m2-day)
2000.anthro.gbl2p5_emit_joined_to_grid
Hgtot_ngm2
<15
15-21
21-24
24-29
29-44
44-80
80-170
170-380
380-900
900-2400
0
5,000
10,000 Kilometers
N

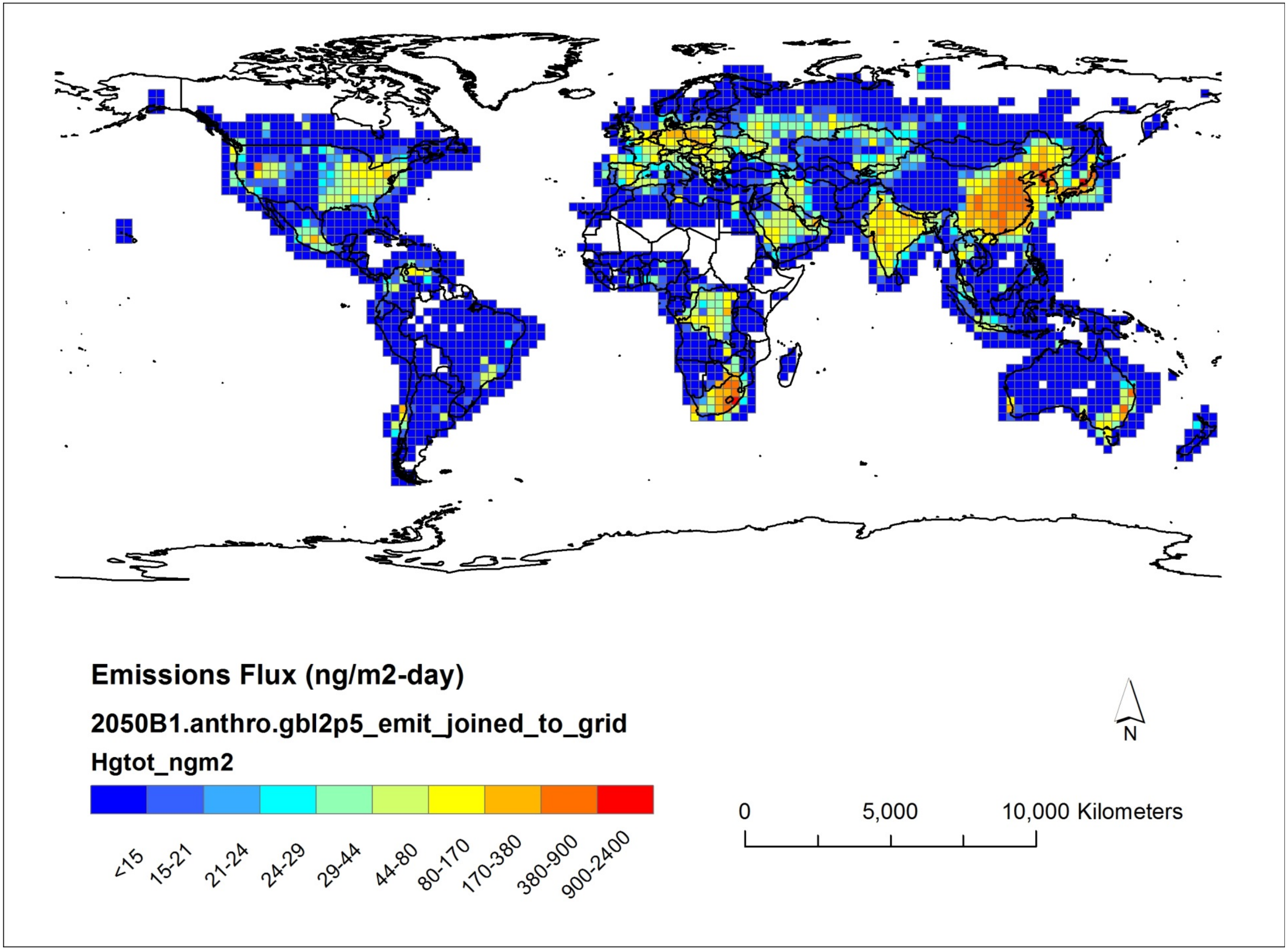
Emissions Flux (ng/m2-day)
2050B1.anthro.gbl2p5_emit_joined_to_grid
Hgtot_ngm2
<15
15-21
21-24
24-29
29-44
44-80
80-170
170-380
380-900
900-2400
0
5,000
10,000 Kilometers
N

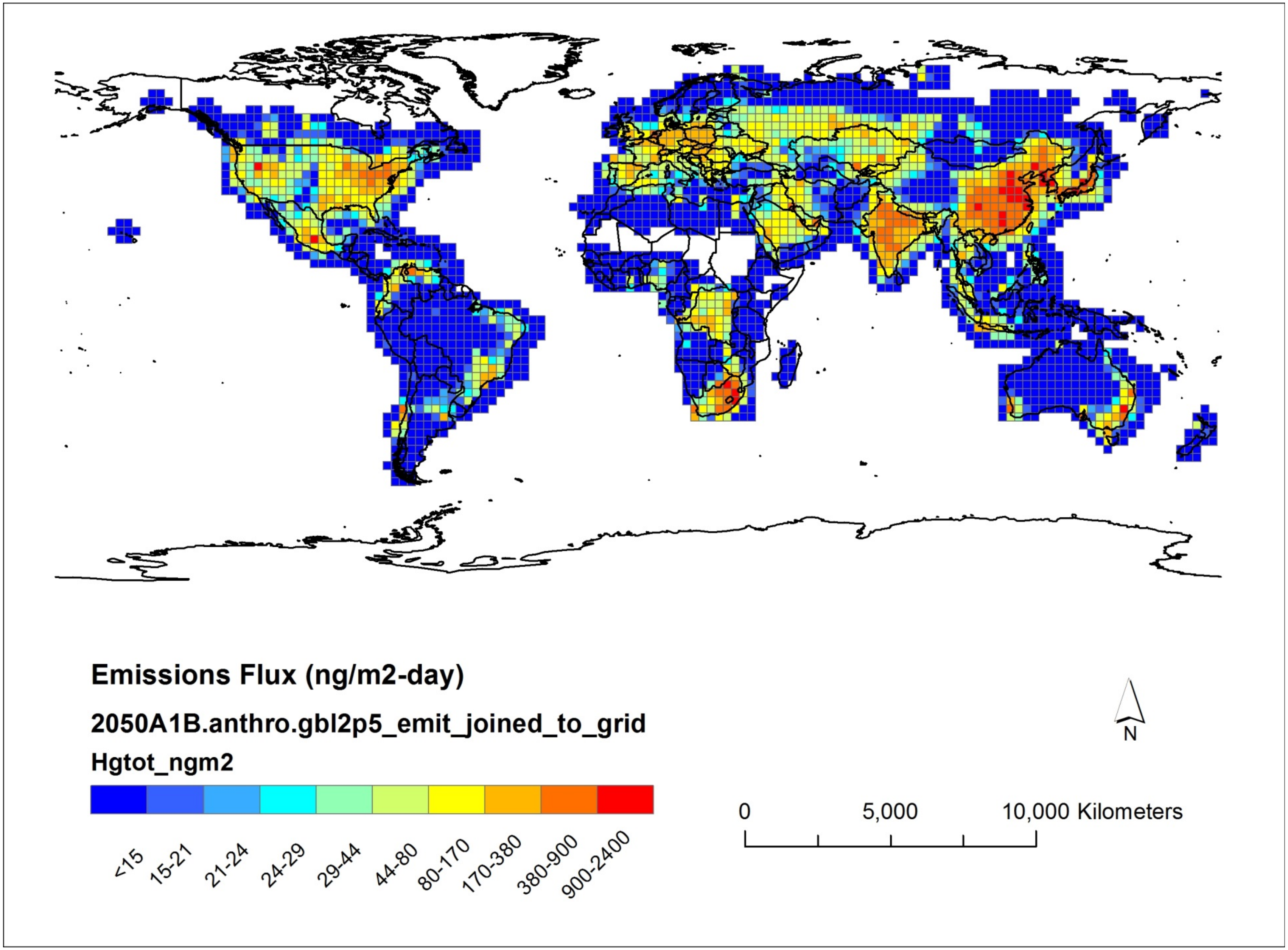
Emissions Flux (ng/m2-day)
2050A1B.anthro.gbl2p5_emit_joined_to_grid
Hgtot_ngm2
<15
15-21
21-24
24-29
29-44
44-80
80-170
170-380
380-900
900-2400
0
5,000
10,000 Kilometers
N

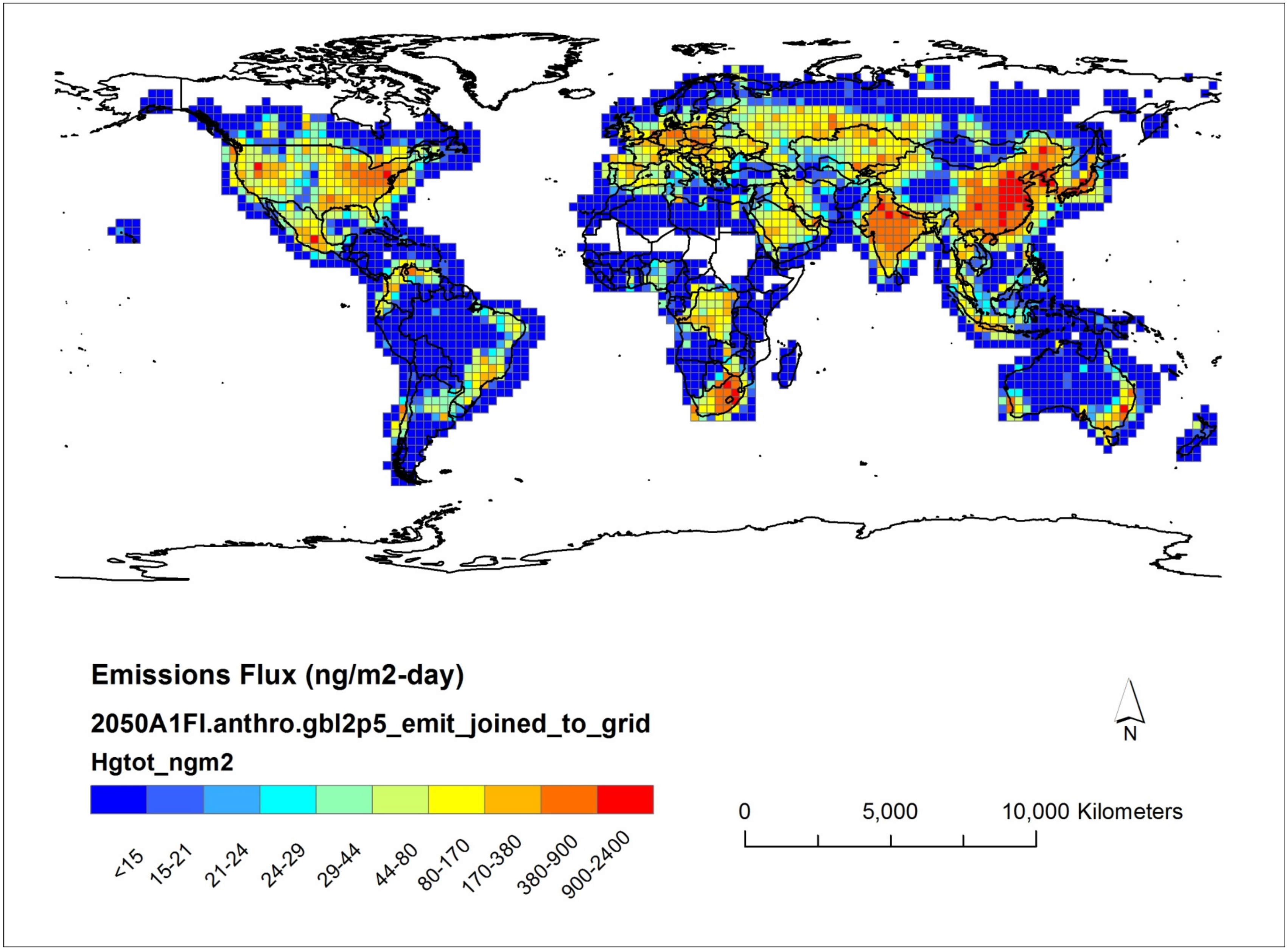
Emissions Flux (ng/m2-day)
2050A1FI.anthro.gbl2p5_emit_joined_to_grid
Hgtot_ngm2
<15
15-21
21-24
24-29
29-44
44-80
80-170
170-380
380-900
900-2400
0
5,000
10,000 Kilometers
N

8.5. Biomass

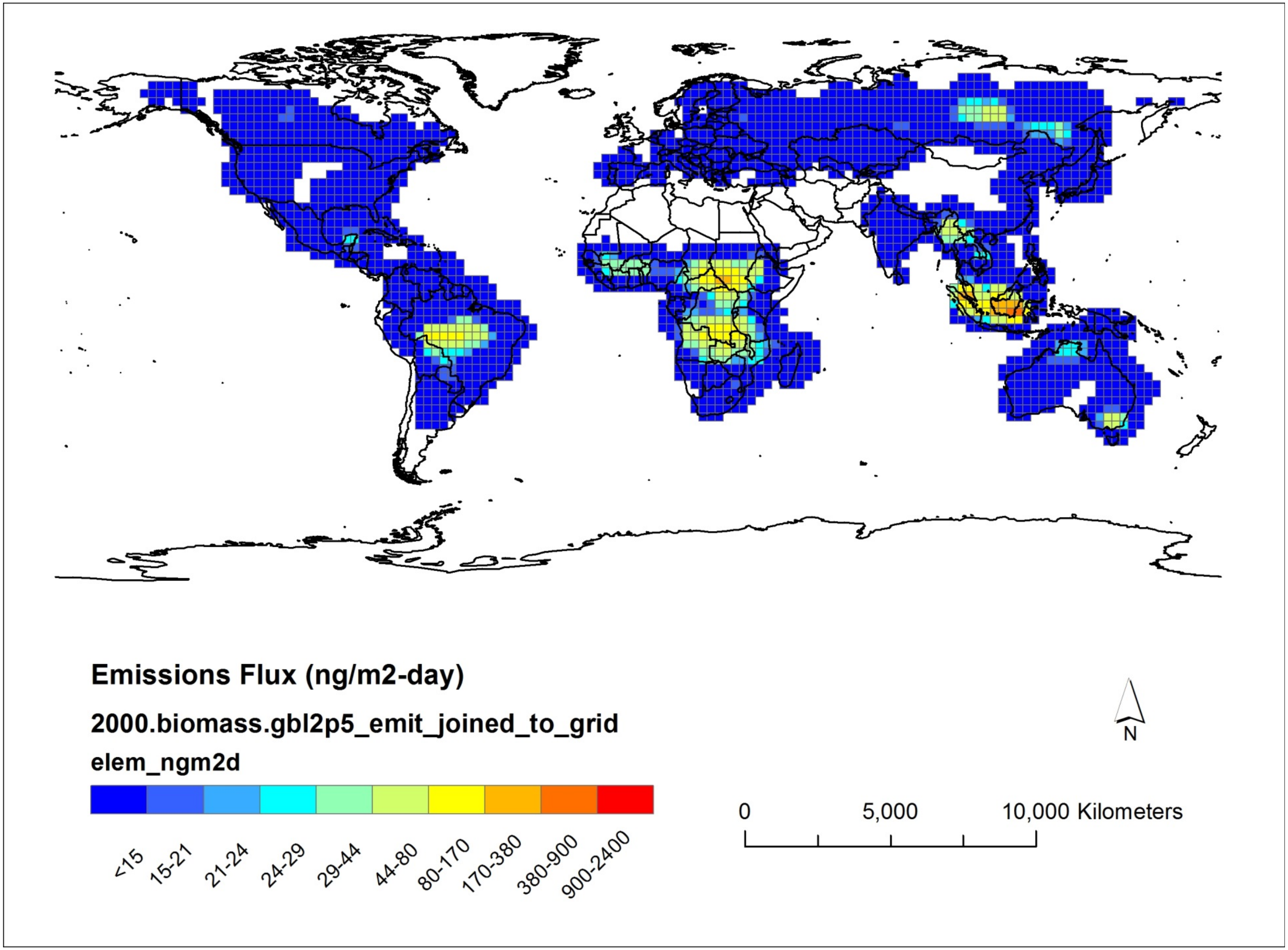
Emissions Flux (ng/m2-day)
2000.biomass.gbl2p5_emit_joined_to_grid
elem_ngm2d
<15
15-21
21-24
24-29
29-44
44-80
80-170
170-380
380-900
900-2400
N
0
5,000
10,000 Kilometers

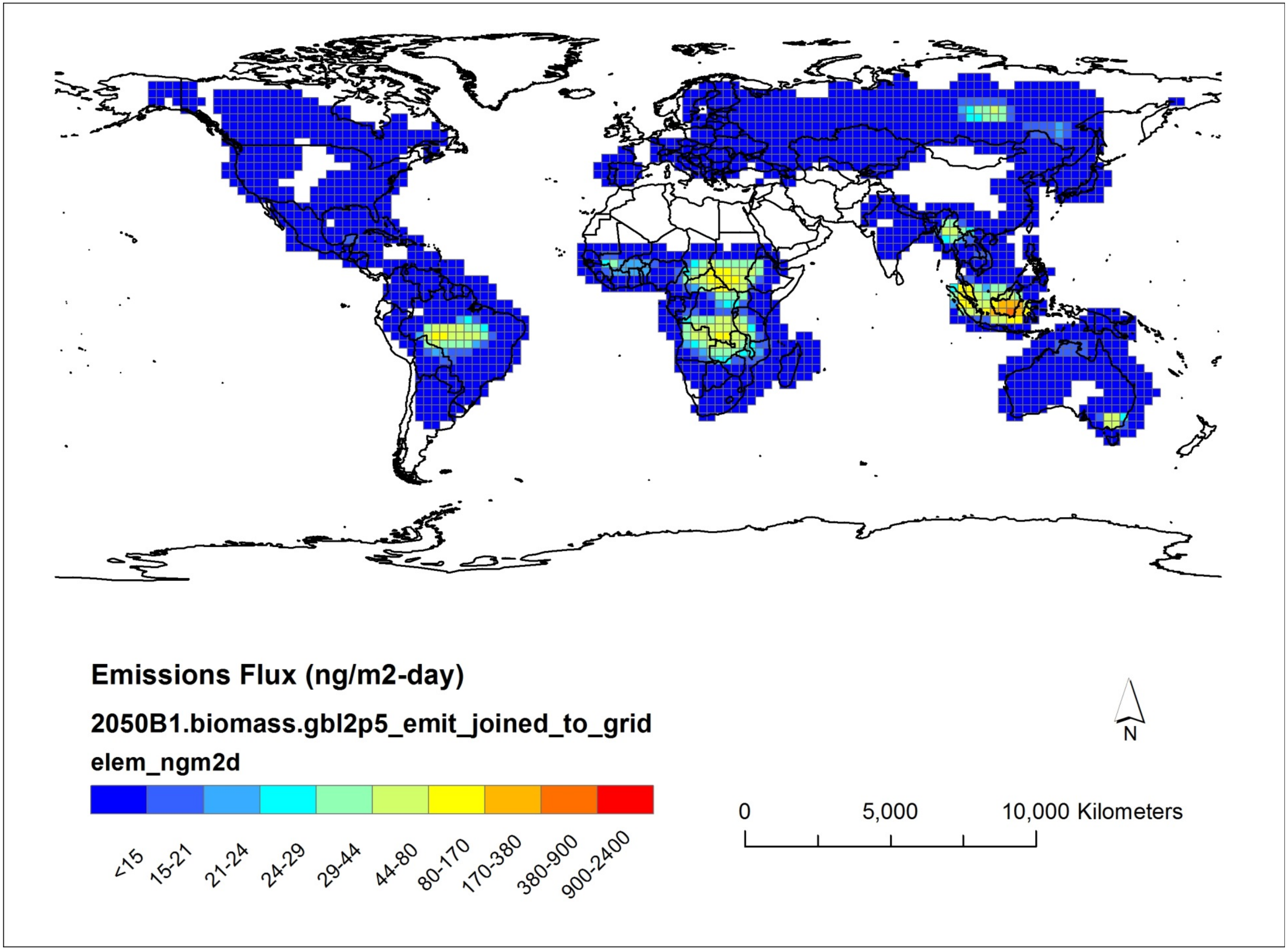
Emissions Flux (ng/m2-day)
2050B1.biomass.gbl2p5_emit_joined_to_grid
elem_ngm2d
<15
15-21
21-24
24-29
29-44
44-80
80-170
170-380
380-900
900-2400
N
0
5,000
10,000 Kilometers

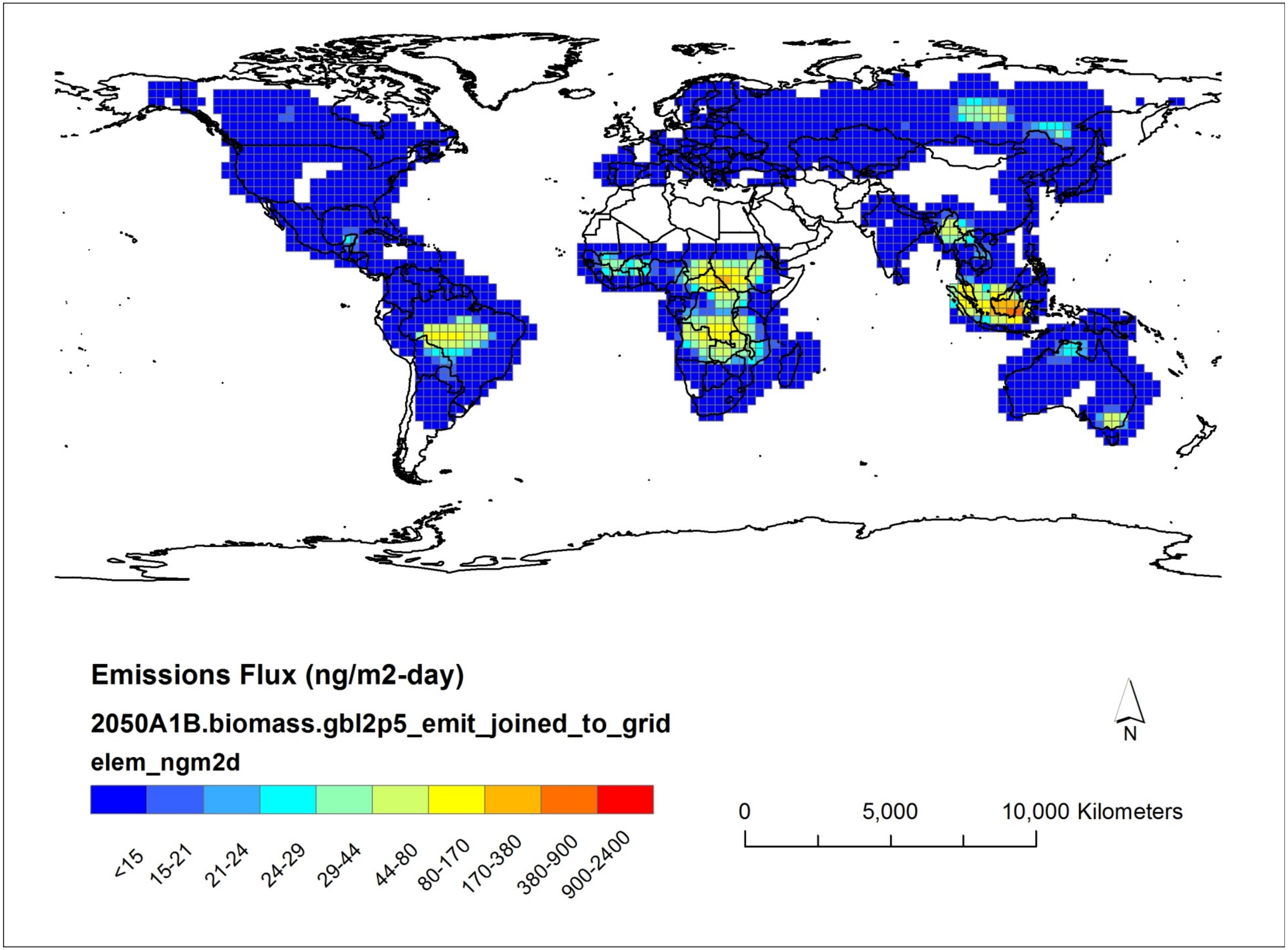
Emissions Flux (ng/m2-day)
2050A1B.biomass.gbl2p5_emit_joined_to_grid
elem_ngm2d
<15
15-21
21-24
24-29
29-44
44-80
80-170
170-380
380-900
900-2400
0
5,000
10,000 Kilometers
N

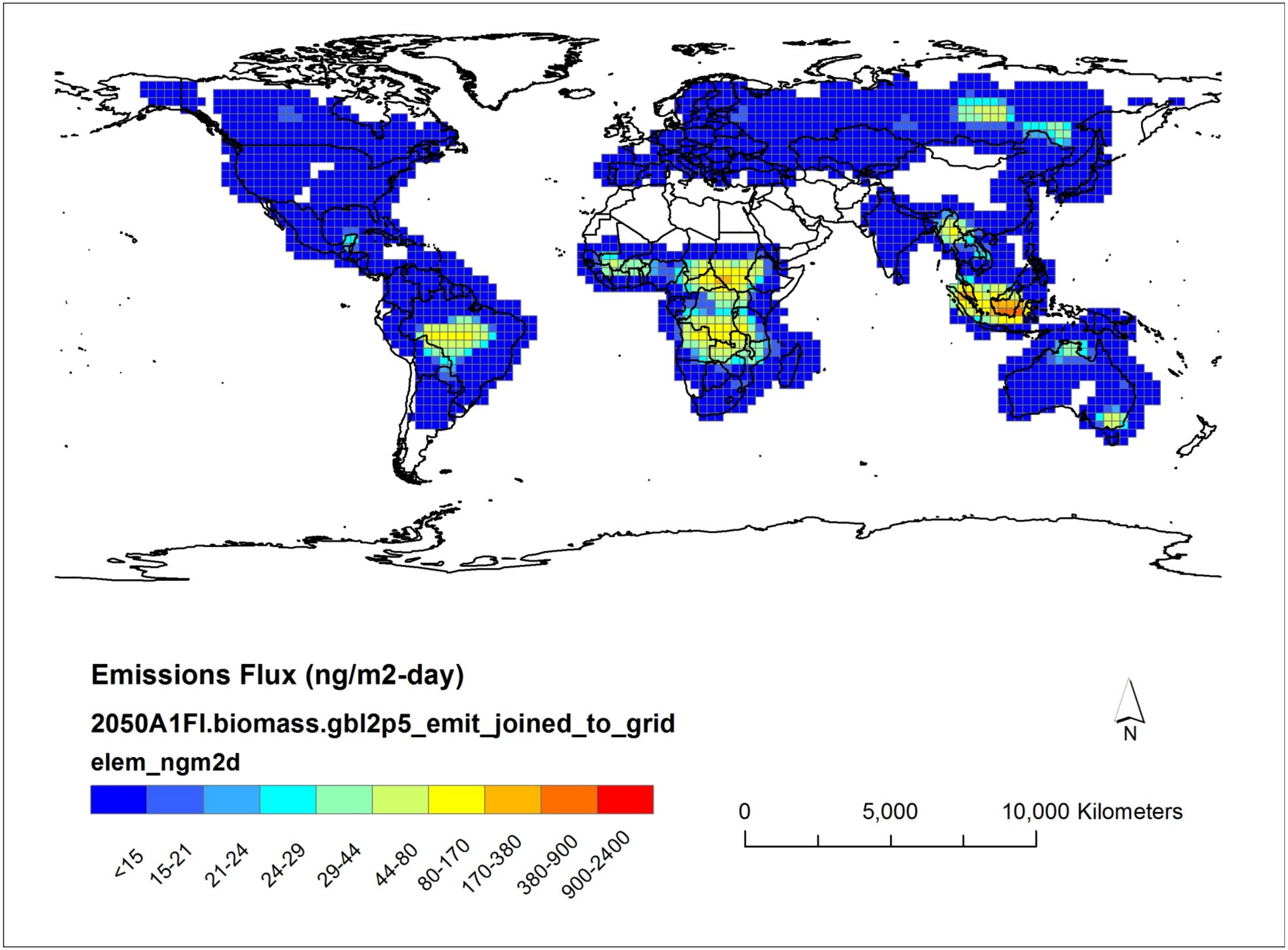
Emissions Flux (ng/m2-day)
2050A1FI.biomass.gbl2p5_emit_joined_to_grid
elem_ngm2d
<15
15-21
21-24
24-29
29-44
44-80
80-170
170-380
380-900
900-2400
0
5,000
10,000 Kilometers
N

8.6. Land

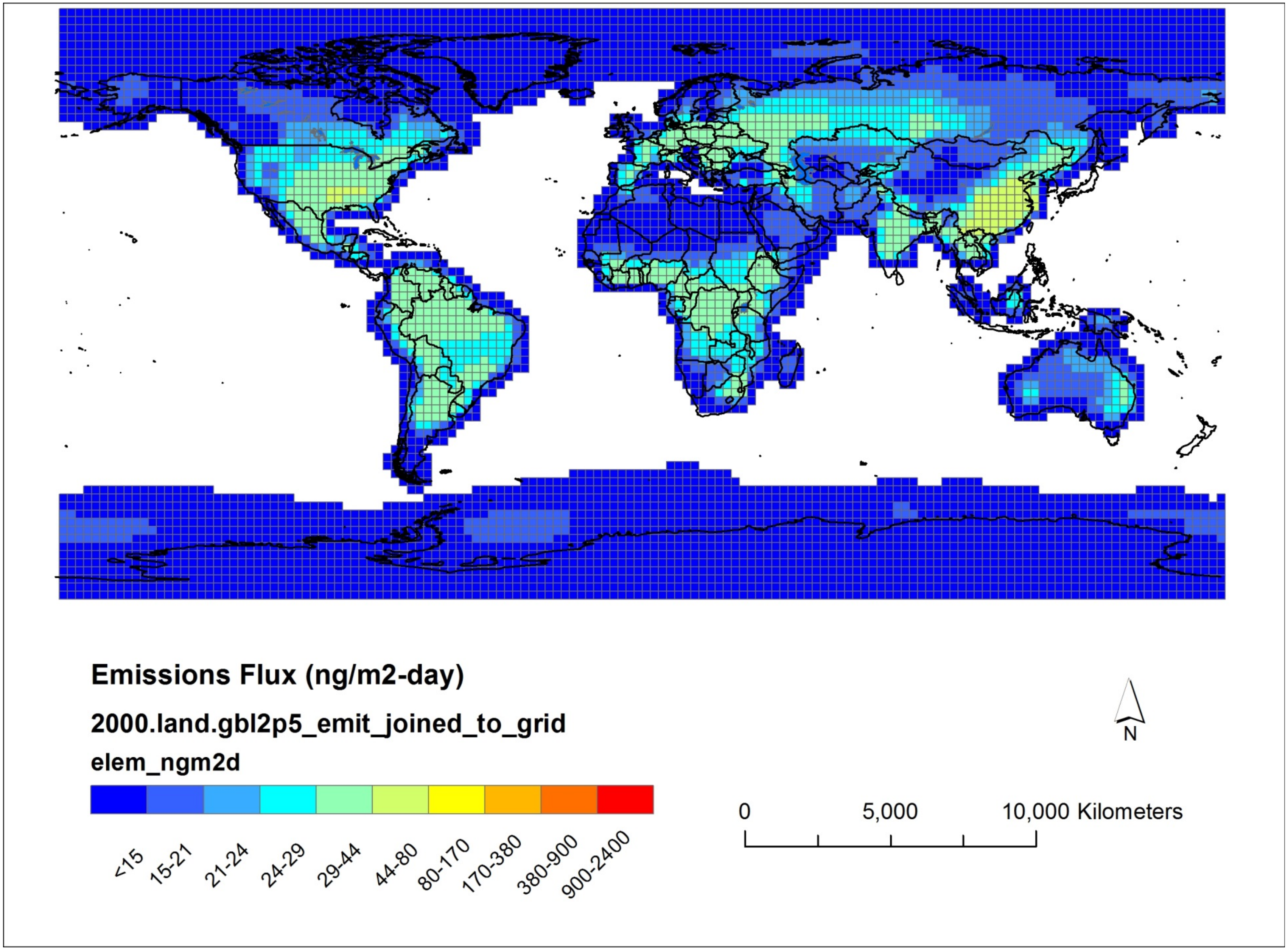
Emissions Flux (ng/m2-day)
2000.land.gbl2p5_emit_joined_to_grid
elem_ngm2d
<15
15-21
21-24
24-29
29-44
44-80
80-170
170-380
380-900
900-2400
N
0
5,000
10,000 Kilometers

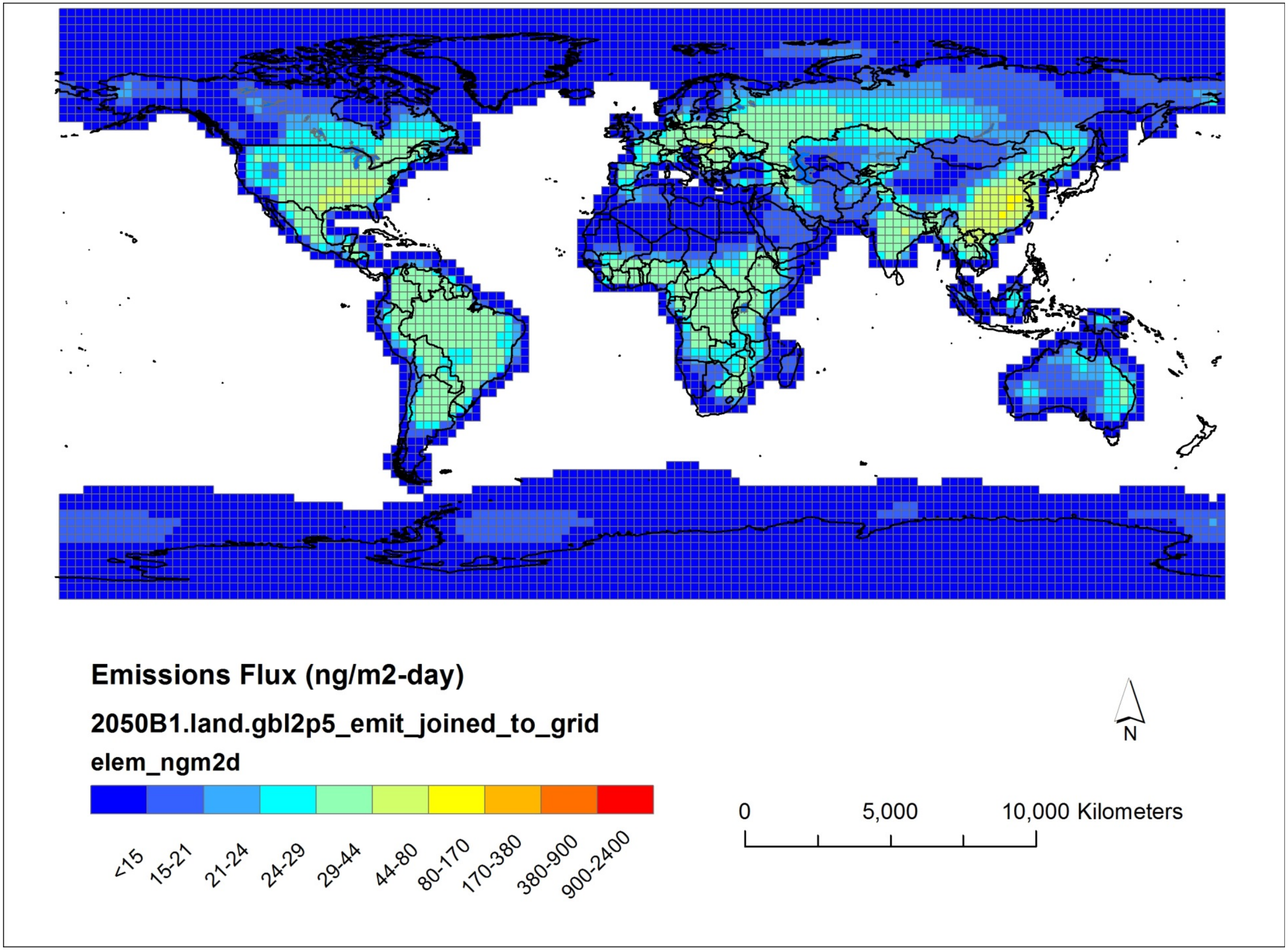
Emissions Flux (ng/m2-day)
2050B1.land.gbl2p5_emit_joined_to_grid
elem_ngm2d
<15
15-21
21-24
24-29
29-44
44-80
80-170
170-380
380-900
900-2400
0
5,000
10,000 Kilometers
N

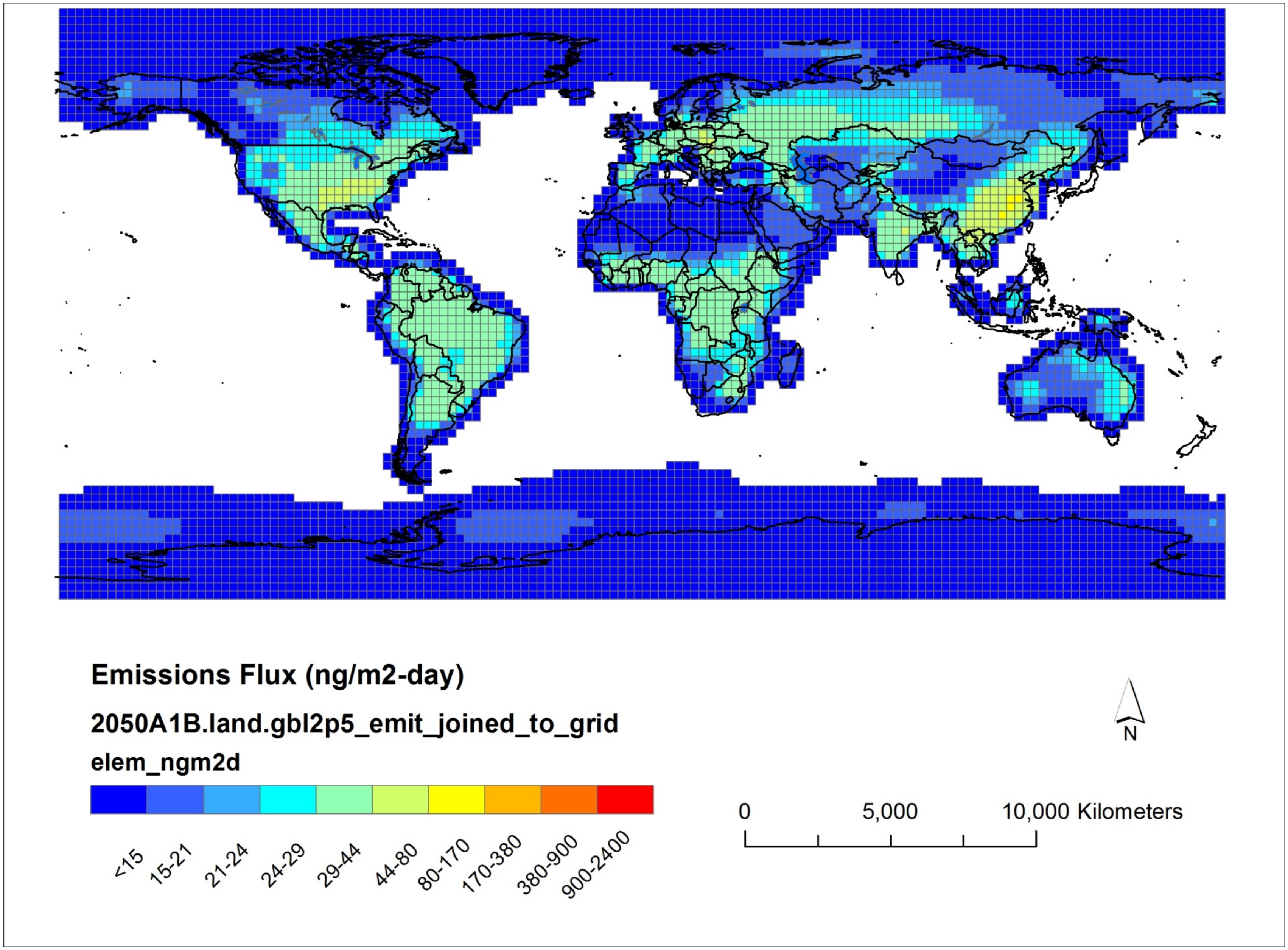
Emissions Flux (ng/m2-day)
2050A1B.land.gbl2p5_emit_joined_to_grid
elem_ngm2d
<15
15-21
21-24
24-29
29-44
44-80
80-170
170-380
380-900
900-2400
0
5,000
10,000 Kilometers
N

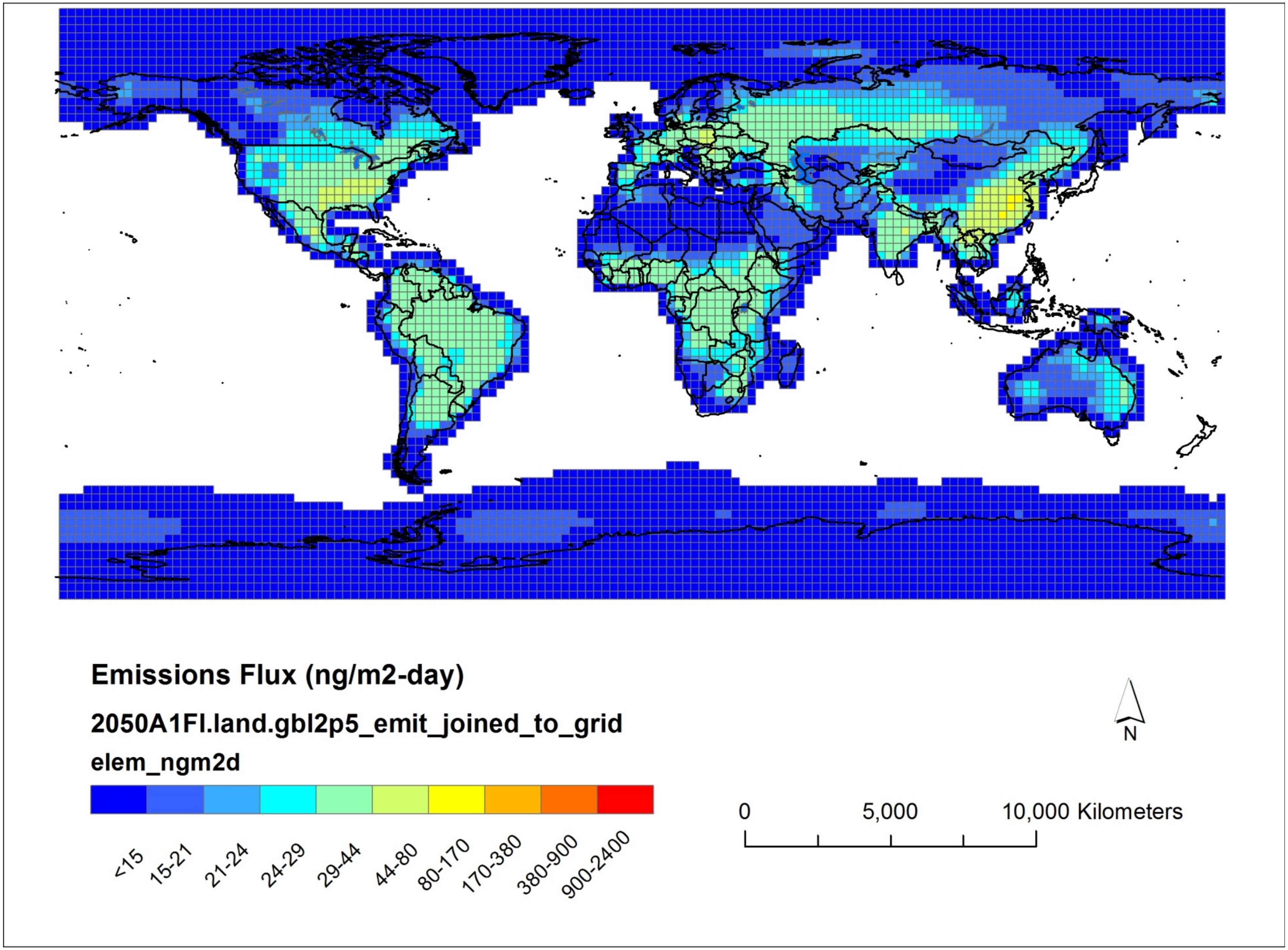
Emissions Flux (ng/m2-day)
2050A1FI.land.gbl2p5_emit_joined_to_grid
elem_ngm2d
<15
15-21
21-24
24-29
29-44
44-80
80-170
170-380
380-900
900-2400
0
5,000
10,000 Kilometers
N

8.7. Ocean

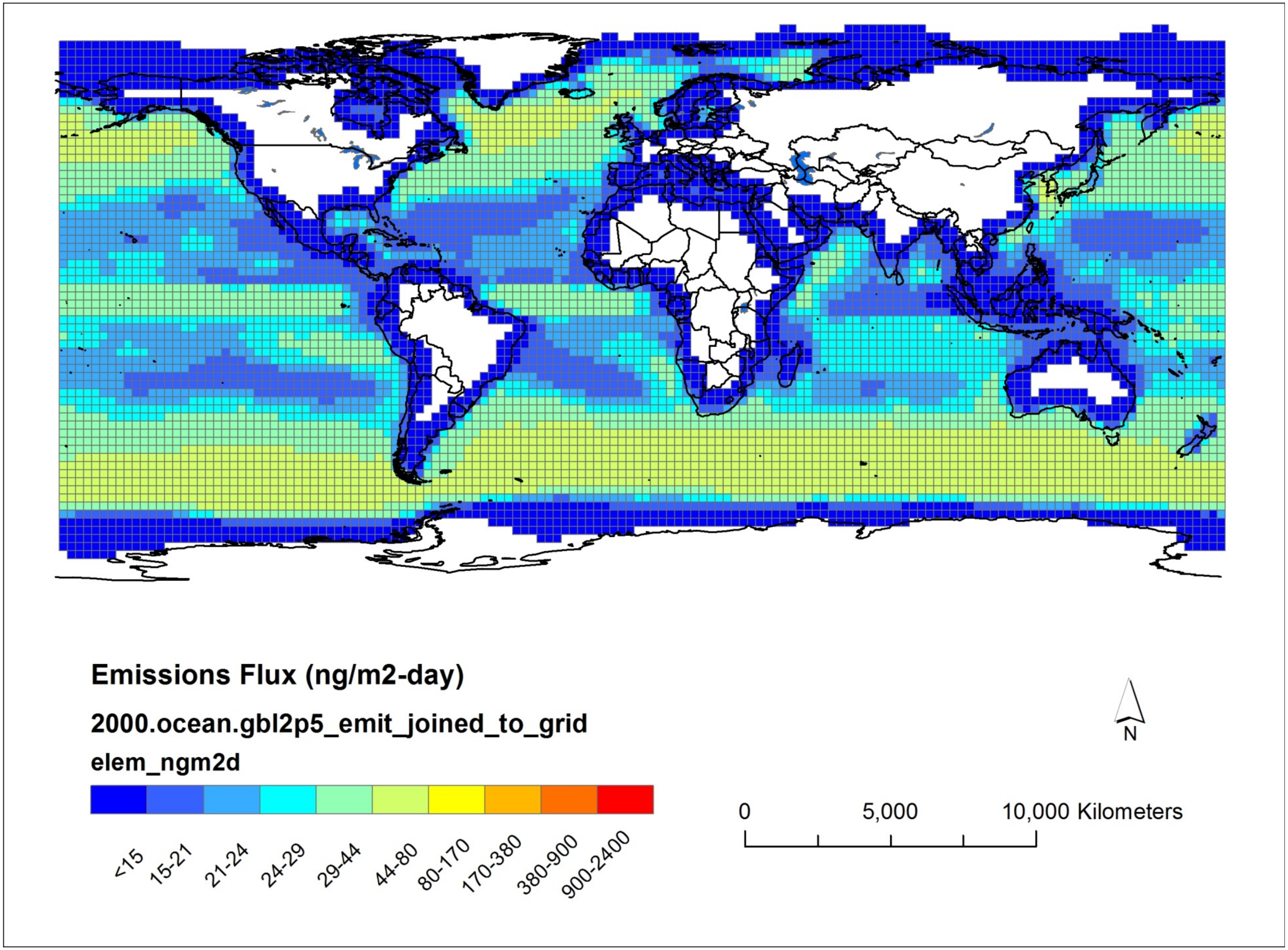
Emissions Flux (ng/m2-day)
2000.ocean.gbl2p5_emit_joined_to_grid
elem_ngm2d
<15
15-21
21-24
24-29
29-44
44-80
80-170
170-380
380-900
900-2400
0
5,000
10,000 Kilometers
N

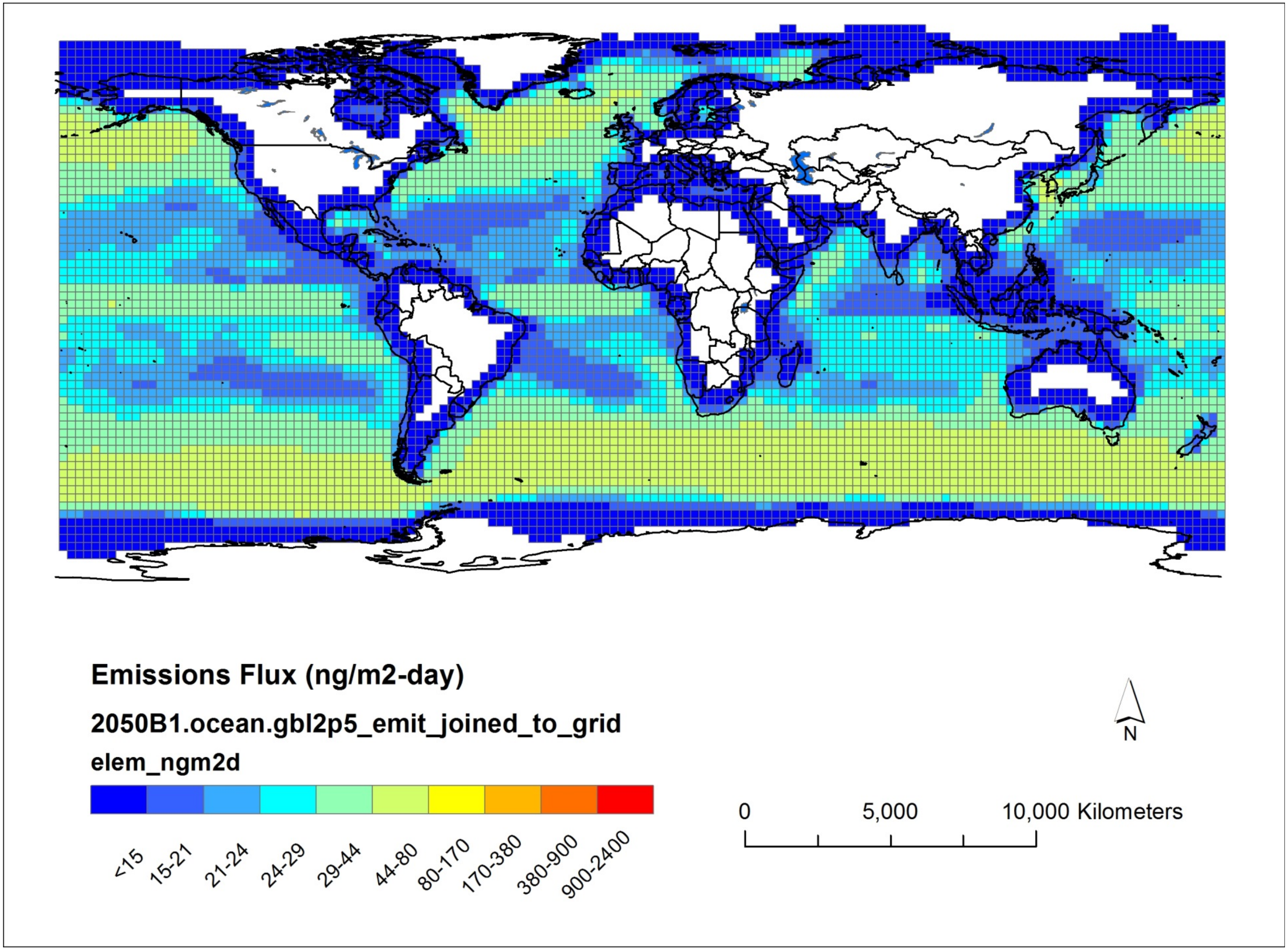
Emissions Flux (ng/m2-day)
2050B1.ocean.gbl2p5_emit_joined_to_grid
elem_ngm2d
<15
15-21
21-24
24-29
29-44
44-80
80-170
170-380
380-900
900-2400
0
5,000
10,000 Kilometers
N

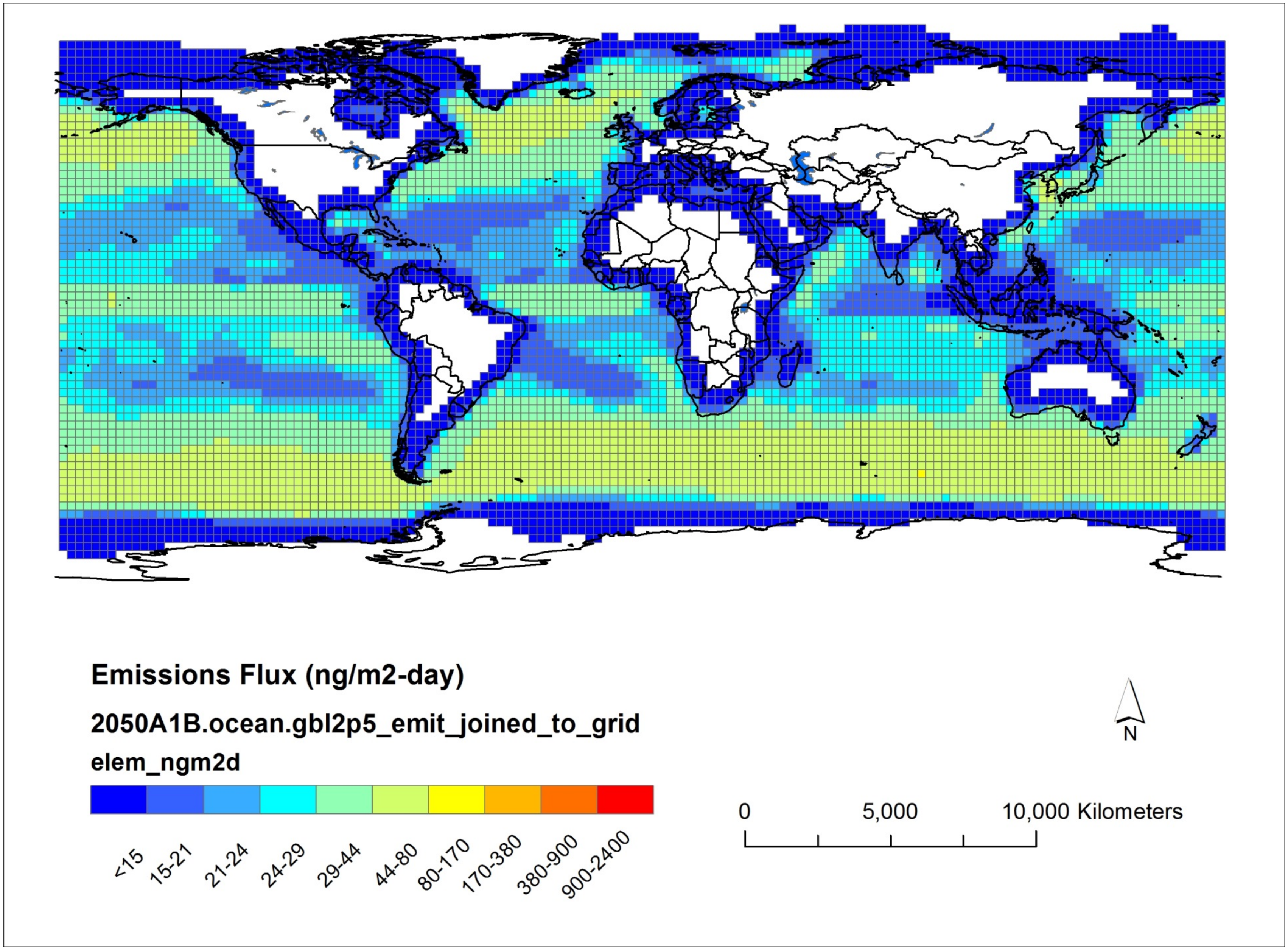
Emissions Flux (ng/m2-day)
2050A1B.ocean.gbl2p5_emit_joined_to_grid
elem_ngm2d
<15
15-21
21-24
24-29
29-44
44-80
80-170
170-380
380-900
900-2400
0
5,000
10,000 Kilometers
N

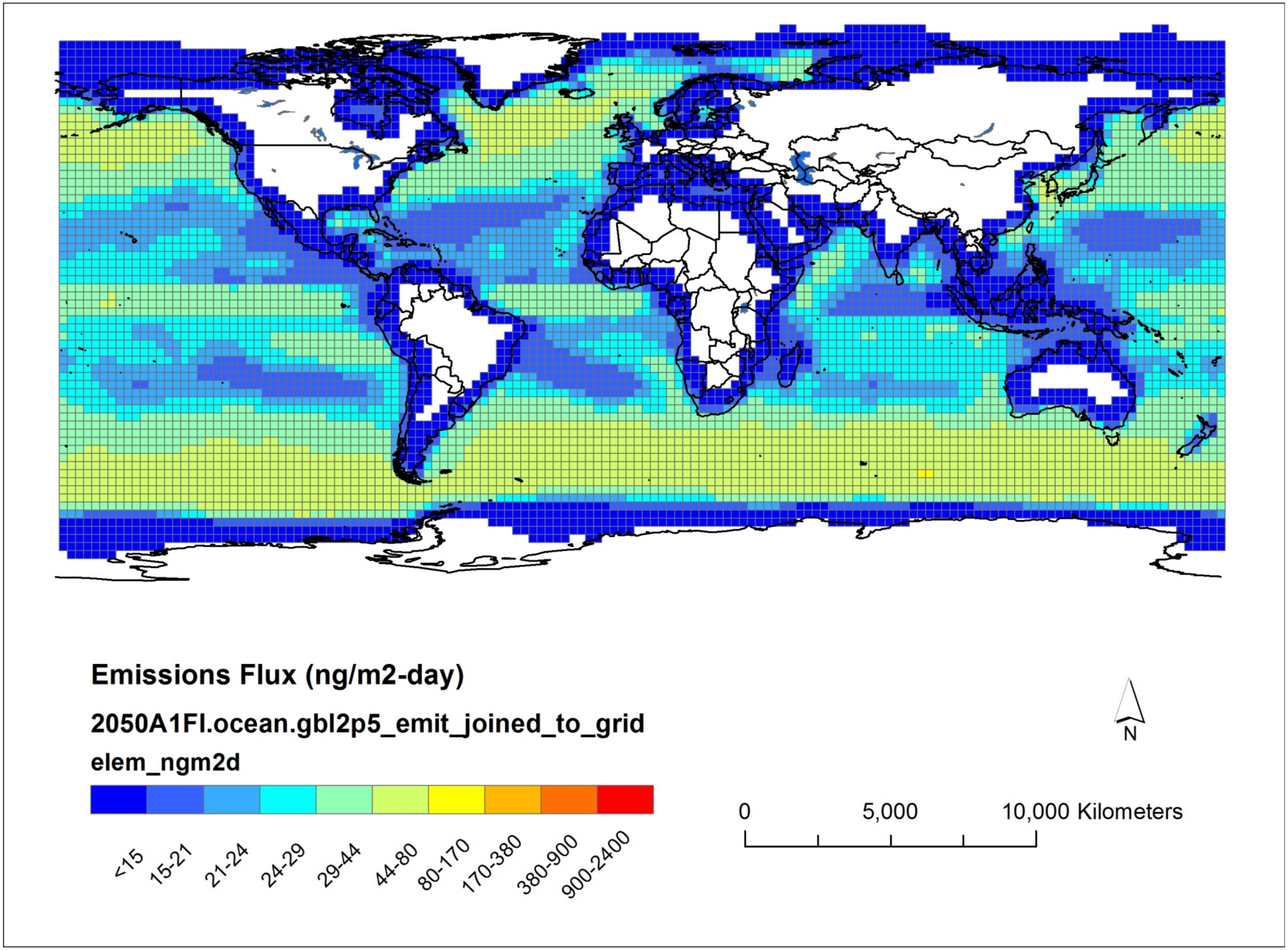
Emissions Flux (ng/m2-day)
2050A1FI.ocean.gbl2p5_emit_joined_to_grid
elem_ngm2d
<15
15-21
21-24
24-29
29-44
44-80
80-170
170-380
380-900
900-2400
N
0
5,000
10,000 Kilometers

8.8. Reemission

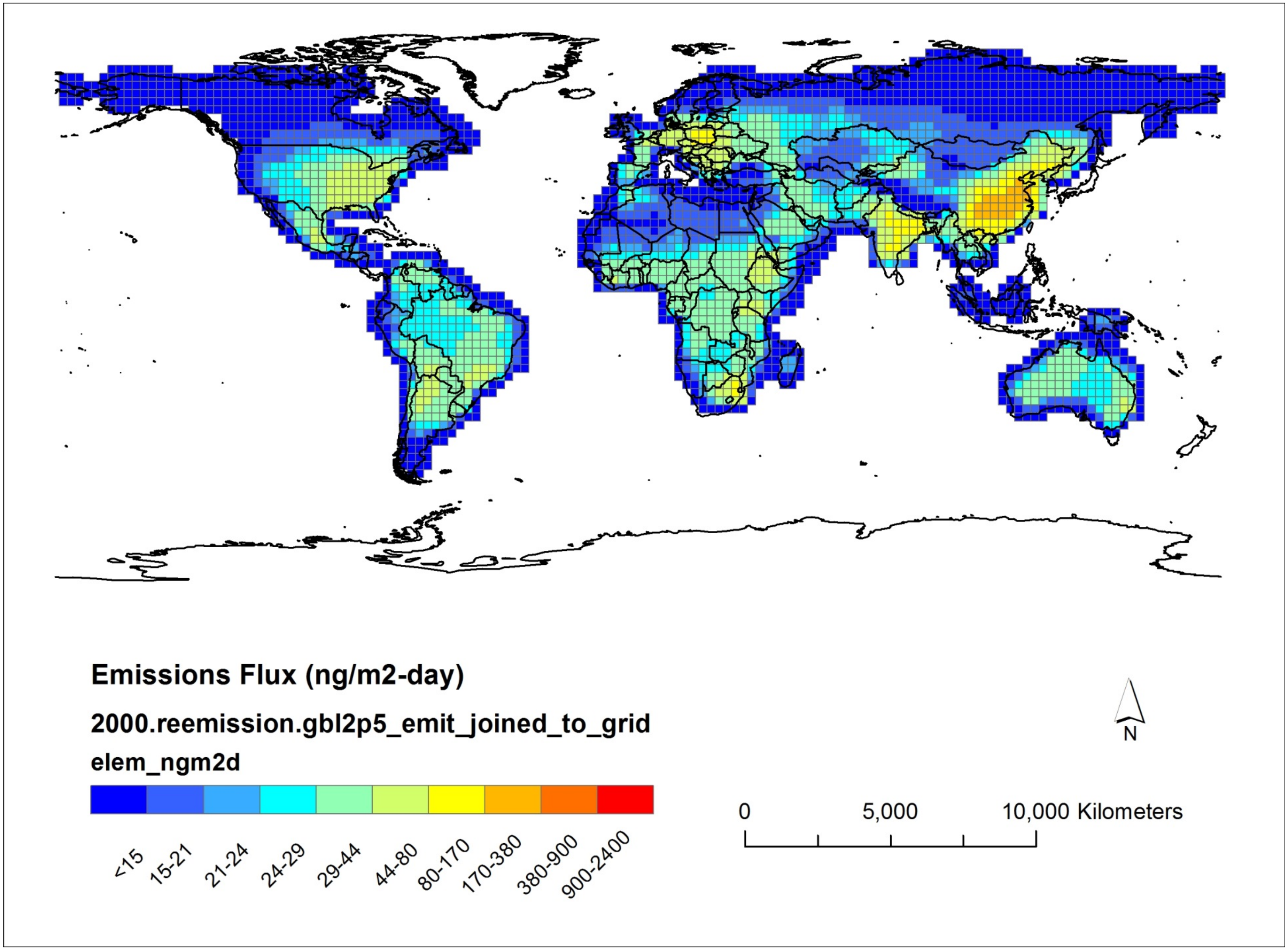
Emissions Flux (ng/m2-day)
2000.reemission.gbl2p5_emit_joined_to_grid
elem_ngm2d
<15
15-21
21-24
24-29
29-44
44-80
80-170
170-380
380-900
900-2400
0
5,000
10,000 Kilometers
N

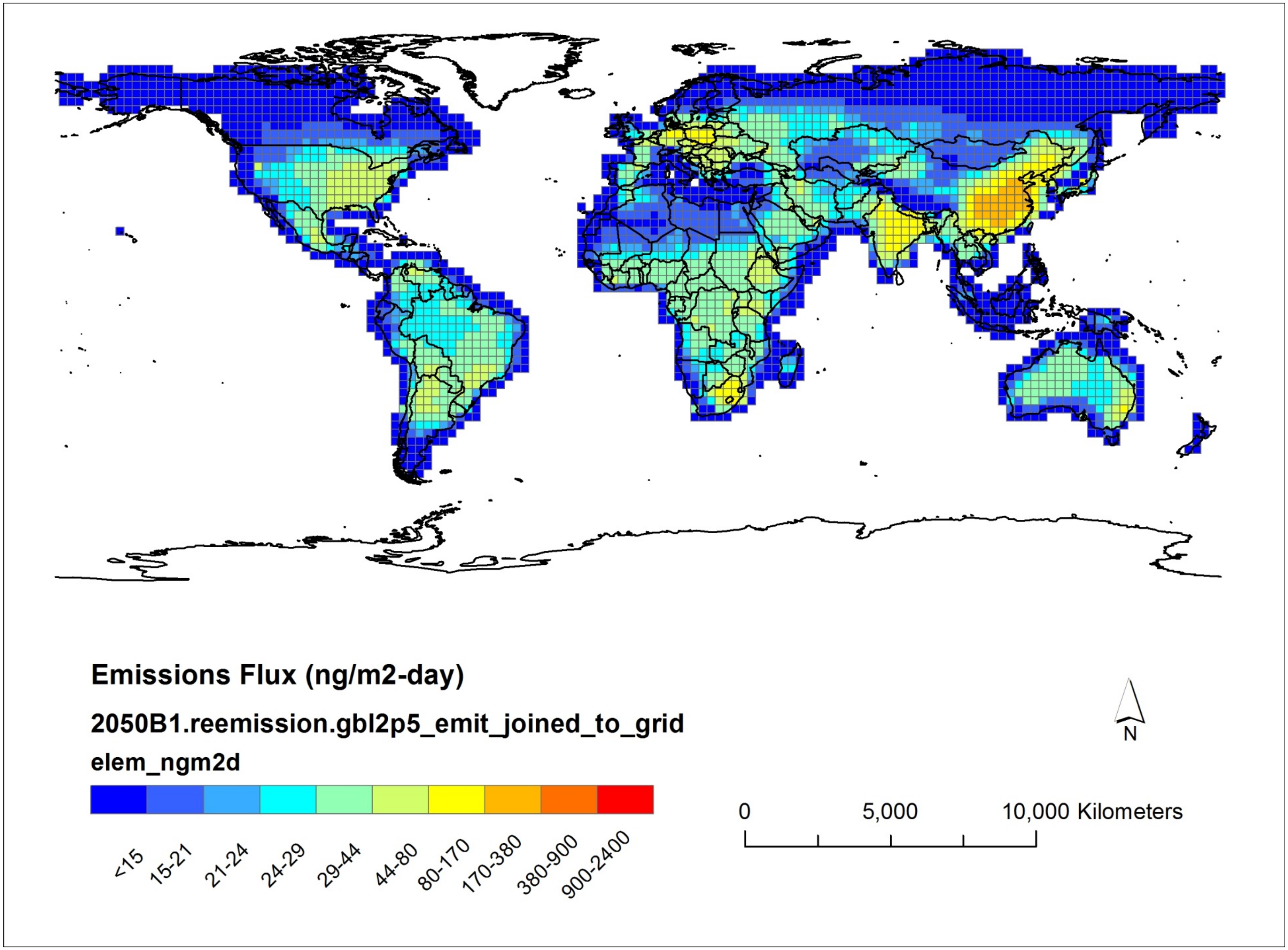
Emissions Flux (ng/m2-day)
2050B1.reemission.gbl2p5_emit_joined_to_grid
elem_ngm2d
<15
15-21
21-24
24-29
29-44
44-80
80-170
170-380
380-900
900-2400
0
5,000
10,000 Kilometers
N

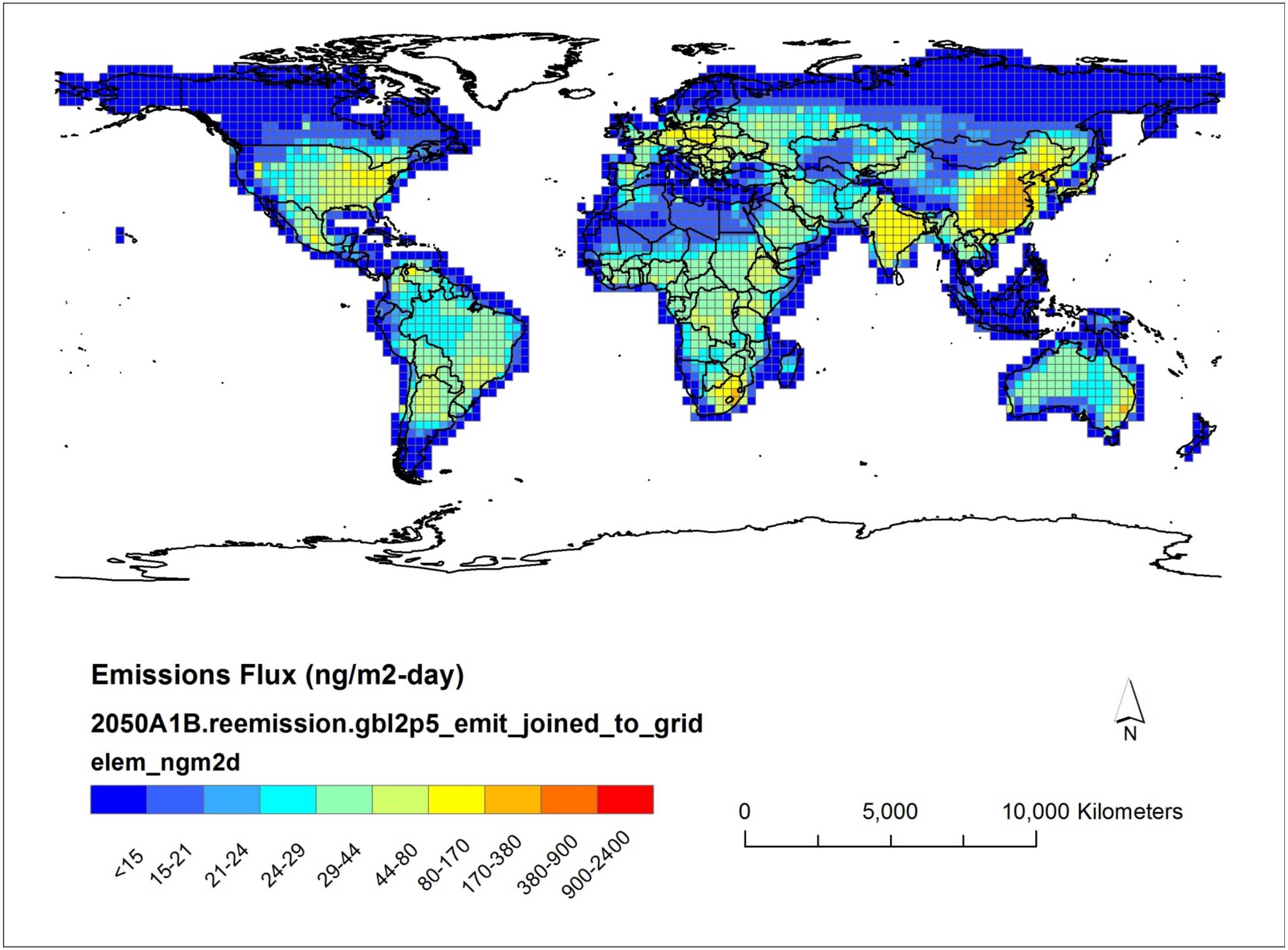
Emissions Flux (ng/m2-day)
2050A1B.reemission.gbl2p5_emit_joined_to_grid
elem_ngm2d
<15
15-21
21-24
24-29
29-44
44-80
80-170
170-380
380-900
900-2400
0
5,000
10,000 Kilometers
N

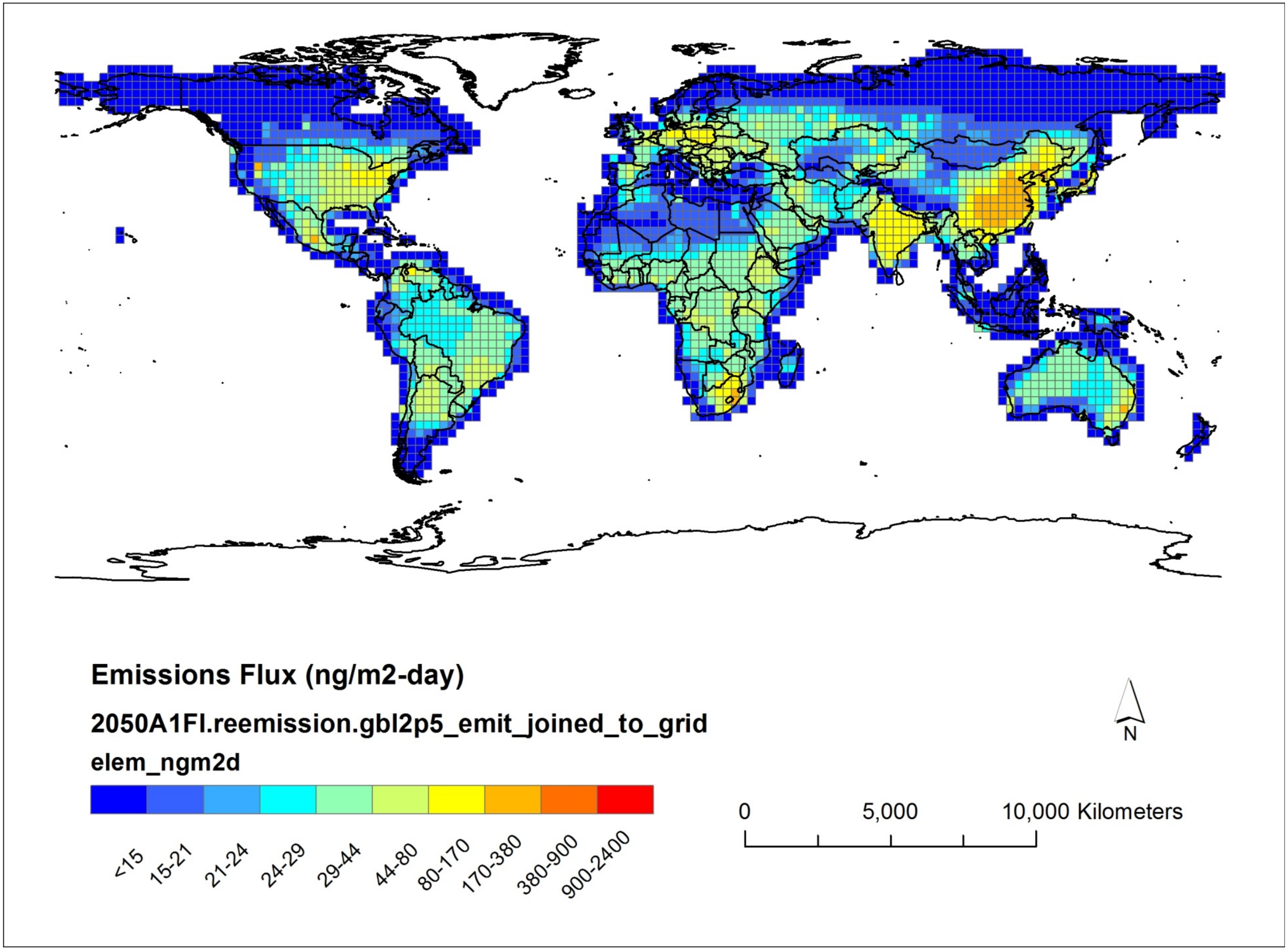
Emissions Flux (ng/m2-day)
2050A1FI.reemission.gbl2p5_emit_joined_to_grid
elem_ngm2d
<15
15-21
21-24
24-29
29-44
44-80
80-170
170-380
380-900
900-2400
0
5,000
10,000 Kilometers
N

8.9. Volcano

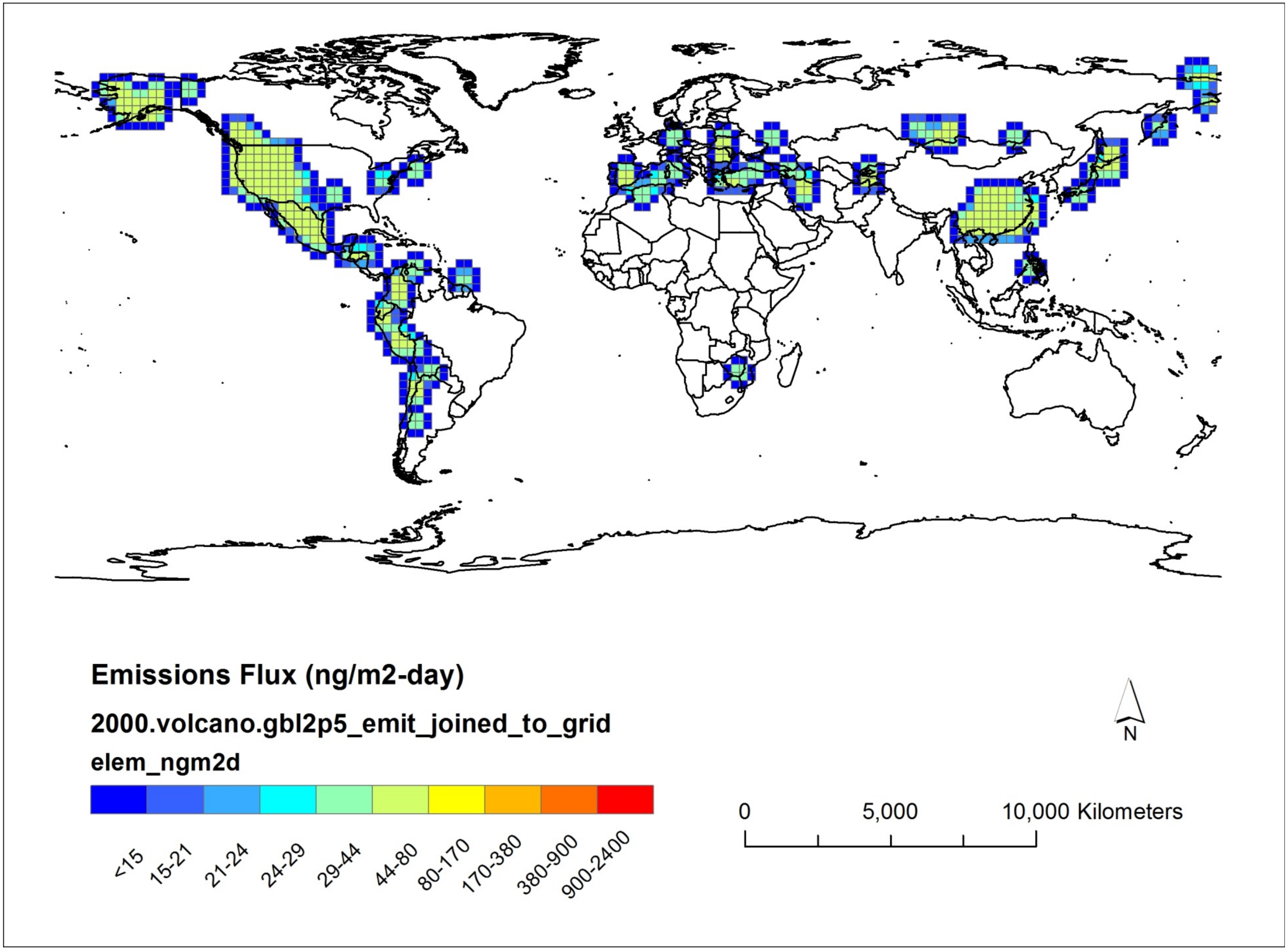
Emissions Flux (ng/m2-day)
2000.volcano.gbl2p5_emit_joined_to_grid
elem_ngm2d
<15
15-21
21-24
24-29
29-44
44-80
80-170
170-380
380-900
900-2400
N
0
5,000
10,000 Kilometers

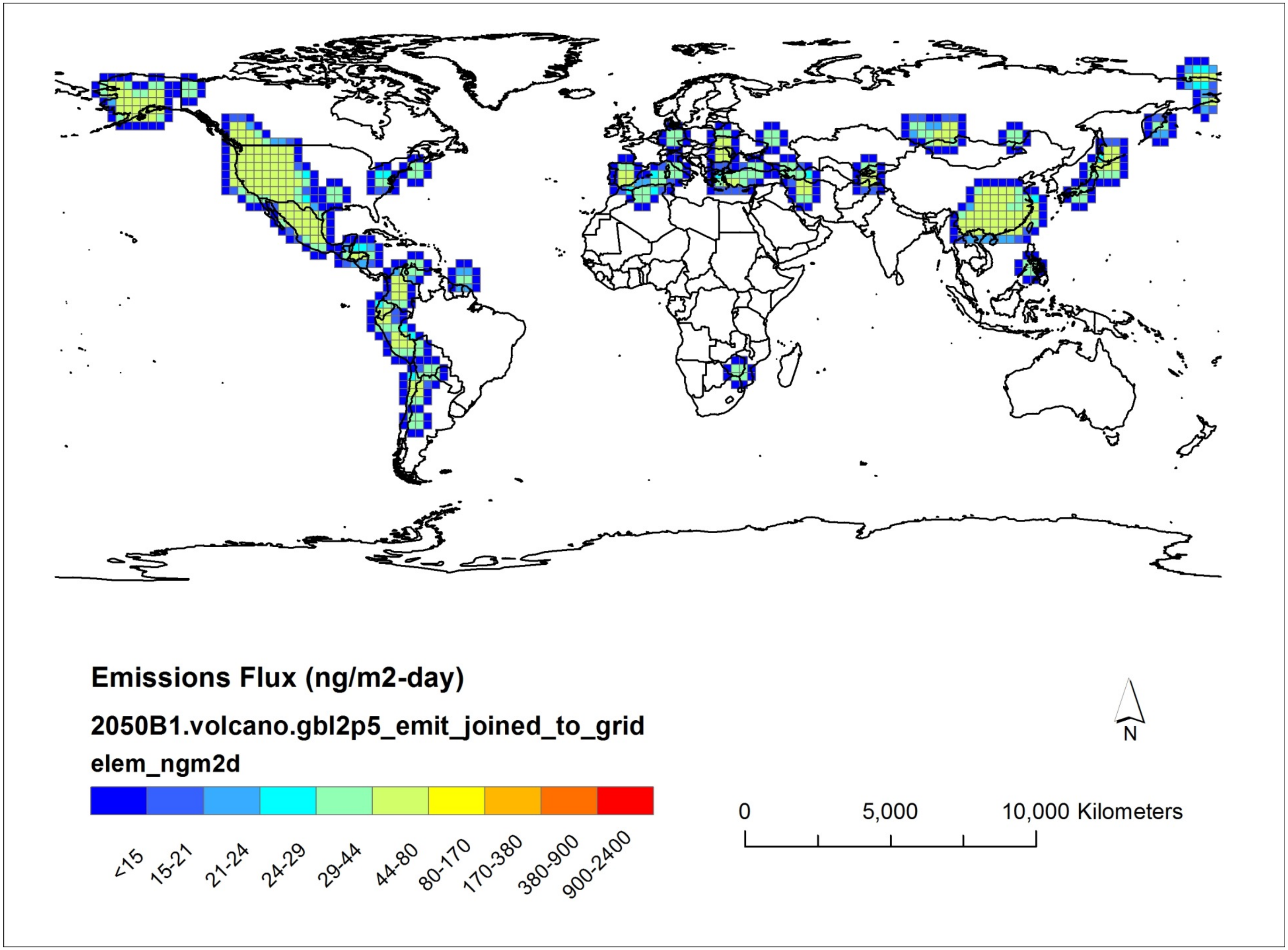
Emissions Flux (ng/m2-day)
2050B1.volcano.gbl2p5_emit_joined_to_grid
elem_ngm2d
<15
15-21
21-24
24-29
29-44
44-80
80-170
170-380
380-900
900-2400
0
5,000
10,000 Kilometers
N

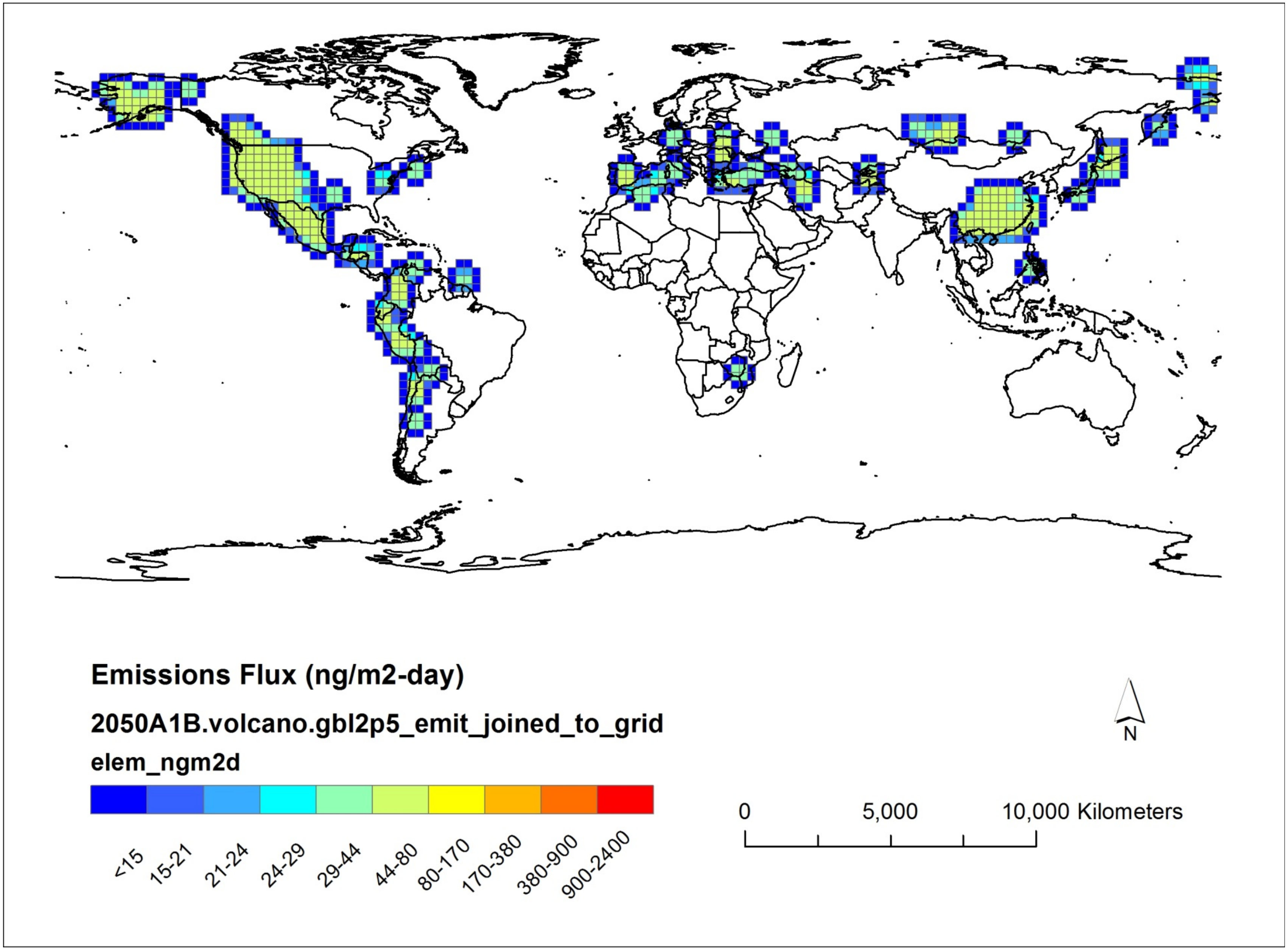
Emissions Flux (ng/m2-day)
2050A1B.volcano.gbl2p5_emit_joined_to_grid
elem_ngm2d
<15
15-21
21-24
24-29
29-44
44-80
80-170
170-380
380-900
900-2400
0
5,000
10,000 Kilometers
N

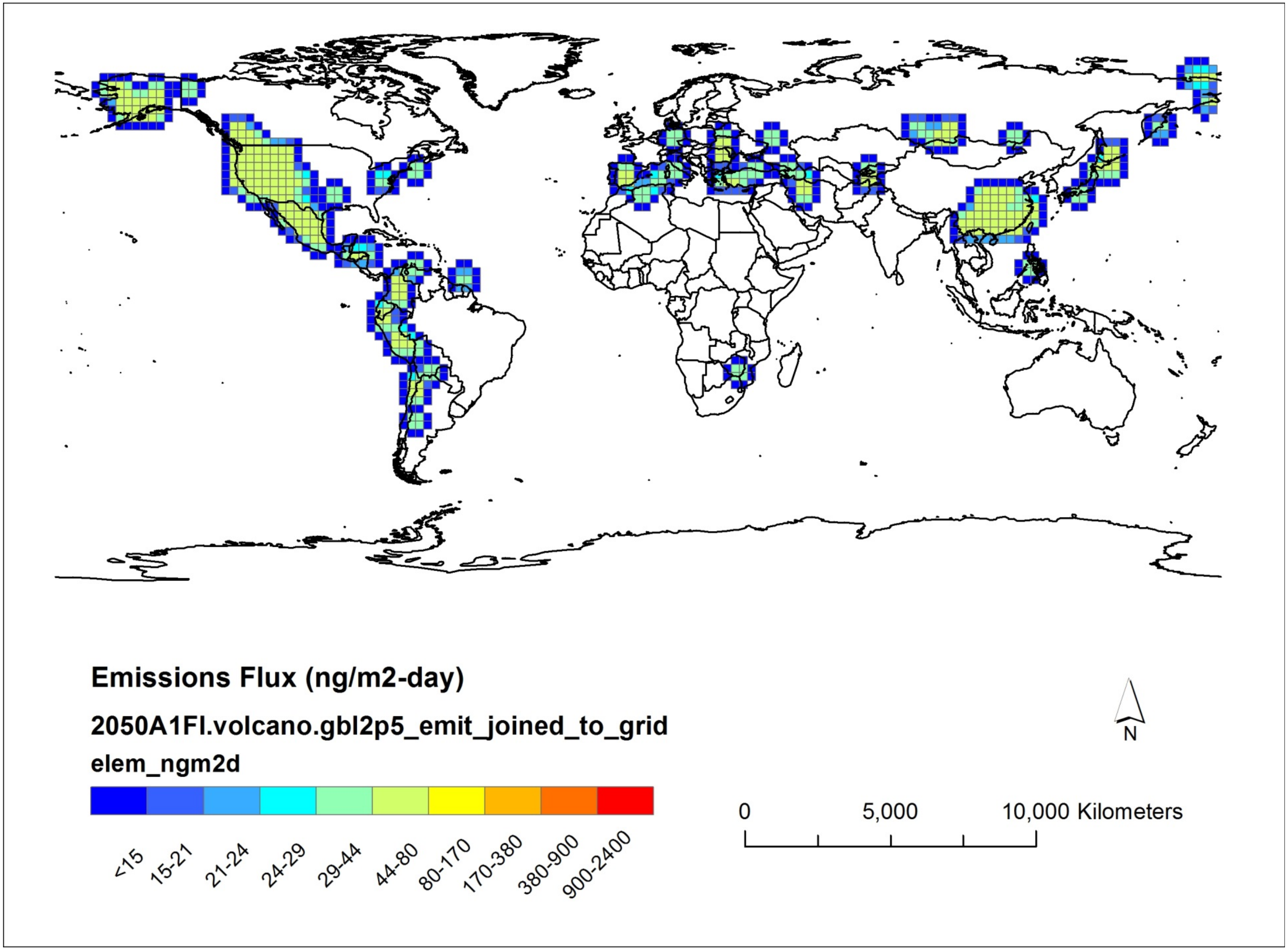
Emissions Flux (ng/m2-day)
2050A1FI.volcano.gbl2p5_emit_joined_to_grid
elem_ngm2d
<15
15-21
21-24
24-29
29-44
44-80
80-170
170-380
380-900
900-2400
0
5,000
10,000 Kilometers
N

8.10. Total

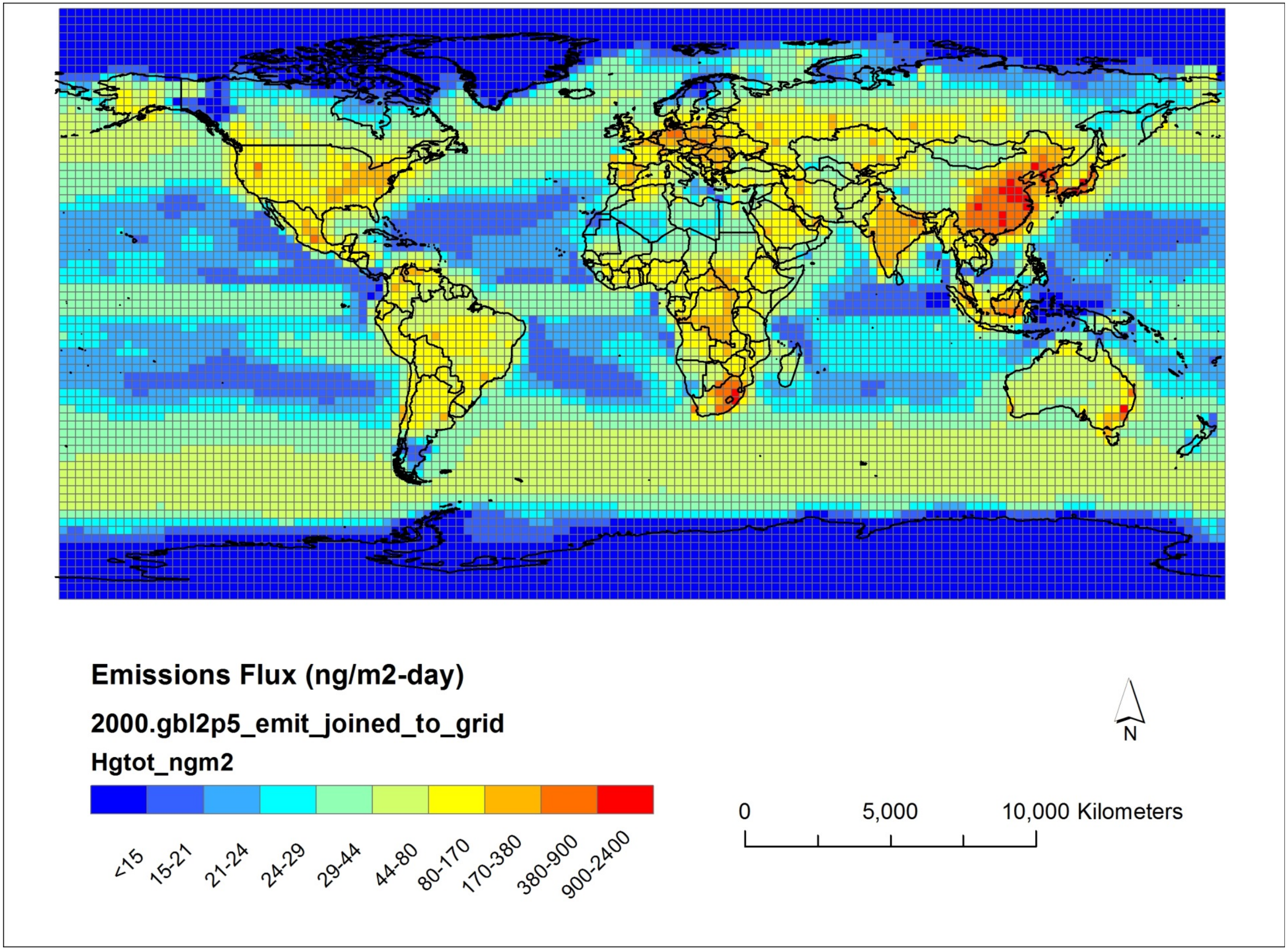
Emissions Flux (ng/m2-day)
2000.gbl2p5_emit_joined_to_grid
Hgtot_ngm2
<15
15-21
21-24
24-29
29-44
44-80
80-170
170-380
380-900
900-2400
N
0
5,000
10,000 Kilometers

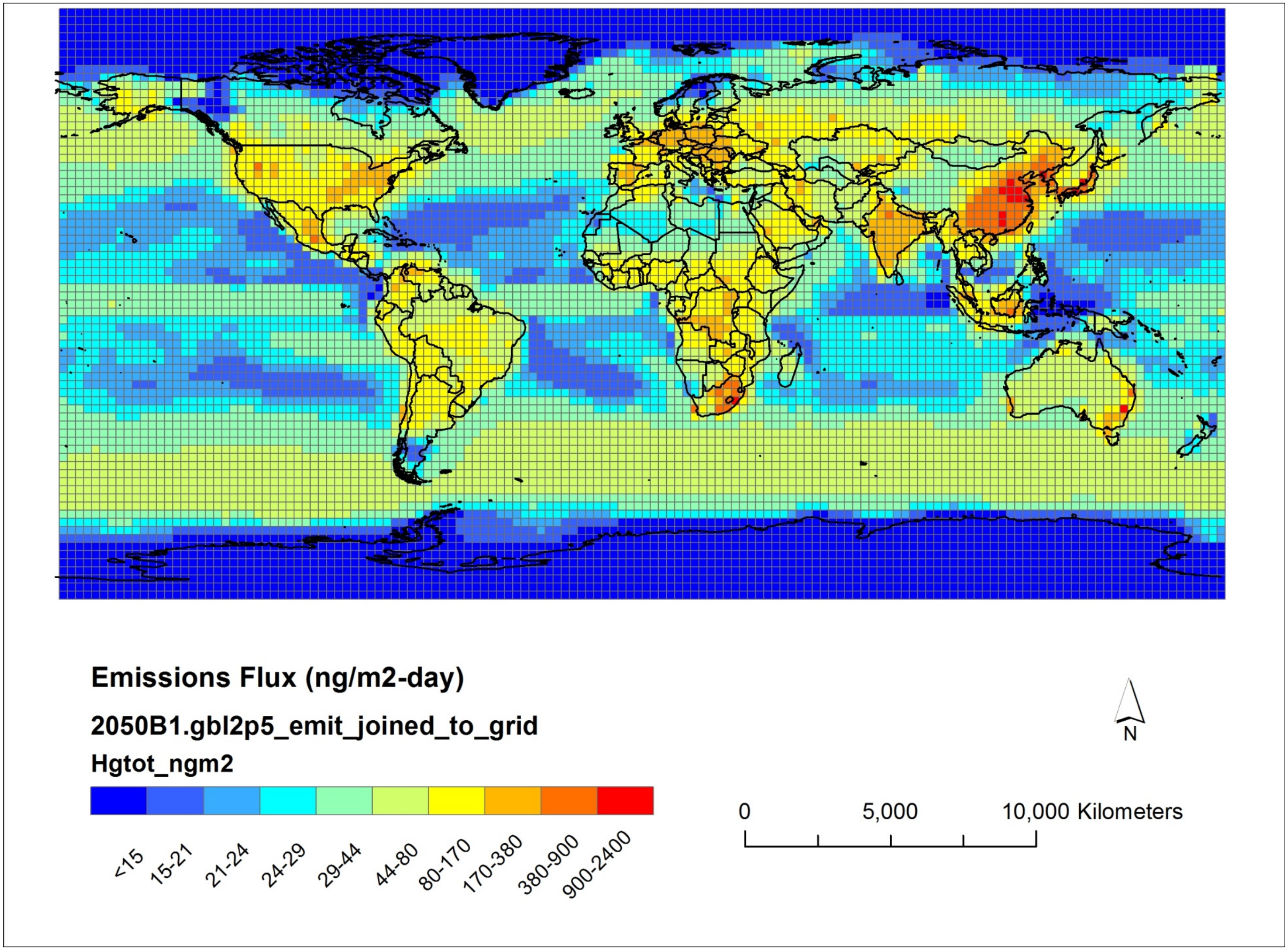
Emissions Flux (ng/m2-day)
2050B1.gbl2p5_emit_joined_to_grid
Hgtot_ngm2
<15
15-21
21-24
24-29
29-44
44-80
80-170
170-380
380-900
900-2400
N
0
5,000
10,000 Kilometers

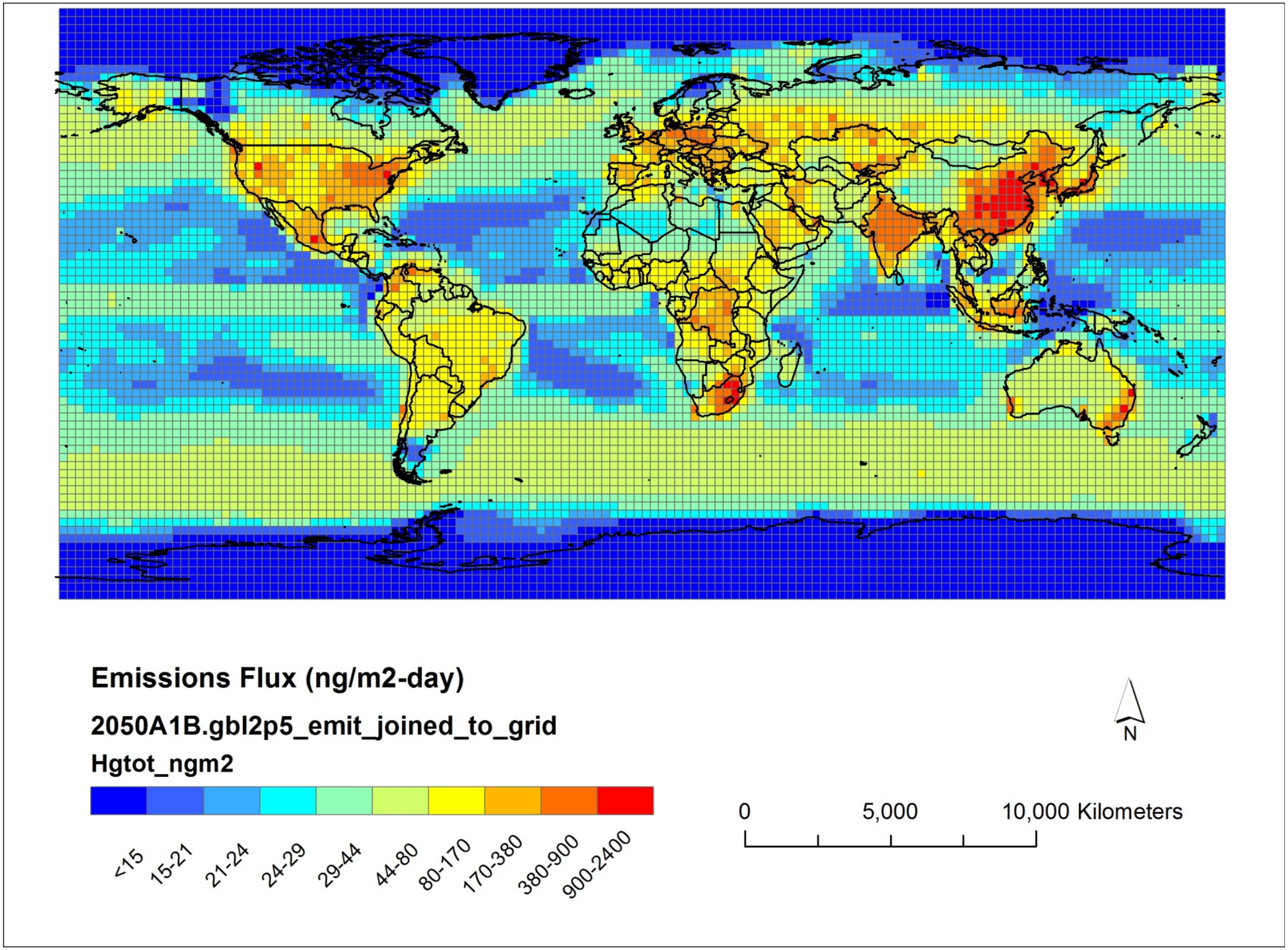
Emissions Flux (ng/m2-day)
2050A1B.gbl2p5_emit_joined_to_grid
Hgtot_ngm2
<15
15-21
21-24
24-29
29-44
44-80
80-170
170-380
380-900
900-2400
0
5,000
10,000 Kilometers
N

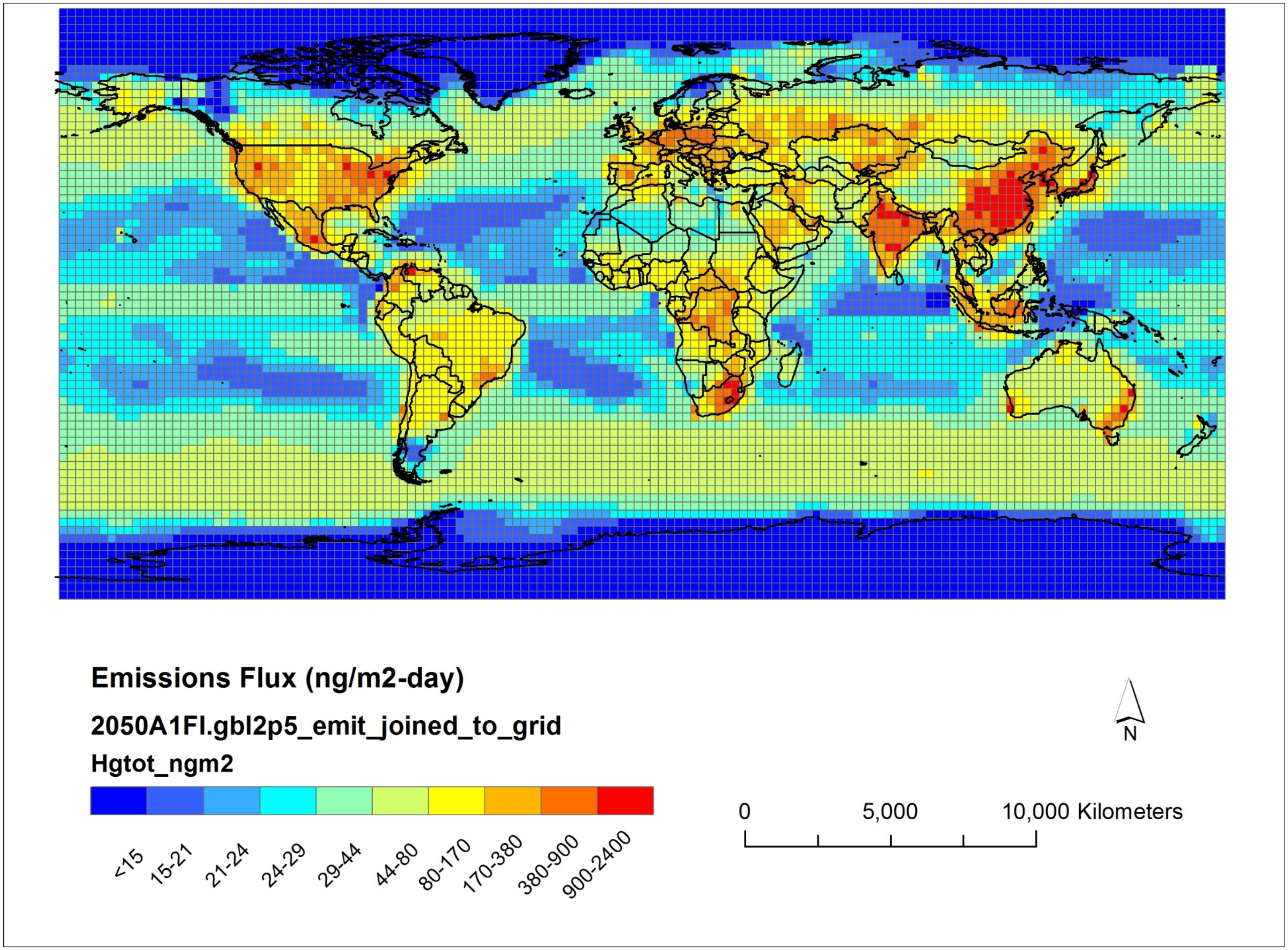
Emissions Flux (ng/m2-day)
2050A1FI.gbl2p5_emit_joined_to_grid
Hgtot_ngm2
<15
15-21
21-24
24-29
29-44
44-80
80-170
170-380
380-900
900-2400
0
5,000
10,000 Kilometers
N

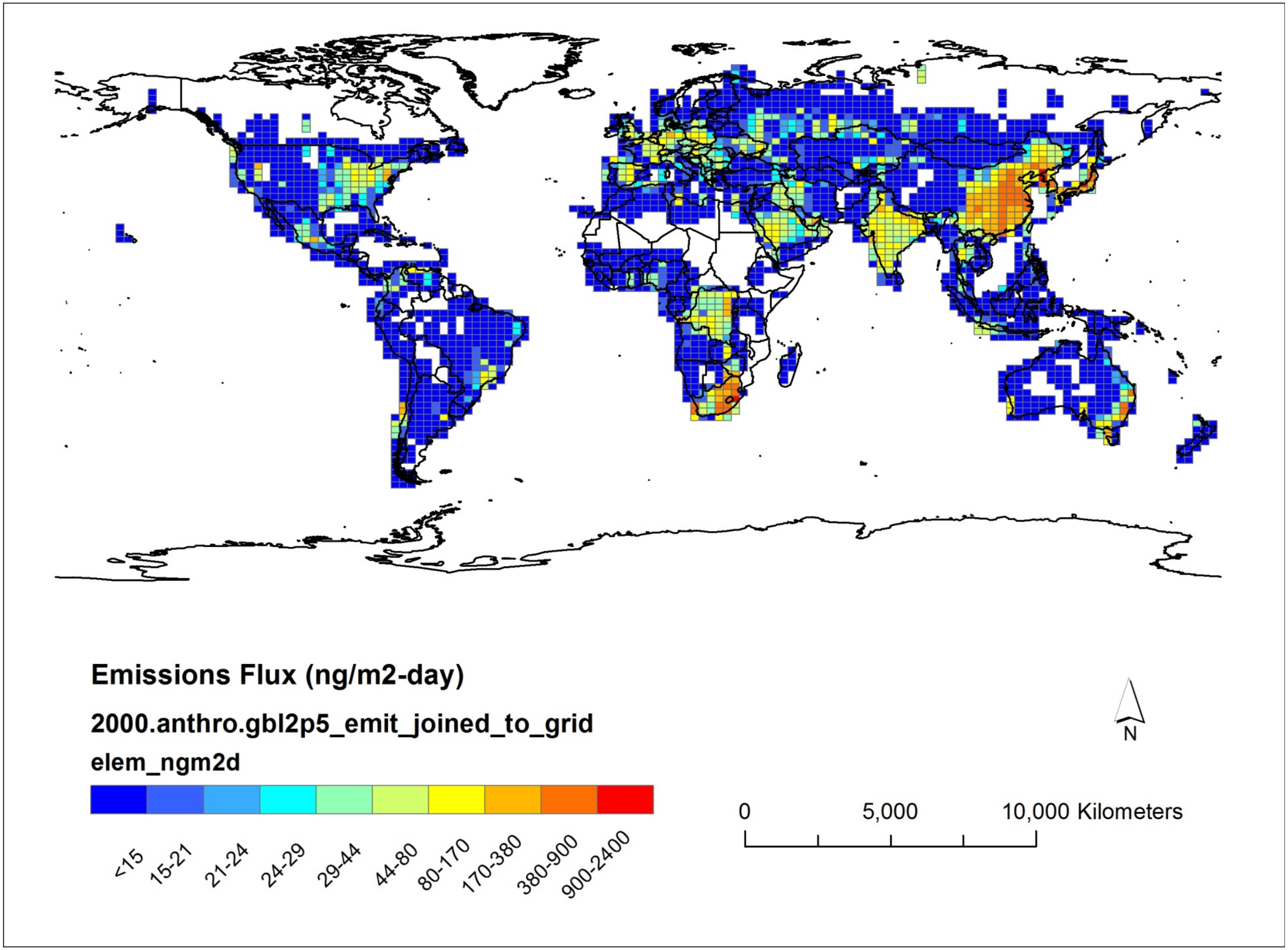
Emissions Flux (ng/m2-day)
2000.anthro.gbl2p5_emit_joined_to_grid
elem_ngm2d
<15
15-21
21-24
24-29
29-44
44-80
80-170
170-380
380-900
900-2400
0
5,000
10,000 Kilometers
N

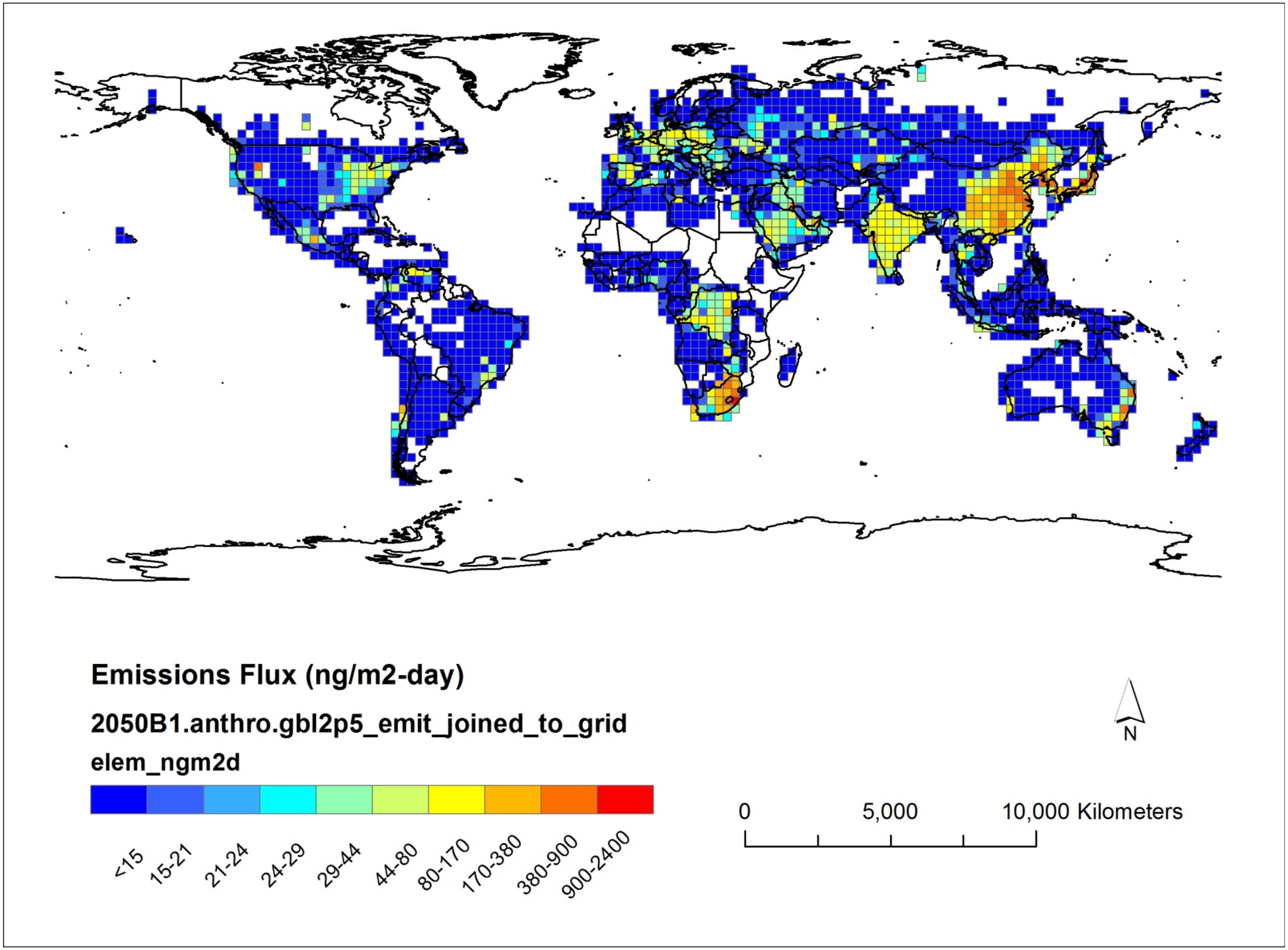
Emissions Flux (ng/m2-day)
2050B1.anthro.gbl2p5_emit_joined_to_grid
elem_ngm2d
<15
15-21
21-24
24-29
29-44
44-80
80-170
170-380
380-900
900-2400
0
5,000
10,000 Kilometers
N

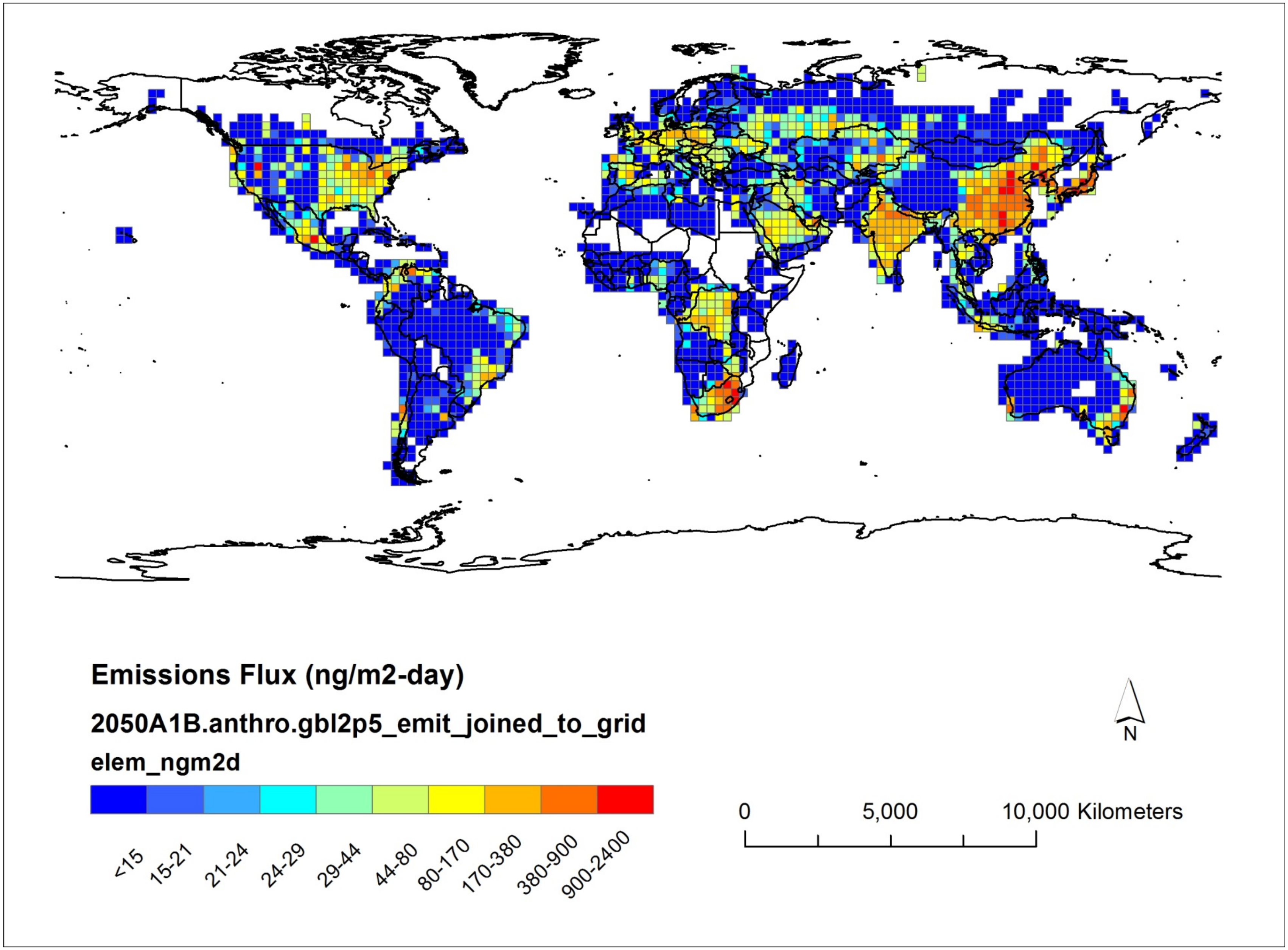
Emissions Flux (ng/m2-day)
2050A1B.anthro.gbl2p5_emit_joined_to_grid
elem_ngm2d
<15
15-21
21-24
24-29
29-44
44-80
80-170
170-380
380-900
900-2400
0
5,000
10,000 Kilometers
N

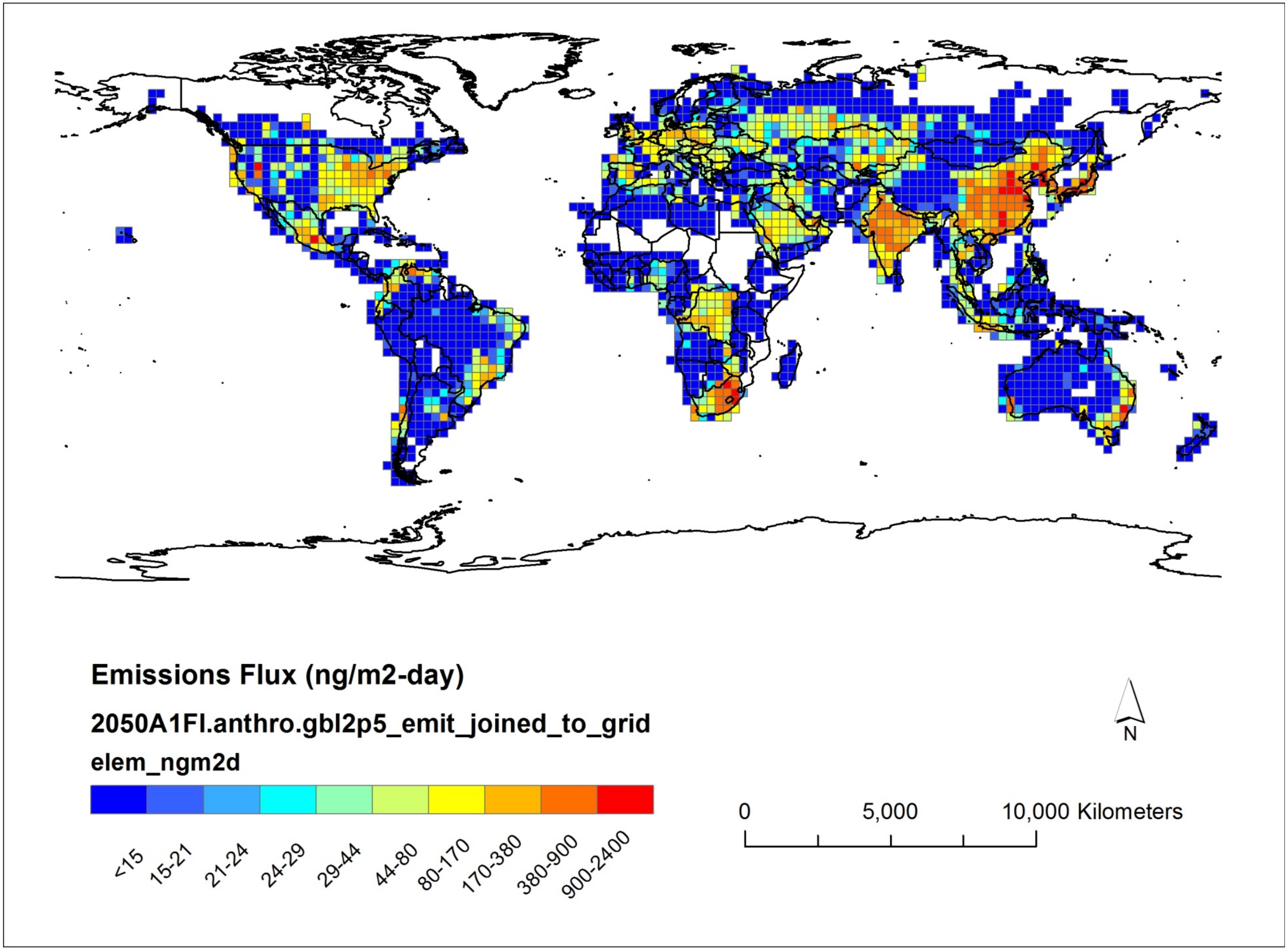
Emissions Flux (ng/m2-day)
2050A1FI.anthro.gbl2p5_emit_joined_to_grid
elem_ngm2d
<15
15-21
21-24
24-29
29-44
44-80
80-170
170-380
380-900
900-2400
0
5,000
10,000 Kilometers
N